NUMERICAL MODELLING OF AGGLOMERATE DEGRADATION

Kek Kiong Yin, B.Eng.

Doctor of Philosophy

THE UNIVERSITY OF ASTON IN BIRMINGHAM

May 1992

The University of Aston in Birmingham.

NUMERICAL MODELLING OF AGGLOMERATE DEGRADATION.

Kek Kiong Yin.

Thesis submitted for the degree of Doctor of Philosophy.

1992.

Summary

In the processing industries particulate materials are often in the form of powders which themselves are agglomerations of much smaller sized particles. During powder processing operations agglomerate degradation occurs primarily as a result of collisions between agglomerates and between agglomerates and the process equipment. Due to the small size of the agglomerates and the very short duration of the collisions it is currently not possible to obtain sufficiently detailed quantitative information from real experiments to provide a sound theoretically based strategy for designing particles to prevent or guarantee breakage. However, with the aid of computer simulated experiments, the micro-examination of these short duration dynamic events is made possible.

This thesis presents the results of computer simulated experiments on a 2D monodisperse agglomerate in which the algorithms used to model the particle-particle interactions have been derived from contact mechanics theories and, necessarily, incorporate contact adhesion. A detailed description of the theoretical background is included in the thesis.

The results of the agglomerate impact simulations show three types of behaviour depending on whether the initial impact velocity is high, moderate or low. It is demonstrated that high velocity impacts produce extensive plastic deformation which leads to subsequent shattering of the agglomerate. At moderate impact velocities semi-brittle fracture is observed and there is a threshold velocity below which the agglomerate bounces off the wall with little or no visible damage. The micromechanical processes controlling these different types of behaviour are discussed and illustrated by computer graphics. Further work is reported to demonstrate the effect of impact velocity and bond strength on the damage produced. Empirical relationships between impact velocity, bond strength and damage are presented and their relevance to attrition and comminution is discussed. The particle size distribution curves resulting from the agglomerate impacts are also provided.

Computer simulated diametrical compression tests on the same agglomerate have also been carried out. Simulations were performed for different platen velocities and different bond strengths. The results show that high platen velocities produce extensive plastic deformation and crushing. Low platen velocities produce semi-brittle failure in which cracks propagate from the platens inwards towards the centre of the agglomerate. The results are compared with the results of the agglomerate impact tests in terms of work input, applied velocity and damage produced.

Key words: Computer simulated experiments
                 Contact mechanics
                 Agglomerates
                 Fracture / Fragmentation
                 Impact
                 Diametrical compression

Dedication.

This thesis is dedicated to my girl friend, Joyce Tam Wai Yee, for the patience and support over the past few years.

.

ACKNOWLEDGEMENTS

CONTENTS

CONTENTS

List of Figures

List of Figures

List of Figures

List of Figures

List of Figures

11

List of Figures

List of Figures

List of Tables

14

1. Introduction

As far as the laws of mathematics refer to reality, they are not
certain; and as far as they are certain, they do not refer to reality.

-Albert Einstein

"To understand how nature works, one has only to start from first principles." Yet to many of us, first principles means producing a set of governing equations or working through a pre-conceived idea. Research is known to be based on man's imagination and the fundamental studies and breakthroughs in the field of science and engineering have always been associated with real physical experiments. Equations are vigorously manipulated mathematically to conform with the experimental data. Man has often been inspired by each new contribution, new idea and strived to make further improvements. Yet along this path to pursue the unknown, man has intuitively been inclined to believe in obtaining the 'answers' through the 'experimental way'. Any other means is but a fallacy until it is confirmed by experimental results.

The introduction of computing power in recent years has made a phenomenal impact on many scientists in their quest for excellence. Computer generated results using numerical analysis have given a better understanding and insight which were once unthought of. New techniques are developed to 'test' and correlate with real experiments to fully justify the authenticity of computer generated results. One common example is the use of the Finite Element Method (F.E.M) which uses a continuum approach to obtain detailed stress/strain distributions within materials by considering the material to be composed of a large number of small elements. However, this technique does not always provide accurate results because it depends on the actual discretisation of the material and on the validity of the constitutive laws incorporated into the formulation. The F.E.M, due to the arbitrarily selected elements and the continuum mechanics constitutive laws, cannot explain how the macroscopic behaviour of particulate materials is related to the properties of the constituent particles.

The Distinct Element Method (D.E.M), Cundall and Strack (1979), was developed in order to examine how the internal micromechanics of systems of discrete particles is related to the complex macroscopic behaviour of the particulate material. The method uses the physical and mechanical properties as input parameters. The 'constitutive laws' are the particle interaction laws which define the contact stiffnesses. Using statistical mechanics, the data can be analysed to provide the bulk mechanical properties of the system as output information. In addition, the detailed evolution of the micromechanical processes may be examined using computer graphics.

Because of its methodology the D.E.M is applicable to a wide range of problems in particulate technology. There is hardly a branch of science and engineering which is not concerned with particulate technology - civil engineers working on problems of soil mechanics, metallurgical engineers working in the area of powder metallurgy, mechanical engineers on pneumatic and hydraulic transport of particulate materials.

The degradation or attrition of particulate materials during handling and processing is a common occurrence in the chemical, agricultural and allied industries. In these industries particle attrition can be the cause of two main problems. Firstly, it changes the physical properties of the material such as particle size distribution, surface area, flowability and density, causing difficulties with subsequent handling and processing operations. Secondly, the generation of fine particles, and hence dust, can result in the loss of valuable material and requires investment in control measures to prevent damage to health and the general environment.

Most particle degradation is a result of some form of motion between a particle and the wall of a vessel or another particle. This relative motion may be caused by flowing fluid, gravity or mechanical vibration. The forces involved in the breakage process may be generated by high speed collisions or may be transmitted through a matrix of comparatively slow moving particles.

Although attrition is a widespread phenomenon, it has rarely been studied in a systematic fashion and there is correspondingly little information published in the open literature. This reflects the difficulties associated with research into a subject in which a large number of parameters control and influence the process. The general paucity of information on attrition is in marked contrast to that on the related subject of comminution. In both processes large particles are broken into smaller ones. However in comminution, unlike attrition, the breakage is intentional.

The object of this research is to examine in detail the breakage of agglomerates using a numerical simulation program based on the methodology of the D.E.M. The underlying physical mechanisms that control the processes are still poorly understood. Consequently, it was proposed to study the basic interactions for a single contact before applying the program to a system of 1000 monodisperse primary particles. One should acknowledge, at this stage, that this research is based on computer simulated experiments with a relatively small number of primary particles modelled as closely as possible to reality.

1.1 Order of Presentation

Chapter 2 and 3 both deal with the mechanics of a single contact between two spherical particles. In Chapter 2 the spheres are considered to be elastic with friction but no adhesion. A detailed description of the theories of Hertz (1882), Mindlin (1949) and Mindlin and Deresiewicz (1953) is provided. These theories are used in the computer simulation program to model the normal and tangential force-displacement behaviour at the interparticle contacts. Results of computer simulated oblique impacts of two elastic spheres are then presented.

Chapter 3 considers the effect of adhesion at the contact. The theory of Johnson, Kendall and Roberts (1971) is used to model the normal interaction between two spheres. The tangential interaction is based on the theories of Savkoor and Briggs

17

(1977) and Thornton (1991). After a description of the theoretical background, the results of computer simulated oblique impacts of particles with adhesion are reported. The computer simulated impact tests reported in both Chapter 2 and Chapter 3 illustrate the complexity of such apparently simple events and demonstrate the effect of impact angle on the energy dissipated during the collisions of elastic spheres.

In Chapter 4 computer simulation is discussed and the methodology used in the computer program is described. In order to simulate agglomerates it was necessary to adapt the computer code so that contact adhesion could be modelled. The main changes made to the program occurred in the subroutine FORD which updates the contact forces. A description of the new subroutine FORD is provided. The application of the new program to computer simulated experiments on agglomerates is described in Chapter 5 and 6.

Chapter 5 presents the result obtained from computer simulations of a 2D monodisperse agglomerate, consisting of 1000 primary particles, impacting with a wall. The work reported is restricted to normal impacts. The results of the agglomerate impact simulations show three types of behaviour depending on whether the initial impact velocity is high, moderate or low. It is demonstrated that high velocity impacts produce extensive plastic deformation which leads to subsequent shattering of the agglomerate. At moderate impact velocities semi-brittle fracture is observed and there is a threshold velocity below which the agglomerate bounces off the wall with little or no visible damage. A detailed description of these different modes of behaviour is provided. Further work is reported to demonstrate the effect of impact velocity and bond strength on the damage produced. Empirical relationships between impact velocity, bond strength and damage are presented and their relevance to attrition and comminution is discussed. The particle size distribution curves resulting from the agglomerate impacts are also provided.

18

Chapter 6 presents results of computer simulated diametrical compression tests on the same agglomerate. Simulations were performed for different platen velocities and different bond strengths. The results show that high platen velocities produce extensive plastic deformation and crushing. Low platen velocities produce semi-brittle failure in which cracks propagate from the platens inwards towards the centre of the agglomerate. The results are compared with the results of the agglomerate impact tests in terms of work input, applied velocity and damage produced.

Finally, some concluding remarks are provided in Chapter 7.

1.2 Why computer simulation?

Although the computer simulation technique is a relatively new tool to enhance research, early results have proven its feasibility. Attempts to understand the microscopic behaviour of granular materials have been assisted by information about load transfer paths, failure mechanisms, energy dissipation and anisotropy which has been made possible through direct numerical simulations of particle assemblies. This thesis is based wholly on the use of a particular program which uses specific contact interaction laws to model the particles as elastic spheres with both friction and adhesion. Although the simulations are all in 2-dimension, the results obtained do agree qualitatively with published experimental work as will be shown in later chapters. In order to model 'correctly' the behaviour of discrete materials, all interaction laws adopted must be as real as possible. This is significant because without realistic interactions laws, it will be classed as computer animation and not computer simulation.

2. Impact Of Spheres Without Adhesion

Among simulationists, the real world is often a special case.

2.1 Introduction

The term 'impact' is synonymously linked to expressions including those used in such diverse fields as psychology, economics, physics and engineering. In all cases, the word denotes the idea of abruptness, coupled with a physical change in the end product. This chapter, however, treats only certain aspects of 'impact', defined as the process involved in the collision of two objects.

Impact applies to a variety of situations as exemplified by the game of snooker, vehicle accidents, air blasts upon structures and even molecular collisions. However, it is essential that the number of collisions must be restricted to a relatively small occurrence, otherwise a condition of repeated loading would prevail. Additionally, the terminology ideally limits the phrase 'impact' to collisions in which the mass effect of both impinging bodies must be taken into account, favouring the argument for the principle of conservation of linear momentum.

The concept of impact is further distinguished from the case of static or rapid loading by the nature of its application. Forces, both normal and tangential, created by collisions are exerted and removed in a very short duration of time (in the region of milliseconds) and initiate stress waves which originate from the contact area travelling outwardly. Static loading is often regarded as a series of equilibrium states and requires no serious consideration of acceleration or wave effects. Rapid loading, in contrast, is not usually produced by means of a collision and normally involves longer loading times than found in impact processes.

The impact behaviour discussed in this chapter is a combination of static loading and the elastic response of the material, which can be readily tackled by the theory of

contact mechanics. The quantitative description of the regime considered is at best only a close approximation to the real world.

The complicated process of energy conservation and loss under impact conditions leads to serious difficulties in the mathematical analysis of this type of problem. Therefore, it has been suggested that models representing any physical system must be idealised to render them amenable to theoretical treatment and the postulated dynamic behaviour of such systems must be verified by suitable physical experiments. As a consequence, complete and thorough solutions have been obtained only for simple geometrical configurations, utilising the laws of conservation of mass, conservation of momentum and a mechanical energy balance. Although many different approaches to the same problem have been recorded, no general impact theory has been developed to date.

In the work presented in this and the following chapter, consideration will be restricted to the impact behaviour of perfectly elastic spheres. Notwithstanding the complications of the real physical world, as mentioned above, it is hoped that the results presented will provide a rational contribution to current and future research.

2.2 Brief Literature Review

The fundamental principle for a rational description of impact and impact associated phenomena was established simultaneously with the evolution of the science of mechanics. The initial approach to the laws of collisions was based on the behaviour of objects as rigid bodies, with suitable correction factors accounting for energy losses. The initial concept of rigid body impact is due to Galileo, who recognised that impact performs work, but confused the ideas of momentum and energy. Newton furnished not only his law of motion but also the notion of the coefficient of restitution, which is still widely adopted in many research fields, though of questionable fundamental significance.

It was only towards the end of the last century when Hertz (1882) (see Johnson (1982)) forwarded his theory of local deformation for perfectly elastic spheres. This theory enables predictions to be made about, for example, the stress and displacement fields in the bodies and the duration of the impact. Lifshitz and Kolsky (1964) carried out validation experiments on elastic rebounds based on the Hertzian theory. Hunter (1957) showed that the Hertzian theory was quasi-static in the sense that the theory neglected loss of energy in transmitted stress waves. Deresiewicz (1968) showed that it is possible to accurately predict the duration of the impact using the basic principle of the Hertzian theory of local deformation.

The tangential response during oblique loading was examined by Mindlin (1949) and Catteneo (1938). As the bodies respond to tangential forces, some of the work done in deflecting the bodies tangentially is stored as elastic strain energy in the solids and is recoverable under suitable circumstances. The relative displacements are not necessarily constant over the contact area and it is possible for some region to stick while others are sliding. Mindlin (1949) showed that even when a small but finite tangential load is present, an annulus of slip is generated at the boundary of the contact. If the tangential load is allowed to increase, the inner radius of this annulus progressively reduces until, when a critical value of tangential force is reached, the bodies starts to slide. Mindlin described these conditions as micro-slip and gross-slip respectively.

Mindlin and Deresiewicz (1953) developed compliance relationships for cases in which both normal and tangential loads may vary. Owing to the presence of slip with its associated energy dissipation and permanent set, the changes in tractions and displacements depend not only upon the initial state of loading, but upon the entire past history of loading and the instantaneous relative rates of change of the normal and tangential forces.

2.3 Normal Impact

The first attempt to incorporate a theory of local indentations or deformation and consequently the analysis of the stresses at a contact was initiated by Hertz (1882) (see Johnson (1985)). A solution was obtained in the form of a potential which described the stresses and deformations in the locality of the contact point as a function of the geometrical and elastic properties of the bodies. This result, although both static and elastic in nature, has been widely adopted for impact situations under non-quasi-static conditions. The use of Hertzian theory beyond the limits of its validity has been justified on the basis that it appears to predict accurately most parameters that can be experimentally verified.

Hertzian theory predicts the static normal compression of two isotropic elastic bodies whose surfaces are assumed to be perfectly smooth. Figure 2.1 shows the geometry of the contact plane due to local deformation.

For two contacting spheres of radii R_i (i=1, 2), the Hertzian pressure distribution acting over the small circular contact area of radius, a, is illustrated in figure 2.2 and expressed as

$$p(r) = p_0 [1 - (r/a)^2]^{1/2} \tag{2.1}$$

which leads to normal displacements over the contact area

$$u_i(r) = (\pi p_0 (1 - v_i^2) / 4E_i a) (2a^2 - r^2) \tag{2.2}$$

where E_i and v_i are Young's modulus and Poisson's ratio for the respective sphere, and equation (2.2) satisfies the following boundary condition for the surface of the contact area

$$u_1(r) + u_2(r) = \alpha - (1/2R^*)r^2 \tag{2.3}$$

as defined in figure 2.1
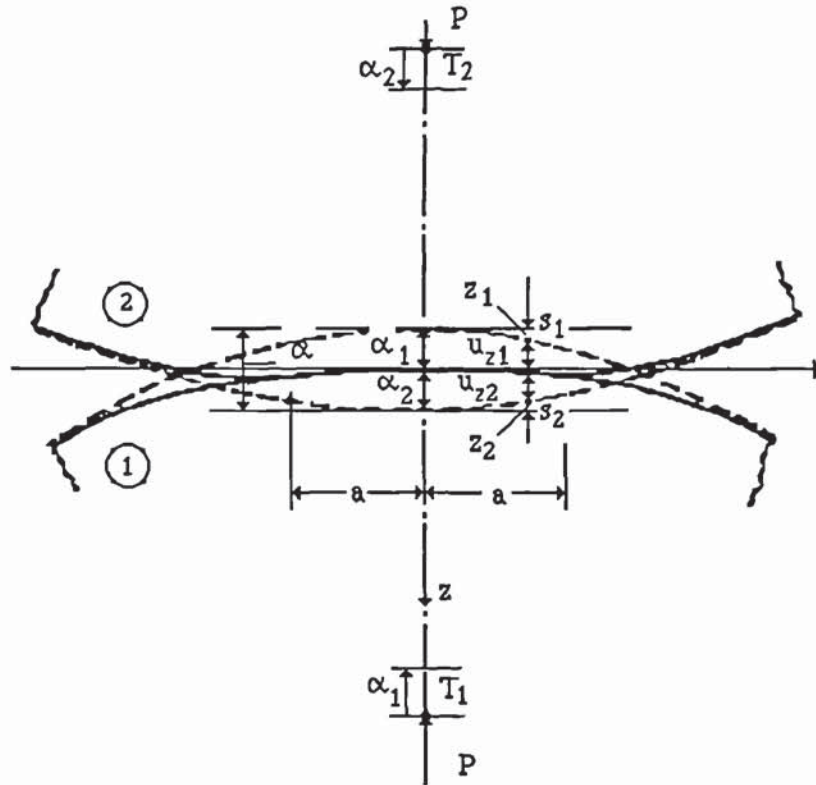
Figure 2.1 Deformation over the contact plane for two conforming spheres
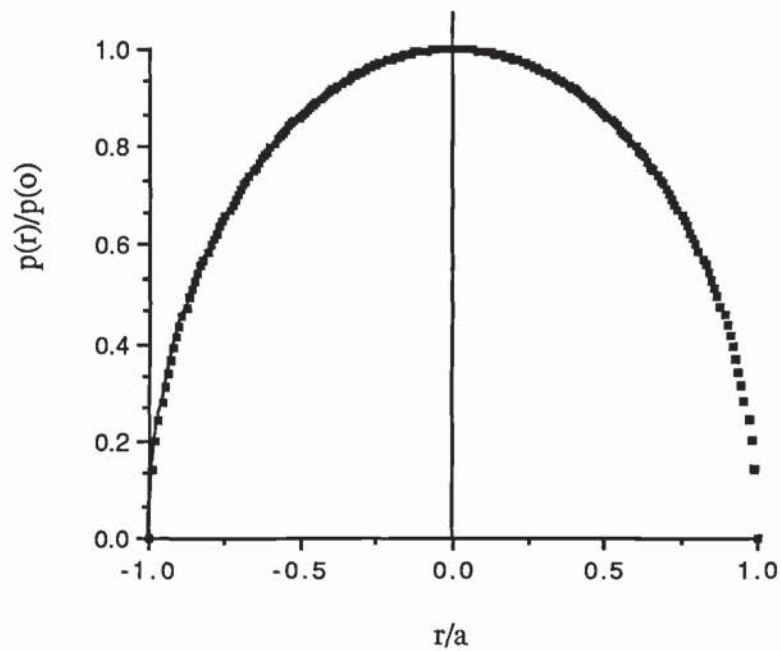
Figure 2.2 Hertzian pressure distribution over contact area

24

where,

$$1/R^* = 1/R_1 + 1/R_2 \qquad (2.4)$$

and α is the relative approach of the centroids of the two spheres in contact.

Substitution of (2.2) into (2.3) for i = 1, 2 leads to

$$(\pi p_o/4aE^*)(2a^2 - r^2) = \alpha - (1/2R^*)\,r^2 \qquad (2.5)$$

where

$$1/E^* = (1 - v_1^2)/E_1 + (1 - v_2^2)/E_2 \qquad (2.6)$$

Substituting r = 0 into (2.5), the relative approach of the sphere centroids is

$$\alpha = \pi p_o a/2E^* \qquad (2.7)$$

and the radius of the contact area is obtained from (2.5) and (2.7) with r = a to give

$$a = \pi p_o R^*/2E^* \qquad (2.8)$$

The total normal load is defined as

$$P = \int_0^a p(r)2\pi r\, dr = 2p_o\pi a^2/3 \qquad (2.9)$$

which may be substituted into (2.7) and (2.8) to give

$$a^3 = 3PR^*/4E^* \qquad (2.10)$$

and

$$\alpha^3 = 9P^2/16R^*E^{*2} \qquad (2.11)$$

noting also that

$$\alpha = a^2/R^* \qquad (2.12)$$

For computer implementation it is necessary to define the normal 'stiffness'. Therefore, rearranging (2.11),

$$P = 4E^*(R^*\alpha^3)^{1/2}/3 \qquad (2.13)$$

from which the 'stiffness' is defined as

$$dP/d\alpha = 2E^*(R^*\alpha)^{1/2} \qquad (2.14)$$

or, using (2.12),

$$dP/d\alpha = 2E^*a \qquad (2.15)$$

However, (2.15) cannot be used for the first contact calculation and therefore if a = 0, then it is necessary to use (2.13) noting that for a = 0, P = ΔP, α = $\Delta\alpha$.

The normal force displacement relationship given by (2.13) is illustrated in figure 2.3.
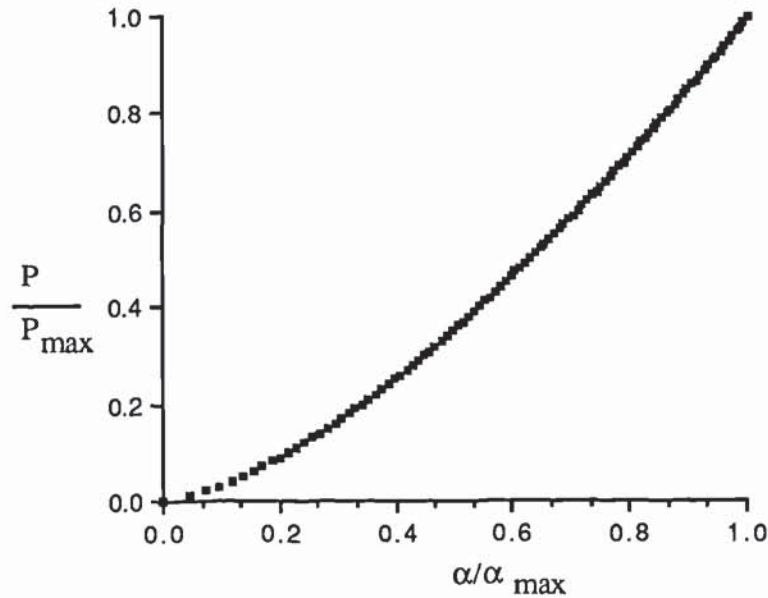
Figure 2.3 Hertzian force displacement curve

The theory can be further extended to predict the impact duration for two perfectly elastic spheres. Deresiewicz (1968) showed that for two spheres of masses m_1 and m_2, and velocities V_1 and V_2 acting normal to their contact, the relative velocity is given as,

$$V_2 - V_1 = d\alpha/dt \qquad (2.16)$$

The normal force between them is,

$$P = m_1 \, dV_1/dt = - m_2 \, dV_2/dt \qquad (2.17)$$

thus,

$$-P/m^* = d(V_2 - V_1)/dt = d^2\alpha/dt^2 \qquad (2.18)$$

where,

$$1/m^* = 1/m_1 + 1/m_2$$

The load-displacement relationship is assumed to be the same as for a static elastic contact, rearranging (2.11),

$$P = (4/3) \, [R^{*1/2}E^*\alpha^{3/2}] = K\alpha^{3/2} \qquad (2.19)$$

26

and hence,

$$m^* \, d^2\alpha/dt^2 = -K\alpha^{3/2} \tag{2.20}$$

Integrating (2.20) gives

$$0.5 \left[V_n^2 - (d\alpha/dt)^2 \right] = (2/5) (K/m^*)\alpha^{5/2} \tag{2.21}$$

where

$V_n = (V_2 - V_1)_{t=0}$ is the approach velocity.

At the maximum compression α^*, $d\alpha/dt = 0$,

$$\alpha = (5m^* \, V_n^2/4K)^{2/5} = [15m^* \, V_n^2/16R^{*1/2}E^*]^{2/5} \tag{2.22}$$

The compression time curve is found by a second integration, thus

$$t = (\alpha^*/V_n) \int d(\alpha/\alpha^*)/\{1-(\alpha/\alpha^*)^{5/2}\}^{1/2} \tag{2.23}$$

This integral has been evaluated by Deresiewicz (1968) and is presented as a force- time curve in figure 2.4. After the instant of maximum compression t^*, the spheres expand again. Since they are perfectly elastic and frictionless, if the energy absorbed in wave motion is neglected, the deformation is perfectly reversible. The total time of impact T_c is therefore, given by,

$$T_c = 2t^* = (2\alpha^*/V_n) \int_0^1 d(\alpha/\alpha^*)/ \{1-(\alpha/\alpha^*)^{5/2}\}^{1/2}$$

$$= 2.94 \, \alpha^*/V_n$$

$$= 2.87 \, (m^{*2}/RE^{*2}V_n)^{1/5} \tag{2.24}$$
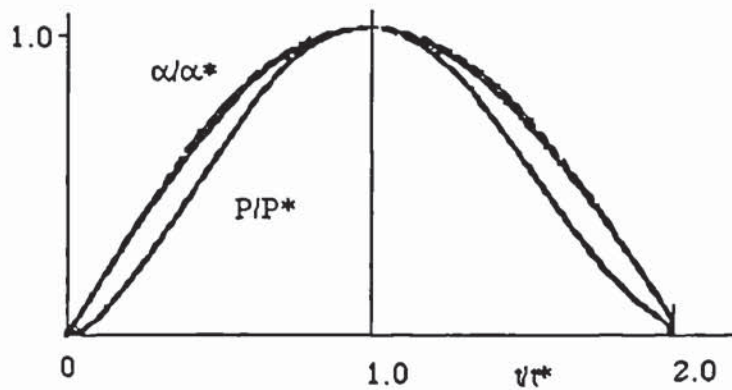
Figure 2.4 Variation of compression α and force P with time during a Hertz impact

2.4 Oblique Impact

An application of a tangential force to a system of two spheres brought in contact, may not give rise to a sliding motion but nevertheless, will induce a tangential traction distribution on the contact interface. It is essential to examine the sequence of tangential tractions that may arise from a combination of normal and tangential forces which does not cause the bodies to slide relative to each other.

The problem is illustrated in figure 2.5. When two bodies are compressed and held together by a constant normal force, P, a finite contact region is established on the contact interface as the result of elastic deformation on the two conforming surfaces.

Figure 2.5   Contact interface with shear deformation due to application of tangential force

The corresponding pressure distribution will, as in the Hertzian assumption, remain unhindered by the presence of the tangential force, T. On the contrary, the application of the tangential force, T, will result in the bodies deforming in shear as indicated by the distorted centreline. It then follows that positions on the contact interface at the deformed regime of each of the two conforming bodies will experience a tangential

28

displacement u_x relative to the distant points T_1 and T_2 in the undeformed regime of each body. If sliding motion were to persist between the two bodies, then all conjugate points on the contact interface deform with no relative motion. However, when there is no sliding motion, then there must be at least one point at the contact interface where the surfaces deform under no relative motion. Therefore for a tangential force less than the limiting friction force, $T < \mu P$ (no sliding) deformation as shown by A_1 and A_2 results and this small but finite relative motion is termed as slip or microslip. The remainder of the interface deforms without relative motion and in such regions the surfaces are said to adhere or stick. For convenience in terminology and to avoid confusion in the next chapter, it is best to use 'stick' as opposed to adhere, for no relative tangential motion.

To proceed with the set of boundary conditions governing 'stick' and 'slip', A_1 and A_2 denote two point on the interface which were coincident before the application of the tangential force. Under the influence of the tangential force, remote points in the body such as T_1 and T_2, move through rigid displacements δ_{x1} and δ_{x2} while the conjugate points at the deformable contact interface, A_1 and A_2 experience tangential elastic displacements u_{x1} and u_{x2} relative to T_1 and T_2. If the absolute displacements of A_1 and A_2 relative to O are denoted by s_{x1} and s_{x2}, then the components of slip between A_1 and A_2 may be written

$$s_x = s_{x1} - s_{x2} = (u_{x1} - \delta_{x1}) - (u_{x2} - \delta_{x2})$$
$$= (u_{x1} - u_{x2}) - (\delta_{x1} - \delta_{x2}) \tag{2.25}$$

If the position of A_1 and A_2 were coincident to each other (in the stick regime) the slip s_x will be zero, equation (2.25) then becomes

$$(u_{x1} - u_{x2}) = (\delta_{x1} - \delta_{x2}) = \delta_x \tag{2.26}$$

The right hand side of this equation denotes a relative tangential displacement between the two bodies as a whole under the influence of the tangential force. Hence, it can be shown conclusively that δ_x is constant and independent of the position of A_1 and A_2 within the 'stick' regime. The condition of no slip embodied by (2.26) is thus the

29

situation where all points on the contact surface within a 'stick' regime undergo no relative tangential displacement.

At points within the stick region the resultant tangential traction cannot exceed its limiting value. Assuming Amonton's law of friction with a coefficient μ, this restriction may be stated

$$q(x) \leq \mu \, |p(x)| \qquad (2.27)$$
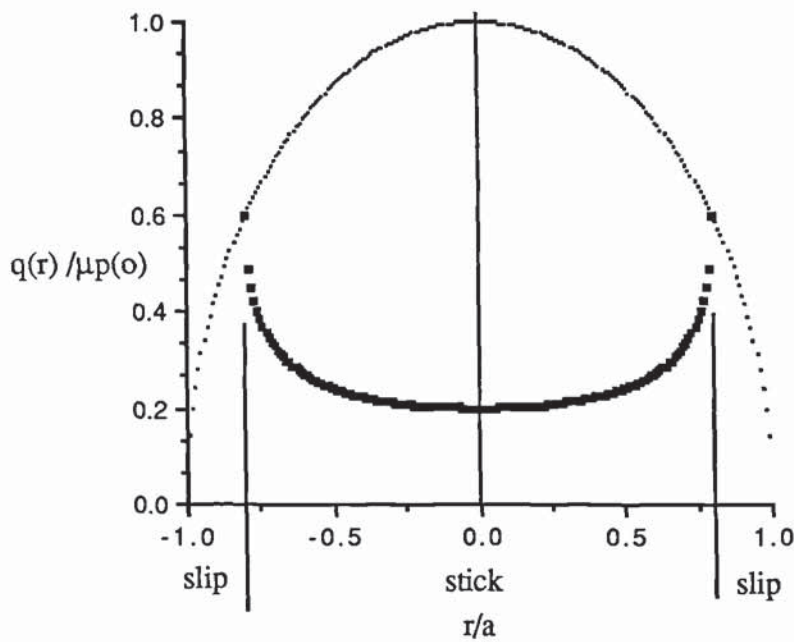
Figure 2.6 Tangential Traction Diagram, showing the stick and slip regions

In the slip region, the condition of (2.26) does not hold, but the tangential and normal tractions (figure 2.6) are related by

$$|q(x)| = \mu \, |p(x)| \qquad (2.28)$$

Difficulty arises in the solution to predict the areas of the stick and slip regimes as neither is known a priori. In a circumstance like this, it would be best to assume a fully no slip solution initially over the contact interface. Slip is then likely to occur when the tangential force exceeds the limiting frictional value.

Having established the co-existence of stick and slip region on the contact interface, it is best to re-examine why it is not possible to have a complete no slip case.

2.4.1 Mindlin's No Slip Solution

Mindlin (1949) first forwarded the theory for no slip over the contact interface. The tangential traction distribution is defined by,

$$q(r) = (T/2\pi a^2) (1 - r^2/a^2)^{-1/2} \tag{2.29}$$

with the corresponding displacement

$$u_x = (2 - v)T / 8Ga \tag{2.30}$$

which must satisfy the boundary condition set in (2.26). Hence, the relative tangential displacement of the two bodies in contact is,

$$\delta = \frac{T}{8a} \left(\frac{2 - v_1}{G_1} + \frac{2 - v_2}{G_2} \right) = \frac{T}{8G^*a} \tag{2.31}$$

This relationship is shown by the dotted line in figure 2.7. The tangential displacement is directly proportional to the tangential force.
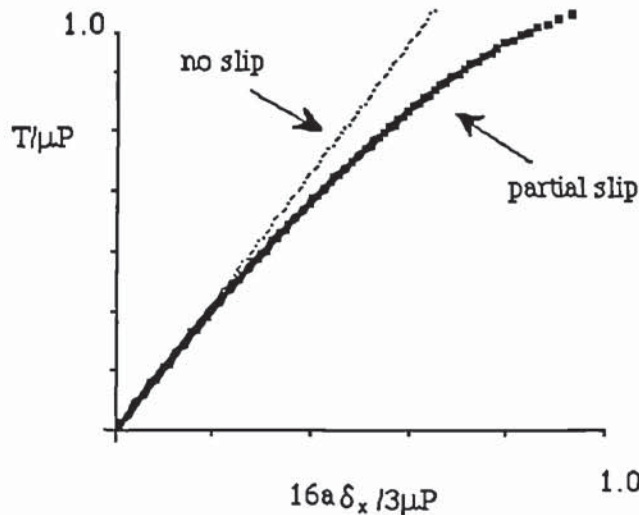
Figure 2.7 Tangential load-displacement relationships for no 'slip'and 'partial slip'

Since this is a no slip solution, it corresponds to the solution for a fully 'adhered' contact and since there is no relative motion between the points on the contact interface

of the two spheres, the solution does not admit the possibility of spin. However, as shown in figure 2.8, there exists a theoretically infinite traction at the periphery of the contact area, which then leads to a situation where some micro-slip will be inevitable at the edge, in order to relieve this infinitely high tangential traction.
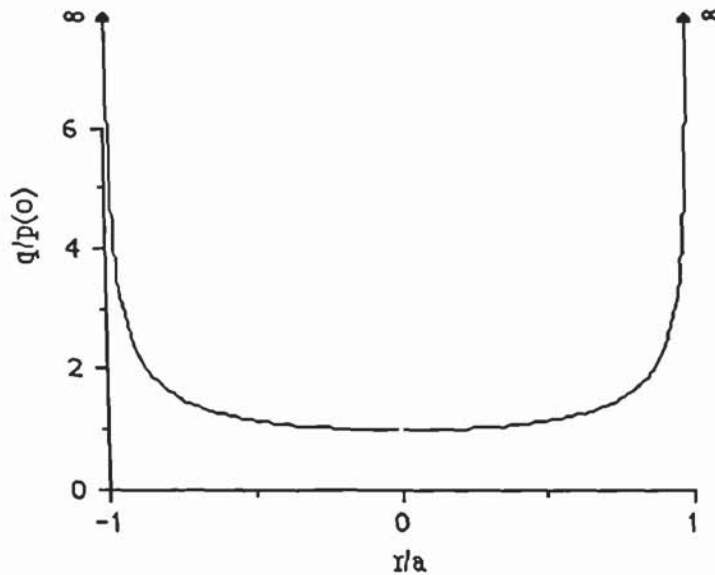
Figure 2.8 Tangential traction with no slip

2.4.2 Mindlin's Partial Slip Solution

In the partial slip approach, for a constant normal force ($\Delta P=0$), the effect of a tangential force, $T<\mu P$, is to cause slip over part of the contact interface. Since the contact area is of circular shape, a slip in the shape of an annulus is subsequently formed. The formation of this slip or annulus is due to the tangential motion of points over the contact interface. This suggests an alternative solution to the otherwise no slip approach.

The partial slip approach suggests the formation of a slip annulus which starts from the circumference of the contact area and progresses radially inwards towards the centre. Hence there exists an outer region of slip, whilst a stick region is present in the centre as long as $T<\mu P$. The theory requires that for any location within the contact surface,

the magnitude of the local tangential traction τ, is at most equal to the product of a constant coefficient of friction μ and the local normal traction σ. In addition, the magnitude of the tangential force and consequently the tangential traction, is a function of the load obliquity. Figure 2.9 shows the formation of slip annuli created at different inclinations of total load.

Aston University

Illustration removed for copyright restrictions

Figure 2.9 Annuli of slip. (*Johnson, 1985*)

Slip, in the direction of the force causing it, progresses radially inward from the boundary of the contact surface, forming an annulus of slip. When $T=\mu P$, the limiting criterion, no part on the contact area is 'stuck' and rigid body sliding occurs. The development of the slip annuli involves a dissipative process. If the tangential force is reduced then slip in the opposite direction or counterslip spreads radially inwards from the perimeter of the contact area. The energy needed to produce the annulus of counterslip is twice that needed to form the original slip annulus since the counterslip has to cancel the original slip and progress the slip in the opposite direction. If the annulus of counterslip did not fully progress to the same extent as the original slip annulus, and the tangential loading is once more reversed, an annulus of slip in the original direction would progress radially inward. This slip annulus would also require

twice the energy of formation of the original annulus due to the cancelling and reversal of the counterslip annulus. In general, all load reversals initiate slip reversals that spread radially inwards from the perimeter of the contact area, rather than causing a recession of the existing slip annulus. Consequently the tangential stiffness is dependent on the loading history.

2.4.3 Tangential Loading

For the limiting condition of $T = \mu P$ to prevail, the distribution of the tangential traction is given by

$$q(r) = (\mu p_o/a) \, (a^2 - r^2)^{1/2} \qquad\qquad 0<r<a \qquad\qquad (2.32)$$

For $T < \mu P$, the corresponding traction distribution is obtained by superimposing on (2.32) a negative traction over the stick regime of radius b ($< a$)

$$q(r) = -(\mu p_o/a) \, (b^2 - r^2)^{1/2} \qquad\qquad 0<r<b \qquad\qquad (2.33)$$
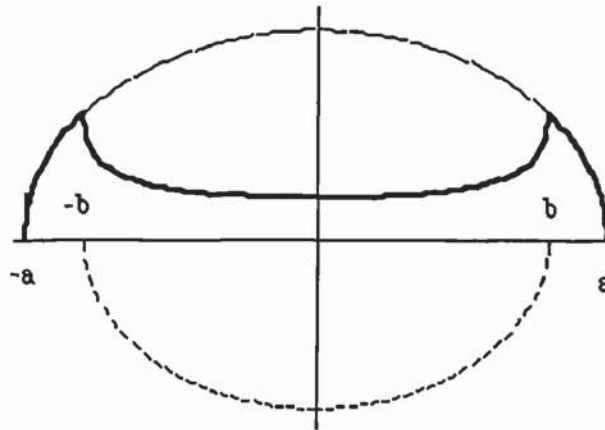
Figure 2.10 Tangential traction distribution (loading)

Hence, the distribution of the tangential traction over the total contact area, shown in figure 2.10, is given as

$$q = (\mu p_o/a) \, (a^2 - r^2)^{1/2} \qquad\qquad b<r<a \qquad\qquad (2.34)$$

$$q = (\mu p_o/a) \, [\, (a^2 - r^2)^{1/2} - (b^2 - r^2)^{1/2}] \qquad\qquad 0<r<b \qquad\qquad (2.35)$$

34

and the displacement of distant points with respect to the uniform displacement of the stick portion is

$$\delta = (3\mu P/16 \; G^*a) (1 - b^2/a^2) \tag{2.36}$$

where

$$1/G^* = (2 - v_1)/G_1 + (2 - v_2)/G_2 \tag{2.37}$$

The magnitude of the tangential force is defined, using (2.34) and (2.35), as

$$T = 2\pi \int_0^a qrdr \tag{2.38}$$

Hence,

$$T = \mu P (1 - b^3/a^3) \tag{2.39}$$

Rearranging (2.39)

$$b/a = (1 - T/\mu P)^{1/3} \tag{2.40}$$

Hence, the tangential force-displacement law is obtained from (2.36) and (2.40),

$$\delta = (3\mu P/16G^*a) [1 - (1 - T/\mu P)^{2/3}] \qquad . \tag{2.41}$$

To obtain the tangential stiffness it is more convenient to differentiate (2.41) to obtain the compliance and then invert. Thus

$$dT / d\delta = 8G^*a (1 - T/ \mu P)^{1/3} \tag{2.42}$$

From (2.42) it is also noted that the initial stiffness is

$$(dT / d\delta)_{T=0} = 8G^*a \tag{2.43}$$

and the tangential displacement to cause sliding δ^*, when $T = \mu P$ in (2.41), is

$$\delta^* = (3\mu P / 16 \; G^*a) \tag{2.44}$$

2.4.4 Tangential Unloading

During tangential loading, slip within the annulus $b<r<a$ is a dissipative process and consequently the tangential force-displacement law is dependent on the loading history.

Mindlin and Deresiewicz (1953) examined several loading sequences involving variations of both normal and tangential forces.

It was shown that, following the application of a monotonically increasing tangential force with the normal force held constant, a subsequent reduction in tangential force will initiate counterslip (slip in the opposite direction to the slip developed during the previous tangential loading) at the perimeter of the contact area (r= a) which will spread radially inwards as the tangential force is further decreased.

The distribution of tangential traction at the start of unloading is given by (2.34) and (2.35). To obtain the traction distribution during unloading a negative traction is superimposed of the form

$$q(r) = -2 \, (\mu p_0 /a) \, (a^2 - r^2)^{1/2} \qquad\qquad c<r<a \qquad\qquad (2.45)$$

$$q(r) = -2 \, (\mu p_0 /a) \, [(a^2 - r^2)^{1/2} - (c^2 - r^2)^{1/2}] \qquad 0<r<c \qquad\qquad (2.46)$$

where c<r<a defines the annulus of counterslip. Figure 2.11 shows a graphical representation of the traction distribution during unloading, with emphasis on the annulus of counterslip shown by the negative traction on the resultant curve.

The resultant distribution is therefore given by adding (2.34), (2.35), (2.45) and (2.46) to obtain

$$q = -(\mu p_0 /a) \, (a^2 - r^2)^{1/2} \qquad\qquad\qquad c<r<a \quad (2.47)$$

$$q = -(\mu p_0 /a) \, [(a^2 - r^2)^{1/2} - 2(c^2 - r^2)^{1/2}] \qquad\qquad b<r<c \quad (2.48)$$

$$q = -(\mu p_0 /a) \, [(a^2 - r^2)^{1/2} - 2(c^2 - r^2)^{1/2} + (b^2 - r^2)^{1/2}] \qquad 0<r<b \quad (2.49)$$

Using (2.47), (2.48) and (2.49) to define q, T is obtained as before from

$$T = 2\pi \int_0^a q r \, dr \qquad\qquad (2.50)$$

Hence,

$$T = \mu P \, (1 - b^3/a^3) - (2\mu P \, (1 - c^3/a^3) \qquad\qquad (2.51)$$

from which
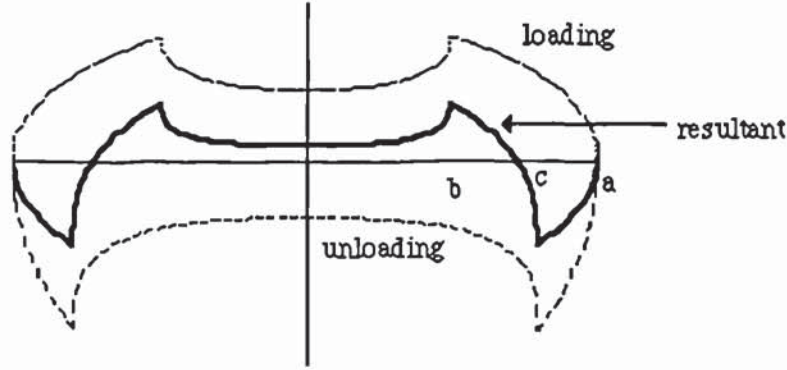
Figure 2.11 Tangential traction distribution (unloading)

$$c = a [1 - (T^* - T)/ 2\mu P]^{1/3} \tag{2.52}$$

where T^* is the initial tangential force from which unloading commenced and is given by (2.39).

The relative tangential displacement of the two spheres is given by

$$\delta = (3\mu P/16G^*a)(2c^2/a^2 - b^2/a^2 - 1) \tag{2.53}$$

or

$$\delta = (3\mu P/16G^*a)[2 (1 - (T^* - T)/2\mu P)^{2/3} - (1 - T^*/\mu P)^{2/3} - 1] \tag{2.54}$$

Differentiating (2.54) to obtain the compliance and then inverting yields the tangential stiffness

$$dT / d\delta = 8G^*a [1 - (T^* - T)/2\mu P]^{1/3} \tag{2.55}$$

The load-displacement curve for a decreasing tangential force or unloading is shown in figure 2.12. If unloading commenced from point A on the loading curve OA*, then the tangential force decreases along ABC. The distribution of tangential traction at point B when $T = 0$, is illustrated in figure 2.11. Counterslip continues to spread radially inwards until point C is reached when $T = -T^*$ and $c = b$. The traction distribution is then a mirror image of that existing when $T = T^*$ and further decreases in T follow the inverse loading curve OCC* on figure 2.12.

37
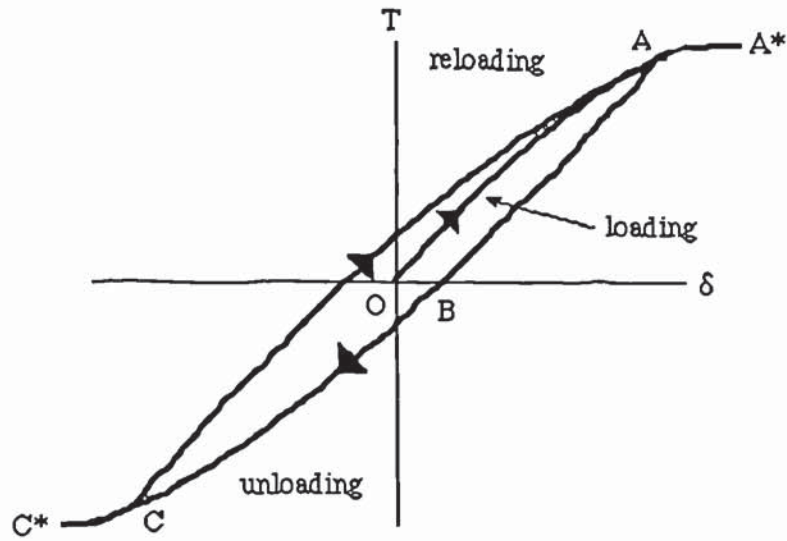
Figure 2.12 Tangential force-displacement plot

2.4.5 Tangential Reloading

Following the sequence of loading and unloading, it is possible that a reversal in the relative tangential displacement of the two spheres will occur which will result in a reloading situation. This case was not fully covered by Mindlin and Deresiewicz (1953). However, the solution follows from the procedural rules given by Mindlin and Deresiewicz (1953) and the derivation of the stiffness during reloading is similar to that presented in the previous sections, and was provided by Randall (1989).

Consider that the initial tangential loading produced slip over the annulus b<r<a and a distribution of tangential traction as shown in figure 2.10. Subsequent unloading produced a counterslip annulus c<r<a and a traction distribution as shown in figure 2.11 when the tangential force was zero. Reloading from this point will initiate slip at the circumference of the contact area, in the same sense as that produced by the initial loading. This 'reslip' will spread radially inwards over an annulus d<r<a with increasing tangential force and to obtain the distribution of tangential traction during reloading a positive traction of the form

$$q' = (2\mu p_0/a) (a^2 - r^2)^{1/2} \qquad\qquad d<r<a \qquad (2.56)$$

$$q'' = (2\mu p_0/a) [(a^2 - r^2)^{1/2} - (d^2 - r^2)^{1/2}] \qquad\qquad 0<r<d \qquad (2.57)$$

is superimposed on the traction distribution at the start of reloading given by (2.47), (2.48) and (2.49). This leads to a distribution for reloading described by summing (2.47), (2.48), (2.49), (2.56) and (2.57) to obtain

$$q = (2\mu p_0/a) (a^2 - r^2)^{1/2} \qquad\qquad d<r<a \qquad (2.58)$$

$$q = (2\mu p_0/a) [(a^2 - r^2)^{1/2} - 2(d^2 - r^2)^{1/2}] \qquad\qquad c<r<d \qquad (2.59)$$

$$q = (2\mu p_0/a) [(a^2 - r^2)^{1/2} + 2(c^2 - r^2)^{1/2} - 2(d^2 - r^2)^{1/2}] \qquad\qquad b<r<c \qquad (2.60)$$

$$q = (2\mu p_0/a) [(a^2 - r^2)^{1/2} - (b^2 - r^2)^{1/2} + 2(c^2 - r^2)^{1/2} - 2(d^2 - r^2)^{1/2}] \quad 0<r<b \quad (2.61)$$

Figure 2.13 shows the resultant distribution of the tangential traction during reloading
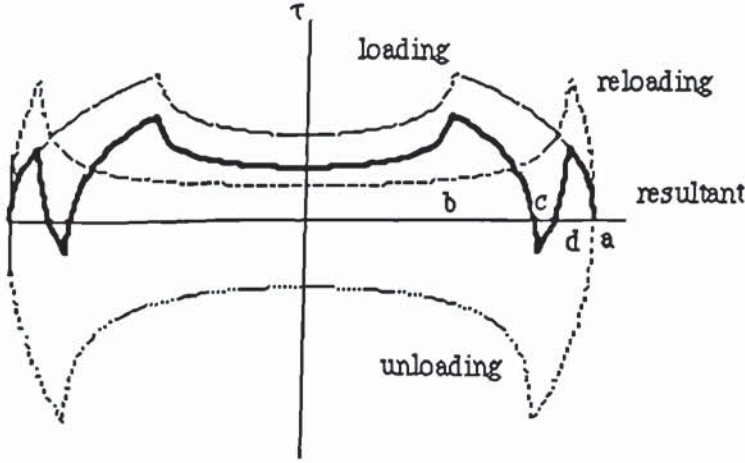
Figure 2.13 Tangential traction distribution (reloading)

Integrating,

$$T = 2\pi \int_0^a q r \, dr \qquad\qquad (2.62)$$

using (2.58) to (2.61) gives,

$$T = \mu P (1 - b^3/a^3) - 2\mu P (1 - c^3/a^3) + 2\mu P (1 - d^3/a^3) \qquad\qquad (2.63)$$

from which

$$d = a [1 - (T - T^{**})/2\mu P]^{1/3} \qquad\qquad (2.64)$$

where T** is the tangential force from which reloading commenced. Hence the relative tangential displacement is

$$\delta = (3\mu P/16G^*a) [1 - b^2/a^2 + 2c^2/a^2 - 2d^2/a^2] \tag{2.65}$$

In a similar approach as the two previous sections, substituting (2.40), (2.52) and (2.64) and differentiating leads to

$$dT/d\delta = 8G^*a [1 - (T - T^**)/2\mu P]^{1/3} \tag{2.66}$$

which defines the tangential stiffness during reloading.

2.5 General Solution

The tangential force is also dependent on the magnitude of the normal force and hence there exists an infinite set of geometrically similar force-displacement curves, each corresponding to a different value of normal force. Figure 2.14 shows two curves; illustrating loading, unloading and reloading conditions. For the case of normal force varying (increasing or decreasing), a detailed analysis of the subsequent tangential force-displacement relationship is fully covered by Randall (1989).

The theoretical investigation presented by Mindlin and Deresiewicz (1953) offered solutions in the form of instantaneous compliances which, due to the dependence on both the initial state and the entire loading history, could not be integrated a priori. However, in computer simulation, it is possible to adopt the incremental approach having identified the general procedural rules of several loading sequences involving variations of both normal and tangential forces. It is necessary to consider tangential displacement rather than tangential force as the criteria for loading, unloading and reloading. This is because it is the displacement increments that are known from the new particle velocities. The procedure is to update the normal force and contact radius followed by calculating ΔT using the new values of P and a. By reanalysing the loading cases considered by Mindlin and Deresiewicz (1953), it was shown by Thornton and Randall (1988) that for loading, unloading and reloading, the tangential incremental displacement may be expressed as

$$\Delta\delta \;=\; \frac{1}{8G^*a}\left(\;\pm\mu\Delta P + \frac{\Delta T \mp \mu\Delta P}{\theta}\right) \tag{2.67}$$

except when, for $\Delta P > 0$,

$$\left|\Delta\delta\right| < \frac{\mu\Delta P}{8G^*a} \tag{2.68}$$

Rearrangement of (2.67) defines the tangential stiffness as

$$K_s = 8G^*a\theta \pm \mu(1-\theta)\frac{\Delta P}{\Delta\delta} \tag{2.69}$$

where

$$1/G^* = (\,2 - v_1\,)/G_1 + (\,2 - v_2\,)/G_2 \tag{2.70}$$

$$\theta^3 = 1 - (\,T + \mu\Delta P)/\mu P \qquad\qquad \text{(loading)} \tag{2.71}$$

$$\theta^3 = 1 - (\,T^* - T + 2\mu\Delta P)/2\mu P \qquad\qquad \text{(unloading)} \tag{2.72}$$

$$\theta^3 = 1 - (T - T^{**} + 2\mu\Delta P)/2\mu P \qquad\qquad \text{(reloading)} \tag{2.73}$$

and the negative sign in (2.69) is only invoked during unloading. The parameters T^* and T^{**} define the load reversal points, as illustrated in figure 2.14, and need to be continuously updated ($T^* = T^* + \mu\Delta P$ and $T^{**} = T^{**} - \mu\Delta P$) to allow for the effect of varying normal force. For a current state given by point 1 in figure 2.14 (during loading, unloading or reloading), a tangential incremental displacement equal to the right hand side of (2.68) will result in a new state given by point 2 on the curve corresponding to the new value of P. Larger values of $|\Delta\delta|$ will result in a state further along the curve such as point 3. A problem occurs if the conditions given in (2.68) occurs, since point 2 is not reached and the new state does not lie on the curve corresponding to the new value of P. This case has been considered analytically by Szalwinski (1985) but, by adopting an incremental approach, a satisfactory solution to the problem is obtained by setting $\theta = 1$ in (2.69) until the following condition is satisfied.

41
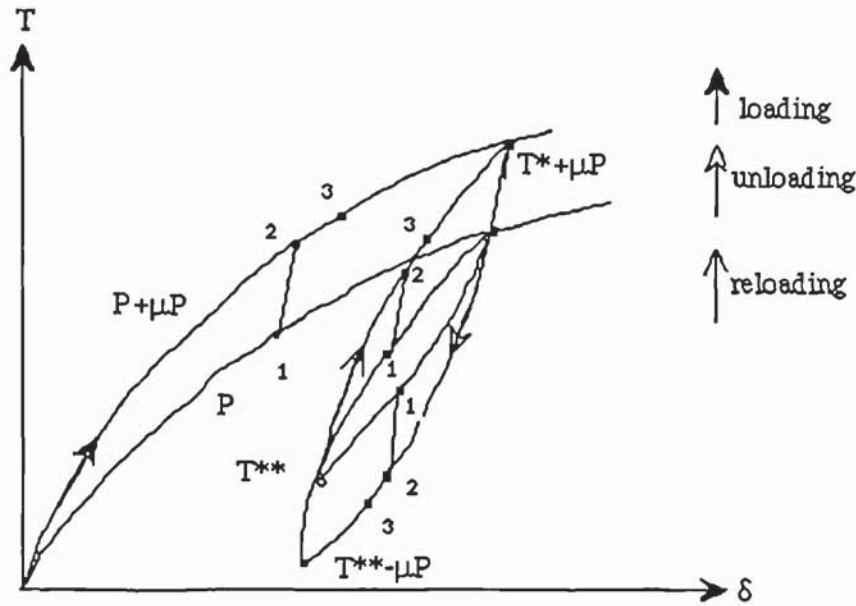
Figure 2.14 Tangential force-displacement

$$8G^*a \, \Sigma \, | \, \Delta \, \delta \, | > \mu \Sigma \Delta P \tag{2.74}$$

A detailed explanation of the computer code is provided in Chapter 4. In the following section results from computer simulated impacts of two identical elastic spheres will be presented.

2.6 Computer Simulated Impact Tests

Two identical spheres were created with the following properties: $R = 100\mu m$, $\rho = 2.65$ Mg/m^3, $E = 70$ GPa, $v = 0.3$ and $\mu = 0.35$. The initial configuration of the system is shown in figure 2.15. Velocities of ± 0.05 m/s in the vertical direction were specified and the evolution of the system was advanced over a sufficient number of calculation cycles to complete the impact simulation.

In the first calculation cycle, the imposed velocities are multiplied by the very small time step used to advance the simulation to give the incremental displacements of the two spheres, which are then added to the original co-ordinates of the spheres centres to
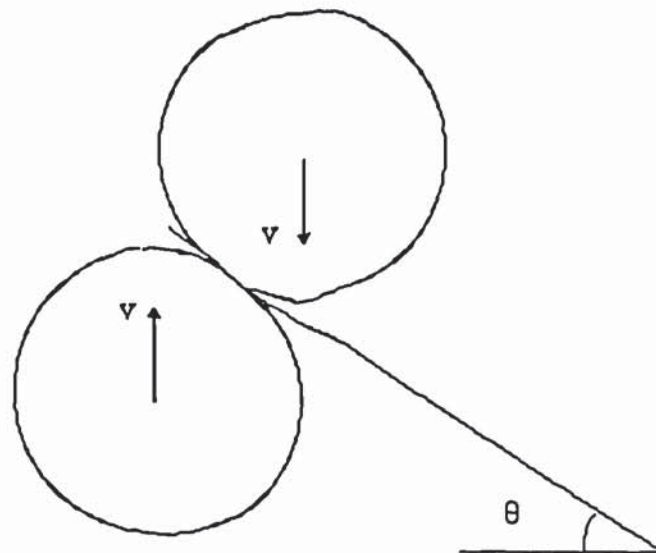
Figure 2.15 Impact configuration

give the new positions. In the second and subsequent time steps, the current positions and velocities of the two spheres are used to obtain the relative normal and tangential displacement increments at the contact, having accounted for any relative spin of the two particles. The relative normal and tangential displacement increments at the contact are multiplied by the current contact normal and tangential stiffnesses to obtain contact force increments which are then used to update the normal and tangential forces at the contact. The new contact forces lead to out-of-balance forces and moments on the particles which are divided by the particle mass and moment of inertia to provide accelerations. The accelerations are multiplied by the small time step to give velocity increments which are used to update the particle velocities. Multiplying the new velocities by the time step, displacement increments are obtained which are used to obtain new particle positions. The above calculation cycle is a repetitive process until the end of impact.

A series of simulations were performed for different values of impact angle θ. Figure

2.16 shows a typical normal force displacement curve obtained for a colinear impact. Excellent agreement with theory is clearly demonstrated.

For a normal impact, Deresiewicz (1968) calculated the total impact duration, T_c, (2.24). Figure 2.17 shows the evolution of the normal force with time indicating a contact duration of 0.96 μs obtained by simulation in exact agreement with the theoretical value.

A series of simulations was performed to examine the effect of impact angle θ on the contact interaction behaviour. Figure 2.18 shows typical loading paths and the corresponding evolution of the tangential force-displacement behaviour is shown in figure 2.19. It can be seen from figure 2.19 that for small impact angles less than the angle of interparticle friction, e.g 15°, the limiting condition $| T | = \mu P$ associated with rigid body sliding, only occurs during the final stages of the impact. The corresponding force-displacement curve, however, clearly shows that prior to rigid body sliding, energy is dissipated as a result of microslip. If the impact angle is greater than the angle of internal friction, e.g 30° and 45°, rigid body sliding occurs from the start of the impact and continues until the decelerating relative tangential motion of the spheres and the accelerating particle spin induced by the tangential force combine to reduce the tangential force increment to $\Delta T < \mu \Delta P$. Subsequently, as the resultant force rotates, the tangential force reduces, reverses in direction and finally towards the end of the impact rigid body sliding recurs. Figure 2.18 shows that, for an impact angle of 60°, the initial rigid body sliding continues into the recovery stage of the impact. For still larger impact angles, e.g., 75°, rigid body sliding continues throughout the impact with no reversal of the tangential force direction.
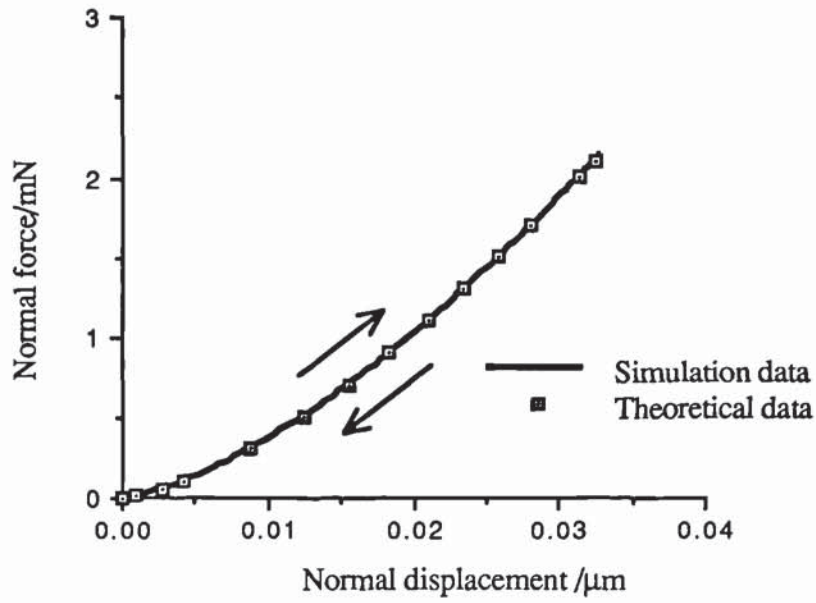
Figure 2.16 Normal force-displacement relationship
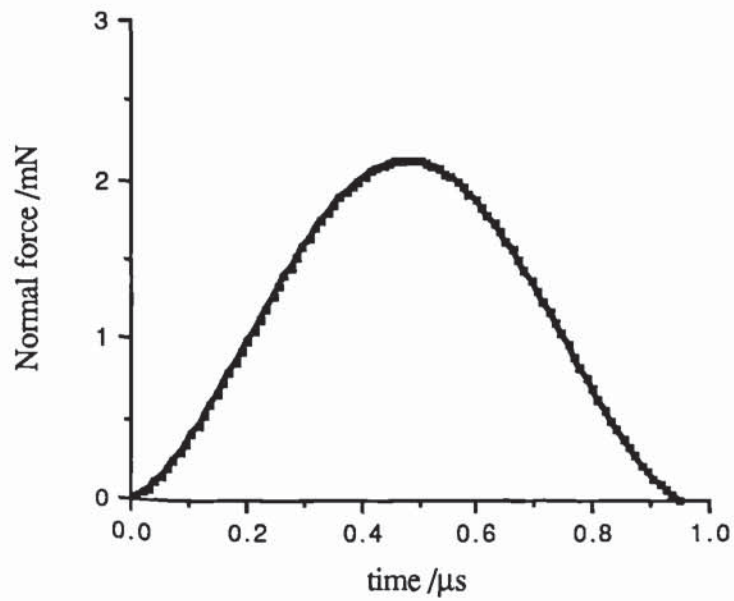
Figure 2.17 Contact duration of an elastic colinear impact
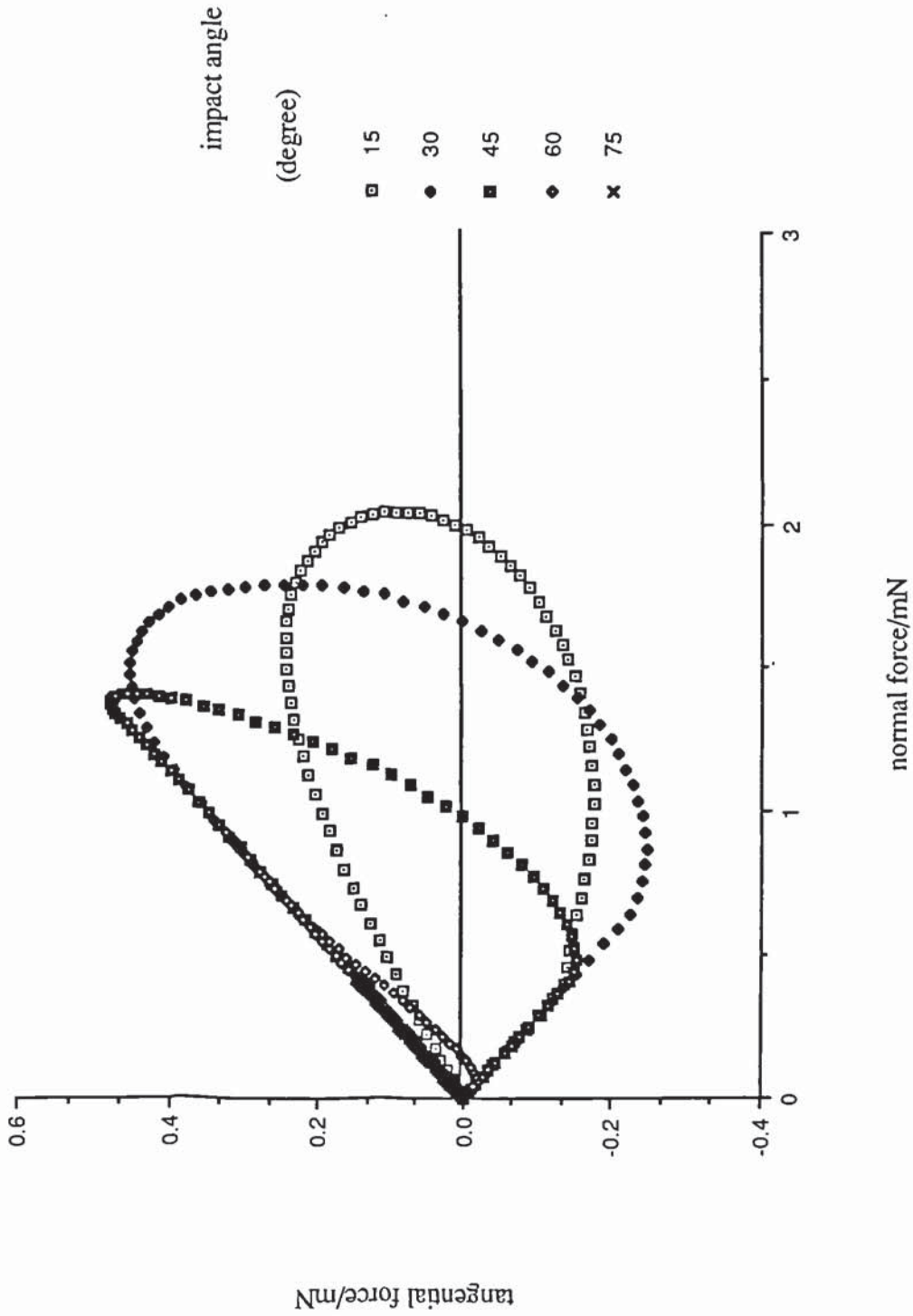
Figure 2.18 Loading paths for various degree of obliquity
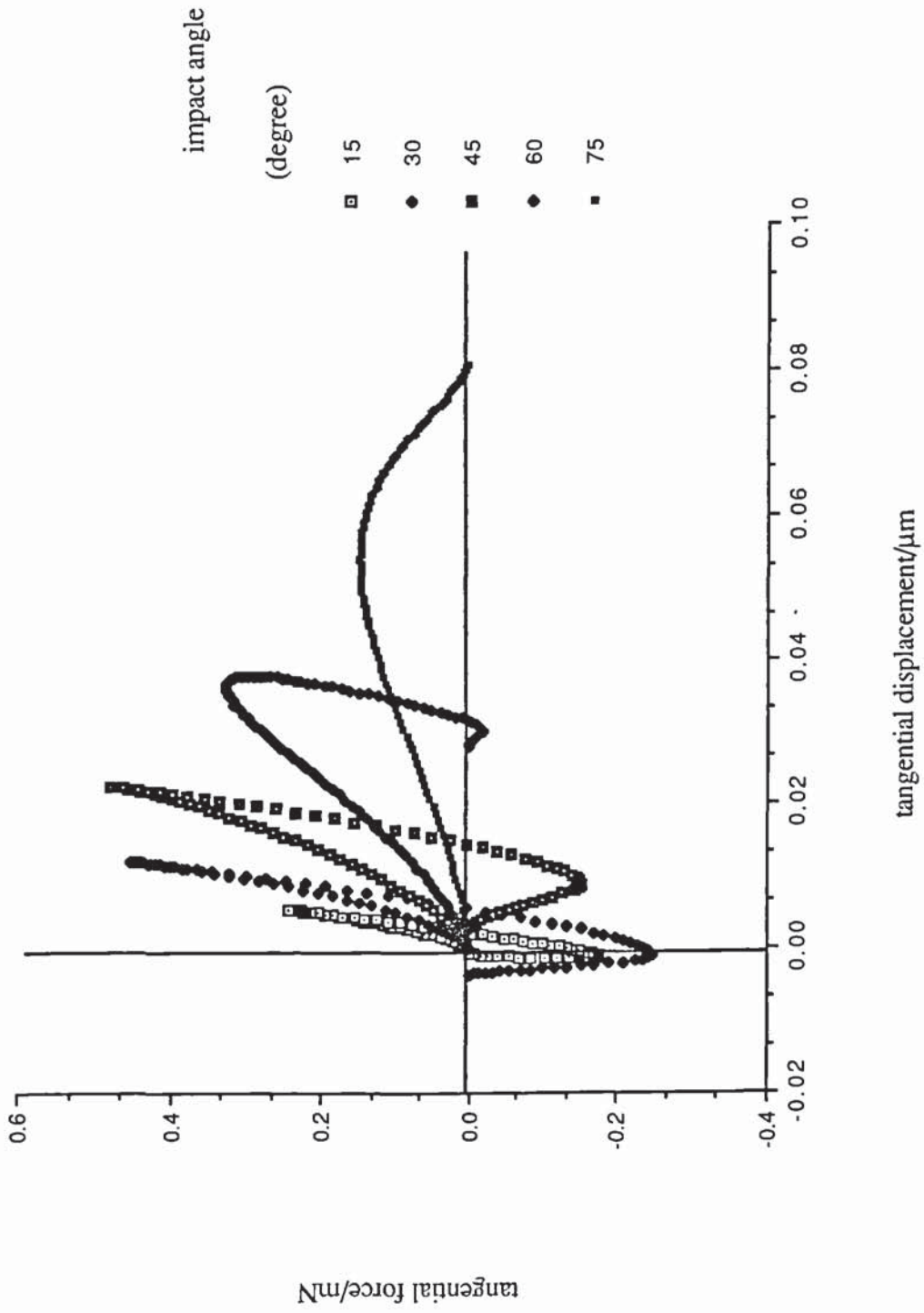
Figure 2.19 Tangential force-displacement for various degree of obliquity

The energy dissipated during oblique impacts of two perfectly elastic spheres is clearly demonstrated by the force-displacement curves shown in figure 2.19 The evolution of the linear kinetic energy during an impact and the way in which the energy is converted into work done by the contact forces are illustrated in figures 2.20, 2.21, 2.22 and 2.23 for impact angles of 0°, 30°, 60° and 80° respectively.

During a colinear impact, figure 2.20, the kinetic energy decreases with a corresponding increase in the work done by the normal force during the first half of the impact period. When the relative approach and the normal force simultaneously reach maximum values, the kinetic energy is zero since the particles are momentarily stationary. During the second half of the impact, the work done by the normal force is progressively recovered and converted into kinetic energy until all the initial kinetic energy has been recovered at the end of the impact. During oblique impacts, the linear kinetic energy never reduces to zero (figures 2.21, 2.22 and 2.23) since the normal and tangential velocities reverse direction at different times. As the impact angle is increased, the minimum kinetic energy increases and the time at which the minimum occurs increases. For large impact angles, which result in rigid body sliding throughout the impact duration, there is no recovery of linear kinetic energy during the rebound stage, figure 2.23.

For all impacts, the work done by the normal force is fully recovered at the end of the impact. The work done by the tangential force is twofold: work done in shear at the contact and work done in rotating the spheres. The way in which these two components of tangential work evolve during an impact is shown in figures 2.21, 2.22 and 2.23. The evolution of the shear component reflects the behaviour shown in figure 2.19. In general, the work done in shear is partially recovered as the tangential force reduces to zero and increases continuously once the tangential force has reversed direction. The work done in rotating the spheres increases until the tangential force direction is reversed, after which there is some partial recovery. However, if sliding

occurs throughout the impact, both components of tangential work increase continuously.
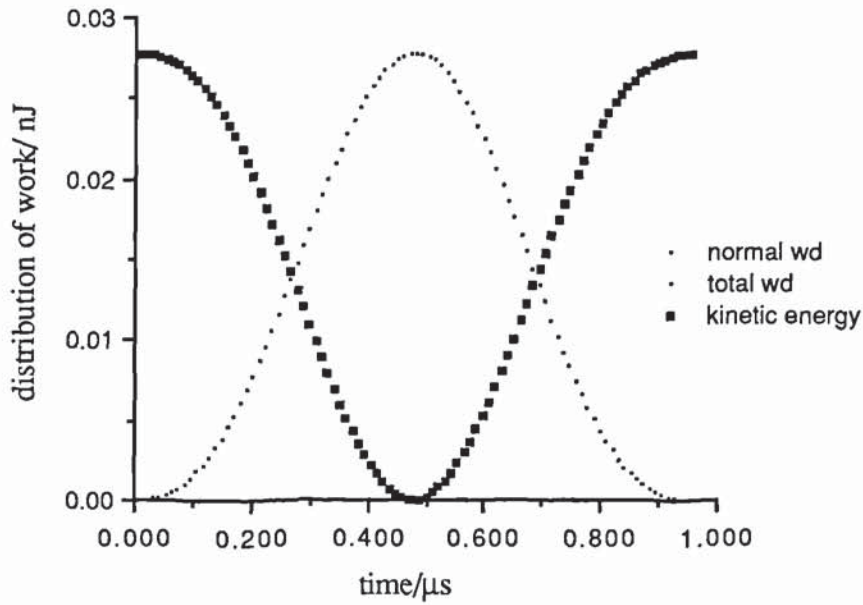
Figure 2.20 Energy Evolution during impact, $\theta = 0°$
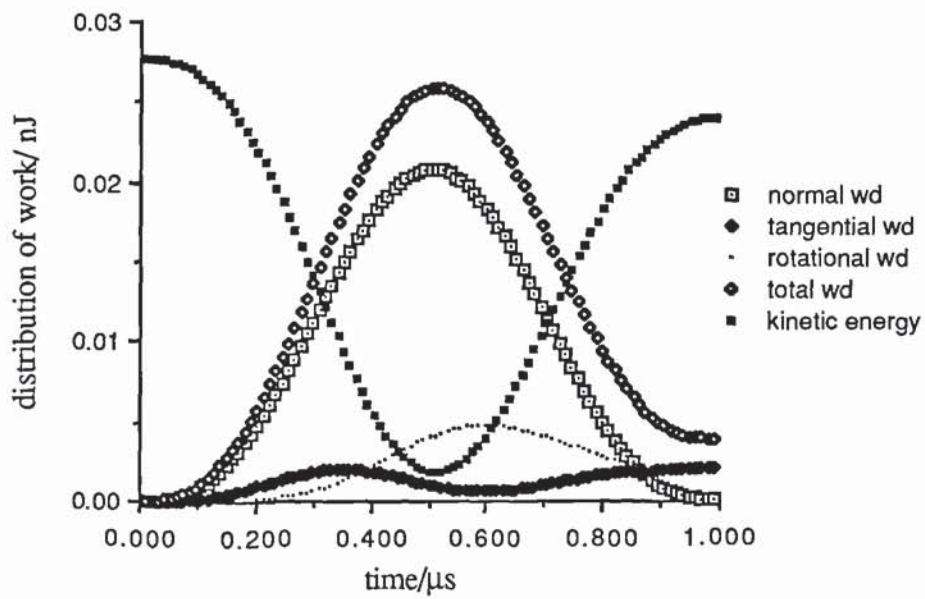
Figure 2.21 Energy evolution during impact, $\theta = 30°$
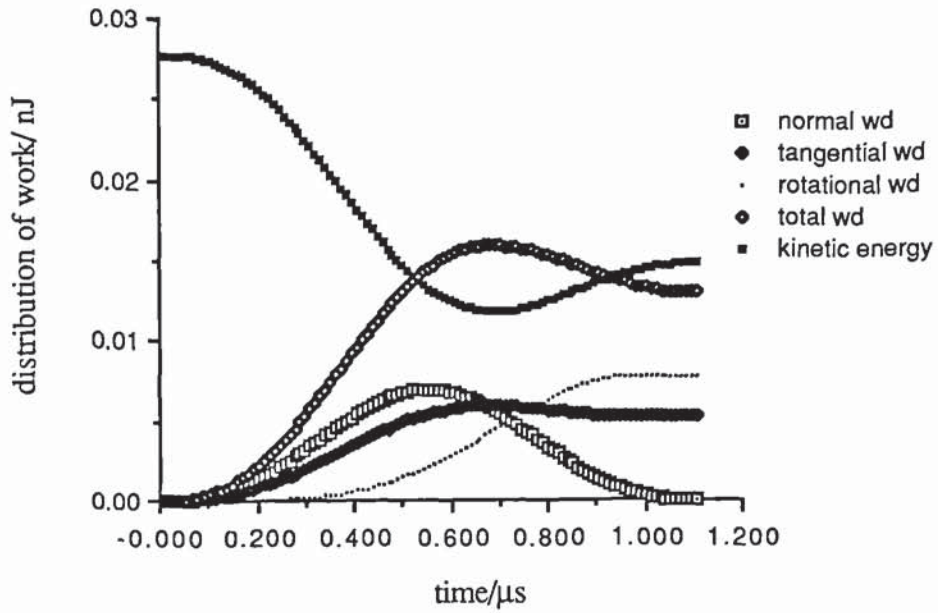
Figure 2.22 Energy evolution during impact, $\theta = 60°$
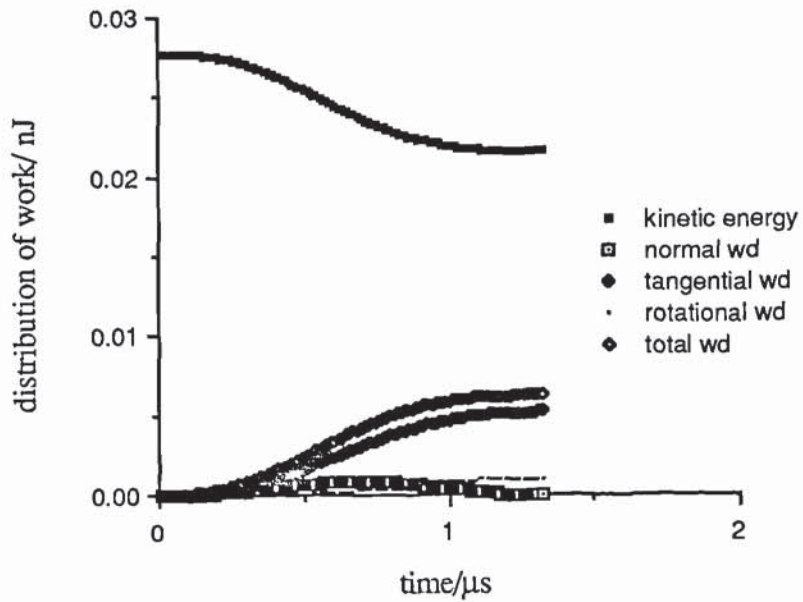
Figure 2.23 Energy evolution during impact, $\theta = 80°$
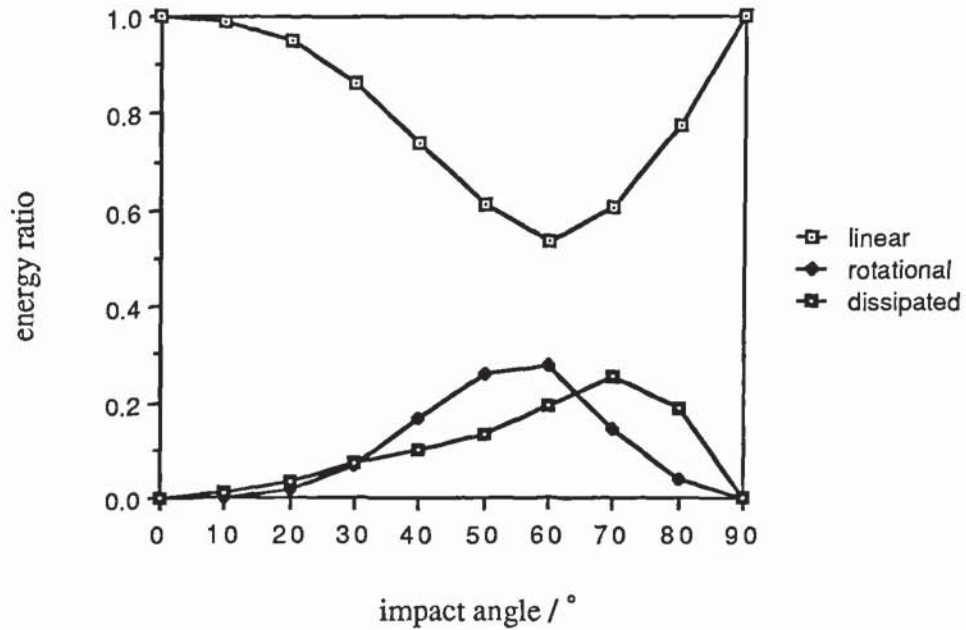
Figure 2.24 Effect of impact angle on linear and rotational kinetic energies and energy dissipated

Figure 2.24 illustrates the effect of obliquity on the percentage loss in linear kinetic energy, the percentage gain in rotational kinetic energy and the percentage energy dissipated due to microslip and rigid body sliding. It can be seen that, as the angle of impact increases, the loss in linear kinetic energy and the gain in rotational kinetic energy increase until the impact angle is sufficiently large to produce rigid body sliding throughout the impact. Further increases in impact angle result in decreases in rotational kinetic energy and corresponding smaller losses in linear kinetic energy. The energy dissipated during an impact increases with obliquity of the impact until the linear and rotational kinetic energies have attained optimum values. The dissipated energy continues to increase as the impact angle is increased further but decreases at very high impact angles due to the friction-limited tangential force.

Maw et al (1976) reported a series of experiments undertaken to validate the analysis presented by Maw et al (1981). A disc-shaped puck was propelled over an air bed

towards a clamped block of an identical material. A heavy launching device, incorporating a pendulum, provided a means of producing repeatable initial conditions and stroboscopic photography was used to measure impact and rebound angles and velocities. Maw et al (1976, 1981) demonstrated both theoretically and experimentally that, for a particle impacting with no initial spin, if sufficient rotation is imparted to the particle during impact the contact patch 'bounces back'. The centroid of the particle, however, always rebounds in a forward direction but at an angle less than the impact angle. This is illustrated diagrammatically in figure 2.25.
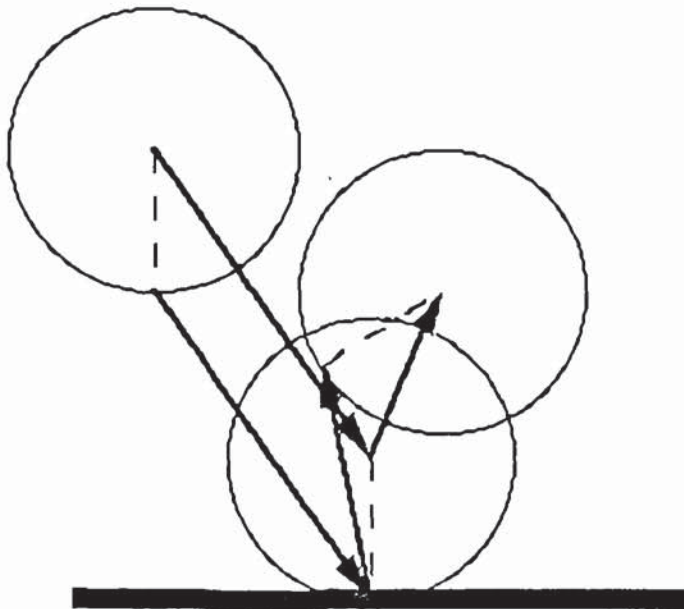
Figure 2.25 Oblique impact trajectories

The results of the computer simulation experiments are provided in figure 2.26 showing the effect of impact angle on both the angle of reflection of the contact patch and the rebound angle of the particle centroid.

It can be seen that there is a range of impact angles over which the angle of reflection of the contact patch is negative and this range of values is primarily dictated by the interparticle friction but also slightly affected by the Poisson ratio of the spheres.

Randall (1989) demonstrated that, when the same properties were used, the computer simulations gave exact quantitative agreement with the theoretical predictions of Maw et al (1976, 1981).
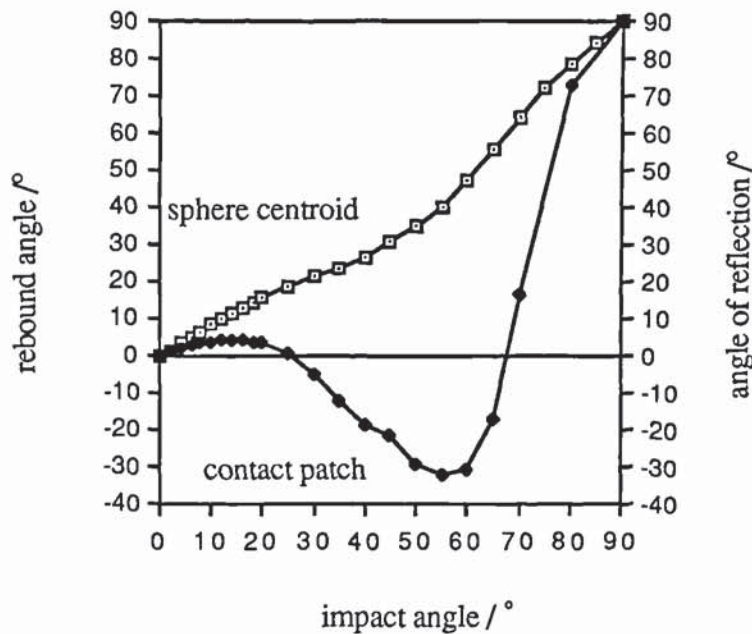
Figure 2.26 Effect of impact angle on rebound angles

Figure 2.27 shows the effect of the angle of impact θ on the coefficient of restitution where the coefficient of restitution is expressed in terms of resultant velocity vectors and defined as the ratio of the rebound velocity to the approach velocity. It can be seen that as θ increases, the coefficient of restitution decreases until a minimum value is attained and then increases at larger impact angles. The curves are, of course, similar to the variation in percentage loss in linear kinetic energy, as shown in figure 2.24 and are therefore a function of both the energy dissipated and the energy converted into rotational kinetic energy as a result of the spin imparted to the particles upon rebound. It follows, therefore, that as indicated in figure 2.27, the coefficient of restitution is dependent on the coefficient of friction. An increase in interparticle friction results in lower coefficients of restitution and an increase in the angle of impact at which the minimum coefficient of restitution occurs.

53

For a smaller coefficient of interparticle friction, $\mu = 0.12$, it was observed that the coefficient of restitution is lower than that obtained when $\mu = 0.35$, at lower angle of impacts. This phenomena can be clearly explained by the governing criteria of limiting friction. Tangential forces generated as the result of an oblique impact can then easily invoke sliding throughout most of the contact duration. This is not very much a case for $\mu = 0.35$, where sliding only commence at the cessation of the contact duration. Consequently, the energy dissipated and therefore the coefficient of restitution is not in excessive.
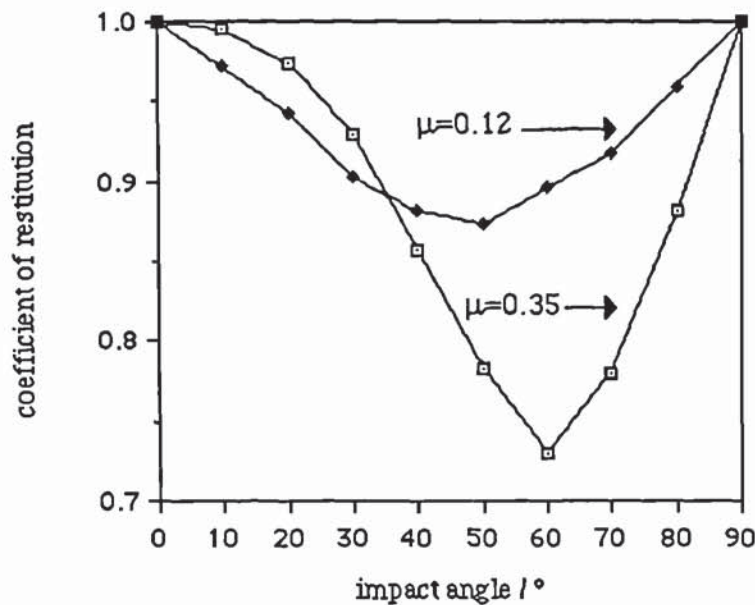
Figure 2.27 Effect of angle of impact, θ, on the coefficient of restitution

2.7 Discussion

Particle interactions within large systems of particles invariably involve oblique contact forces yet relatively little information is provided in the literature about the tangential contribution to oblique impacts. This chapter has illustrated the complexity of such apparently simple events.

Following an oblique impact, the rebound angle, velocity and particle spin are all functions of the total loading history of the impact duration. The computer simulations of oblique impact of elastic spheres have shown that the energy dissipated and changes in both linear and rotational kinetic energy are significant and are complex functions of the angle of impact.

In the numerical modelling of particle transport problems, which may involve both particle-particle and particle-wall collisions, it is necessary to predict the change in particle spin and either the normal and tangential rebound velocities or the resultant rebound velocity and the angle of rebound. The results of the computer-simulated impacts show that, as a result of the complex tangential load-displacement behaviour, there would appear to be no simple rules (e.g., coefficient of restitution, scattering probability) that will satisfactorily achieve this.

3. Impact Of Elastic Spheres With Adhesion

The trouble with doing something right the first time
is that nobody appreciates how difficult it was   *- IBM*

3.1 Introduction

Adhesion is a significant phenomenon in both industry and nature. In industry, the phenomenon plays a major role in filtration, separation of dry materials, cleaning of surfaces, electrophotography, treatment of plants with pesticides and many other processes. In particulate technology, adhesion properties sometimes have a decisive effect on the choice of methods and conditions for the preparation, storage, application, and transport of powdered materials. Adhesion is a major factor in processes taking place in nature. If there was no adhesion, dust settling on the ground would be continuously returned to the atmosphere by air currents, and the dust concentration in the atmosphere would reach vast proportions.

Although there are very few publications devoted solely to the investigation of particle adhesion, there are many publications in which adhesion is considered in conjunction with other phenomena. A phenomenon closely related to adhesion is cohesion. Cohesion is understood to be the interaction between molecules within a single solid body. Adhesion is often defined as molecular coupling between two unlike contiguous bodies. This interpretation of adhesion does not reflect the great number of processes taking place in the adhesion of particles to a solid surface or to another particle. Microscopic particles in an air medium adhere to a solid surface not only because of surface energy, but also because of the capillary forces of liquid condensed in the space between contiguous particles and the electrical double layer formed.

It is generally considered that surface effects due to van der Waals forces become significant for the particle sizes less than 100 μm. The phenomenon is frequently referred to as autoadhesion. The theoretical model described in this chapter can be shown to be relevant to the case of autoadhesion but it will, for convenience of

computer simulation, be considered to be also applicable to other types of particle-particle adhesion.

3.2 Brief Literature Review.

Adhesion is frequently discussed in relation to the strength of joints as determined experimentally but a joint is a relatively complex system where the stresses are unlikely to be uniform and when failure occurs it may be in the layer of adhesive or in either component of the joint. The term adhesion should be reserved strictly for the bonding at the interfaces since a third form of bonding, as in joints, is a different form of adherence altogether. If it is assumed that the interfaces represent the weakest points so that failure occurs under stress, the empirical strength of most bonding can be explained by van der Waals' forces alone acting at the interface. This was pointed out by de Bruyne (1947), and shows that relatively weak bonding at the interfaces can explain experimentally measured joint strengths, provided that there is intimate contact over the entire interface.

Since adhesion involves intimate contact of two surfaces, it is often convenient to think in terms of energies of the surfaces involved. Fox and Zisman (1950) introduced the distinction between high and low energy surfaces. Solids with surface free energies below 0.1 J/m^2 are termed soft solids or low surface energies, whereas hard solids having surface free energies above 0.5 J/m^2 are termed high surface energy. Organic polymers, waxes and similar materials generally have low surface energies whilst metals, metal oxides and glasses have high surface energies. The surface energy approach was originated by Dupre more than 100 years ago. He suggested that the work done in breaking the bond is given by the equation

$$\Gamma = \gamma_1 + \gamma_2 - \gamma_{12} \qquad (3.1)$$

where Γ = the Dupre energy of adhesion

γ_1 and γ_2 = the intrinsic surface energies

γ_{12} = energy of the interface

It is difficult to test the validity of this equation because none of the parameters are measurable but this empirical relationship does form the basis for many fundamental ideas in dealing with adhesion.

There is much evidence to suggest that attractive forces act between solids close together, Adamson (1967), and such forces explain qualitatively why a mechanical load is required to separate two solid bodies placed in intimate contact. Extensive measurements have been made of the range of action of these surface forces. In some studies strong adhesion was found, in others none. For example, Tomlinson (1928) found strong adhesion between dry glass surfaces, which he attributed to molecular attraction, and Bradley (1932) found good adhesion between quartz and sodium pyroborate spheres. Budgett (1911), Stone (1930) and McFarland and Tabor (1950) found that adhesion between dry glass spheres was small, but when a thin film of water was present strong adhesive forces could be observed. Kendall (1969) found reasonably strong adhesion between dry glass surfaces and was able to show that the contact area was greater than that of the Hertzian type.

In support of their adhesion theory of friction, Bowden & Tabor (1950) have made careful measurements to find a force of adhesion between metal surfaces but little could be observed except for the very soft metals e.g. indium, for which plastic rather than elastic deformation takes precedence and surfaces are less readily contaminated in air and elastic limits are much lower. Tabor and Winterton (1969) obtained supporting evidence for van der Waals forces acting at the nano-scale. They provided a direct measure of the magnitude of the van der Waals forces for mica and the way in which these forces vary with distance for separations ranging from 5 to 30 nm. The experiments showed that the normal van der Waals forces predominate for separations less than 10 nm and the retarding forces for separations greater than 20 nm.

In 1971 Johnson, Kendall and Roberts (henceforth referred to as JKR) extended the Hertzian theory to two adhering solids, i.e. to solids that adhere together when in contact, due to the presence of surface energy or van der Waals forces. The JKR theory considers the adhesion between the two spheres simply as a change in surface energy only where they are in contact, i.e., that the attractive force between them is infinitely short range. In contrast, Deryaguin, Muller and Toporov (DMT) (1975) suggested that any attractive force between the solids must have a finite range and therefore act in the region just outside the contact zone where the surfaces are a small distance apart. Muller et al (1980) have formulated more complete descriptions of the problem by allowing the solid-solid interaction to be a prescribed function of the local separation between the surfaces. However, the complete solution is difficult to achieve as it needs to consider the stress distribution in the solids which in turn is dependent on the shape of the deformed surfaces but this is unknown unless the stress distribution is known. The complete solution will only be tractable if the surface force as a function of surface separation is known and solving this nonlinear integral equation involves numerical method with a suitable Leonard-Jones potential to describe the molecular interactions between the solids.

3.3 Normal Loading With Adhesion

In recent years, there has been a continuing debate about the appropriate theoretical model for the normal loading of elastic spheres in the presence of adhesion. Johnson et al (1971) (the JKR model) extended the Hertzian model to two adhering elastic spheres, assuming that the adhesion between the two spheres resulted only in a change of surface energy over the contact area, thereby implying that the attractive interparticle forces are of infinitely short range. The theory predicted a much larger contact area than that predicted by Hertz, with an infinite tensile stress at the perimeter. Consequently, there existed an outer annulus which experienced tensile stresses surrounding an inner circular region over which a Hertzian-type compressive stress

distribution acted, see figure 3.2b. This inner compressed region was also larger than that predicted for no adhesion.
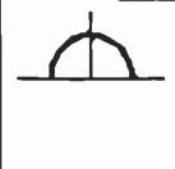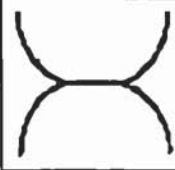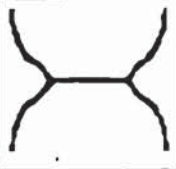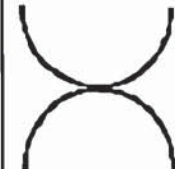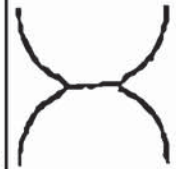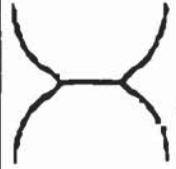
Hertz	JKR	DMT	MYD
Forces between surfaces			
Stress under compressive load			
Shape under compressive load			
Shape under zero load			
Adhesion (Pull-off force)			
0	$3\gamma\pi R*$	$4\pi\gamma R*$	$(3-4)\gamma\pi R*$

Figure 3.1 A comparison of the main features of various theories of the deformation and adhesion of elastic spheres. Column 1 summarises the results obtained by Hertz, column 2, those of Johnson et al., column 3 those of Deryaguin et al and the last column shows the results of Muller et al

In contrast, Deryaguin et al (1975), the DMT model considered the attractive forces to have a finite range and hence must be significant just outside the contact zone where the surface separation is small. It was assumed that the surface forces have no effect on the shape of the particles and hence the contact area experiences a Hertzian compressive

stress distribution and, outside the contact, there is a tensile stress which decreases with surface separation.

Much of the debate about the relevance of the two (JKR and DMT) theories has been centred on the predicted 'pull-off force' which , according to JKR theory is

$$P_C = 3\pi\gamma R^* \tag{3.2}$$

whereas DMT theory predicts

$$P_C = 4\pi\gamma R^* \tag{3.3}$$

where γ is the Dupre energy of adhesion given by (3.1). Muller et al (1980) showed that the prediction was governed by the parameter

$$\lambda = (32/3\pi z_0) \, (\gamma^2 R^*/E^{*2})^{1/3} \tag{3.4}$$

where z_0 is the equilibrium separation, and that the JKR and DMT theories were accurate to within 10% for values of $\lambda>3$ and $\lambda<1$, respectively. Similar conclusions were drawn by Greenwood and Johnson (1981) who adopted a fracture mechanics approach to investigate the effect of the shape of the surface profile on the predicted pull-off force.

In the theory developed in the next section for oblique loading, the JKR model will be used for normal loading of adhered elastic spheres. Before proceeding into the next section, it is best to understand the principles of the energy approach adopted in the JKR theory. Consider the contact of two smooth perfectly elastic spheres of radii R_1 and R_2. In the absence of adhesive forces the stress and deformation due to a contact force P are given by the Hertz theory, (2.1) and (2.10) respectively. If, in addition, attractive forces act between the surfaces the contact radius in equilibrium will be a_1, figure 3.2(a and b), which is greater than a_0 the Hertzian contact radius. Although the applied load remains at P, an apparent Hertz load P_1 corresponding to the contact radius a_1 may be defined by point A in figure 3.2. The resulting distribution of surface traction is found by subtracting the stress under a flat cylindrical punch from the Hertz pressure distribution, viz:

$$\sigma(r) = (3P_1/2\pi a^3) (a^2 - r^2)^{1/2} - (P_1 - P)/2\pi a (a^2 - r^2)^{-1/2} \qquad (3.5)$$

This traction is tensile (negative), at the edge of the contact and compressive (positive), in the centre, as shown by curve B in figure 3.2b.

(a)   (b)

(c)
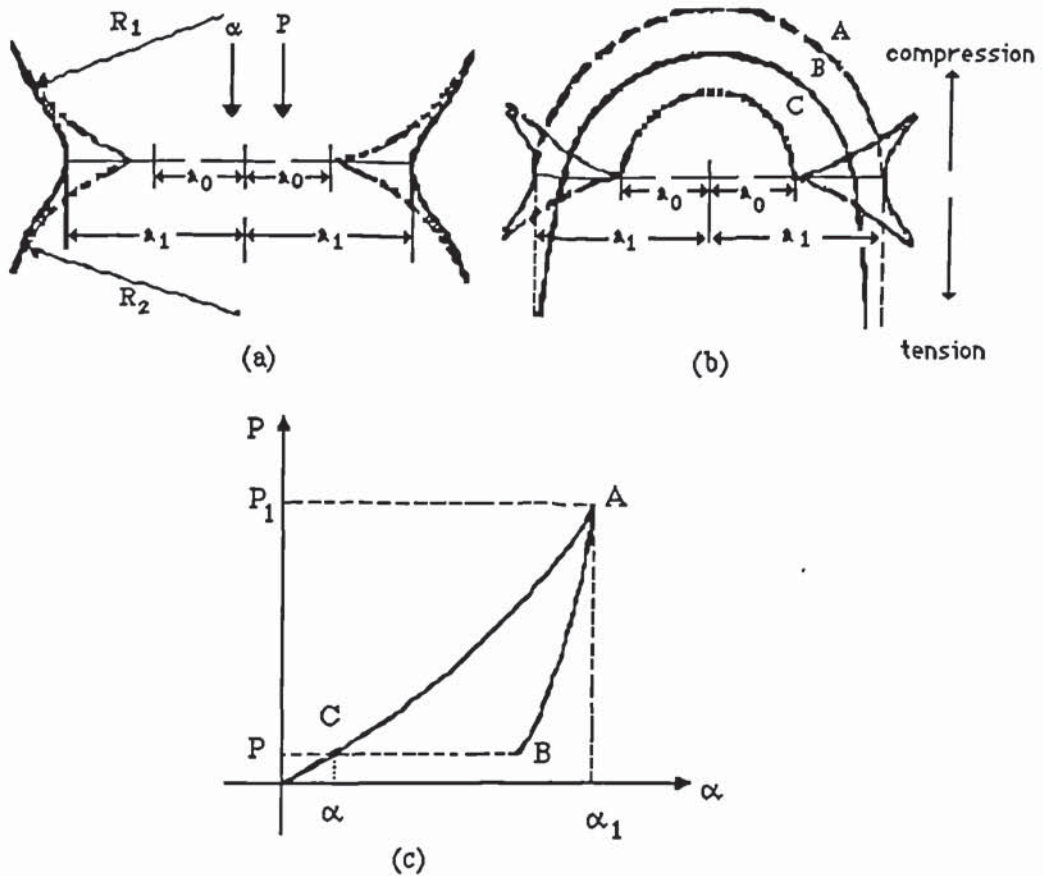
Figure 3.2 The contact between two elastic solids both in the presence (contact radius a_1) and absence (contact radius a_0) of surface forces.

(a) Shows the contact between two convex bodies of radii R_1 and R_2 under normal load of P ; α is the elastic displacement. (b) Indicates the distribution of stress in the contacting spherical surfaces. When surfaces are maintained in contact over an enlarged area by surface forces, the stresses between the surfaces are tensile at the edge of the contact and only remain compressive in the centre. Distribution A is the Hertz stress with $a = a_1$ and $P = P_1$; distribution B the actual stress (Johnson, 1958) with $a = a_0$ and $P = P$. Distribution C is the Hertzian distribution over area of contact radius a_0.

(c) Represents the load-displacement relation for the contacting surfaces.

The total energy U_T of this system is made up of three components, the stored elastic energy U_E,

$$U_E = [(P_1^{5/3}/15) + (P^2 P_1^{-1/3}/3)] / (16E^{*2}R^*/9)^{1/3} \qquad (3.6)$$

the mechanical potential energy

$$U_M = \{-P[(P_1^{2/3}/3) + (2P P_1^{-1/3}/3)]\} / (16E^{*2}R^*/9)^{1/3} \qquad (3.7)$$

and the surface energy

$$U_S = -2\pi\gamma \left(3R^* P_1/4E^* \right)^{2/3} \qquad (3.8)$$

The total energy U_T is

$$
\begin{aligned}
U_T &= U_E + U_M + U_S \\
&= [(P_1^{5/3}/15) + (P^2 P_1^{-1/3}/3)] / (16E^{*2}R^*/9)^{1/3} \\
&\quad + \{-P[(P_1^{2/3}/3) + (2P P_1^{-1/3}/3)]\} / (16E^{*2}R^*/9)^{1/3} \\
&\quad -2\pi\gamma \left(3R^* P_1/4E^* \right)^{2/3} \qquad\qquad (3.9)
\end{aligned}
$$

Equilibrium ensues when

$dU_T/da_1 = 0$. This is equivalent to $dU_T/dP_1 = 0$

$$
\begin{aligned}
dU_T/dP_1 &= [(16E^{*2}R^*/9)^{-1/3}] \{ P_1^{2/3}/9 - P^2 P_1^{-4/3}/9 - 2PP_1^{-1/3}/9 + 2P^2 P_1^{4/3}/9\} \\
&\quad - (4/3)\gamma\pi(3/4)^{2/3}R^{*2/3} P_1^{-1/3}/E^{*2/3} \\
&= [P_1^{-4/3}(3/4)^{2/3}/9E^{*2/3}R^{*1/3}]\{ P_1^2 - P^2 - 2P P_1 + 2P^2 - 12\gamma\pi R^* P_1\}
\end{aligned}
$$

$$\dotfill (3.10)$$

Therefore at equilibrium

$$P_1^2 - 2 P_1(P + 6\gamma\pi R^*) + P^2 = 0, \qquad (3.11)$$

remembering (3.1), hence,

$$P_1^2 - 2 P_1(P+2P_c) + P^2 = 0$$

$$P_1 = P + 2P_c \pm (4PP_c + 4P_c^2)^{1/2} \qquad (3.12)$$

Equation (3.12) shows that the apparent Hertz load P_1 acting between two elastic bodies of surface energy γ is larger than the applied load P.

The Hertz equation, modified to take into account the surface energy effect, is

$$a^3 = (3R^*/4E^*) [P + 2P_c + (4PP_c + 4P_c^2)^{1/2}] \qquad (3.13)$$

When $\gamma = 0$ this reverts to the simple Hertz equation as shown by (2.10). At zero applied load the contact area is finite and given by

$$a^3 = (3R^*/4E^*) [4P_c] \tag{3.14}$$

When the load is made negative the contact radius decreases. For a real solution to be obtained to equation (3.13),

$$4PP_c \leq 4P_c^2$$

$$P \geq -P_c \tag{3.15}$$

Separation of the spheres will just occur when $P = -P_c$, which is termed the pull-off force and is independent of the elastic modulus.

The load displacement relationship was provided by Johnson (1976) and is illustrated in figure 3.3. The corresponding distribution of normal traction over the contact area is described by (3.5), and is illustrated in figure 3.4.

The radius over which the compressive stresses act, r_0, is obtained by setting $\sigma(r) = 0$ in (3.5) which leads to

$$r_0 = a[1- (P_1 - P)/3 P_1]^{1/2} \tag{3.16}$$

which is greater than the radius of the contact area given by the Hertzian solution, (2.10).

In computer simulation, it is necessary to compute the normal stiffness. Johnson (1985) argued that the relative approach is defined by,

$$\alpha = (\pi a/2E^*) [p_0 + 2 p'_0] \tag{3.17}$$

where

$$p_0 = 2aE^*/\pi R^* \tag{3.18}$$

and

$$p'_0 = - (4\gamma E^*/\pi a)^{1/2} \tag{3.19}$$

Hence (3.17),

$$\alpha = (\pi a/2E^*) [(2aE^*/\pi R^*) - 4(\gamma E^*/\pi a)^{1/2}]$$

$$= a^2/R^* - 2(\gamma \pi a/E^*)^{1/2}$$

$$d\alpha/da = 2a/R^* - (\gamma \pi/E^* a)^{1/2} \tag{3.20}$$

The applied normal force can be calculated from (3.5),
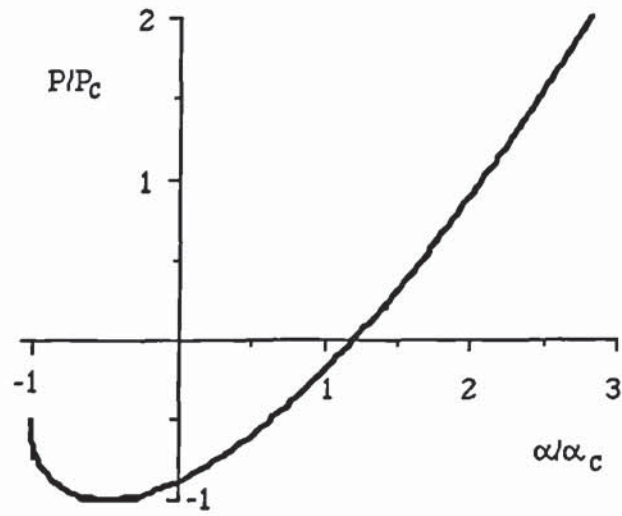
Figure 3.3 Normal force-displacement curve (JKR theory)
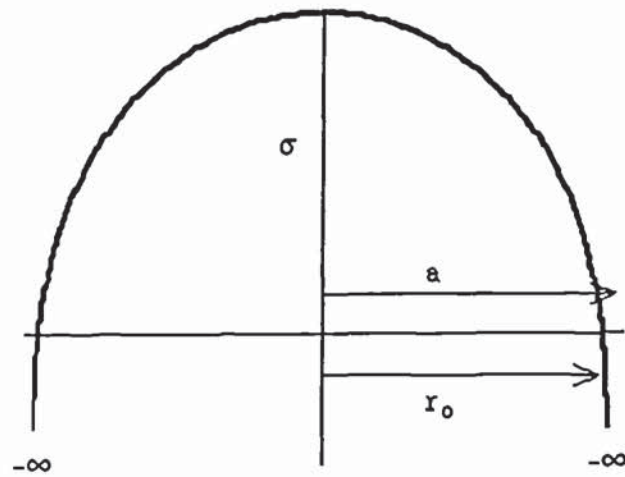
Figure 3.4 Normal traction distribution (JKR theory)

$$P = 2\pi \int_0^a p(r)rdr$$

$$= 2\pi \int_0^a (p_0/a)(a^2 - r^2)^{1/2}rdr - 2\pi \int_0^a (p'_0a)(a^2 - r^2)^{-1/2}rdr$$

$$P = 4E^*a^3/3R^* - (16\gamma\pi E^*a^3)^{1/2} \tag{3.21}$$

$$dP/da = 4E^*a^2/R^* - 6(\gamma\pi E^*a)^{1/2}$$

Therefore,

$$dP/d\alpha = \{4E^*a^2/R^* - 6(\gamma\pi E^*a)^{1/2}\} / \{2a/R^* - (\gamma\pi/E^*a)^{1/2}\}$$

$$= \{4E^{*2}a^3 - 6(\pi\gamma R^{*2} E^{*3}a^3)^{1/2}\} / \{2E^*a^2 - (\gamma\pi R^{*2}E^*a)^{1/2}\}$$

$$= 2E^*a \left[(2E^*a^2 - (9\gamma\pi R^{*2}E^*a)^{1/2}) / (2E^*a^2 - (\gamma\pi R^{*2}E^*a)^{1/2}) \right]$$

$$= 2E^*a \left\{ [1 - (9\gamma\pi R^{*2}E^*a/4E^{*2}a^4)^{1/2}] / [1 - (\gamma\pi R^{*2}E^*a/4E^{*2}a^4)^{1/2}] \right\}$$

and, since $P_c = 3\gamma\pi R^*$

$$dP/d\alpha = 2E^*a \left\{ [1 - (3P_cR^*/4E^*a^3)^{1/2}] / [1 - (P_cR^*/12E^*a^3)^{1/2}] \right\}$$

However, from Johnson (1976), when $P = -P_c$, $a = a_c = (3P_cR^*/4E^*)^{1/3}$

therefore the normal stiffness is

$$k_n = dP/d\alpha = 2E^*a \left\{ [3 - 3(a_c^3/a^3)^{1/2}] / [3 - (a_c^3/a^3)^{1/2}] \right\} \tag{3.22}$$

which reduces to (2.15) for zero adhesion.

3.4 Oblique Loading With Adhesion

Savkoor and Briggs (1977) extended the JKR analysis to account for the effect of oblique loading in the presence of adhesion. It was argued that the tangential stress distribution over the contact area would be prescribed by the 'no-slip' solution of Mindlin (1949) given by equation (2.29). If no slip is permitted at the contact interface, material points inside the contact undergo no relative tangential displacement δ, as shown by (2.31). Noting that the distribution of this traction is axially symmetric and that the traction tends to be unbounded at the edge of the contact, Mindlin argued that slipping must occur, section 2.3.1. This is only true in the absence of adhesion. However, in the presence of surface adhesion the slip annulus hypothesis will be inappropriate. The actual finite tractions at the edge of the contact cannot be resolved

66

with the help of the linear elastic theory. Instead it would be more realistic to treat the contact as an adhesive joint and hence adopt a fracture mechanics approach.

Savkoor and Briggs (1977) suggested that the application of a tangential force reduces the potential energy by an amount $T\delta/2$. Hence, the total energy balance (3.9) becomes,

$$U_T = [(P_1^{5/3}/15) + (P^2 P_1^{-1/3}/3)] / (16E^{*2}R^*/9)^{1/3}$$
$$+ \{-P[(P_1^{2/3}/3) + (2PP_1^{-1/3}/3)]\} / (16E^{*2}R^*/9)^{1/3}$$
$$-2\pi\gamma (3R^*P_1/4E^*)^{2/3} - T^2/16\gamma^* a \qquad (3.23)$$

but

$$a^3 = (3R^*P_1/4E^*)$$

therefore

$$U_T = [(P_1^{5/3}/15) + (P^2 P_1^{-1/3}/3)] / (16E^{*2}R^*/9)^{1/3}$$
$$+ \{-P[(P_1^{2/3}/3) + (2PP_1^{-1/3}/3)]\} / (16E^{*2}R^*/9)^{1/3}$$
$$-2\pi\gamma (3R^*P_1/4E^*)^{2/3} - (T^2/16\gamma^*)(3R^*P_1/4E^*)^{-1/3} \qquad (3.24)$$

Differentiating (3.24) with respect to P_1 to obtain equilibrium,

$$dU_T/dP_1 = [(16E^{*2}R^*/9)^{-1/3}] \{P_1^{2/3}/9 - P^2 P_1^{-4/3}/9 - 2PP_1^{-1/3}/9 + 2P^2 P_1^{-4/3}/9\}$$
$$- (4/3)\gamma\pi(3/4)^{2/3}R^{*2/3}P_1^{-1/3}/E^{*2/3} + (T^2(3R^*/4E^*)^{-1/3}P_1^{-4/3}/48\gamma^*)$$
$$= [P_1^{-4/3}(3/4)^{2/3}/9E^{*2/3}R^{*1/3}]\{P_1^2 - P^2 - 2PP_1 + 2P^2 - 12\gamma\pi R^*P_1$$
$$+ T^2 E^*/4\gamma^*\} \qquad (3.25)$$

Therefore at equilibrium, when $dU_T/dP_1 = 0$,

$$P_1^2 - 2P_1(P + 6\gamma\pi R^*) + P^2 + T^2 E^*/4\gamma^* = 0,$$

remembering (3.2),

$$P_1^2 - 2P_1(P+2P_c) + P^2 + T^2 E^*/4\gamma^* = 0$$

$$P_1 = P + 2P_c \pm (4PP_c + 4P_c^2 - T^2 E^*/4\gamma^*)^{1/2} \qquad (3.26)$$

$$a^3 = (3R^*/4E^*) [P + 2P_c + (4PP_c + 4P_c^2 - T^2 E^*/4\gamma^*)^{1/2}] \qquad (3.27)$$

Equation (3.27) indicates a reduction in the contact radius under increasing tangential force. Savkoor and Briggs (1977) suggested that this corresponds to a 'peeling'

mechanism which continues in a stable manner until a critical value of T is reached, given by the equation

$$T_c = 4 \, [\, (PP_c + P_c{}^2 \,) \gamma^* / E^*]^{1/2} \qquad\qquad (3.28)$$

It is also noted that when $T = T_c$, (3.28) reduces to

$$a^3 = (3R^*/4E^*) \, (P + 2P_c) \qquad\qquad (3.29)$$

If the relative tangential displacement increases beyond that corresponding to $T = T_c$, the peeling process is complete. According to Savkoor and Briggs (1977), if $T > T_c$, then the rate of energy release was more rapid than the rate at which the work of adhesion could absorb the energy and, hence, the quasi-static approach became inappropriate since kinetic energy terms began to play a significant role. It was argued that it was reasonable to expect the contact area would diminish to the Hertzian area, with the radius defined by (2.10), when $T > T_c$. It was also suggested that, for larger values of $T > T_c$, a shear mode of separation may occur resulting in a behaviour somewhat similar to Mindlin's (1949) concept of slip.

In considering what happens during the post peeling phase, it is more appropriate to consider what will happen when the tangential displacement is increased beyond the value of $\delta = \delta_c$ required to complete the peeling process, since the corresponding value of $T = T_c$ may be larger than the tangential force required to cause sliding. The major assumption of Savkoor and Briggs (1977) is that, when peeling is complete, the contact area 'immediately' reduces to the Hertzian value corresponding to the applied normal force P. However, it is noted that the equation for the contact radius, a, given by (3.26) reduces to (3.29) when $T = T_c$. In contrast to Savkoor and Briggs (1977), a new hypothesis is postulated to deal with post peeling mechanism. Accepting the arguments put forward by Savkoor and Briggs (1977) with regard to the peeling mechanism, which results in a reduction in the contact area as expressed by (3.26), it is suggested that there is a smooth transition from peeling to sliding in that when $T=T_c$ the contact radius is given by (3.28). Recognising that the JKR model is only an approximation to the true solution, it can be reasonably assumed that for $\delta = \delta_c$ the

68

contact area defined by (3.28) is subject to an equivalent Hertzian-like normal stress distribution corresponding to an effective normal force $(P + 2P_c)$. It then follows that the situation is well disposed to the micro-slip proposition of Mindlin (1949).

In the context of this hypothesis, if the tangential force T_c is less than that required to cause rigid body sliding, it is nevertheless sufficient to generate micro-slip over an annular region of the area defined by (3.28). The energy dissipated as a result of this micro-slip may well account for the excess rate of energy release referred to by Savkoor and Briggs (1977) when $T > T_c$. If the tangential force T_c exceeds the value required for rigid body sliding then, when $\delta > \delta_c$, the tangential force immediately drops to the sliding value. It follows from the above arguments that, since the contact area is larger than the Hertzian area and is defined by (3.28), the sliding criterion is given as

$$T = \mu (P + 2P_c)$$ (3.30)

which may be compared with $T = \mu (P + P_c)$ as suggested by Deryaguin (1975).

It also follows that for $T > T_c$, the behaviour can be described by Mindlin's (1949) theory with the substitution of $P + 2P_c$ for P. Hence, for monotonic loading with $T > Tc$,

$$T = \mu (P + 2P_c) [1 - (1 - \delta/\delta_s)^{3/2}]$$ (3.31)

where

$$\delta_s = 3\mu [(P + 2P_c)/16G^*a]$$ (3.32)

The proposed model suggests two 'failure criteria'. The first criteria is defined by the peeling mechanism, (3.28), followed by a sliding criteria, defined by (3.30). The corresponding failure envelopes are shown in figure 3.5 and intersect when P is given by the equation

$$P^* = 2P_c \{(\chi - 1) \pm [\chi(\chi - 1)]^{1/2}\}$$ (3.33)

where

$$\chi = 4G^*/\mu^2E^*$$ (3.34)
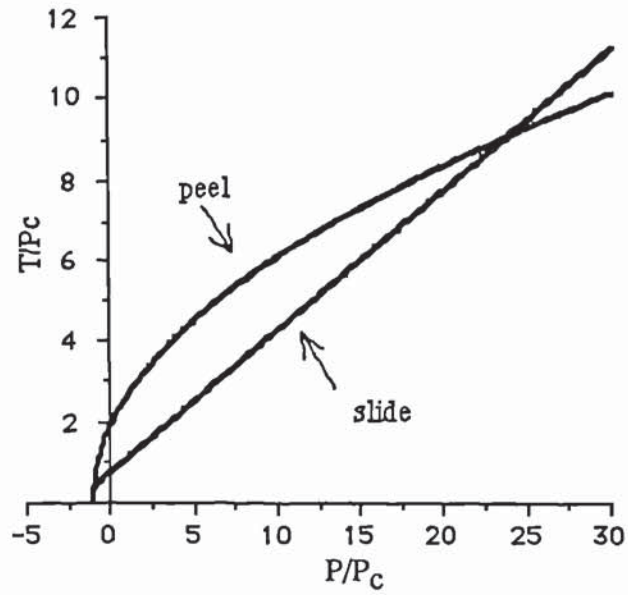
Figure 3.5 Failure envelopes

Taking the positive root in (3.33), if $P > P^*$, then peeling is followed by the development of a slip annulus which spreads radially inwards until, when $T = \mu(P + 2P_c)$, sliding occurs. The tangential force-displacement relationship is illustrated in figure 3.6.
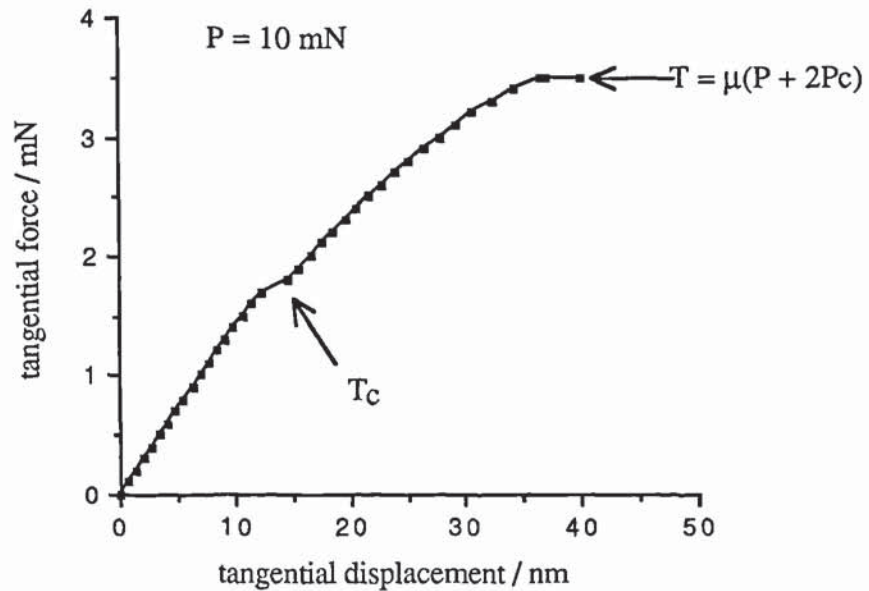
Figure 3.6 Tangential force-displacement curve when $P > P^*$

If P < P*, the tangential force at the end of peeling is greater than that necessary for sliding and hence , when $\delta = \delta_c$, T falls to the value given by (3.30), as shown in figure 3.7.
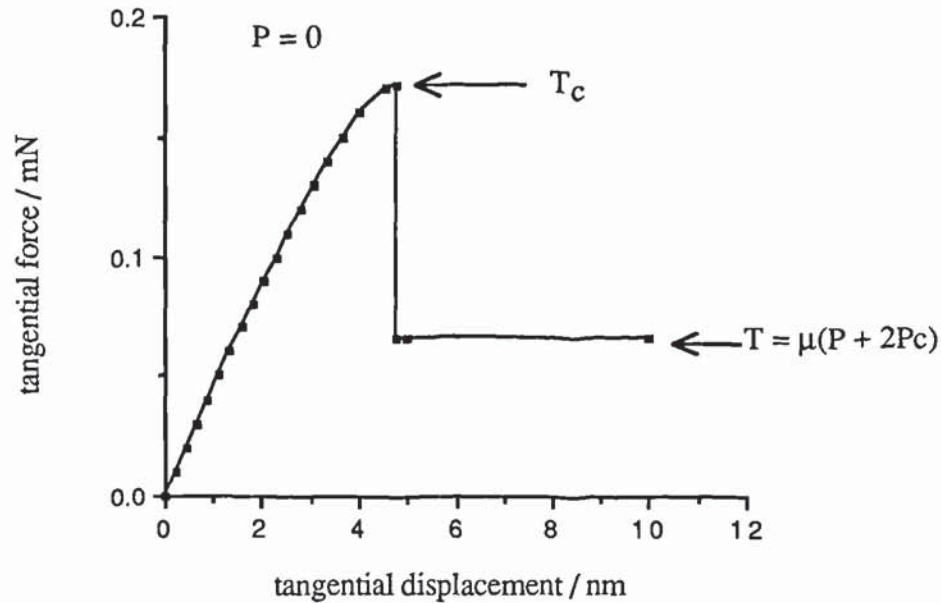
Figure 3.7 Tangential force-displacement curve when P < P*

Figure 3.7 implies that, once sliding has occurred, there is no readhesion of the contact. If this is not the case, then it might be expected that, if the sliding velocity is sufficiently slow to permit the contact to readhere, there will be a corresponding increase in the contact area. The contact will then stick until a tangential force has been mobilised sufficient to cause peeling once more. This process may repeat itself continuously thereby exhibiting the phenomenon of 'stick slip' behaviour. It is therefore implied by the theory that this type of stick slip behaviour will not occur when the normal load P is greater than that given by (3.33).

3.4.1 The Sliding Criterion

A new hypothesis has been proposed to describe the transition from peeling to sliding under oblique loading. As shown above, this leads to a new sliding criterion given by (3.30). The proposed model rests on the assumption that, when peeling is complete,

71

the contact radius is defined by (3.29) and that this is reduced but nevertheless larger than the Hertzian area. The normal stress distribution at the post peeling stage is assumed to be everywhere compressive, contrary to the argument put forward by JKR where the infinite tensile stress at the edge remained. This is essential in order to justify the immediate transition from peeling to the micro-slip mechanism of Mindlin (1949). For this condition to be satisfied, it is necessary that the value of a given by (3.29), is not greater than the value of r_0 given by (3.16). The ratio of these two radii can be written in the form

$$r_0/a = [m / (n + 2)]^{1/3} / [(n + 2m)/3m]^{1/2} \qquad (3.35)$$

where

$$m = n + 2 + 2(1 + n)^{1/2} \qquad (3.36)$$

and

$$P = nP_c \qquad (3.37)$$

An examination of the variation of r_0/a with the ratio P/P_c shows that the condition $r_0 \geq a$ is satisfied except when $P < -0.3P_c$, figure 3.8.
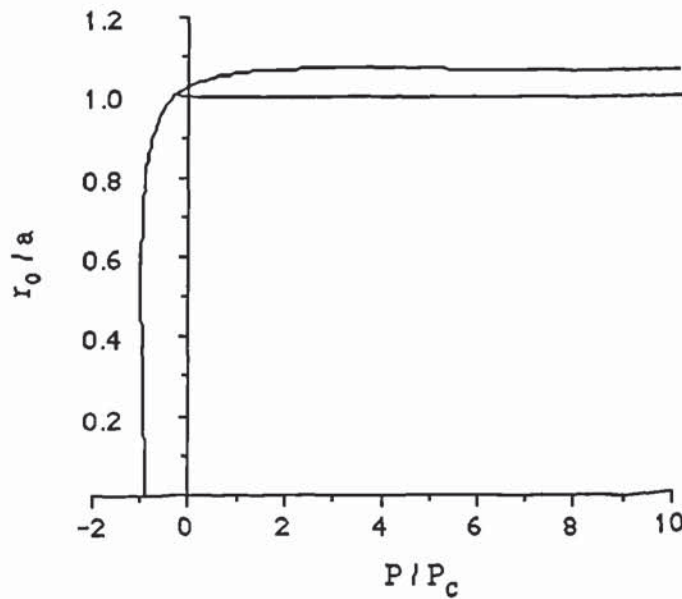
Figure 3.8 The variation of r_0/a with the ratio P/P_c

An alternative hypothesis is that the contact radius reduces to r_0 after peeling for any values of $P < -0.3P_c$.

Using (3.12), (3.13) and (3.16),

$$r_0{}^3 = (3R*P_1/4E*) [1 - (P_1 - P)/3P_1]^{3/2}$$

or,

$$r_0{}^3 = (3R*/4E*) P_2 \qquad (3.38)$$

where

$$P_2 = P_1[1 - (P_1 - P)/3P_1]^{3/2} \qquad (3.39)$$

and leads to the alternative sliding criterion

$$T = \mu P_2 \qquad (3.40)$$

which may be contrasted with

$$T = \mu P_1 \qquad (3.41)$$

as suggested by Kendall (1986), who did not consider the need for peeling to occur prior to sliding. A comparison between the two sliding criteria as defined by (3.40) and (3.30) for the negative normal loads is shown in figure 3.9.
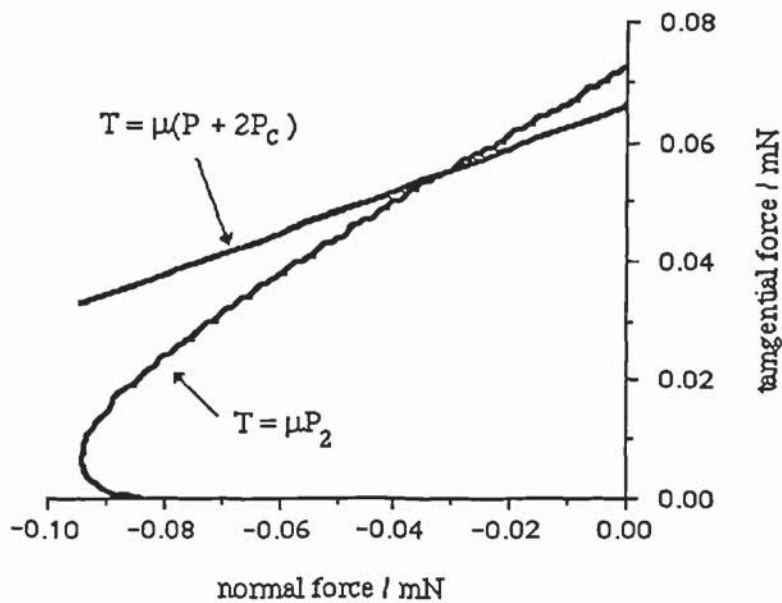
Figure 3.9 Sliding criterion when $P < -0.3P_c$
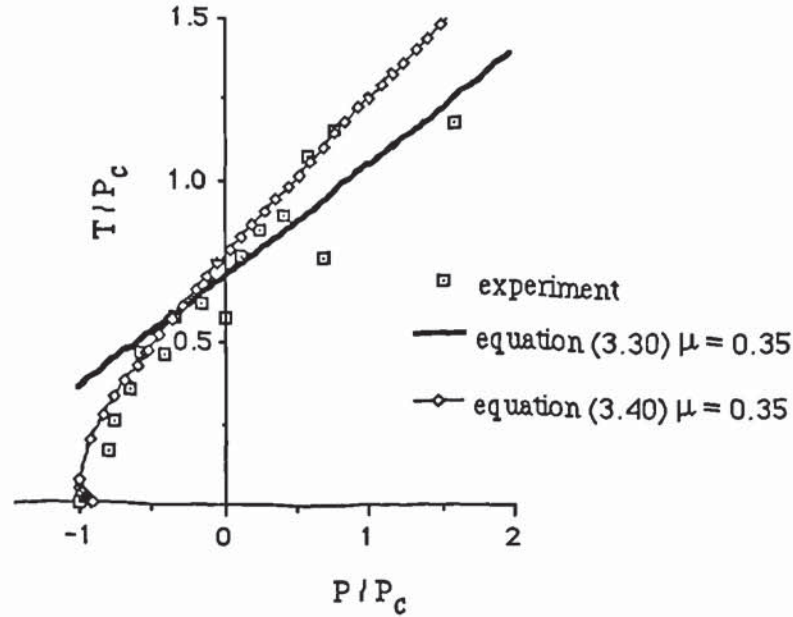
Figure 3.10 Comparison of equation (3.40) with experiment at small normal loads

The analysis of Savkoor and Briggs (1977) contains an approximation in that the tangential energy $T\delta / 2$ assumes a linear response, although the tangential force displacement law (2.31) is non-linear since the contact radius, a, varies with T, as shown by (3.27). A rigorous analysis accounting for the non-linear tangential response would appear intractable. Consequently, in the context of the JKR model of adhesion, (3.40) may well be the true sliding criterion. It must be noted, however, that the sliding criterion given by (3.40) is not consistent with peeling criterion (3.28) which is obtained from (3.27). For the computer simulations reported in the subsequent section, the sliding criterion given by (3.30) is used only when $P < -0.3P_c$ and (3.40) for $P > -0.3 P_c$. Superimposing the two sliding criteria with experimental data reported by Briscoe and Kremnitzer (1979) for polyethylene terephthalate monofilaments clearly demonstrate the viability of using the two sets of sliding criteria to give a reasonable representation (figure 3.10). In considering the experimental data for negative loads, figure 3.10, it is clear that the sliding criterion defined by (3.40) with $\mu = 0.35$, provides the best overall fit to the experimental data.

74

Figures 3.11 show the results of friction measurements reported by Briscoe and Kremnitzer (1979) for polyethylene terephthalate monofilaments in full spectrum, in contrast to that of figure 3.10, where emphasis is placed on fitting the theoretical curve for negative loads. Briscoe and Kremnitzer (1979) measured experimentally the pull-off force and quote a value of $P_c = 1.6$ μN. Superimposed on figure 3.11 are the two sliding criteria given by (3.30) and (3.40) assuming values of $\mu = 0.35$, for $P > -0.3P_c$ and $P < -0.3P_c$ respectively. Both theoretical curves agree well with the experimental data over the complete range of experimental results.

In order to deal with the post-peeling behaviour the only other modifications to the Mindlin and Deresiewicz (1953) general solution, given in section 2.4, is that (2.71), (2.72) and (2.73) are modified by substituting $P + 2P_c$ for P if $P > -0.3P_c$ and substituting P_2, given by (3.38), for P if $P < -0.3P_c$.
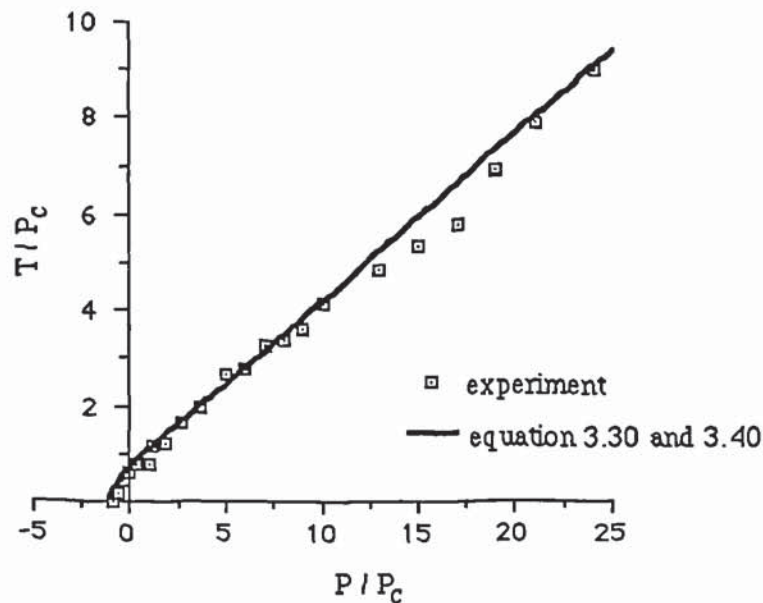

Figure 3.11 Sliding criteria in comparison with experiment

3.5 Computer Simulated Impact Tests

The simulated oblique impacts of two elastic spheres reported in section 2.5 were repeated using identical particle properties and initial velocities ($\pm$ 0.05 m/s) but with surface energies, $\gamma_1 = \gamma_2 = 0.2$ J/m^2.

For all values of impact angle $\theta > 0$, at the start of the impact the ratio $\Delta T/\Delta P$ is almost constant and slightly greater than tan θ, due to the difference between the tangential and normal contact stiffnesses. Except for the small impact angles, the contact peels and then slides as the normal force increases. Subsequent behaviour is similar to that for no adhesion with rigid body sliding recommencing towards the end of the impact. Although more work is dissipated as a consequence of the larger contact area due to adhesion, once peeling has occurred, the behaviour is essentially similar to the case with no adhesion. Hence the rebound angles are not significantly affected by adhesion. On the other hand, for small angles of impact (e.g. 5°), the particles rebound along the initial impact trajectories, the mechanics of the contact during impact is very different when adhesion is present.

A comparison between figures 3.12 and 2.18, shows that, for small impact angles, much higher tangential forces are generated and, provided that the impact velocity is small enough to prevent a peeling failure when the normal force is increasing, peeling is only completed at the end of the impact. Thus, for any impact, if the impact velocity is not large enough to cause a peeling failure as the normal force is increasing then peeling will only occur at the end of the impact with the consequence that the particles will rebound back along the initial impact trajectory. The tangential force-displacement behaviour shown in figure 3.13 is very similar to that shown in figure 2.19 for the case of no adhesion, once peeling has occurred. Except for the case of small impact angles when peeling did not occur during increasing normal force, peeling was immediately followed by rigid body sliding. Figure 3.13 clearly shows the significant energy dissipated when this sudden switch occurred.

76
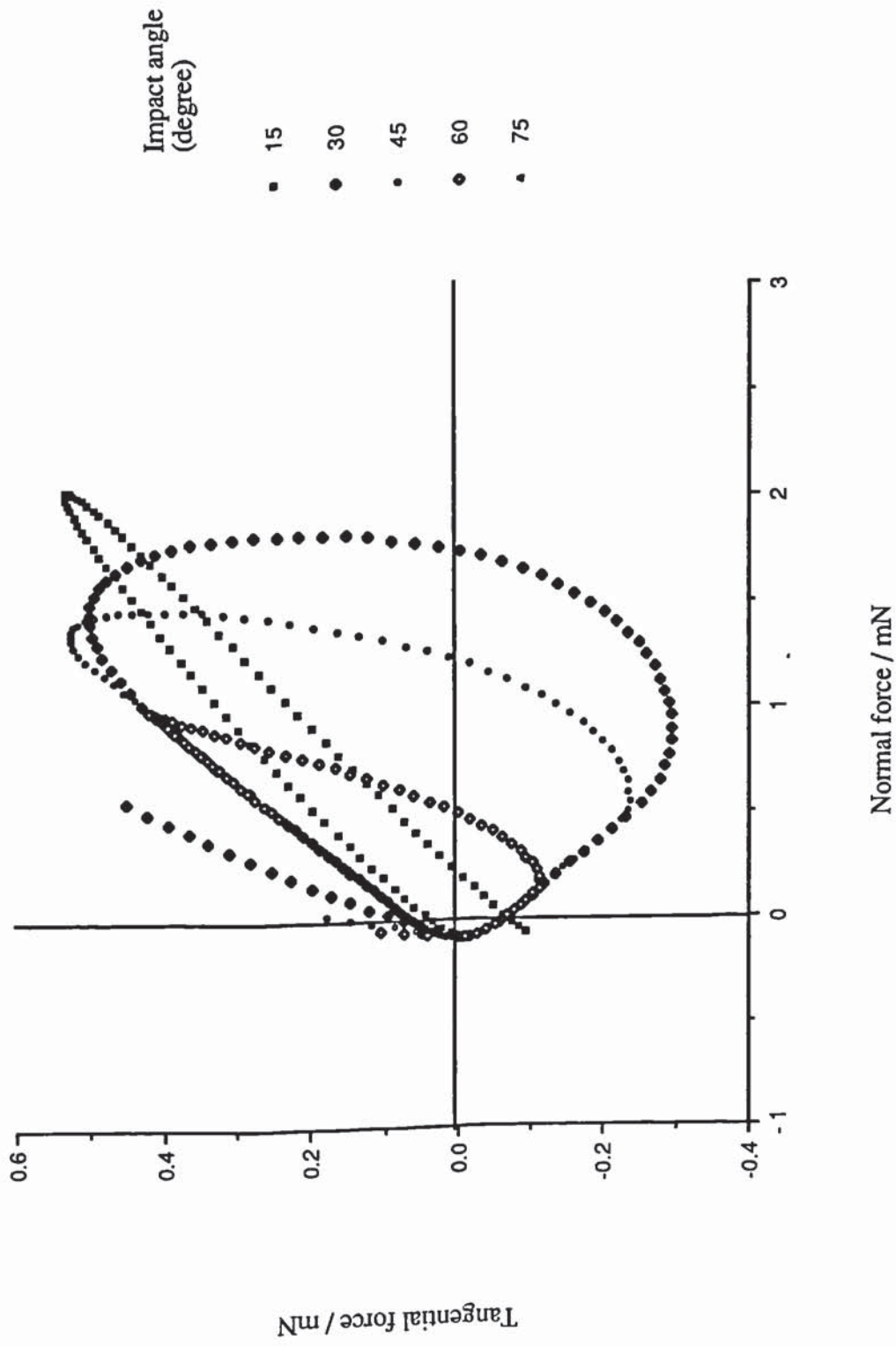
Figure 3.12 Loading paths for various degree of obliquity
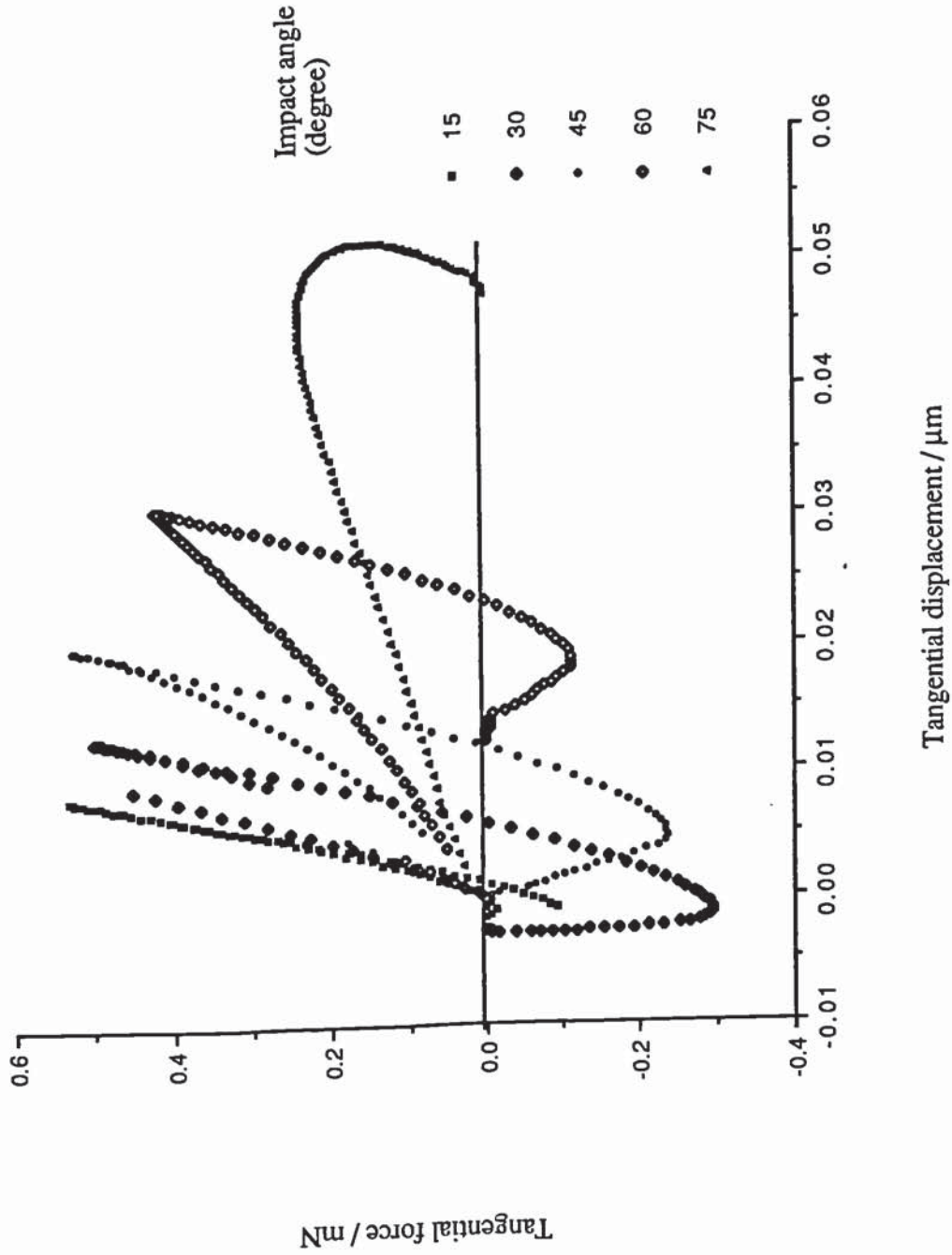
Figure 3.13 Tangential force-displacement for various degree of obliquity

The evolution of the linear kinetic energy during an impact and the way in which energy is converted into work done by the contact forces is illustrated in figures 3.14, 3.15, 3.16 and 3.17 for impacts angles of $0°$, $30°$, $60°$ and $80°$ respectively. During a colinear impact, figure 3.14, the elastic strain energy is initially negative due to the action of surface forces that exert an instantaneous tensile pull on the contact. This effect, although small, is not insignificant when the impact velocities are sufficiently small to allow the two particles to stick together. During a colinear impact there is, contrary to the case of no adhesion, a net loss in the kinetic energy as a result of the work done in breaking the 'adhesive bond'. This point will be returned to in section 3.6.

During oblique impacts, the general trends illustrated in figures 3.15 to 3.17 are very similar to those reported in chapter 2 for the case of no adhesion, except that the work done by the normal force is not fully recovered at the end of the impact.

Figure 3.14 Energy evolution during impacts, $\theta = 0°$

Figure 3.15 Energy evolution during impacts, $\theta = 30°$

Figure 3.16 Energy evolution during impacts, $\theta = 60°$

Figure 3.17 Energy evolution during impacts, θ = 80°
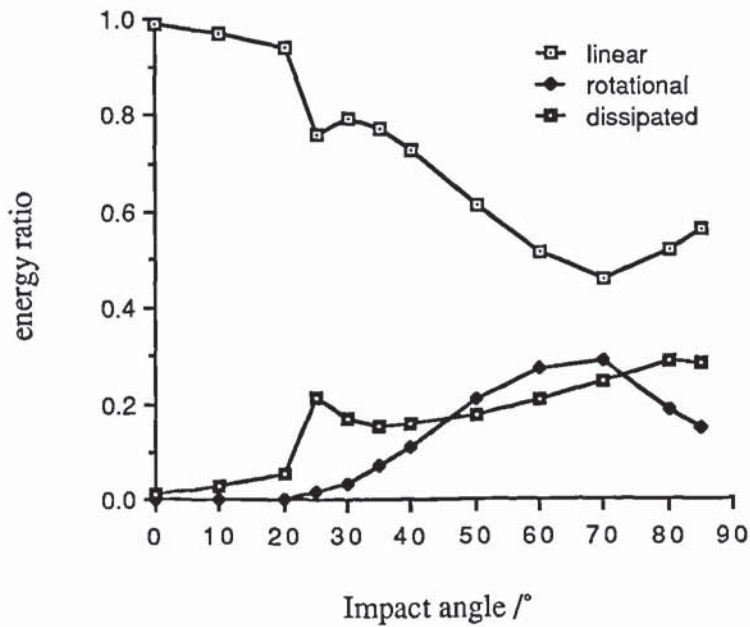
Figure 3.18 Effect of impact angle on linear and rotational kinetic energies and energy dissipated

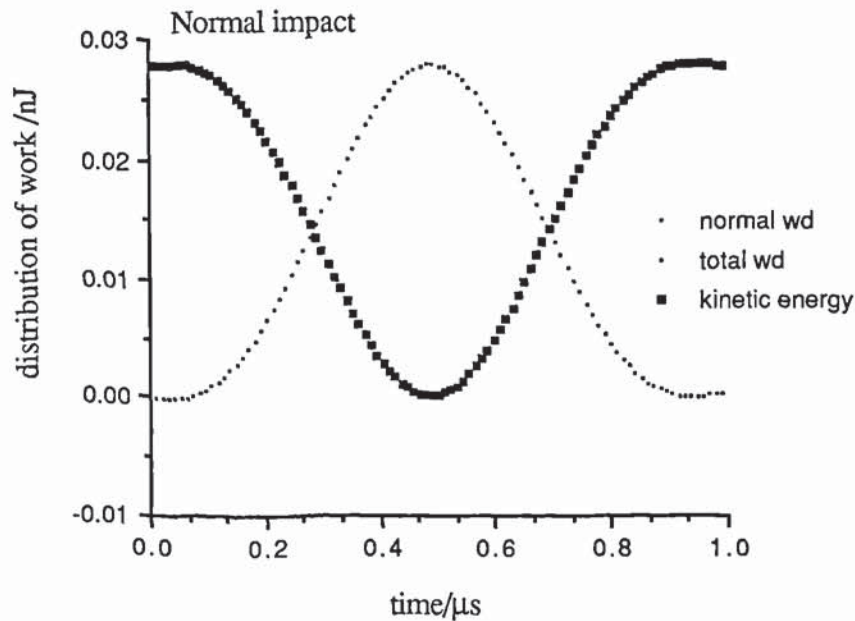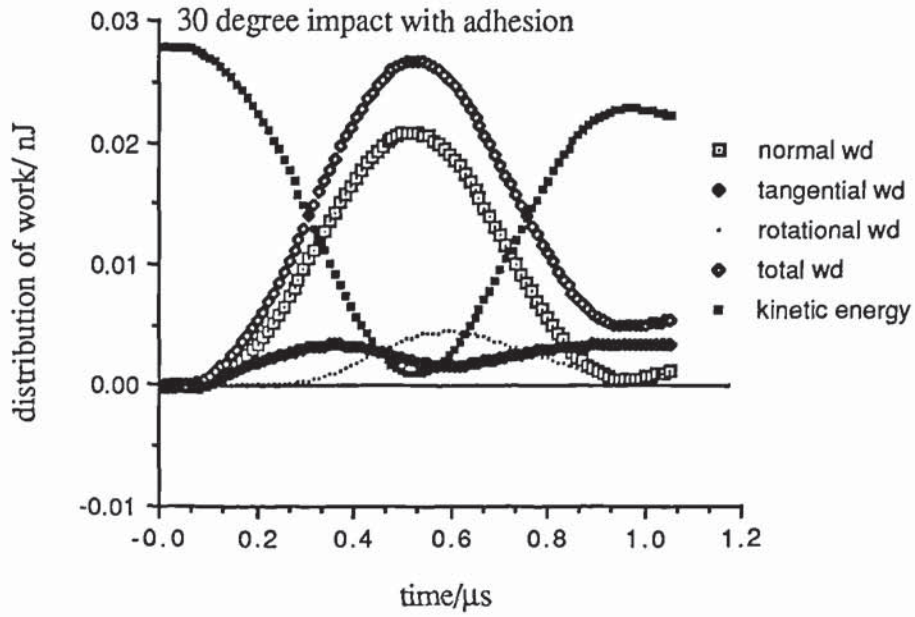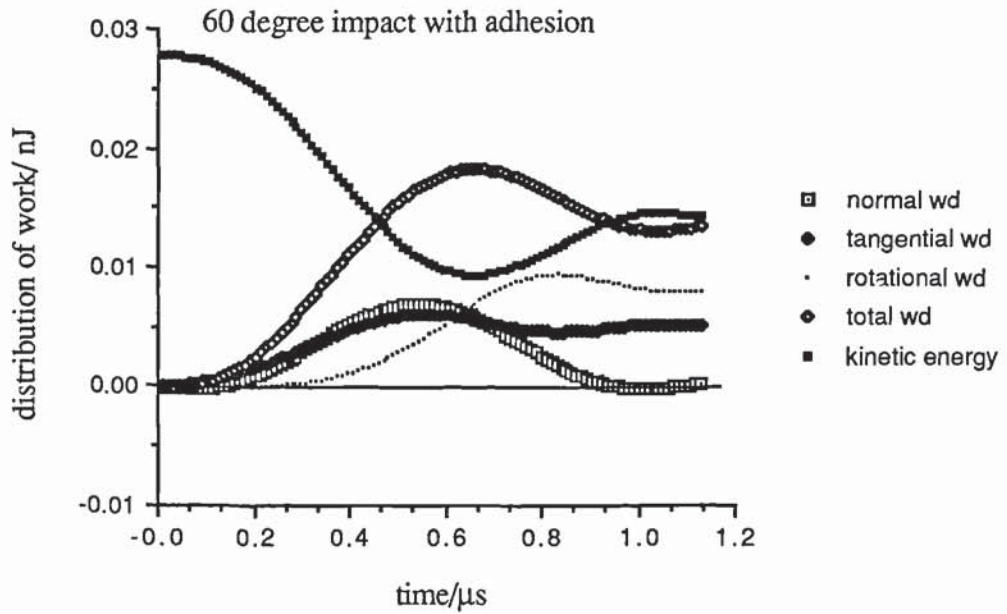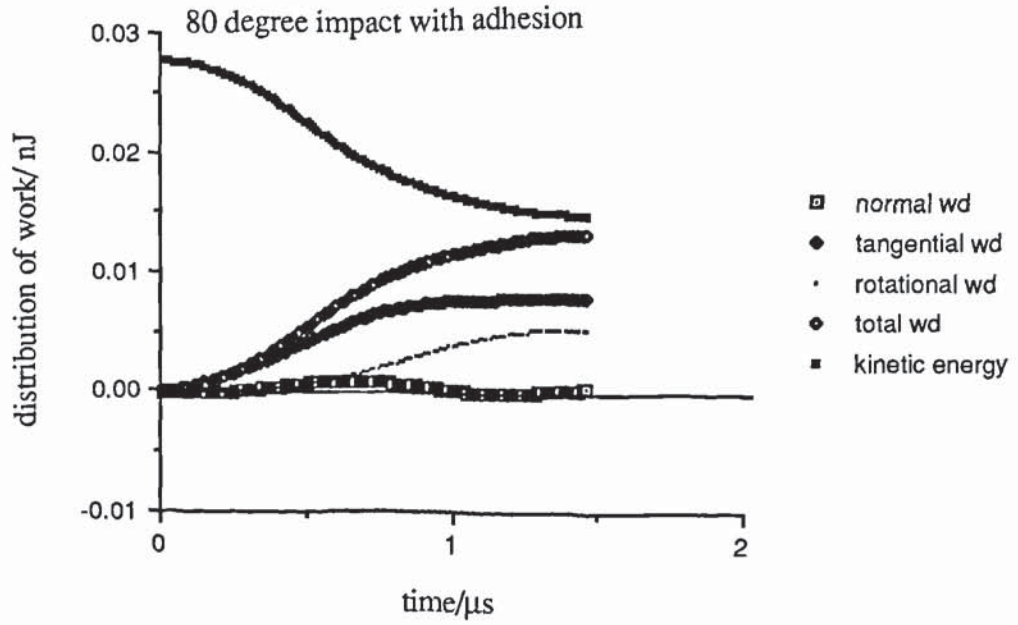For the relative impact velocity of 0.1 m/s, figure 3.18 shows the effect of adhesion on the percentage loss in linear kinetic energy, the percentage gain in rotational kinetic energy and the percentage energy dissipated due to interparticle friction. For impacts during which peeling failure occurs as the normal force is increasing, the effect of impact angle on the linear and rotational kinetic energies is similar to the case for no adhesion, figure 2.24, but with the optimum occurring at a larger impact angle. For small impact angles which result in a peeling failure at the end of the impact, there is no rotational kinetic energy developed, but there is a loss in linear kinetic energy due to the energy dissipated in adhesive peeling.

Figure 3.19 illustrates the effect of adhesion on the angle of reflection of the contact patch and the rebound angle of the particle centroid. For small angles of impact, adhesion provides sufficient kinematic constraint on the particle movements such that the contact behaviour is simply that of an oblique elastic spring, resulting in both the contact patch and particle centroid rebounding back along the initial impact trajectory. However, above a certain critical impact angle, there is a rapid transition to behaviour very similar to that experienced by the particles with no adhesion, figure 3.20.

At larger impact angles, the effect of adhesion on the rebound trajectory of the particle centroid is negligible. The effect of adhesion on the contact patch trajectory is significant, however, as can be seen from comparing figure 3.20 with figure 2.26. The rebound trajectories are independent of the impact velocity if there is no adhesion but, in the presence of adhesion, the impact angle at which the simple elastic spring effect breaks down increases with decrease in initial impact velocity.

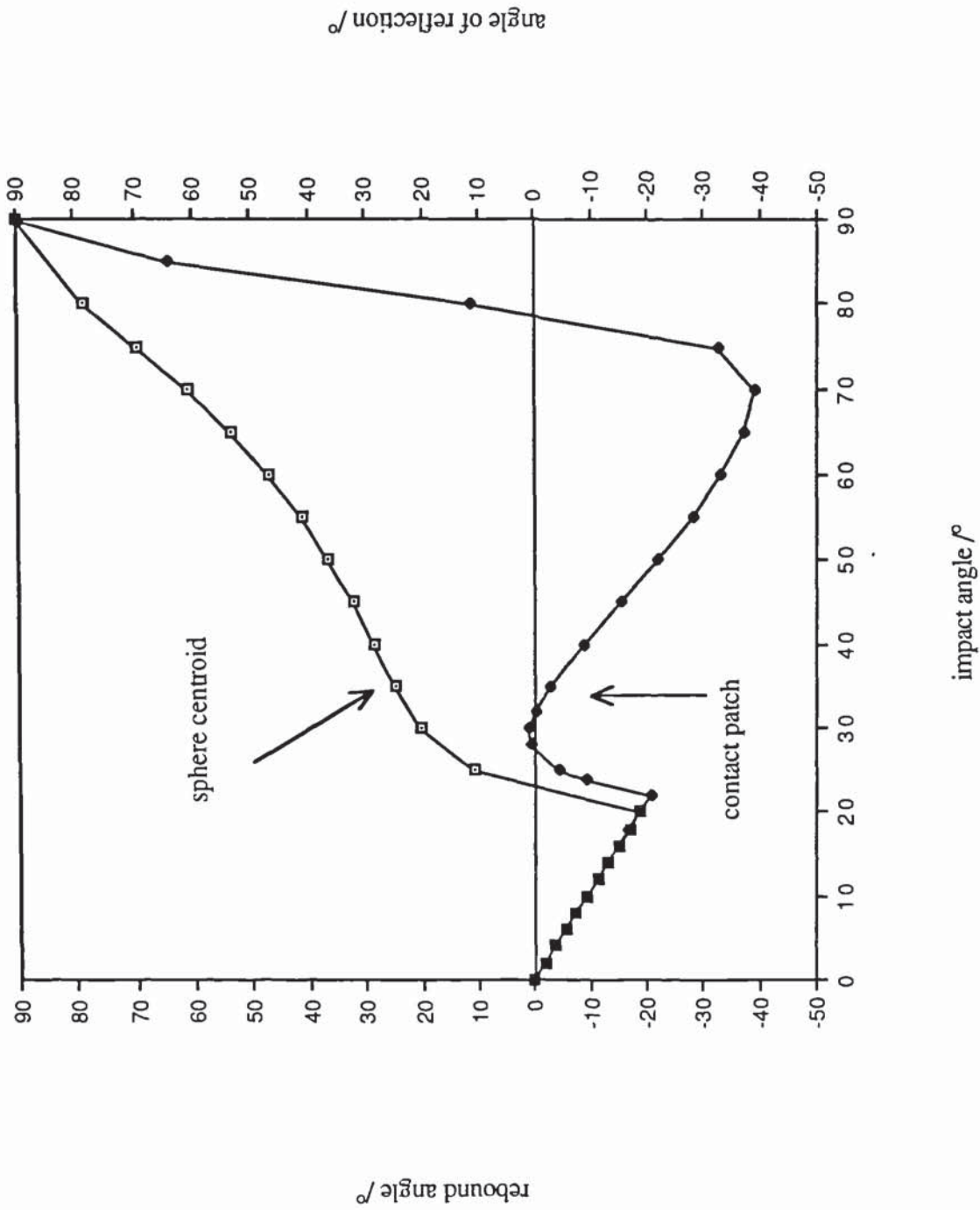Figure 3.19 Angle of reflection of contact patch and rebound angle of particle centroid under various degree of obliquity
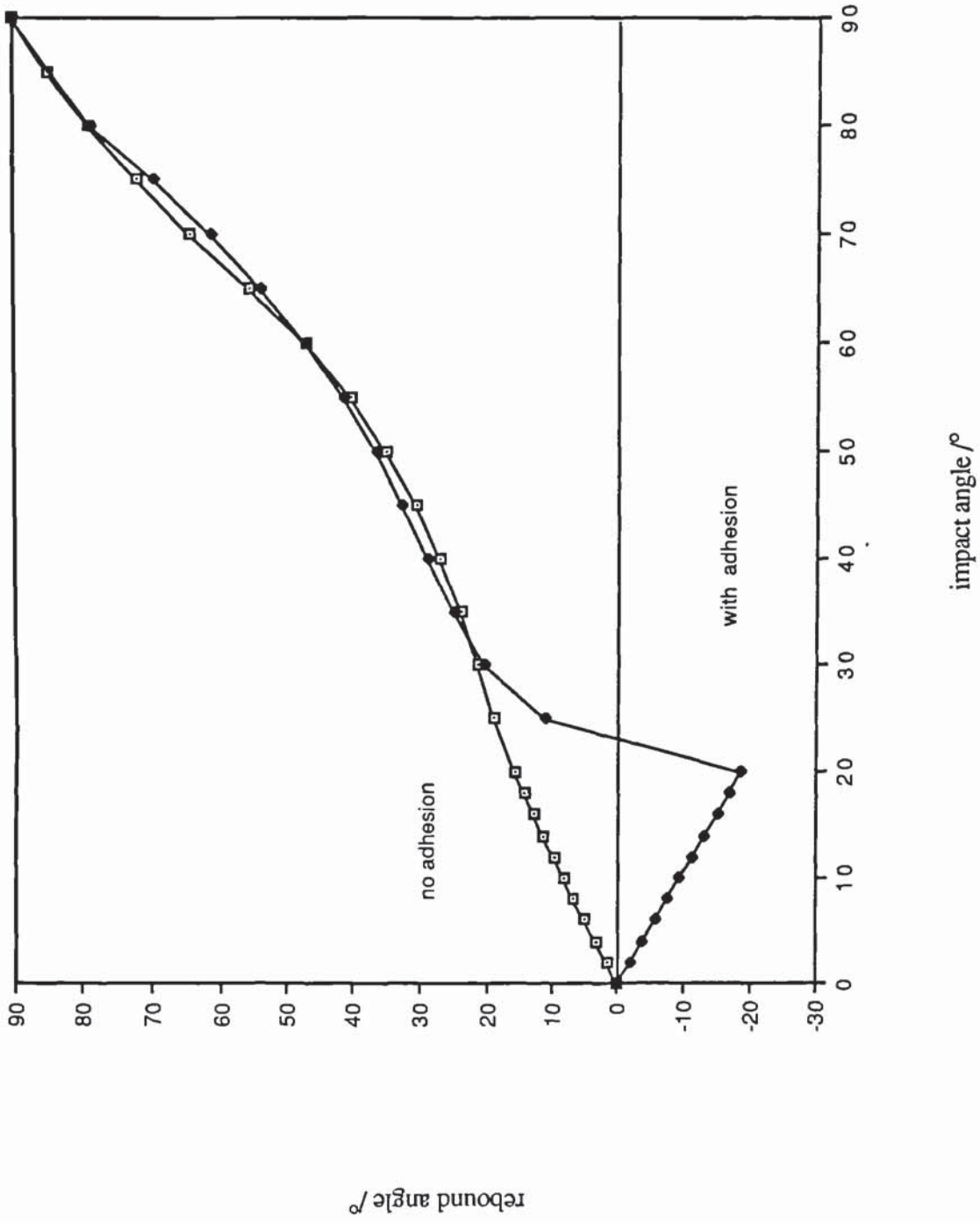
Figure 3.20 Rebound angles of particle centroid with and without adhesion under various degree of obliquity

3.6 Work Done In Adhesive Peeling

The above observations are for cases in which particles rebound after impact. Another possibility, of relevance to a wide area of particulate technology, for example, aerosol industry, is that the particles may adhere and rebound. Figure 3.21 displays the various stages of work on a typical JKR curve during a colinear impact.
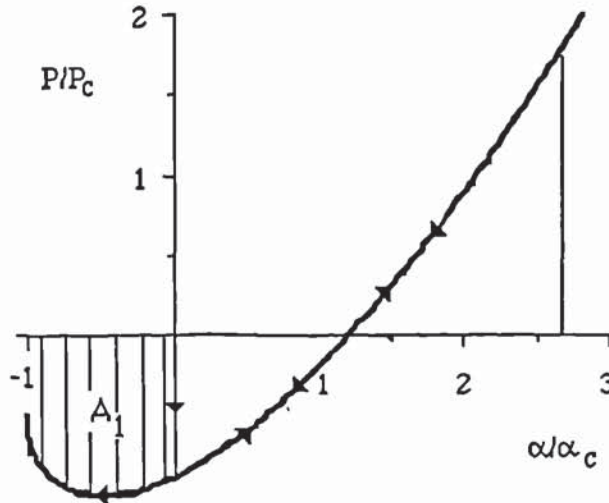
Figure 3.21 JKR curve, showing the various stages of work

On approach, surface forces do not come into play until the sphere surface are within a few angstroms separation, i.e. at the origin O. At that instant adhesive forces rapidly pull the surfaces together so that a tension is established without any measurable change in α. The spheres proceed to compress until work done by P reduces the kinetic energy to zero. On rebound the process is elastic whilst α is positive, but the surfaces then remain adhered up to the separation point. The work done by the adhesive force, denoted by area A_1 in the figure, reduces the kinetic energy of rebound and may even prevent it altogether if the initial velocity is low or the surface energy is large. This energy is accounted for by the strain energy component of the JKR equation.

In order to fully appreciate the small but finitely significance work done and hence the value of a critical velocity, a mathematical analysis is essential. Figure 3.22 shows the JKR normal displacement-force curve.
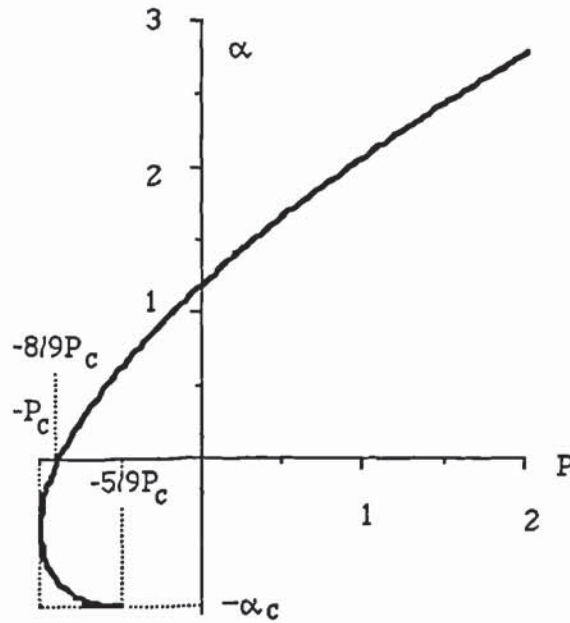
Figure 3.22 Normal displacement against normal force

The force-displacement curve is defined, Johnson (1976), by

$$\frac{\alpha}{\alpha_c} = \frac{3(P/P_c) + 2 \pm 2(1 + P/P_c)^{1/2}}{3^{2/3}\{P/P_c + 2 \pm 2(1 + P/P_c)^{1/2}\}^{1/3}} \tag{3.42}$$

The work done may be obtained from

$$WD = (5/9)P_c\alpha_c + \int_{-5P_c/9}^{-P_c} \alpha \, dP - \int_{-8P_c/9}^{-P_c} \alpha dP \tag{3.43}$$

Substituting $y = \alpha/\alpha_c$ and $x = P/P_c$ so that (3.42) may be written as

$$y = [3x + 2 \pm 2(1 + x)^{1/2}] / (3^{2/3})[(x + 2 \pm 2(1 + x)^{1/2}]^{1/3} \tag{3.44}$$

the work done becomes

$$WD = P_c\alpha_c \{ (5/9) + \int_{-5/9}^{-1} y dx - \int_{-8/9}^{-1} y dx \} \tag{3.45}$$

Further substitution of $z = 1 + x$ leads to

86

$$WD = P_c \alpha_c \left\{ (5/9) + \int_{4/9}^{0} y\,dz - \int_{1/9}^{0} y\,dz \right\} \tag{3.46}$$

with

$$y = \frac{3z - 1 \pm 2z^{1/2}}{3^{2/3}(z + 1 \pm 2z^{1/2})^{1/3}} \tag{3.47}$$

or

$$y = (3^{-2/3})(3z^{1/2} \mp 1)(z^{1/2} \pm 1)^{1/3} \tag{3.48}$$

Substituting $s = z^{1/2} \pm 1$ gives

$$y = (3s \mp 4)(s/9)^{1/3} \tag{3.49}$$

in which the negative sign applies over the range $-8P_c/9 > P > -P_c$ and the positive sign applies for $-5P_c/9 > P > -P_c$. Hence the work done may be written as

$$WD = P_c \alpha_c [(5/9) + (2/3^{2/3}) \int_{-1/3}^{-1} (3s + 4)s^{1/3}(s+1)\,ds - (2/3^{2/3}) \int_{4/3}^{1} (3s - 4) s^{1/3}(s-1)\,ds]$$

$$\dots\dots\dots\dots\dots\dots(3.50)$$

$$WD = P_c \alpha_c \left\{ (5/9) + \frac{2}{3^{2/3}}(0.414647108) - \frac{2}{3^{2/3}}(0.019486067) \right\} \tag{3.51}$$

Therefore,

$$WD = 0.9355\, P_c \alpha_c \tag{3.52}$$

Since,

$$P_c = 3\pi\gamma R*$$

and

$$\alpha_c = [\pi^2\gamma^2 R*/2E*^2]^{1/3}$$
$$= [3P_c^2/16E*^2R*]^{1/3} \tag{3.53}$$

$$P_c \alpha_c = (9/2) [\pi^5\gamma^5 R*^4/2E*^2]^{1/3} \tag{3.54}$$

$$WD = 4.21 [\pi^5\gamma^5 R*^4/2E*^2]^{1/3}$$
$$= 22.5 [\gamma^5 R*^4/E*^2]^{1/3} \tag{3.55}$$

Since the work done, as defined above is the excess work required for peeling, the critical velocity below which peeling does not occur may obtained from

$$(0.5mV^2) = WD \tag{3.56}$$

assuming perfectly elastic spheres for which the coefficient of restitution e = 1.

Hence,

$$V_c = \{ (45/m) [\gamma^5 R*^4/E*^2]^{1/3} \}^{1/2} \tag{3.57}$$

Since the mass, m = $4\pi\rho R^3/3$ and, for like spheres, R* = R/2, (3.57) may be rewritten as

$$V_c = 2.065 (\rho)^{-1/2}(E*)^{-1/3} (\gamma/R)^{5/6} \tag{3.58}$$

3.7 Critical Impact Velocity

A series of investigative simulations were performed to gain an insight into the behaviour of the particle's tendency to adhere or rebounce and hence the critical velocities. Equation (3.58) shows that the critical velocity, V_c, is a function of the mass, the Dupre energy of adhesion, the radii and the Young's modulus of the particles. Of the four parameters, the radii and the Dupre energy of adhesion contribute a significant role in determining the critical velocity and the pull of force as presented in equation (3.2). It is on the basis of these governing factors that the simulations were performed by varying each of the two parameters separately while keeping the rest constant.

Figure 3.23 shows the effect of varying the size of the particles on the critical velocity below which the particles remain adhered together. It can be seen that an order of magnitude reduction in the particle radius leads to an order of magnitude increase in the critical velocity. For a given particle size, R =100μm, figure 3.24 illustrate the effect of surface energy on the magnitude of the critical velocity. The effect of surface energy on the magnitude of the critical velocity. The figure shows that the critical velocity increases by an order of magnitude if the surface energy is increased by an order of magnitude.
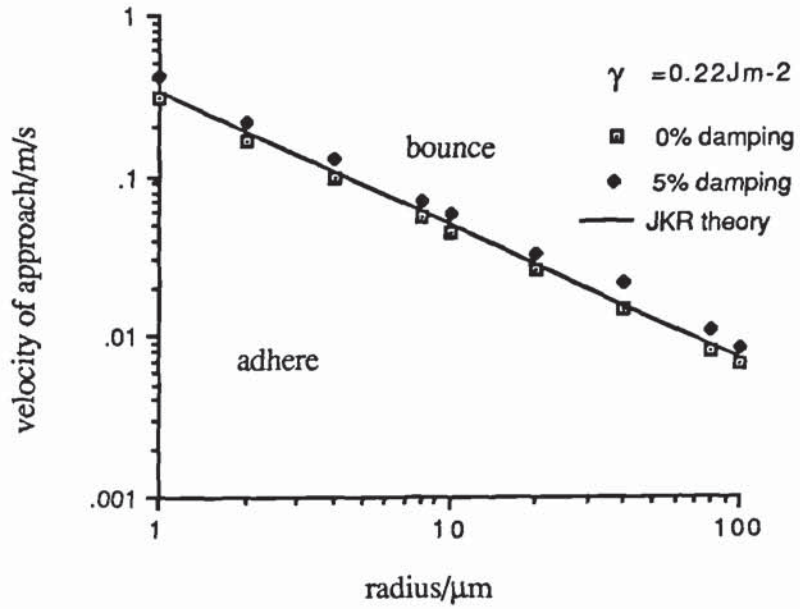
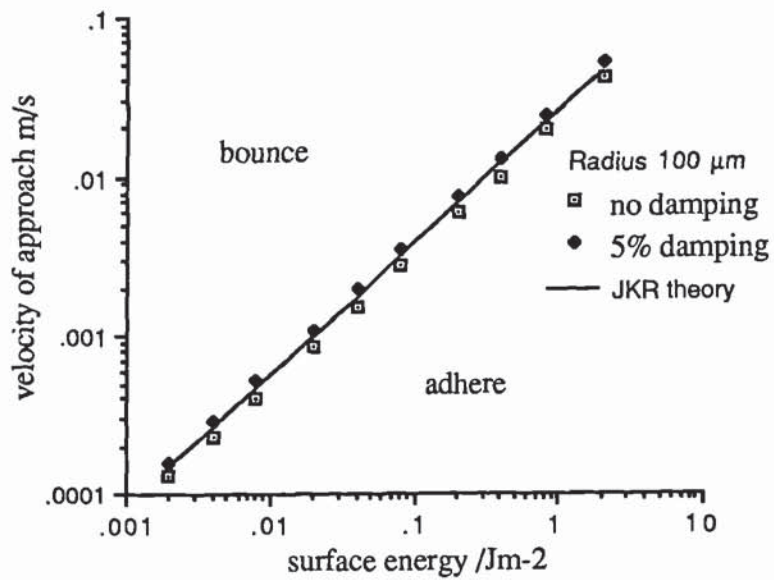Figure 3.23 Effect of size to rebounce and adhere

Figure 3.24 Effect of surface energy to rebounce and adhere

The above order of magnitude effects are, explained by equation (3.57) which, for equal sized spheres, indicates that the critical velocity is proportional to $(\gamma/R)^{5/6}$. Whether sticking occurs or not depends on the competition between the kinetic energy and the energy required to break the 'adhesion bond'. Large stiff dense particles will tend to bounce unless the impact velocity is small or the adhesion energy is high. Small soft light particles will tend to stick unless the velocity is high or the surface energy is low.

Figures 3.23 and 3.24 show that the results of the simulations of perfectly elastic spheres, with no contact damping employed, agree exactly with the prediction of the JKR theory provided by (3.57). If, in these simulations, the velocity is sufficiently small that the particles remain adhered together then the normal force oscillates indefinitely and an equilibrium state is not achieved. This is, of course, unrealistic and would cause problems when simulating large system of particles. Consequently it is necessary to incorporate a small amount of damping (5% of the critical damping) in order to attenuate the force oscillations. This corresponds to the natural dissipation process that occurs as stress waves travel through the solid material of the particles themselves. Figures 3.23 and 3.24 show that this small additional energy dissipation mechanism results in a small increase in the critical velocities. The attenuation of the contact force as a consequence of contact damping is illustrated by the envelope to the force oscillations shown in figure 3.25.

3.8 Discussion

The effect of adhesion has been illustrated by simulations of oblique impacts for an initial relative impact velocity of 0.1m/s. The results show that, although adhesion affects the dissipation and redistribution of energy for all angles of impact, the effect is most pronounced when peeling is only completed at the end of the impact. The angles of impact at which this occurs depend on the impact velocity. For all impact angles, if the impact velocity is not large enough to complete the peeling process when the normal
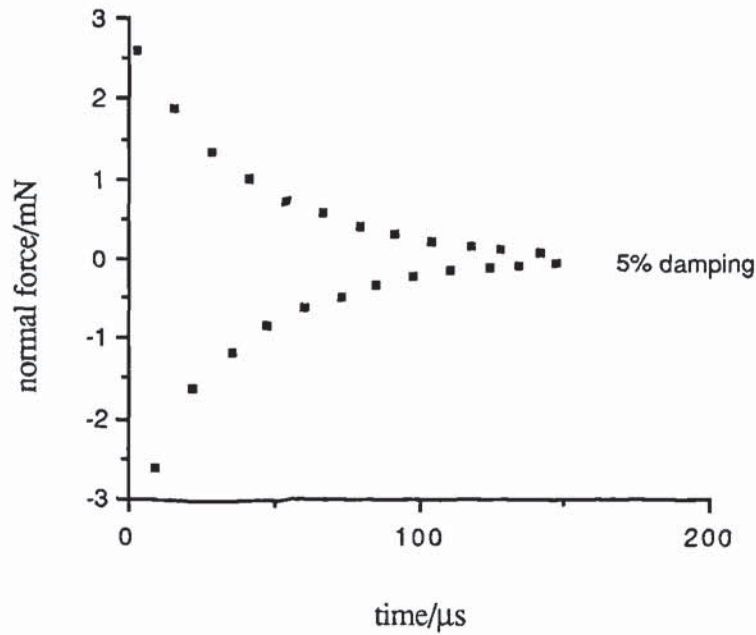
Figure 3.25 Effect of damping in attenuating the normal force

force is increasing, then the particles will rebound back along the initial impact trajectory, unless the impact velocity is sufficiently small that sticking occurs.

For colinear impacts with adhesion, the computer-simulated experiments identified critical impact velocities above which particles bounce and below which particles adhere together. As expected, the observations agreed with the predictions of the JKR theory and presented a similar pattern of adherence and bounce to that reported by Reeds (1987).

In order to simulate oblique impacts with adhesion, it has been necessary to extend and combine the theoretical approaches of Savkoor and Briggs (1977) and Mindlin and Deresiewicz (1953). The resulting theory, however, is not a rigorous solution, due to the approximations in existing theories and the speculative nature of the proposed sliding criteria. Nevertheless, it is believed that the proposed theoretical model is qualitatively correct in describing the tangential response as one which requires peeling to occur prior to sliding.

91

The adhesion between two bodies is even more complicated if they are allowed to be viscoelastic rather than simply elastic. In this case, energy losses due to the effect of plasticity will make the situation different for increasing and decreasing loads and, in general, dependent in the history of the sample. Even with this degree of complexity the theories do not describe the real world, for they assume perfectly smooth surfaces. Any attempts to describe friction, cold welding or adhesion in a real situation must consider surface roughness, and theories then become semi-quantitative or empirical.

In simulation experiments, the question of how much surface energy governs the choice of theoretical models like JKR, DMT, and even MYD, proved to be a predicament. In recent years, there was the argument that 'hard' materials fits in better with DMT while 'soft' materials are a better fit for JKR. Any quantitative results obtained from simulations, especially those involving impacts received no specific experimental backing and the validity of these results needs further real confirmation.

4. The Distinct Element Method

Discrete Numerical Modelling and the Methodology

It is easier to write an incorrect program than understand a correct one   - Murphy's law of computing

4.1 Introduction

Discrete or Distinct element methods (DEMs) are a family of related numerical techniques designed specifically to solve problems in applied mechanics which exhibit gross discontinuous material and geometrical behaviour. For example, many DEM models are capable of analysing multiple interacting rigid or deformable bodies undergoing large dynamic or pseudo static absolute or relative motions, governed by complex constitutive behaviour. In many of these discontinuous situations, the continuity constraints are either inappropriate or relaxed because of the physics of the problem and are either intractable or very difficult to analyse with the set of procedures based upon continuum principles such as the conventional finite element method, boundary element or finite difference methods.

Useful experimental observations of micromechanical parameters such as contact forces have been made in granular media, for example using photoelastic techniques. However, the interpretation of these experiments are very time consuming. Numerical experiments using computers have increasingly become the preferred tool to investigate in detail the micromechanical behaviour of granular media as improved techniques and more powerful computers become easily available.

Although computer simulated experimentation using the DEM was originally developed as a tool for examining geomechanical problems, Cundall (1971), the dynamic nature of the methodology used lends itself readily to many other areas of scientific and industrial interest. One such area is that of process engineering in which the physical and geometrical formation of agglomeration processes and agglomerate breakdown, either by attrition or comminution, are also amenable to investigation by the DEM.

93

4.2 Brief Literature Review

A discontinuous system is an assembly of discrete particles with interactions taking place only at points of contact. Therefore it is essential to establish methods of identifying contacts and modelling the contact interactions in all discrete element methods. For all methods, general allowances are made to cater for contacts to be broken or slide, and they are divided into two main categories according to the treatment of the behaviour in the normal direction of motion. In the first group, using the hard contact approach, (or the rigid particle model) the interpretation is regarded as non-physical and algorithms are coded to prevent any interpenetration of the two bodies that form a contact, Campbell (1982). In the second group, using the soft contact approach (or the soft particle model) a finite normal stiffness is taken to represent the measurable normal stiffness that exists at a contact, Cundall (1978) or the extensions by Thornton and Randall (1989) where the normal stiffness is derived through the non-linear behaviour of the Hertz theory (see Johnson 1985).

In the rigid particle model, collisions are assumed to be instantaneous and no interpenetration of the two bodies occur. Post collision trajectories are determined from the initial trajectories and an inelastic, frictional collisional operator governing the dynamics of idealized binary collisions. The 'predictor' strategy is used so as to ensure displacement compatibility in the normal direction at all contacts, while satisfying equilibrium and the constitutive laws. A list of collisions in order of precedence is maintained and simulation proceeds by variable time steps between successive collisions. The hard contact assumption is especially appropriate in simulations of 'molecular dynamics', in which sparse populations of bodies move around at high speed and interact by collision. The collisions are very brief, and can be modelled as instantaneous exchanges of momentum and energy may or may not be conserved by the particle pair. The rigid particle model for granular flow was developed by Campbell (1982), who modelled rectilinear uniform shear flows using streamwise periodic boundaries. Hopkins (1987) developed a dynamical rigid particle numerical simulation

program similar to Campbell's for comparison with the two -dimensional air table experiments of Sanders and Ackermann (1987). In Hopkins (1987) simulations, the collisional operator used is capable of explicitly accounting for finite values of friction. The search strategy devised does not require complicated maintenance of a collision list but rather allows for small overlaps between particles. Potential overlaps, similar to those of the soft particle model, are searched only among neighbouring particles.

The soft particle approach requires that collisions are of finite duration. The duration of contact is related to a non-infinite contact stiffness which is specified as a contact property. The force at the contact is continuously varying as the particles are being deformed. Deformation of the particle is represented as a small overlap. A well known example of a soft contact formulation is the Hertz theory (see Johnson 1985), in which the assumption of elasticity is used to derive the normal stiffness at the contact between two deformable spheres. A further assumption is that the radius of the contact area is small compared to the radius of the spheres. Forces at all the contacts are determined at one instant and Newton's equations of motion are then numerically integrated to obtain new particle velocities and positions. The derived normal stiffness is non-linear and may be used directly in numerical simulations. Simulation proceeds by small timesteps which are usually a function of the physical properties of the discrete elements. In order to accurately integrate the equations of motion the usual explicit schemes require more time steps during a collision. This approach is more efficient than a rigid particle approach for dense systems. More significantly, this approach is applicable to all configurations including both quasi-static and dynamic situations.

Cundall and Strack (1979, 1982, and 1983) developed the first discrete particle model based on the soft particle approach. They used linear springs to model the normal and tangential contact stiffnesses with the tangential force limited by a Mohr-Coulomb criterion. Although their calculation method treats the full dynamics of the system of particles, it was used primarily to investigate the behaviour of granular material

undergoing slow, quasi- static deformations and the simulation results were in good qualitative agreement with experimental measurements.

Walton (1982, 1983) developed an explicit particle-dynamics model for granular materials, similar to the model of Cundall and Strack (1979). One difference is the inclusion of the damping or dashpot normal force in determining the total normal force used for the friction limit. It was suggested that this is more suitable for rapid particle flows involving dynamic impacts. This model is intended to be used for rapid deforming granular material. Walton and Braun (1985) used a different force model in their study of assemblies of nearly rigid, inelastic, frictional discs undergoing steady state shearing. The normal force model was a partially latched spring model which provided different stiffnesses for loading and unloading. Consequently, energy dissipation due to normal interactions was modelled in a way similar to that due to plastic deformation in real systems. The tangential friction force model was similar to that of Mindlin and Deresiewicz (1953).

4.3 Methodology For Modelling Discontinuous Systems

In order to reliably model discontinuous media a program must be able to accommodate finite displacement and rotation of the discrete bodies. Other issues like the ability to identify contact breaking and to recognise new or potential contacts as the simulation progresses are also essential features. The logic of identifying interacting pairs of particles efficiently is important because it will save many computing hours especially when dealing with large systems of particles. Cundall and Strack (1979) developed an efficient systematic data structure for the program Ball which, with only minor modifications, is the basis of the program used in the work reported in this thesis.

The program identifies a rectangular 'workspace' which is divided up by a grid to form a series of boxes or cells. Particles are mapped into their respective boxes according to the locations of the corners of a circumscribing square. In this way a particle may map

into 1, 2 or 4 boxes. Only the boxes into which a particle is mapped are searched for potential contacts. During a simulation, when the accumulated displacement of a particle (items B11 and B12, see figure 4.2) exceeds a specified amount, a check is made to determine whether or not the particle needs to be remapped into different boxes (reboxing).

4.3.1 Data Structures

The memory map which contains all the information on particles, walls, boxes and contacts is stored within a single real array A(I) which is continuously updated. The array contains 32 bit words except for the box data and link data which are stored in 16 bit half-words. The array A(I) is equivalenced to an integer array IA(I) so that integers may also be stored. Figure 4.1 shows the overall memory map with the particle, wall, box and contact information stored in separate sections. Pointers M1 to M5 identify the subdivision of the array into these different sections.

Particles, walls and contacts require 13, 22 and 10 items of information to be stored respectively. These are identified in figures 4.2, 4.3 and 4.4 (the actual x, y coordinates of a particle centroid are given by summing the items B1+B12 and B2+B12, figure 4.2). In the box data list each box is represented by a 32 bit word which is subdivided into two 16 bit half-words. Each half-word contains an integer which acts as a pointer. One pointer indicates the address of the start of a linked list of contacts that map into the box. The other pointer indicates the starting address of a linked list of particles that map into the box. The program systematically considers each box in turn and thereby deals with all particles and contacts during each calculation cycle. For further details of the program structure the reader is referred to Cundall (1978), Barnes (1985) and Randall (1989).
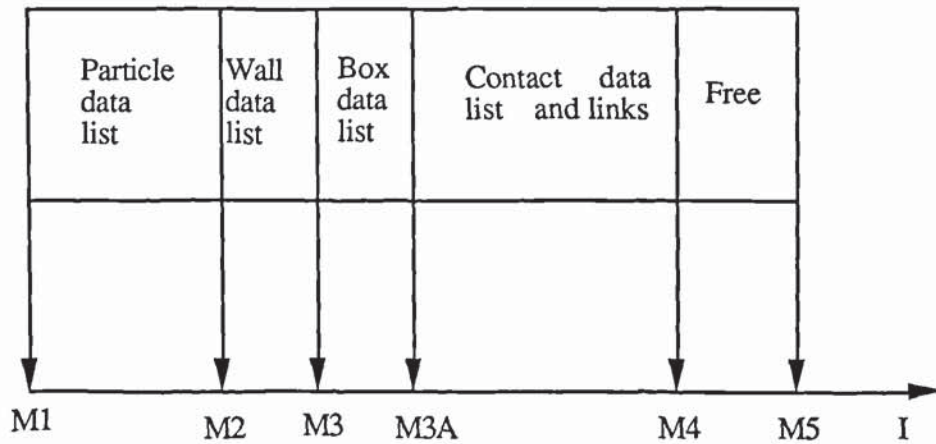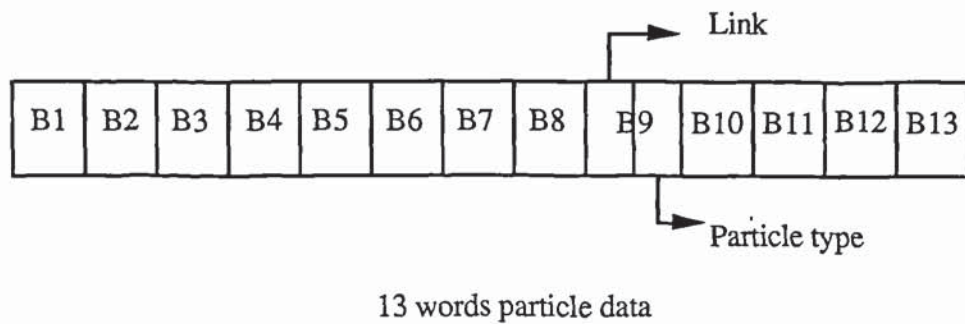
Figure 4.1 The overall memory map of array A(I).

13 words particle data

B1 - x coordinate of particle, see text

B2 - y coordinate of particle, see text

B3 - x velocity of particle

B4 - y velocity of particle

B5 - angular velocity of particle

B6 - x component force at the centroid of the particle

B7 - y component force at the centroid of the particle

B8 - moment about the centroid of the particle

B9 - pointers

B10 - angular displacement of particle

B11 - accumulated displacement in the x direction, see text

B12 - accumulated displacement in the y direction, see text

B13 - accumulated angular displacement, explanation as in B11 and B12

Figure 4.2 Ball information

22 words in Wall data
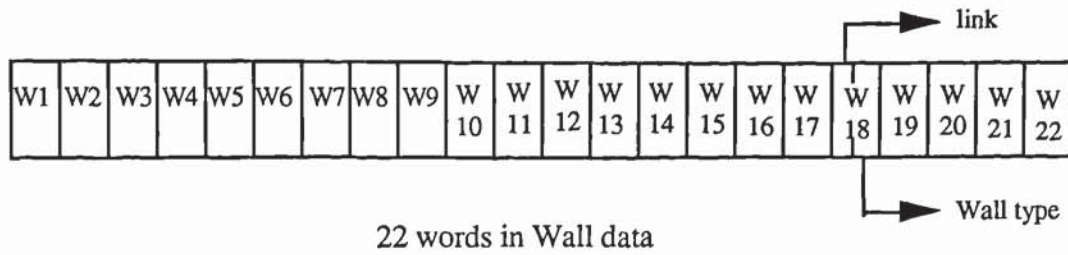
W1 - distance of end of wall to origin of rotation

W2 - distance of start of wall to origin of rotation

W3 - x coordinate of origin of rotation

W4 - y coordinate of origin of rotation

W5 - angle of wall in radians (anti-clockwise)

W6 - velocity in the x1 direction

W7 - velocity in the x2 direction

W8 - angular velocity

W9 - Sin (W5)

W10 - Cos (W5)

W11 - x coordinate at start of wall

W12 - y coordinate at start of wall

W13 - x coordinate at end of wall

W14 - y coordinate at end of wall

W15 - Force on wall (X)

W16 - Force on wall (Y)

W17 - Moment on wall

W18 - Pointers

W19 - Wall name

W20 - accumulated displacement in the x direction

W21 - accumulated displacement in the y direction

W22 - accumulated angular displacement

Figure 4.3 Wall information
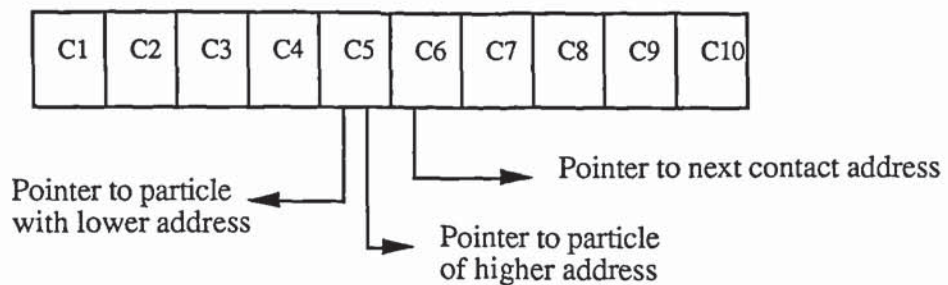
Contact and link data

C1 - Contact radius
C2 - Cumulative sliding displacement
C3 - Contact normal force
C4 - Contact tangential force
C5 - Pointers
C6 - Pointers
C7 - Marker for pre and post-peeling
C8 - T*, see section 4.4.1
C9 - T**, see section 4.4.1
C10 - Critical displacement,DD, see section 4.4.2

Figure 4.4 Contact array.

99

4.3.2 Choice Of Timestep

In the distinct element method, the contact forces and displacements within an assembly of spheres are found through a series of calculations tracing the movements of the individual particles. These movements are the result of the propagation through the medium of disturbances originating from some applied external field, e.g. gravity, boundary strain, or wall displacement. The speed of propagation is a function of the physical properties of the discrete medium. The evolution of the system is advanced in time by carrying out repeated calculations over a large number of small timesteps. It is assumed that during a small timestep the velocities and accelerations are constant.

The distinct element method is also based upon the idea that the timestep chosen is so small that, during a single timestep, disturbances cannot propagate from any sphere further than its immediate neighbours. Thus, at all times the resultant forces on any sphere are determined exclusively by its interaction with the spheres with which it is in contact. It is this underlying feature of the distinct element method that makes it possible to follow the non-linear interaction of a large number of spheres without excessive memory requirements.

4.3.3 Particle-particle Interactions

The main calculation cycle performed in the distinct element method alternates between the application of Newton's second law of motion to the spheres and the force-displacement laws to the contacts. The motion of a particle obeys Newton's second law from the forces acting on it. The force-displacement laws are then used to find contact forces from the displacements, see figure 4.5.

In the program, the particles are allowed to overlap one another at the contact points to model elastic deformation of the surface. Normally this overlapping is very small in comparison with the diameter of the particle. Large overlapping will cause numerical

instabilities as it will create excessive contact forces leading to a large out-of-balance force and high accelerations.
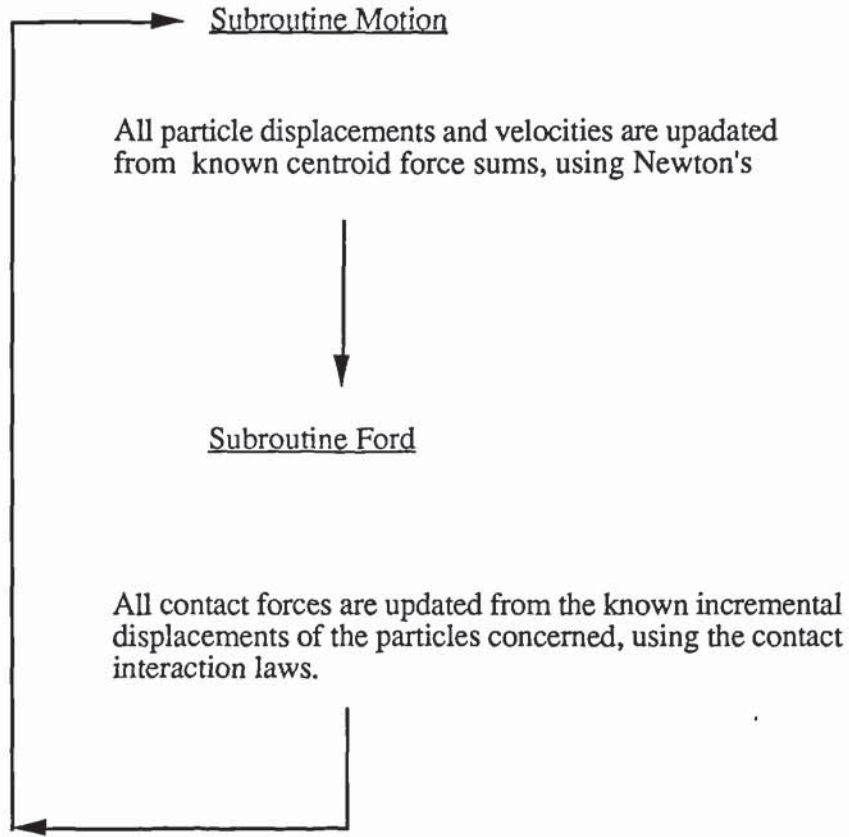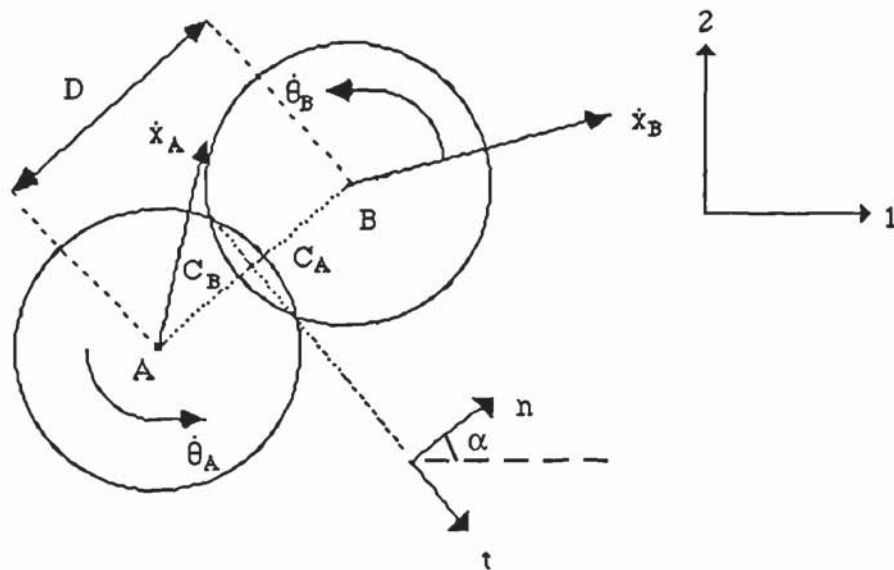
> Subroutine Motion
>
> All particle displacements and velocities are upadated from known centroid force sums, using Newton's
>
> Subroutine Ford
>
> All contact forces are updated from the known incremental displacements of the particles concerned, using the contact interaction laws.

Figure 4.5 The main calculation cycle

Figure 4.6 Kinematics of contacting spheres
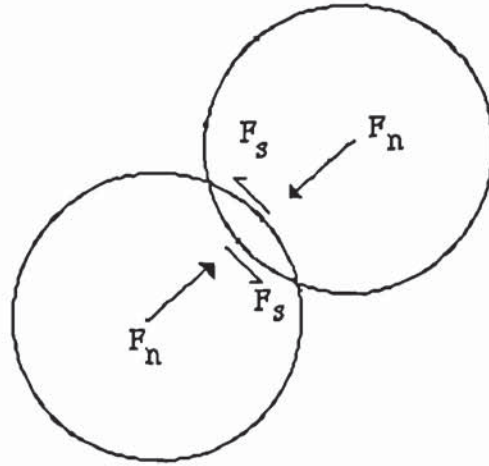
Figure 4.7 Interparticle contact forces

In order to demonstrate how forces and displacements are determined during a calculation cycle, the typical case represented in figures 4.6 and 4.7 will be considered. For simplicity, consider the case of no adhesion with the contact stiffnesses represented by linear springs. The coordinates of the centres of spheres are X_{Ai} and X_{Bi} with i = 1, 2 and the indices 1 and 2 refer to the Cartesian coordinate system indicated in the figure. Contact between the particles exist if

$$D < R_A + R_B \tag{4.1}$$

where $D^2 = (x_{Bi} - x_{Ai})^2 + (y_{Bi} - y_{Ai})^2$ (4.2)

The contact point, however, is midway between the point C_A and C_B as shown in figure 4.6. Unit vectors *n* and *t* are orthogonal, *n* being in the normal direction to the contact plane and in the direction of the line joining the centres. The direction cosines n_i are as defined as

$$n_i = (x_{Bi} - x_{Ai}) / D \tag{4.3}$$

and, in 2D, may be written as $n_1 = \cos \alpha$ and $n_2 = \sin \alpha$ where α is the inclination of the contact normal vector to the 1 axis of the global reference frame.

Since n and t are orthogonal

$$n_i t_i = 0 \tag{4.4}$$

The kinematics at the contact point may be understood as the velocity of point C_B relative to C_A

$$\dot{x}_{Ci} = (\dot{x}_{Bi} - \dot{x}_{Ai}) - (\dot{\theta}_A R_A + \dot{\theta}_B R_B)t_i \tag{4.5}$$

and resolving vector $\dot{x}_{Ci}$ into components $\dot{n}$ and $\dot{s}$ that are normal and tangential to the contact

$$\dot{n} = \dot{x}_{Ci}\, n_i \tag{4.6}$$

$$\dot{s} = \dot{x}_{Ci}\, t_i \tag{4.7}$$

and using (4.5) equations (4.6) and (4.7) may be written as,

$$\dot{n} = (\dot{x}_{Bi} - \dot{x}_{Ai})n_i \tag{4.8}$$

$$\dot{s} = (\dot{x}_{Bi} - \dot{x}_{Ai})t_i - (\dot{\theta}_A R_A + \dot{\theta}_B R_B) \tag{4.9}$$

The increments in displacement may be obtained by multiplying equations (4.8) and (4.9) by the timestep, Δt

$$\Delta n = [(\dot{x}_{Bi} - \dot{x}_{Ai})n_i]\Delta t \tag{4.10}$$

$$\Delta s = [(\dot{x}_{Bi} - \dot{x}_{Ai})t_i - (\dot{\theta}_A R_A + \dot{\theta}_B R_B)]\Delta t \tag{4.11}$$

Force increments can then be calculated by multiplying the obtained displacements by their respective stiffnesses.

$$\Delta F_n = K_n\, \Delta n \tag{4.12}$$

$$\Delta F_s = K_s\, \Delta s \tag{4.13}$$

Once the new force increments have been accrued, an update procedure is followed,

$$F_n = F_n + \Delta F_n \tag{4.14}$$

$$F_s = F_s + \Delta F_s \tag{4.15}$$

A further condition is imposed that restricts the maximum tangential force that may be developed at the contact,

$$F_s \leq \mu\, F_n \tag{4.16}$$

Once the normal and tangential forces have been determined for each contact of a sphere, they are resolved into components in the 1 and 2 directions, i.e. globally. For each sphere, the sum of these contact force components gives the resultant forces $\sum F_1$ and $\sum F_2$. The resultant moment acting on the sphere $\sum M$, is taken positive if

acting in the counter-clockwise direction and is found from $\sum M = \sum F_s R$, where the summation is taken over all contacts for a given sphere.

The above calculations are performed in subroutine FORD. When the program has updated all the contact forces in an assembly of particles and new out-of-balance forces and moments have been obtained for each particle, the program moves to subroutine MOTION to update the particle positions and velocities.

The new resultant forces and moments acting on each sphere at time t are used to determine the new accelerations $\ddot{x}_i$ and $\ddot{\theta}_i$ according to Newton's second law of motion.

$$m\ddot{x}_i = \sum F_i \tag{4.17}$$

$$I\ddot{\theta} = \sum M \tag{4.18}$$

where I is the moment of inertia of the particle. New particle velocities are obtained from the equations

$$(\dot{x}_i)_{t+\Delta t/2} = (\dot{x}_i)_{t-\Delta t/2} + [\sum F_i /m]_t \, \Delta t \tag{4.19}$$

$$(\dot{\theta}_i)_{t+\Delta t/2} = (\dot{\theta}_i)_{t-\Delta t/2} + [\sum M /I]_t \, \Delta t \tag{4.20}$$

These equations are applied to each sphere in turn. The new value for the velocities are used to update the positions and rotations of the spheres by further numerical integration

$$(x_i)_{t+\Delta t} = (x_i)_t + (\dot{x}_i)_{t+\Delta t/2}\Delta t \tag{4.21}$$

$$\theta_{t+\Delta t} = \theta_t + \dot{\theta}_{t+\Delta t/2}\Delta t \tag{4.22}$$

The finite difference equations of (4.19) to (4.22) represent a time-centred system. Body forces, such as gravitational forces, are also featured in the program. The term $mg_i\Delta t$ is included in equation (4.19), where $g_i = (g_1, g_2)$ represents the two components of acceleration vector due to the body force.

4.3.4 Damping

In order to control the energy in large assemblies of interacting elastic spheres various forms of energy dissipation mechanisms are necessary. Energy is dissipated during sliding when the absolute value of the tangential force exceeds the frictional limit. Adhesive peeling also results in energy dissipation. Energy dissipation also occurs as a consequence of the non-linear, history dependent, tangential interactions defined by the theory of Mindlin and Deresiewicz (1953). In addition to these dissipative mechanisms that occur naturally from the contact mechanics based interaction laws, two types of viscous damping are incorporated in the program, BALL.

In real systems energy losses occur as energy is transferred through the solid bodies. In order to account for this type of energy dissipation "contact damping" is used. This type of damping is modelled by a viscous dashpot and is a function of the relative velocity of the two particles in contact. Having calculated the contact forces for a contact using equations (4.14) and (4.15) the program then calculates normal and tangential damping forces which are added to the contact forces to give the contributions of that contact to the out-of-balance forces and moments of the two contacting spheres. This type of damping is always used and it is normal to adopt a damping coefficient equal to 5% of the critical damping coefficient. The importance of this type of damping is demonstrated when simulating particles with adhesion. If two particles stick together and contact damping is not used then the contact forces will continue to oscillate and an equilibrium state will never be reached.

The second type of viscous damping available may be described as either global or mass-proportional damping. It takes the form of Rayleigh damping and is incorporated into the equations of motion (4.19) and (4.20). The effect of global damping is like immersing the system of particles in a viscous liquid. For example, consider the simulation of a single sphere falling under the influence of gravity. By incorporating global damping into the equations of motion, the sphere will reach a terminal velocity

105

within a small number of timesteps. Except for quasi-static simulations, global damping is not normally used. It is, however, a useful device which may be introduced whenever it is required to reach an equilibrium state within a reasonable amount of computing time. It is, therefore, useful to introduce global damping during the final stages of simulating pluvial deposition or agglomerate preparation.

4.4 Program BALL To Model Surface Adhesion

The original BALL program developed by Cundall and Strack (1979) was used mainly for quasi-static shear deformation simulations using linear springs to model both the normal and tangential stiffnesses. The inclusion of non-linear interaction laws into BALL by Randall (1989) provided a more realistic simulation in comparison to the early version of BALL. In order to account for adhesion at the contacts major changes have been made to the program to accommodate this effect.

Whilst adopting Randall's version of FORD, the new version also makes allowances for adhesion based on the combination of theories due to Johnson et al (1971), Savkoor and Briggs (1977) and Thornton (1991). These theories have been discussed in chapters 2 and 3. The following sub-section will provide an explanation of the flow and logistic guide through the subroutine FORD. A listing of subroutine FORD is provided in Appendix A.

4.4.1 Subroutine FORD

When there is a contact between a particle and a wall, a logical flag is set as true and sends the program to calculate their relative positions based on the particle and wall coordinates. The equivalent radius for the contact is set to that of the particle. If the logical flag is set as false, i.e no wall, the program skips to calculate the relative positions of the two particles from the coordinates of the particle centroids.

106

Particle contacts or potential contacts are first checked in subroutine BTEST before passing to FORD. In BTEST, any two particles within the tolerance limit are considered as potential contacts. In FORD, however only particles that are in contact are analysed before updating the new forces, otherwise the contact data will be zeroed. This is determined by examining if the distance between the centres of the two particles is less than the sum of their radii. If, however, there is a potential contact between a particle and a wall, then a check is performed to determine if the normal distance between the centre of the particle and the wall is less than the radius of the particle after checking that the particle centre lies between the two ends of the wall.

The program then calculates the relative properties of the contact.

The equivalent radius:

$$R^* = R_1 R_2 / (R_1 + R_2) \qquad (4.23a)$$

$$R^* = R_1, \text{ for wall/particle contact} \qquad (4.23b)$$

equivalent mass:

$$M^* = M_1 M_2 / (M_1 + M_2) \qquad (4.24a)$$

$$M^* = M_1, \text{ for wall/particle contact} \qquad (4.24b)$$

equivalent Young's modulus:

$$E^* = E_1 E_2 / (E_1(1 - v_1^2) + E_2(1 - v_2^2)) \qquad (4.25)$$

and finally, the relative shear modulus:

$$G^* = G_1 G_2 / (G_1 + G_2) \qquad (4.26)$$

where

$$G_1 = E_1 / (2(1 + v_1)*(2 - v_1)) \qquad (4.27a)$$

$$G_2 = E_2 / (2(1 + v_2)*(2 - v_2)) \qquad (4.27b)$$

and v is Poisson's ratio.

If adhesion is specified, the program then calculates the following parameters:

$$\gamma = (\gamma_1 + \gamma_2)/2 \qquad (4.28)$$

where γ_1 and γ_2 are the intrinsic surface energies of the two particles in contact,

$$P_c = 3R^* \gamma \pi \qquad (4.29)$$

$a_c = (0.75R* P_c/E*)^{1/3}$ (4.30)

which is the contact radius when $P = -P_c$, and

$a_i = (0.75)^{-2/3} a_c$ (4.31)

which is the initial radius of the contact which is instantaneously established due to surface attraction when contact is first made. In order to determine when a contact is broken the program also calculates the rupture separation distance

$\alpha_c = (0.1875 P_c^2/E*^2R*)^{1/3}$ (4.32)

Having calculated all these parameters, the program then proceeds to calculate the relative particle velocities making allowance for any imposed external strain field. From the relative velocities the increments of normal and tangential displacement at the contact are calculated.

For particle/particle contacts:

$\Delta n = (\dot{x}\cos \theta + \dot{y}\sin \theta)\Delta t$ (4.33)

$\Delta s = (\dot{x}\sin \theta - \dot{y}\cos \theta - \omega_1 R_1 - \omega_2 R_2)\Delta t$ (4.34)

For wall/particle contacts:

$\Delta n = (\dot{y}\cos \theta - \dot{x}\sin \theta + X_r\Omega)\Delta t$ (4.35)

$\Delta s = (\dot{x}\cos \theta + \dot{y}\sin \theta - \omega_1 R_1)\Delta t$ (4.36)

where,

$\dot{x}$ and $\dot{y}$ are the relative velocities in the global Cartesian reference frame,

θ = angle of contact for particle/particle contacts and angle of wall for wall/particle contacts,

R_i = radius of particles i,

ω_i = angular velocity of particle i,

Ω = angular velocity of wall

and $X_r \Omega$ is the additional normal relative velocity due to wall rotation.

A series of conditional statements are set to create a logical pathway to deal with the inclusion or exclusion of surface adhesion. The conditional statements are based on the

parameter P_c, the contents of memory cells $C(1)$, $C(3)$ and $C(7)$ (see figure 4.4) and RDIF which is the difference between the sum of the two particle radii and the distance between their centres for a particle/particle contact or, for the case of a particle/wall contact, the difference between the particle radius and the distance between the particle centre and the wall in the direction normal to the wall.

The program then proceeds to calculate the normal force increment but must, first of all check whether the contact is new.

If no adhesion is specified and there is no existing normal force, as indicated by $C(3)$, this indicates a new contact and the normal force increment is calculated from

$$\Delta n = -RDIF \tag{4.37}$$

$$\Delta P = (4/3)E*(R* \Delta n^3)^{1/2} \tag{4.38}$$

If the contact has already been established the stiffness and normal force increment are calculated

$$K_n = 2E*a \tag{4.39}$$

$$\Delta P = K_n \Delta n \tag{4.40}$$

For the case of adhesion, a new contact is identified if the contact radius is zero, as indicated by $C(1)$. If so then the initial normal force is calculated as

$$P = -8P_c/9 \tag{4.41}$$

and the normal force increment is obtained from

$$\Delta a = \Delta n/((2a_i/R*) - (\pi\gamma/E*a_i)^{1/2}) \tag{4.42}$$

$$\Delta P = \Delta a((4E*a_i{}^2/R*) - (6(\pi\gamma E*a_i)^{1/2})) \tag{4.43}$$

If the contact has already been established the normal stiffness depends on whether tangential peeling has been completed or not. If not and $T < T^*$, as indicated by $C(7) \leq 0.0$, then

$$K_n = 2E*a((3 - 3 a_r)/(3 - a_r)) \tag{4.44}$$

$$\text{where} \quad a_r = (a_c / a)^{3/2} \tag{4.45}$$

If $C(7) > 0.0$ this indicates that the tangential peeling process has been completed and the normal stiffness is obtained from (4.39). For both cases, the normal force increment is then calculated using (4.40).

The program then updates the normal contact force using

$$P = C(3) + \Delta P \tag{4.46}$$

where $C(3)$ contains the old value of normal force. For the case of no adhesion a check is then made to determine whether or not the contact still exists. If it does then the new normal force is stored in $C(3)$ and the normal damping force is calculated from

$$P_d = 2 \beta (M*2E*a)^{1/2}(\Delta n / \Delta t) \tag{4.47}$$

where β is the specified percentage of critical damping and depends on whether the contact is between two particles or between a particle and a wall. The damping force is then added to the contact force to give the "total force" P_t which is later used for calculating the out-of-balance forces on the two contacting particles.

Having calculated the new normal force the program then updates the contact radius. For the case of no adhesion

$$a = (0.75 \ PR*/E*)^{1/3} \tag{4.48}$$

The procedure for the adhesion case depends on the current state of the tangential interaction. If the contact is still in the process of peeling then

$$a = (0.75 \ P_1 R*/E*)^{1/3} \tag{4.49}$$

where $P_1 = P + 2P_c \pm (4PP_c + 4P_c{}^2 - T^2E*/4G*)^{1/2} \tag{4.50}$

If the tangential peeling process has been completed, as indicated by $C(7) > 0.0$, then, if $P \leq -0.3P_c$

$$a = (0.75 \ P_e R*/E*)^{1/3} \tag{4.51}$$

where $P_e = P_1((2P_1 + P)/3P_1)^{3/2} \tag{4.52}$

else, if $P > -0.3 \ P_c$

$$a = (0.75 \ P_1 R*/E*)^{1/3} \tag{4.53}$$

with $P_1 = P + 2P_c \tag{4.54}$

Having updated the contact radius the new value is stored in C(1). The program is then ready to consider the tangential interaction and, first of all, deals with frictionless contacts. Having determined the minimum coefficient of friction for the two spheres in contact, the program sets ΔT, T and T_t (the total tangential force to be used for out-of-balance force summations) to zero if the coefficient of friction is zero.

The direction of tangential loading is determined and a logical flag is set in accordance to the program's sign convention. In short, for all contacts with a positive loading direction,

$$CDF = 1 \qquad\qquad (4.55)$$

and for a negative loading direction,

$$CDF = -1 \qquad\qquad (4.56)$$

For virgin loading CDF = 1 for T>0. For the cases of unloading and reloading the sign of CDF is controlled by the sign of T* which is the tangential force at which unloading was initiated and the sign of the T** which is the tangential force at which reloading was initiated.

The program then calculates the tangential force increment using the value of θ as determined by the function THETA which also sets the unloading flag UFL. For the case of adhesion, θ is equal to unity whenever in the process of peeling. Otherwise the value of θ is set by the function THETA. The increment of tangential force over a time step is,

$$\Delta T = CDF(\ \theta(8G^*a\ \Delta sCDF - \mu\ \Delta P.UFL) + \mu\ \Delta P.UFL) \qquad (4.57)$$

Once the tangential force increment is calculated a check is made to see whether the contact has peeled during the timestep. If peeling has not occurred the new tangential force is calculated and stored in C(4). If the new tangential force is greater than T_c where

$$T_c = 4((PP_c + P_c{}^2)G^*/E^*)^{1/2} \qquad\qquad (4.58)$$

111

then C(7) is set to the absolute value of T_c to indicate that the contact has peeled and the tangential force increment is recalculated. If peeling has previously occurred, or there is no contact adhesion, then the program calculates the parameter DD which is used in function THETA, see section 4.4.2.

The program then proceeds to test for load reversals. If the tangential displacement (Δs) multiplied by CDF is positive, and $T^* \neq 0.0$ but $T^{**} = 0.0$ it implies that reloading has commenced. T^{**} is consequently set to the old value of the tangential force. If the tangential displacement multiplied by CDF is negative and T^* and T^{**} are both zero, then unloading must have been initiated and T^* is set to the old value of the tangential force.

The program then proceeds to update the tangential force and to check for sliding. If the tangential force is greater than the limiting value T_{max} then it is reset to T_{max} and the sliding displacement is accummulated.

For the case of no adhesion,

$$T_{max} = \mu P \tag{4.59}$$

For the case of adhesion, if $P < -0.3P_c$

$$T_{max} = \mu P_e \tag{4.60}$$

otherwise

$$T_{max} = \mu(P+2P_c) \tag{4.61}$$

The tangential force is stored in C(4) and the tangential damping force is calculated from

$$T_d = 2\beta(M^*|\Delta T/ \Delta s|) \Delta s/ \Delta t \tag{4.62}$$

Adding the damping force to the tangential force gives the tangential contribution to the out-of-balance forces and moments for the two contacting particles.

In preparation for the next timestep, it is necessary to identify the correct normal force constant curve, see figure 2.14, and to check whether there has been a change from

reloading to loading or from re-unloading to unloading. In order to identify the new curve the program updates T* and T** using

$$T^* = T^* + CDF\mu\Delta P \tag{4.63}$$

$$T^{**} = T^{**} - CDF\mu\Delta P \tag{4.64}$$

and T* and T** are restored in C(8) and C(9) respectively. If there has been a change from reloading to loading then both C(8) and C(9) are set to zero. If the change is from re-unloading to unloading then only C(9) is set to zero.

As described above, damping forces are added to the contact forces to give the "total" normal and tangential forces P_t and T_t. These forces are used to calculate the contact's contribution to the out-of-balance forces and moments acting on the two contacting particles.

At various points in subroutine FORD there are checks to test whether contact has been broken. If this is true the contact address is not necessarily deleted from the linked list in the memory map since contact may be re-established within a few timesteps. Consequently, when a contact is broken, the program checks the size of the gap between the two particles and compares it with a user specified tolerance. Only if the gap is greater than the tolerance is all information about the contact deleted from the memory map. If the gap is less than the tolerance all the contact data are zeroed except for the pointers in C(5) and C(6). Finally, when subroutine FORD ends control is passed back to subroutine CYCLE.

4.4.2 Function THETA

The function THETA is used in subroutine FORD to determine the appropriate value of θ to be used in calculating the tangential force increment, equation (4.57). The unloading flag UFL is also set in function THETA.

As explained in section 2.5, if the normal force increases, the tangential displacement may not be sufficient to increase the tangential force to a point on the tangential force-

displacement curve corresponding to the new normal force, see figure 2.14. This is the case if $\Delta T < \mu \Delta P$. The critical tangential displacement is

$$\Delta s_c = \mu \Delta P / 8G^*a \qquad (4.65)$$

and is calculated in function THETA. The problem occurs when $\Delta s < \Delta s_c$ and may continue over a number of consecutive timesteps. It is, therefore, necessary to determine when $\Sigma \, \Delta s \geq \Sigma \, \Delta s_c$. This is done by calculating DD in subroutine FORD. The parameter DD is stored in $C(10)$ and is calculated as

$$DD = DD + (\Delta s_c - \Delta s) \qquad \text{for } \Delta P > 0 \qquad (4.66)$$

$$DD = DD + \Delta s_c \qquad \text{for } \Delta P < 0 \qquad (4.67)$$

with the condition that if DD becomes negative it is reset to zero.

In function THETA the program tests for all the different possible loading cases and for the case of normal force increasing identifies whether the above problem exists. By a process of elimination the program determines when $\Delta s < \Delta s_c + DD$ and sets $\theta = 1.0$. For all other cases a flag is used to identify which of the following expressions should be used.

$$\theta = (1 - (T.CDF + \mu \Delta P)\mu P')^{1/3} \qquad \text{if loading} \qquad (4.68)$$

$$\theta = (1 - (T^*.CDF - T.CDF + 2 \, \mu \Delta P) / \, 2\mu P'))^{1/3} \qquad \text{if unloading} \qquad (4.69)$$

$$\theta = (1 - (T.CDF - T^{**}.CDF + 2 \, \mu \Delta P) / (\, 2\mu P'))^{1/3} \qquad \text{if reloading} \qquad (4.70)$$

where $P' = P$ for no adhesion and $P' = P + 2P_c$ for adhesion.

5. Agglomerate Impact

If the facts do not conform to the theory, they must be disposed of - Maier's Law

5.1 Introduction

In the powder industries, engineering problems associated with the prevention of excessive generation of dust or fines remains of prime importance. Faced by the potentially hazardous environmental and health impact on people, scientists and researchers have been trying various techniques to curb such phenomena. Methods like properly sealed cyclones, closed piping and agglomeration are a few typical examples of the many techniques introduced to date.

In agglomeration, individual discrete particles are compacted or moulded together to form a larger mass. The main advantage of this method is that it reduces the possible generation of fines that would occur in the subsequent processes during transportation or conveying. Two terms closely associated with agglomerate breakdown are attrition and comminution. The former relates to unintentional breakage of the agglomerate that arise during processing. In contrast, the latter refers to the intentional breaking up of the agglomerate to facilitate ensuing processes. However, both phenomena are controlled by the interactions between the primary particles.

This chapter will explore and attempt to explicitly clarify physical phenomena like stress wave transmission, crack initiation and propagation, and shattering, all of which may possibly occur in agglomerate attrition and comminution. Current work reported in this chapter begins with the problem of arbitrarily creating an agglomerate, the problems faced and the technique adopted in preparing an agglomerate with specific 'bond' strength. Once the desired agglomerate 'bond' strength had been achieved, impact simulations were carried out and the results are duly reported. Using simple but realistic interaction laws as described in chapters 2 and 3 at the local points of contact, the global behaviour was found to be very similar to what is observed in real experiments. This can be visually appreciated by the computer graphics presented in

115

this chapter and Appendix B. Detailed analysis of the micromechanics of particulate material, for the case of a dense packing, can be studied via the simulation data and an attempt is made to provide a clear explanation of such fundamental behaviour.

5.2 Brief Literature Survey

Impact phenomena provide a good and arguably critical testing ground for theories of mechanical behaviour. Experimental impact studies are difficult and expensive to carry out and a good theory that minimises the number of required measurements is invaluable. Experimental difficulties occur primarily due to the short time scale in which the micromechanical aspects need to be examined and the destructive nature of strong impacts. Further complications arise due to time and temperature effects on the material properties.

Until recently, neither experimental nor theoretical techniques had advanced sufficiently to demonstrate what actually takes place when a specimen is impacted. Available experimental techniques did not have sufficient simultaneous time and space resolution to determine important features of the behaviour such as crack initiation and propagation. Also, the theoretical models that were used to describe the behaviour were grossly simplified. In retrospect, this was because complex models were impractical before the advent of electronic computers.

The first step in developing an understanding of impact phenomena is to consider the elastic waves that are present and how these result from the equation of motion. The plane part of a propagating mechanical disturbance is necessarily immersed inside the material and therefore is quite inaccessible except to techniques such as flaşh x-radiography, Venables (1964). Furthermore, the wave front may be very sharp with substantial changes occurring in about 0.1µs. These specifications can only be satisfied by very fast sensing equipment applied at an external surface. It has become a standard practice to measure the back surface velocity as a function of time. Early

116

measurements of back-surface velocities used a series of contact pins that had slightly different lengths, so that the wave reached their ends and thereby closed the contacts at slightly different times, Minshall (1955). This method measures average velocities accurately but has insufficient time resolution for acceleration measurements. Later an optical wedge method was developed, Marsh and McQueen (1960), but the first methods with adequate resolving power used capacitance changes. Hughes et al (1961) used radio-frequency excitation of the capacitor whereas Rice (1961) used a static excitation voltage to maximise the time resolution. Quartz transducers can also be used to measure surface velocities (Jones et al (1962)), because the short circuit current from the thin quartz disc is directly proportional to the specimen quartz interface stress for times less than the wave transit time in the disc. High speed interferometers were used by Barker et al (1965) to measure displacements as a function of time.

The passage of an elastic wave will create excessive damage to the region of high stress concentration. Most materials exhibit flaws, dislocation lines, micro-cracks etc. The pioneering work of Griffith (1920), a follow up of Inglis (1913)'s concept of stress concentration factors in the region of the tip of the flaws, made a significant contribution to the origins of fracture analysis. Griffith (1920) considered an isolated crack in a solid subjected to an applied stress and formulated a criterion for its extension in terms of the fundamental energy theorems of classical mechanics and thermodynamics. However, the main problem facing early workers in fracture mechanics was how to add quantitative substance to the concept of Griffith (1920). The singularity of a perfectly linear elastic event does not hold when one examines the local rupture region. Hence, the work of Irwin (1958) and Orowan (1955), working independently, proposed the hypothetical division of the crack system into two defined zones. The two zones were distinctly identified as the linear elastic outer surrounding zone of the crack tip and, the nonlinear elastic inner surrounding zone of the extended crack tip. The outer surrounding zone, consisting only of linear elastic material,

117

transmits the applied traction to the inner, extended cracktip zone where the non-linear separation process operates, Irwin (1958).

Both the theories of Griffith and Irwin-Orowan are only focussed on a static crack system. If an unbalanced force acts on any volumetric element within a cracked body, that element will be accelerated and will acquire kinetic energy. The system, therefore, is a dynamic one and the equilibrium conditions of Griffith and Irwin-Orowan are no longer valid. A general approach to the dynamic fracture problem was outlined by Mott (1948) in an extension of the Griffith concept. The fundamental idea is to add a kinetic energy term to the expression for the total system energy and seek a configuration which maintains this total energy content constant.

Some experimental work has been carried out to identify the characteristics of the theories stipulated above. These include, works reported by Yuriger et al (1987), Puttick et al (1987) and Arbiter et al (1969). The attrition of particulate solids is directly linked to material properties and is highly dependent on the local modes of load application as explained by Ghadiri et al (1990). It is therefore essential to distinguish between the various modes of local loading as crack morphology and subsequently the attrition products differ vastly as a result. Ghadiri et al (1990) found that the complicated inter-dependency between material properties and the application of loading made it difficult to obtain a good prediction of the attrition rate. This was largely due to the problem associated with quantifying the stresses experienced during load application as the result of insufficient data on materials properties. The work concentrated on building up melt-grown ionic crystals as 'model' granular materials and made clear observations and agreements with the general theories discussed above. In the work of determining impact attrition of the sodium chloride crystals, the severity of attrition was found to be greatest at corners and edges where plastic deformation occurred. This resulted in the formation of diagonal cracks and detachment of platelets from the free face adjacent to the impact site. Detachment of the platelets was attributed

to the formation of subsurface lateral cracks which, as captured by high speed photography, indicated that such cracks arise during the unloading stage.

Arbiter et al (1969) reported on work concerning comminution through a free-fall impact, double impact and slow compression tests. Fundamentally, these works involved an effort to study products resulting from a single-stage operation, such as the breakage of a specimen under single fracture conditions. The goal of their research was to study the energy utilisation in the single fracture of brittle specimens and to relate the pattern of breakage and the resultant fragment size distribution with the nature of the material, specimen size, the manner of load application and the rate of loading. For all three types of tests conducted, it was found that breakages started from the region of contact between the sphere and the loading surfaces and failure, in general, occurred along a conical surface (plastic deformation) whose base was the area of contact. In the free-fall test, the area of plastic deformation or volume of permanent deformation was found to be proportional to the energy input and independent of specimen size. In the slow compression and double impact tests, breakages were observed to have been caused by the wedging action of the plastic deformation cones and by the hoop-tension existing in the peripheral part of the specimen. With the sand-cement spheres, similar breakage efficiency was observed from all the different type of tests conducted with the exception that free-fall impacts needed twice the energy required by slow compression to initiate fracture. The qualitative findings of the paper reported by Arbiter et al (1969) are comparable with the computer simulated impact results presented in this chapter.

It should be noted that the above literature survey is restricted to a continuum viewpoint. Though customarily treated in mechanics as continua, granular media exhibit essentially discontinuous or discrete behaviour. When subjected to static or dynamic stress or strain, the stress distribution and transfer of load from a particle to its neighbour along a load transfer path can be systemmatically visualised through photoelastic experiments. The works of Drescher and de Josselin de Jong (1972),

119

Drescher (1979) and Rossmanith et al (1982), utilising photoelastic techniques, showed a good visualisation of the stress propagation produced through isochromatic fringe patterns.

The work of Rossmanith et al (1982), in particular, showed that dynamic wave propagation in granular media differs extensively from the classical wave propagation in continuum mechanics because of the peculiar structure in discrete materials. The wave propagation process, as observed in the experiments, is governed by the Rayleigh wave which increases the density of contacts in the propagation direction. Upon passage of the wave, contact is partially released and the spatial orientation of the granular media may be altered. A simple study of dynamic load transfer along specific load transferring chains provided basic knowledge about wave velocities, contact duration and directional stability. Though the work contributed some strong concluding remarks on the nature of wave propagation in a granular environment and the subsequent load transfers, photoelastic techniques are not without limitations. High speed photography is essential in order to capture the necessary important events sequentially and secondly, photoelastic experiments only give good information about the normal component of the interactions.

5.3 Computer Simulations Of Agglomerate Impact

Having adapted the BALL code, as described in Chapter 4, to model contact adhesion according to the theories described in Chapter 3, a series of simulations of agglomerate impact were performed. Results obtained from the computer simulated experiments are presented in the remainder of this chapter together with discussion of observed phenomena.

Computer simulated impacts of a small polydisperse agglomerate consisting of 100 primary particles were carried out at an early stage of the research programme. The work was of an exploratory nature and is not reported in this thesis. It was decided to

concentrate on the simulated impact of a two-dimensional dense monodisperse system of 1000 primary particles in order to obtain clear and unambiguous information about the agglomerate damage processes. Emphasis was placed on the normal impact of the agglomerate with a wall although a few simulations of oblique impact were performed but are not reported in this thesis.

The prepared agglomerate is illustrated in figure 5.1a. The radius of the primary particles $R = 100$ μm and the other properties of the particles and the wall are listed below in Table 5.1.

		particle	wall
density	ρ (Mg/m^3)	2.65	2.65
Young's modulus	E(GPa)	70	70
Poisson's Ratio	ν	0.3	0.3
coefficient of friction	μ	0.35	0.35

Table 5.1 Mechanical properties of particles and wall

From figure 5.1a the agglomerate would appear to have a regular structure. The actual structure is more clearly demonstrated by the equivalent space lattice, figure 5.1b, in which each blue line joins the centres of two spheres which are in contact with each other. This type of representation clearly identifies the microstructure showing that the assembly is regularly packed except for three vacancies and some additional small structural irregularities, especially to the left-hand side of the agglomerate. The distribution of contact forces prior to impact is shown in figure 5.1c where the blue lines indicate compressive forces and the red lines tensile forces. The thickness of the lines indicate the magnitude of the forces scaled to the current maximum compressive force. It can be seen that the compressive forces are of a similar magnitude as the tensile forces and that the force distribution is random. The preparation of agglomerates like the one shown in figure 5.1 is discussed in the next section.
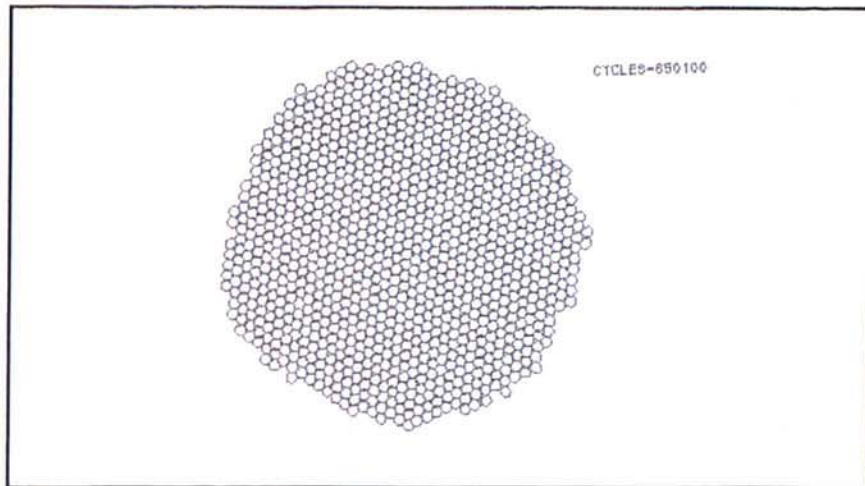
Figure 5.1a Initial primary particles layout in the agglomerate
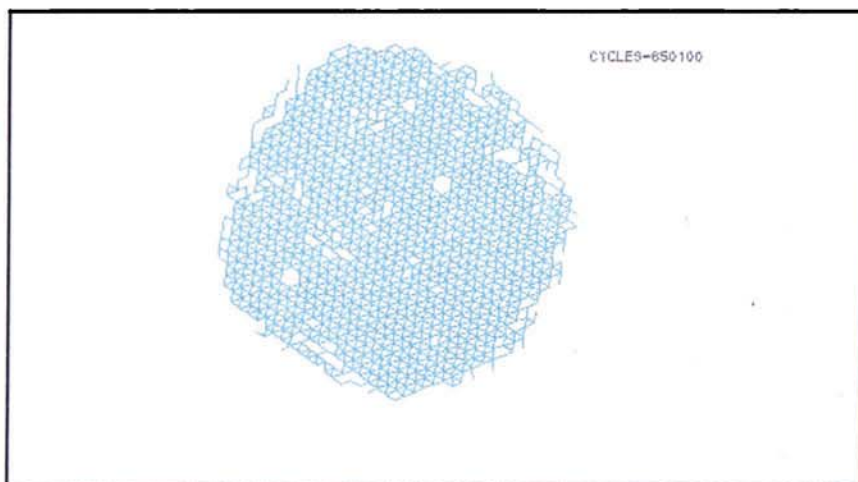
Figure 5.1b Equivalent space lattice showing initial structure
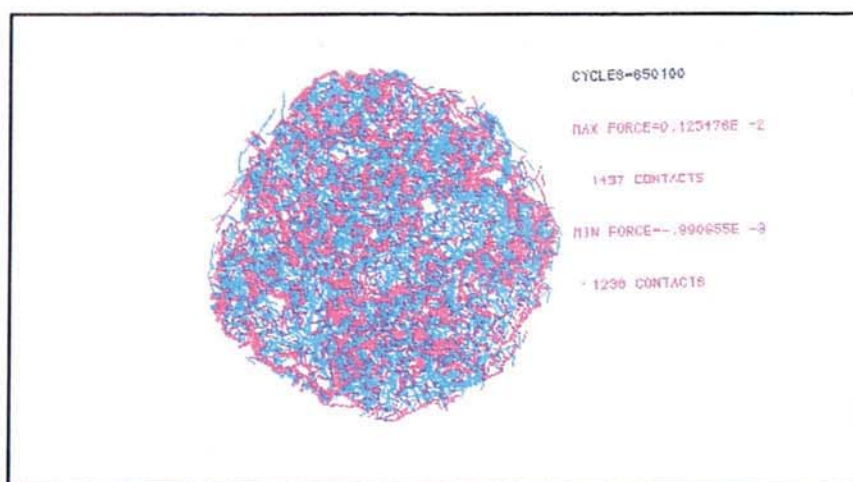
Figure 5.1c Initial distribution of contact forces

5.3.1 Agglomerate Preparation Procedures

In computer simulated experiments it is a very time consuming task to bring a system of particles together in a realistic manner and to allow sufficient time for the compact assembly of particles to attain an equilibrium state.

The technique adopted to create agglomerates was by generating the particles randomly within a specified circular area and then imposing a centripetal gravity field to bring the particles together. Although this may not simulate realistically the way that real agglomerates are formed, the particles are brought together in a natural way with the result that even for a monodisperse system, voids or cavities of the size of a single particle are sometimes visible in the final system. Slightly irregular boundaries are also a natural consequence of the process simulated. Once a compact or dense assembly has been created the surface energy is brought to the desired value in an incremental manner and the centripetal gravity field is gradually changed to the usual unidirectional gravity field.

The time step normally used to advance a computer simulated experiment is based on the Rayleigh wave speed. This ensures that the rate of load transfer from one particle to another is as close as possible to that in a real physical system. The time step is defined as

$$\Delta t = \pi <R>(\rho/G)^{1/2}/\alpha \qquad (5.1)$$

where $<R>$ is the average particle radius, ρ and G are the density and shear modulus of the particles respectively and α is a function of Poisson's ratio and is calculated from, Randall (1990)

$$\alpha = 0.1631\nu + 0.876605 \qquad (5.2)$$

For the 1000 particle monodisperse system simulated, $E = 70GPa$, $\nu = 0.3$ and $\rho = 2650Kg/m^3$. Since the particles are all the same size, $<R> = 100\mu m$, the calculation timestep would normally be 0.1065 micro seconds.

Initially the particles were generated in a circular area of radius equal to 0.004 m and the final agglomerate, as will be seen later, had an average radius approximately equal to 0.0032 m. Hence, the total resultant movement of a boundary particle, ~0.001m, would take about 10000 timesteps to complete if the effects of the particle interactions were ignored. The result of particles interacting with each other as they are brought together is that once a central core starts to form the outer particles tend to bounce off. Although the centripetal gravity field gradually reverses the outward velocities and brings the particles back together again this process can be repeated many times. This increases significantly the computational time required. When the outer particles have settled the cluster of particles continues to vibrate and the natural attenuation of the oscillating velocities to reach an approximate equilibrium state requires a large number of calculation timesteps.

By adjusting various parameters, it is possible to 'speed up' the agglomerate preparation stage of a simulation. However, no matter what technique is used, readjustment of the parameters will then be necessary before the impact stage is simulated. The number of calculation timesteps required to bring the particles together may be drastically reduced by changing the order of magnitude of the parameters that control the timestep. Either the elastic modulus may be decreased or the density increased. Alternatively a supergravity may be used.

The choice of which parameter to adjust is irrelevant until the time when particles first start to make contact. Once contacts start to be made certain problems can then arise. If a supergravity system or increasing the density by a few orders of magnitude is imposed, the initial contact between two particles can immediately produce a relatively large contact force which leads to large out of balance forces and hence, high velocities. This will result in difficulty and delay in reducing the large contact forces.

By subjecting the assembly to the influence of friction at the very beginning, the relatively large contacts forces were greatly diminished. However, there remained a high degree of porosity in the final assembly. This is not favoured as in the context of this research a densely packed assembly is envisaged, that is achieving the maximum 6 contacts per particle where possible. The 'best' way to successfully generate a well desired agglomerate is to specify a circular boundary as small as possible, just big enough to fit in all the randomly generated particles. This will reduce the time for the boundary particles to travel to their intended positions. Once the particles are brought together, mass proportional damping should be introduced to reduce any undesirable high particle velocities at the boundary and reduce the out-of-balance forces which result.

impact velocity, V (m/s)	Surface energy γ (J/m²)			
	0.3	1.0	2.0	3.0
0.008	▨			
0.01		▨	▨	
0.03	▨			
0.04				⧄
0.05	▨	▨	▨	⧄
0.06				⧄
0.07				⧄
0.08	▨			⧄
0.09				⧄
0.1	▨	▨	▨	⧄
0.2				⧄
0.4				⧄
0.5		▨	▨	⧄
0.8				⧄
1.0		▨	▨	⧄
2.0				⧄
5.0				⧄
10.0				⧄

Table 5.2 Normal impact test series

5.3.2 Normal Impact Test Series

The major series of simulations performed during the research period is indicated in Table 5.2. For the agglomerate shown in figure 5.1a, the surface energy was increased to $\gamma = 0.3$, 1.0, 2.0 and 3.0 J / m^2. For each value of γ a range of initial velocities were chosen to produce the impacts with the wall. In Table 5.2, the shaded boxes indicate the impact velocities used for the different values of surface energy.

Increasing surface energy leads to a stronger agglomerate since it results in a higher "pull-off" force, $P = -P_c = -3\gamma\pi R^*$, and more work needed to be dissipated in breaking the contact, WD as defined by (3.55). For the values of γ used in the simulations, the corresponding values of P_c and WD are provided in Table 5.3.

surface energy	"pull-off" force	work dissipated
γ (J/m^2)	P_c (mN)	WD (μJ)
3.0	1.4137	2.2698e-5
2.0	0.9425	1.1548e-5
1.0	0.4712	3.6374e-6
0.3	0.1414	4.8902e-7

Table 5.3 Bond strength parameters

The results of all the simulations performed, as indicated in Table 5.2, are presented in Appendix B in the form of computer generated graphics as well as data analysis.

In addition to the types of representations shown in figure 5.1, velocity fields may be selected in which the velocity of each particle is represented by an arrow originating from the particle centroid. The magnitude of the velocity is indicated by the length of the arrow and is scaled to the current maximum velocity which is also printed out. It is also useful to identify where interparticle sliding is occurring. This is illustrated by the cumulative sliding displacement increments which are represented as lines of fixed

length located on the contact planes and have a thickness representing the accumulated sliding displacement that has occurred during a selected time interval.

5.4 Normal Impact: Visual Observations

From an examination of all the test data obtained from the series of normal impact simulations, it was concluded that there were three types of behaviour depending on whether the initial impact velocity was high, moderate or low. In this context, high /moderate /low are relative terms depending on the strength of the agglomerate which is a function of the surface energy specified. In this section, typical results are presented for the strongest agglomerate, that is, surface energy $\gamma = 3.0$ J/m^2. The observations and discussion that follow, however, also apply to all the simulated impacts listed in Table 5.2.

5.4.1 High Velocity Impact

A typical example of high velocity impact behaviour is provided by the results obtained for $V = 1.0$ m/s. The interaction with the wall as the result of collision initiates a compressive stress wave that propagates from the wall through the agglomerate, as observed in figure 5.2. Behind the wavefront, all but a few contacts are observed to be in compression. The locations of sliding contacts are shown in figure 5.3 for the same elapsed times as depicted in figure 5.2. Figure 5.3 shows the cumulative sliding displacements that have occurred since the start of the impact. It can be seen that there are four distinct orientations of the sliding contact planes and that all the sliding contacts are located behind the wavefront shown in figure 5.2. Figure 5.4 shows the locations where contacts have been broken at the same corresponding elapsed times. Contact breakage is illustrated in figure 5.4 by the equivalent space lattice in which the red lines join the centres of particles which were initially in contact but have now been broken. It can be seen that the region of contact breaking corresponds to the region of sliding locations shown in figure 5.3. It can also be seen that except for a few locations near the perimeter of the agglomerate, the contacts that have been broken are oriented in one

127

of two directions depending on which side of the agglomerate they are located. It is clear from figures 5.2, 5.3 and 5.4 that the compressive wave produced by the impact with the wall causes plastic deformation of the agglomerate. Clearer examination of the data revealed that volumetric expansion occurred within the plastic deformation zone although this is not clearly visible from the computer graphics. A more detailed discussion of the plastic deformation mechanism will be provided in Section 5.5.

Figure 5.5a shows the contact force distribution at the time when the compression wavefront reaches the boundary at the rear of the agglomerate. This corresponds to an elapsed time of approximately 8.5µs which implies an average compression wave speed of 824 m/s. The compression wave is then reflected back through the agglomerate and figure 5.5b shows the contact force distribution when the wavefront returns to the agglomerate/wall interface at t = 17µs. Note that the maximum contact force given in figure 5.5b is an order of magnitude smaller than that shown in figure 5.5a. Figure 5.6 shows the equivalent space lattice when t ~32µs. The number of contacts broken as shown by the red lines, is now a maximum and the initial damage caused by the impact is complete. If the simulation is continued further for high impact velocities, a relatively small further number of contacts are broken but these appear to be due to secondary collisions between the fragments or between broken fragments and the wall. The simulation was continued in order to observe the subsequent breakup stage and was terminated when the time after the start of the impact was approximately 1.3 ms. This "final" state of the agglomerate is shown in figure 5.7 (a to c) illustrating the residual contact forces, particle locations and velocity distribution respectively.

From the above observations, it is concluded that high velocity impacts generate a compression wave that propagates through the assembly of primary particles causing extensive plastic deformation of the agglomerate. Since plastic deformation occurred, the dense initial structure of contact is no longer stable and will break eventually as the compressive wave attenuates through the assembly.
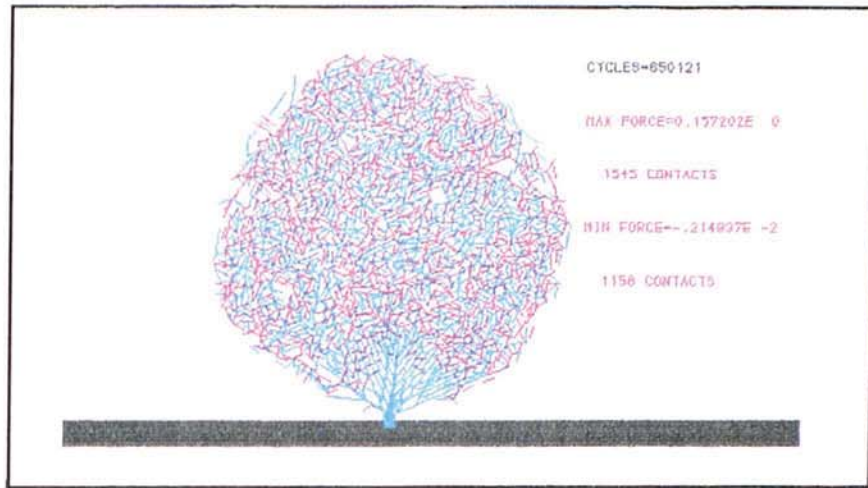
Figure 5.2a Compressive wave propagation, t = 2.1 µs
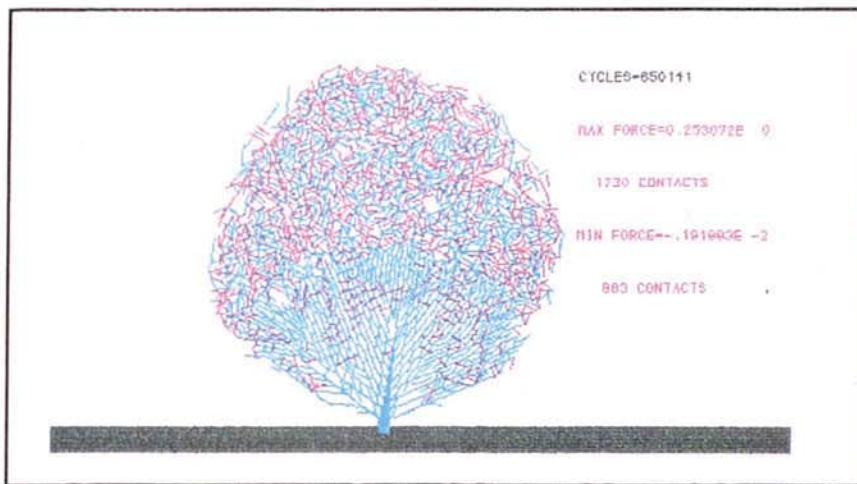
Figure 5.2b Compressive wave propagation, t = 4.3 µs
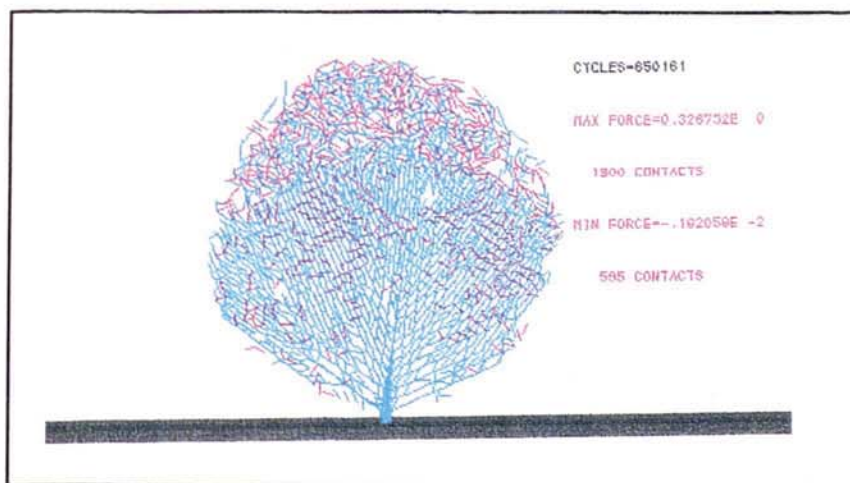
Figure 5.2c Compressive wave propagation, t = 6.4 µs
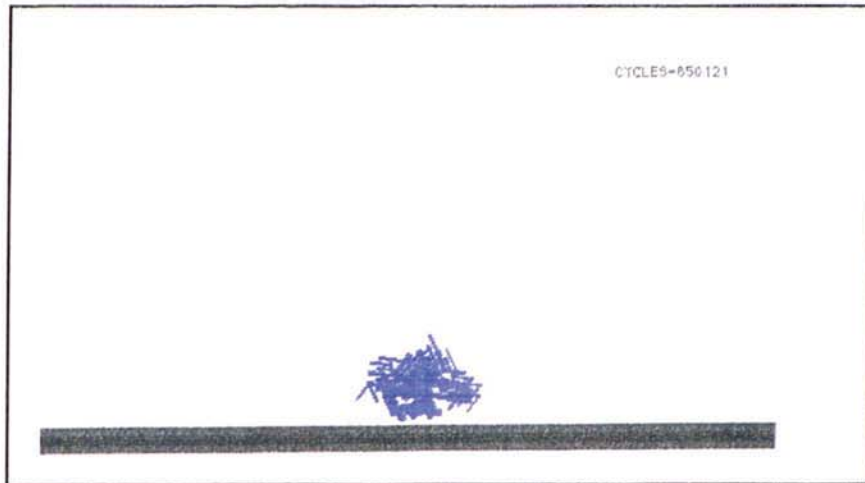
Figure 5.3a Contacts in sliding, t = 2.1 μs
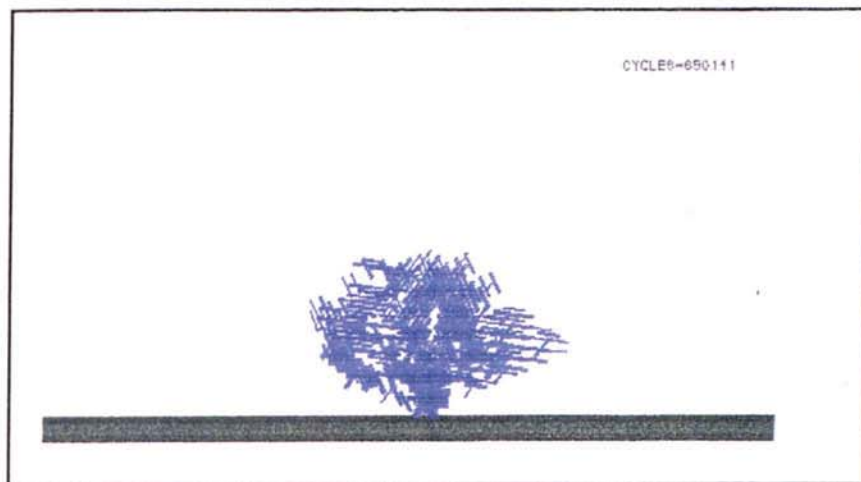
Figure 5.3b Contacts in sliding, t = 4.3 μs
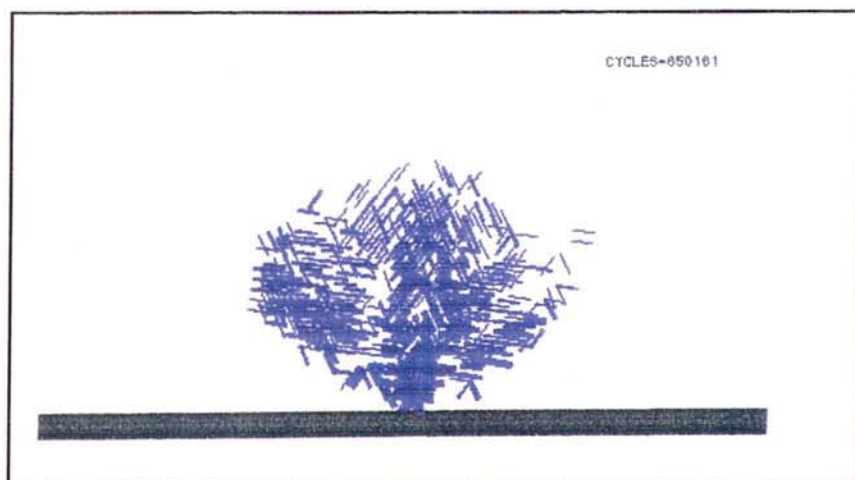
Figure 5.3c Contacts in sliding, t = 6.4 μs
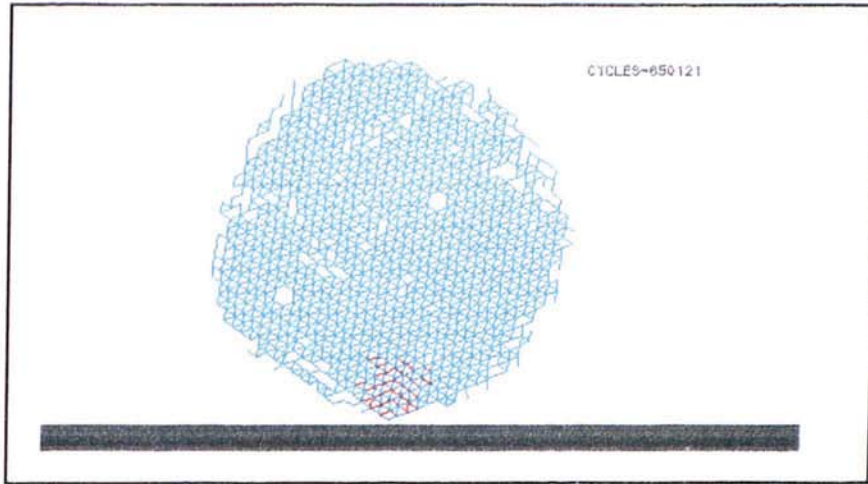
Figure 5.4a Equivalent space lattice, t = 2.1 μs
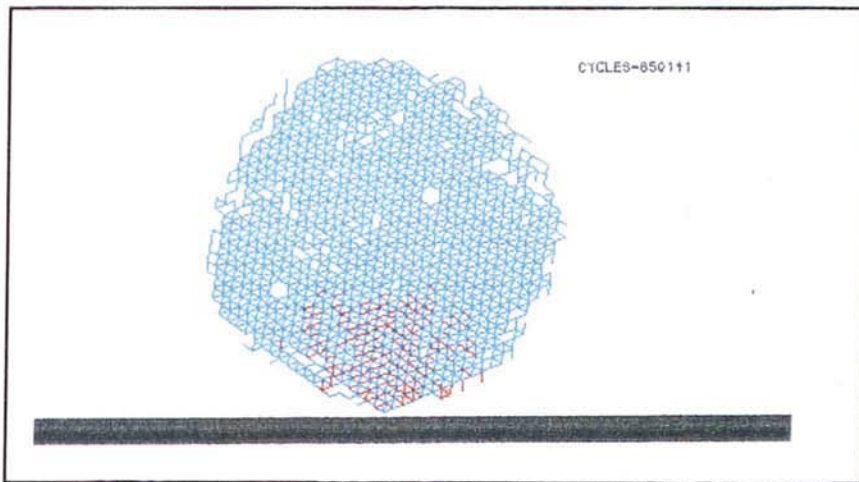
Figure 5.4b Equivalent space lattice, t = 4.3 μs
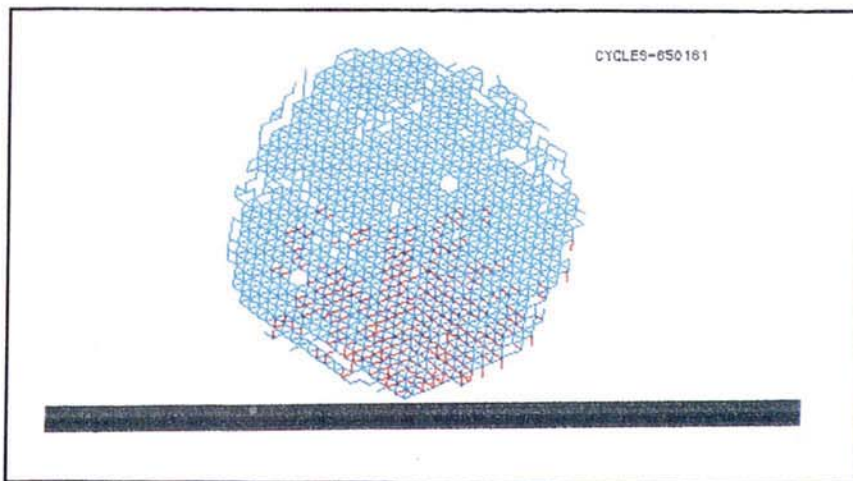
Figure 5.4c Equivalent space lattice, t = 6.4 μs
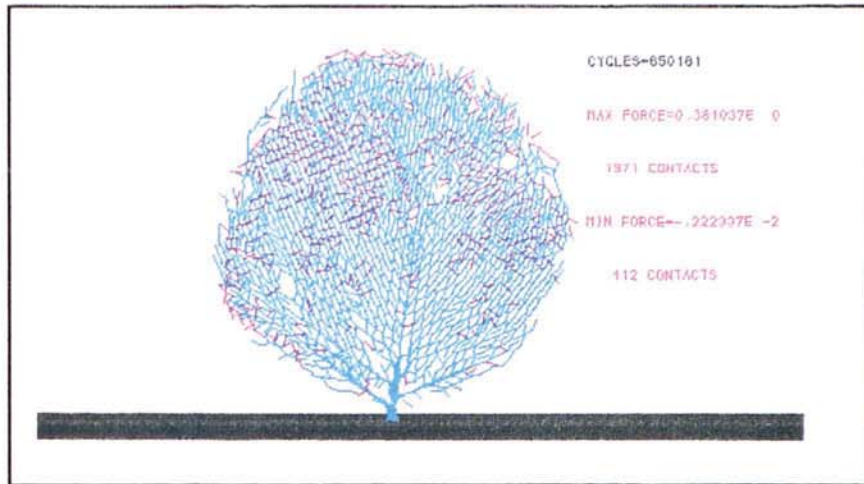
Figure 5.5a Wave propagation reaching rear of agglomerate, t = 8.5 μs
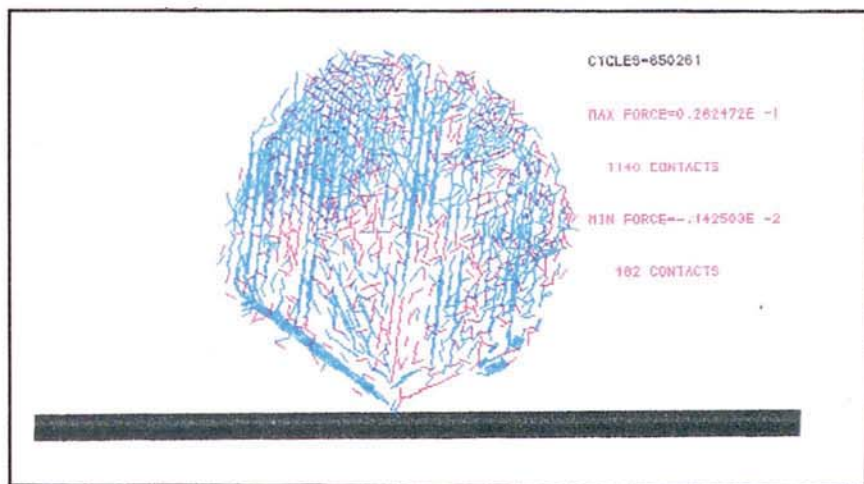
Figure 5.5b Wave propagation on rebound, t = 17.0 μs
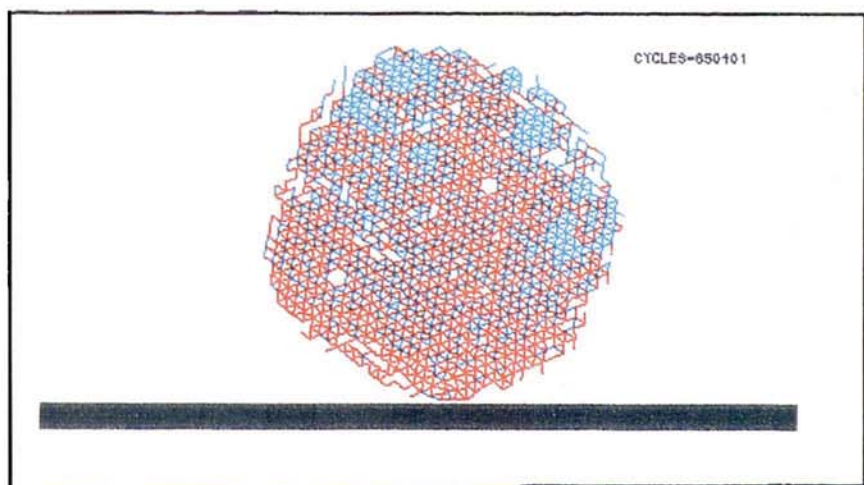
Figure 5.6 Equivalent space lattice at end of primary impact, t = 32 μs
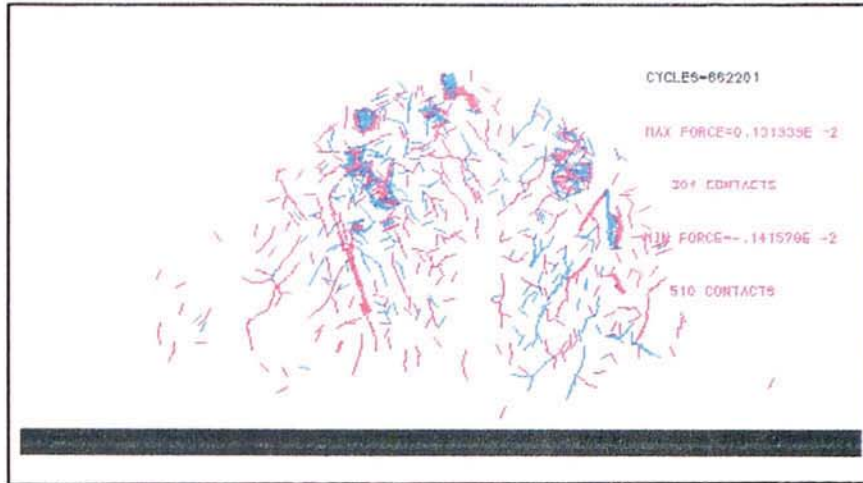
Figure 5.7a Residual contact forces, t = 1.3 ms
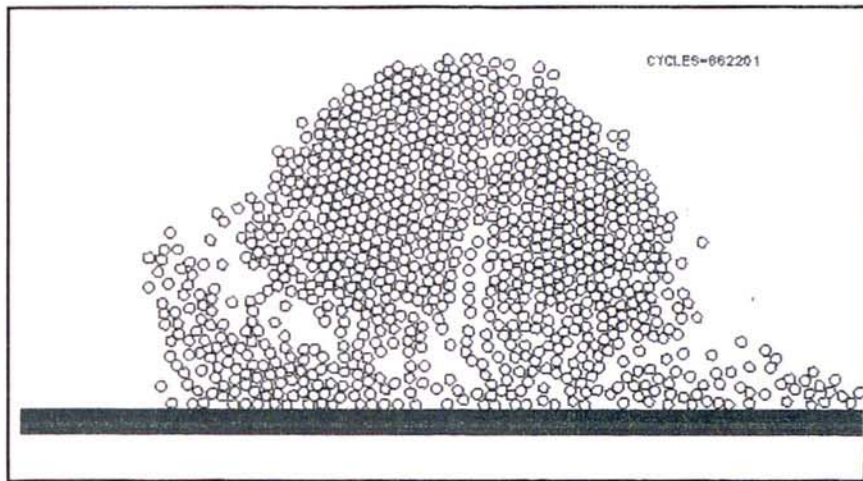
Figure 5.7b Orientation of primary particles, t = 1.3 ms
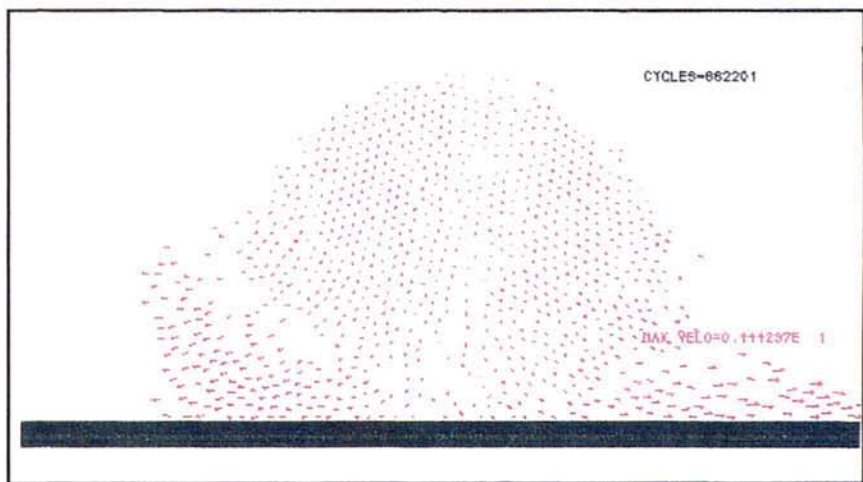
Figure 5.7c Velocity distribution, t = 1.3ms

5.4.2 Moderate Velocity Impact

If the impact velocity is reduced by an order of magnitude to V = 0.1 m/s, then the behaviour is very different from that described in the previous section. Initially, a compression wave propagates from the wall producing the sliding and contact breaking associated with plastic deformation. However, since the force generated at the wall is much smaller than that generated by an impact velocity of 1.0 m/s, the effect is less extensive. Due to attenuation of the stress wave, the plastic deformation zone is restricted to a small localised region near the point of impact, as shown in figure 5.8 (a to c). Figure 5.8 shows the contact force distribution, sliding locations and contacts broken at an elapsed time of 16µs which corresponds to the end of plastic deformation stage.

This initial stage is followed by the initiation of cracks at the perimeter of the plastic deformation zone which then propagate outwards towards the boundary of the agglomerate. The evolution of crack propagation is clearly illustrated in figure 5.9 (a to f). It can be seen that for an impact velocity of 0.1 m/s, the crack system consisted of a primary, near-vertical crack plus other secondary inclined cracks on each side of the agglomerate. The final crack pattern is shown in figure 5.9f, corresponding to an elapsed time of 53µs. Once the crack pattern is established there is a long period during which the cracks open. Because of the existing velocity field, the cracks open from the agglomerate boundary inwards as can be seen in figure 5.10a. This figure shows the equivalent space lattice at the elapsed time of 1.3 ms. The corresponding contact force distribution, particle locations and velocity field are shown in figures 5.10 (b to d) respectively.

From the visual evidence provided in this section, it is clear that the agglomerate breakage may be described as semi-brittle in contrast to the far more destructive shattering experienced at high impact velocities.

5.4.3 Low Velocity Impact

Figure 5.11 (a to c) illustrates the deceleration of the velocity field during the first 26.6μs of impact for an initial velocity of 0.04 m/s. The gradual deceleration of particles, as illustrated, resembles the behaviour of an elastic sphere. The evolution of the contact force distribution during the same period is shown in figures 5.12 (a to c). It can be seen that, as a result of the low impact energy and the small force generated at the wall, the compression wave is easily attenuated out. At an elapsed time of 53.2μs, all the particle velocities have reversed in direction, as shown in figure 5.13a, and the agglomerate begins to rebound. At this point, the contact forces have redistributed into a random distribution of compressive and tensile forces similar to that existing prior to the impact, figure 5.13b. The corresponding equivalent space lattice, figure 5.13c, clearly shows only a small insignificant amount of plastic deformation adjacent to the point of impact with the wall.

All the simulations were initialised to produce a normal impact with the wall. However, since the actual contact with the wall was not exactly in line with the centre of mass of the agglomerate, the force on the wall produced a torque on the agglomerate. This resulted in rotation of the agglomerate as clearly seen, figure 5.14a, at an elapsed time of 1.3 ms. The corresponding particle locations and equivalent space lattice are shown in figure 5.14 (b and c) respectively. It can be seen that there are a few particles breaking off from the agglomerate surface as the agglomerate is rebounding and "spinning".

For impact velocities below 0.04 m/s, the agglomerate behaviour was similar to that described in this section. The imparted rotation was also observed in large fragments produced by higher velocities which produced semi-brittle behaviour as described in the previous section. For a velocity of 0.04 m/s and lower the behaviour indicates that the agglomerate behaves in a way similar to that of a large solid sphere.

140
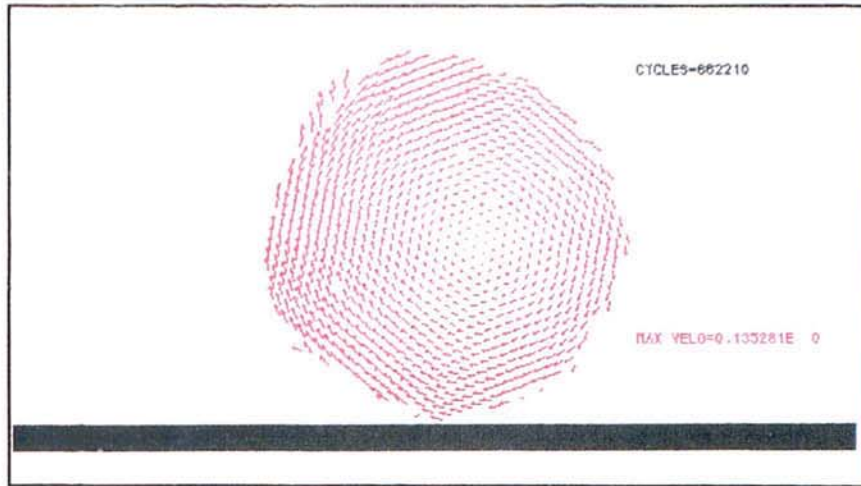
Figure 5.14a Spinning velocity indicating agglomerate rotation , t = 1.3ms
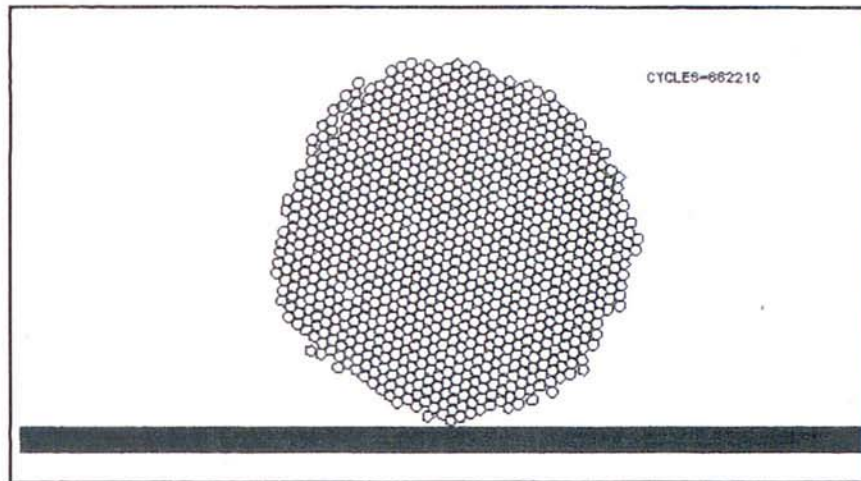
Figure 5.14b   Orientation of particles in a spinning agglomerate, t = 1.3ms
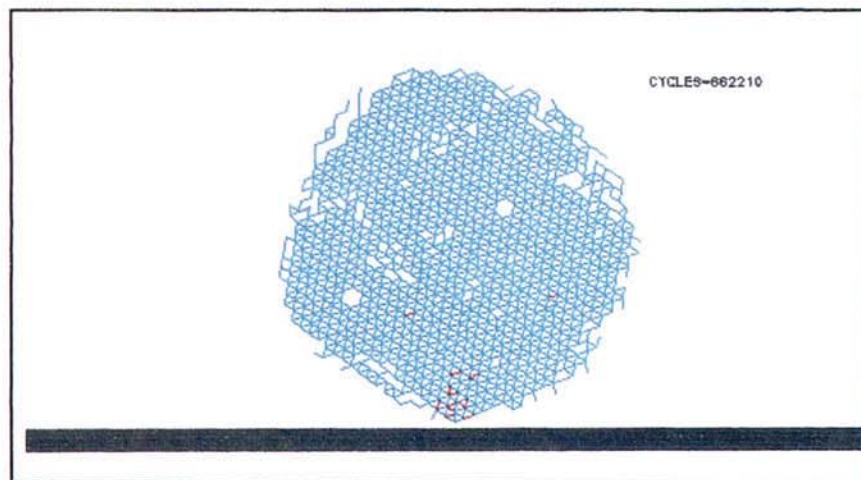
Figure 5.14c Equivalent space lattice for a spinning agglomerate, t = 1.3ms

144

5.4.4 Discussion

Three regimes of behaviour, ductile, semi-brittle and 'elastic', were discussed in the above subsections under the influence of different loading conditions. The results observed is a direct response of the external loading in which the system's energy is reduced due to initial retardation upon impact, regained through the release of the elastic stored strain energy and the load transfer from the wall to the assembly.

Figure 5.15a shows the force acting on the wall as the result of an impact velocity of 1.0 m/s. Only the normal force generated on the wall is taken into account as the initial setup is a colinear impact. The tangential force, though present, is not significant and can be ignored. In terms of the force on the wall, the loading phase is represented by the increase in wall force and the unloading stage by the decrease. Figure 5.15a shows the evolution of the force generated at the wall as the result of the impact. It can be seen that, essentially, the evolution is like that experienced by a solid sphere impacting on to a wall with the maximum force of 0.4N occurring at 8.5µs (as denoted by the dotted interpolation on figure 5.15a). However, as can be seen in the figure, there appears to be another small impact event superimposed which gives an actual maximum force on the wall of approximately 0.6N at 10µs. This is probably due to the stress wave propagating back from the plastic deformation zone. Following the dotted interpolation on figure 5.15a, the apparent maximum force on the wall does not correspond to the minimum value in kinetic energy (figure 5.15b). This is due to individual primary particles not achieving zero velocity at the same time. When the force on the wall reached a zero value, the time coincides with the maximum value in kinetic energy.

Figure 5.15b shows the evolution of the kinetic energy with time. The kinetic energy initially follows an uniformly sharp drop before increasing rapidly to a maximum value larger than the initial input energy. Once the maximum point is reached, the kinetic energy gradually declined again. The initial sharp decline in kinetic energy is due to the retardation or deceleration of the discrete particles in the system as the compressive

145

wavefront traversed from the source of impact. The minimum level in kinetic energy corresponds to the exact time when the first compressive wave reached the boundary of the agglomerate with all velocities within the assembly retarded, figure 5.5b. The time for the compression wave to reach the rear boundary of the agglomerate is around 8.5µs (figure 5.5a), and at this instant, almost all contacts are in compression with very few tensile contacts remaining, figure 5.15c. Since this is the case of a high speed collision, it is also worth noting that the minimum kinetic energy is not zero because the individual primary particles do not all reach zero velocity at the same time. In the second phase, the kinetic energy was observed to increase to a maximum value larger than the initial input. The gain in kinetic energy can be explained by the sudden release of the elastic stored strain energy previously held within the contacts as a result of contacts broken by the shattering of the agglomerate. The 'peak' value of kinetic energy corresponds with the cessation of the unloading phase, figure 5.15b. Subsequently, as seen in figure 5.15b, the kinetic energy gradually declined in a series of 'steps'. It would appear from detailed examination of the data that a probable explanation for this phenomenon is the occurrence of secondary impacts and consequently further retardation of some primary particles.

Figure 5.15c shows how the number of contacts within the agglomerate changed as a result of the impact. The total contact number is observed to decrease immediately upon impact before achieving a constant rate at around 30µs. The maximum number in compression marks the event when the compression wave reached the rear boundary of the agglomerate at around 8.5µs. This coincides with the apparent minimum number of contacts in tension. The real minimum number of tensile contacts, however, occurred at a later stage and this is probably due to boundary particles approaching contact deletion. It is observed in figures 5.15 (a and b) that although the primary collision event ended at around 16µs, the contact number attained a constant value at
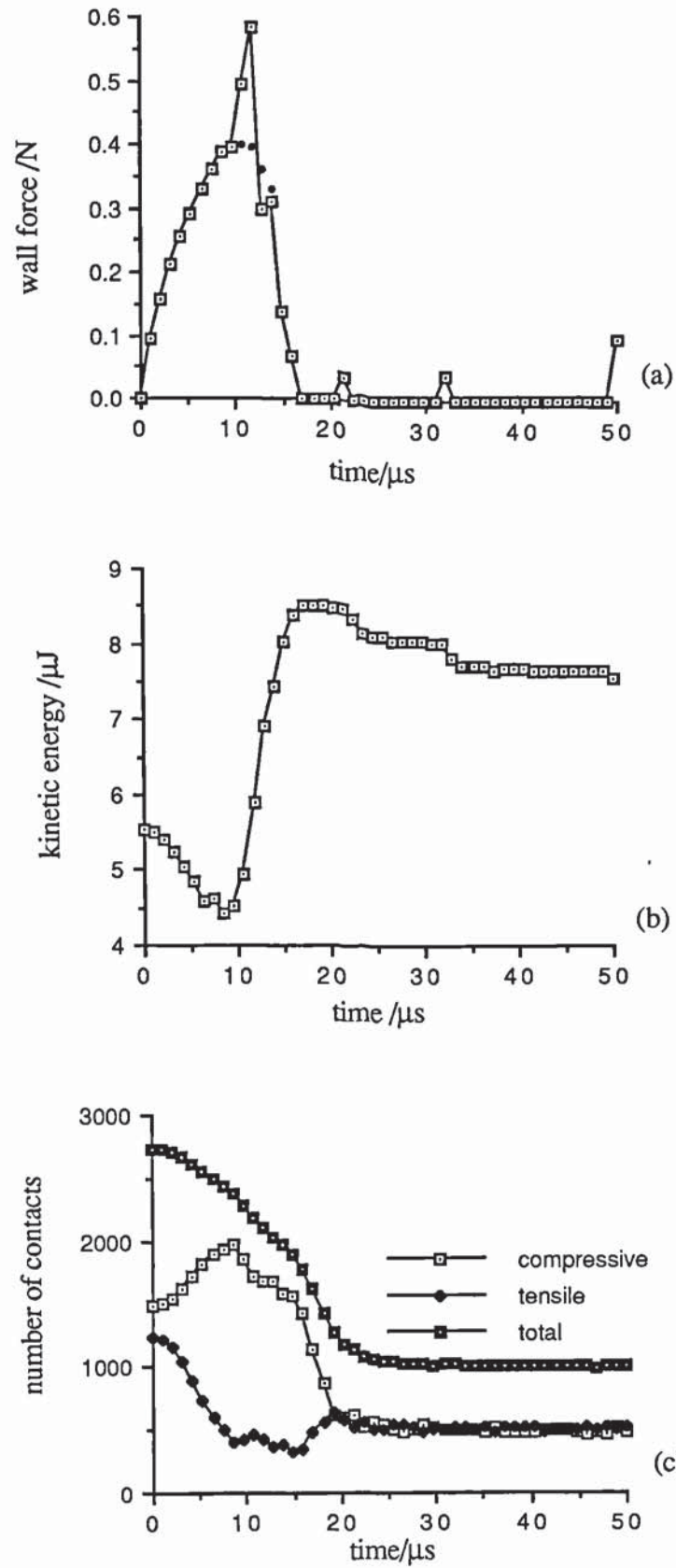
Figure 5.15 Evolution of a) Wall force, b) kinetic energy , and c) number of contacts

around 25 to 30 µs. This lag in time is largely due to residual wave propagation through the assembly.

From a high speed impact, where shattering phenomena dominates the breakage behaviour, the moderate speed collision provided some contrasting features which will be discussed below. Figure 5.16a shows the evolution of wall force during the first 100µs of impact. Qualitatively, the evolution of wall force is similar to that obtained from an impact velocity of 1.0 m/s. Quantitatively, the maximum wall force is approximately an order of magnitude less than the high speed impact. The force on the wall reaches a maximum value just before the kinetic energy is a minimum, figure 5.16b. As explained previously, there is no crack propagation during the loading phase. The loading stage only creates the contained plastic deformation zone. The evolution of crack propagation shown by figures 5.9 (a to f) occurred from the beginning of the unloading stage. Similar observation have been made by many experimentalists, see Lawn and Wilshaw (1975). After 52.5µs the force on the wall remained zero and the primary impact was complete. However, further secondary impacts could occur subsequently. These are not considered in this thesis.

The evolution of kinetic energy is shown in figure 5.16b. Compared with figure 5.15b, the kinetic energy takes longer to reach a minimum value due to the lower impact velocity, (this is the same as for a single particle impact, see equation 2.23). For an agglomerate, a further complication arises due to the wave propagation through the media. Most of the contacts remained undisturbed at this stage with some possible readjustments in the local contact angles, figure 5.16c. Contacts that were deleted, however, were located in the contained plastic deformation zone, figure 5.8c. The kinetic energy then increases but not to the same extent as observed for a velocity of 1.0 m/s. It can be seen from figure 5.16b that the final kinetic energy is less than the initial. This is because elastic stored energy was only released from the plastic deformation zone and along the cracks. The net loss in kinetic energy was about 70% of the original
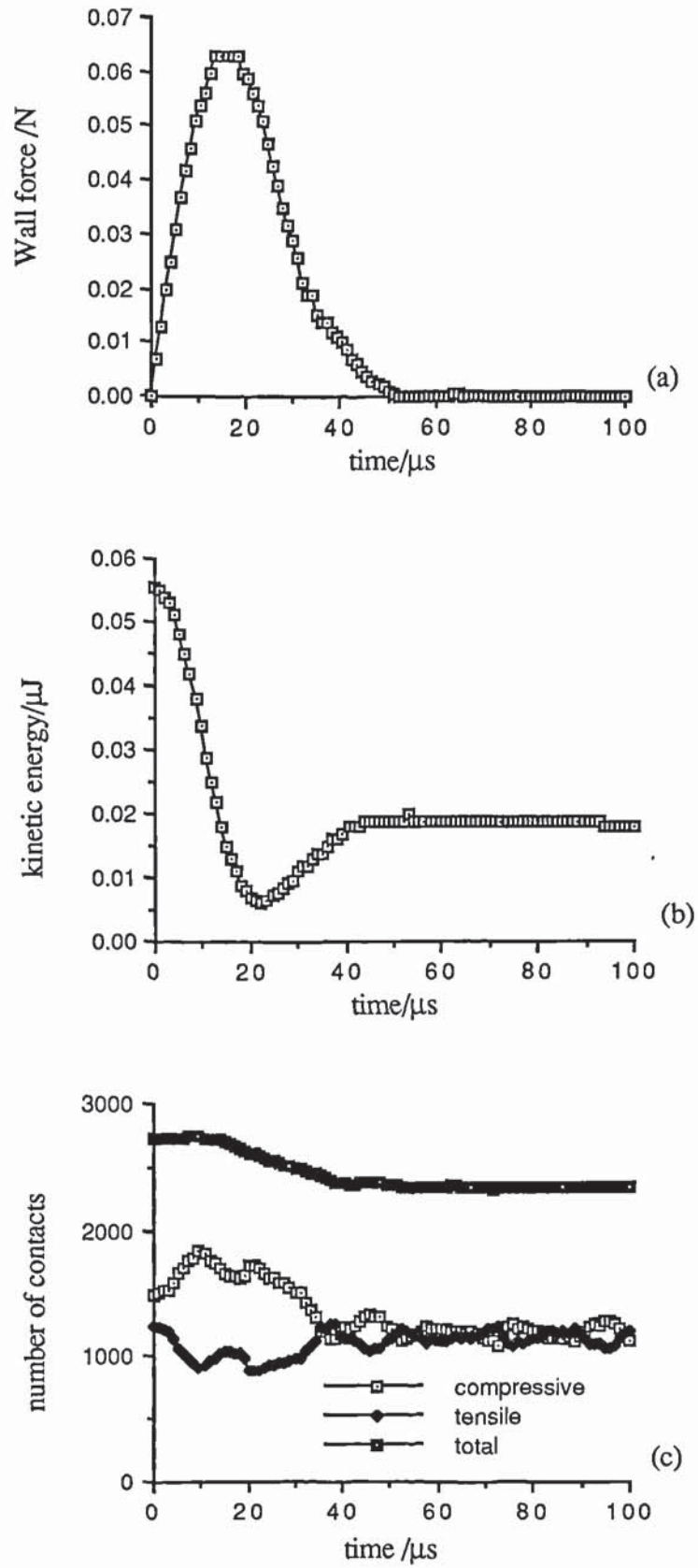
Figure 5.16 Evolution of a) Wall force, b) kinetic energy, and c) number of contacts

149

value. As will be shown in section 5.6, the net loss in kinetic energy is due to large proportions of the original agglomerate remaining intact. In other words, the breakage of the agglomerate was in the form of large clusters separated from each other by the cracks produced by the semi-brittle behaviour observed in figure 5.9f. In contrast, at high impact velocities, shattering released almost all the elastic stored energy and produced very small clusters plus many individual primary particles.

Figure 5.16 shows the evolution of the number of contacts with time. It can be seen that the total number of contacts remained unchanged during the first 10 μs of the impact. However, this is largely due to the increase in compressive contacts and a decrease in tensile contacts as the compression traversed through the assembly. The total number of contacts start to decrease gradually after 10μs before coming to a constant value at around 52.5μs. The initial drop is due to the deletion of contacts in the plastic deformation zone, figure 5.8c, while the latter drop is largely associated with crack propagation, figure 5.10a.

Having seen the behaviour of both high and moderate speed impacts and their responses, it will be appropriate to examine the case of 'elastic' behaviour. When no damage is done to the agglomerate and the assembly is seen to bounce off the target, it is logical to treat this case as a big elastic sphere.

The wall force evolution for the case of a low speed case (velocity = 0.04 m/s) is shown in figure 5.17a. The figure shows good qualitative agreement with both the cases of high and moderate speed impacts except for the variation in the quantitative value of the wall force. Contrary to the ductile and semi-brittle behaviour shown above, the loading phase for this case only produced a very small region of plastic deformation. In fact, as will be illustrated in figure 5.36c, the attenuation of the compression wave is relatively too small to create any substantial plastic deformation zone or provide enough energy to break contacts. The maximum force on the wall
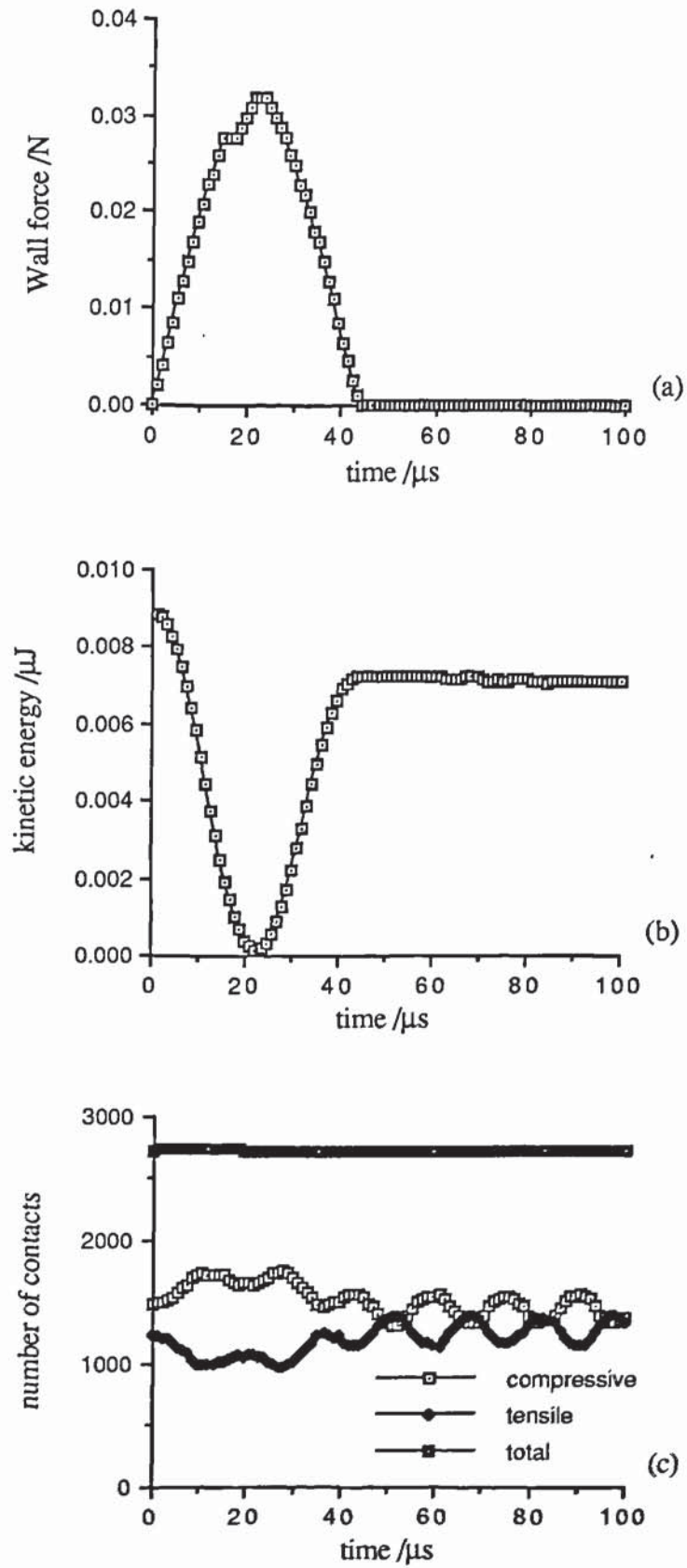
Figure 5.17 Evolution of a) Wall force, b) kinetic energy, and c) number of contacts

from a low speed impact coincides exactly with the minimum level in kinetic energy. Since the contact deletion is minimal (2 or 3), the agglomerate essentially resembles a large spherical ball, with the maximum deformation occurring when the kinetic energy level is at zero.

Figure 5.17b shows the evolution of kinetic energy with time for an impact velocity of 0.04 m/s. As observed from the figure, the kinetic energy reaches a minimum of zero at approximately 21μs. This zero value indicates the agglomerate is momentarily at rest and behaved in a manner similar to a large single sphere and, as a result of the collision, merely bounced off with no visible sign of internal damage. For this reason, the kinetic energy curve shown in figure 5.17b resembles that of a bouncing ball having a coefficient of restituition of 0.91.

The distribution of contacts, both compressive and tensile, shows no significant alteration in the total number of contacts, figure 5.17c. The low impact velocity does not create a compression wave that is large enough to break contacts as it traversed through. The sinusoidal behaviour in the evolution of both the compressive and tensile contact indicate that the agglomerate is re-establishing a state of equilibrium.

5.5 Normal Impact - Agglomerate Damage

5.5.1 Effect Of Impact Velocity

A series of simulations with different impact velocities was carried out and using the same basic assumption of selecting the appropriate number of deleted contacts, as indicated by the end of primary collision, a relationship between the degradation and impact velocity was established. Figure 5.18 shows the calculated damage ratio plotted against the logarithmic value of velocity. The empirical relationship between damage ratio and impact velocity can be represented in the form,

$$D = m \ln (V / V_0) \qquad (5.3)$$

where

V is the impact velocity, V_0 is the threshold velocity and m is the gradient and has a value of 0.1771, and the damage ratio,

$$D = [1 - (N / N_{max})] \qquad (5.4)$$

where N is the number of contacts remaining in the agglomerate and N_{max} is the number of contacts originally.
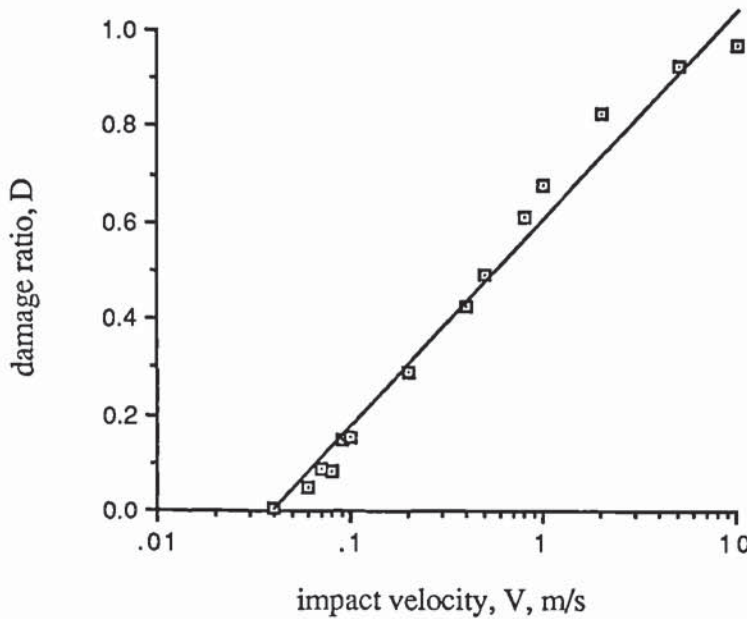
Figure 5.18 Damage /velocity relationship

The points are scattered evenly, figure 5.18, above and below the 'best' fit line. All points on the figure reasonably follows a 'linear' relationship, showing that high velocities cause more damage than low velocities as expected. It is apparent from figure 5.18, there is a deviation from the linearity by higher impact velocities where secondary collisions occurred at the same time as the primary impact. It is also clear from the figure that there is an apparent threshold velocity below which the agglomerate simply bounces off the wall with essentially no damage. The threshold velocity, for the case of $\gamma = 3.0$, is approximately 0.04 m/s.

5.5.2 Effect Of Bond Strength

The strength of an agglomerate depends on the strength of the individual bonds at the contact which according to equation (3.2) is directly proportional to the surface energy for a monodisperse system.

The effect of impact velocity on the degradation of the agglomerate as shown in section 5.5.1 applies to the case of a surface energy of 3.0 J/ m^2. Simulated agglomerate collisions were also carried out for other values of surface energy and the initial damage was calculated, as explained in the previous section, at the end of the primary collision. The results, as summarised in figure 5.19, for the different values of surface energy showed consistent qualitative behaviour.
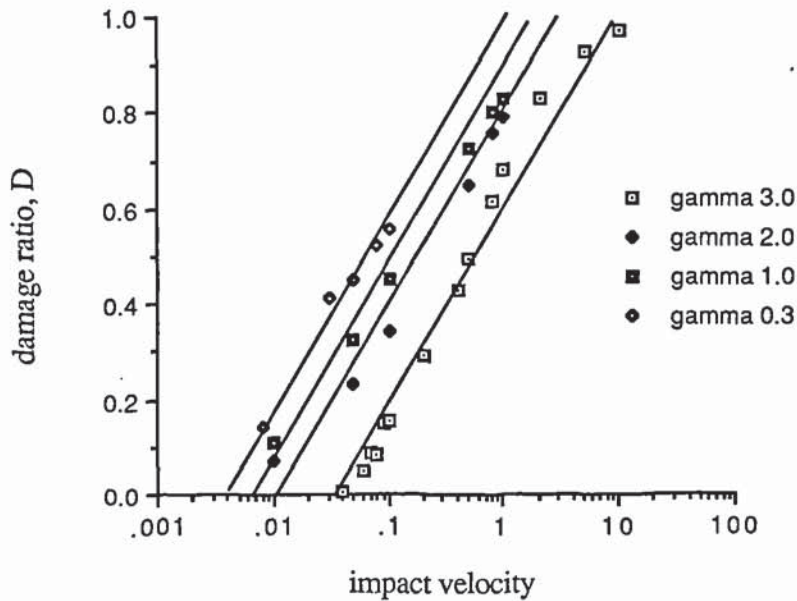
Figure 5.19 Damage /velocity relationships

Figure 5.19 shows a consistent trend in the damage - velocity relationship as the surface energy is varied. As the surface energy, γ, is increased, the threshold velocity, V_o, increases but the slope of the line shown in figure 5.19 remains essentially constant. Figure 5.19 shows that stronger agglomerates require higher impact

154

velocities to produce a given amount of damage. This demonstrates that the computer simulation produces sensible results.

Figure 5.19 also shows that there exists a threshold velocity for each bond strength, below which the agglomerate suffers minimal or no damage and simply bounces off the wall. Figure 5.20 shows a plot of threshold velocities, as derived from figure 5.19, against the surface energy.
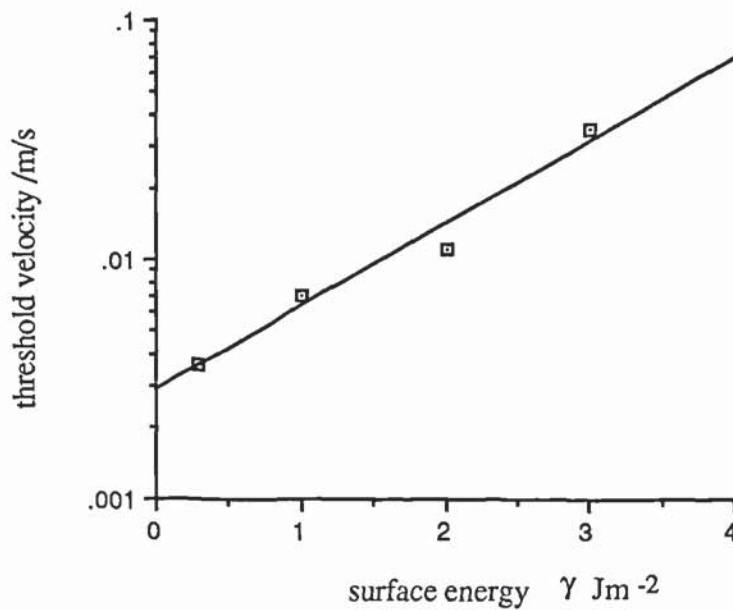
Figure 5.20 Threshold velocity against surface energy

Figure 5.20, indicates that the relationship between the threshold velocity and surface energy (bond strength) is essentially exponential and obeys the relationship

$$V_o = 0.003 \exp(0.8\gamma) \qquad (5.5)$$

Attrition or degradation of the agglomerate will occur for any velocity of impact above the threshold line and similarly there is a likelihood that the agglomerate will bounce off the target with no damage for any values below this threshold. The relationship between the damage ratio and the surface energy (bond strength) can be derived by substituting (5.5) into (5.4),

$$D = 0.1771 \ln \{ V/ (0.003 \exp (0.8\gamma))\} \qquad (5.6)$$

Substituting $\gamma = 0$ into (5.6) defines the limit of applicability of the equation since negative surface energies are not physically possible.

A: Work done in peeling all possible bonds
B: Work done in peeling a single bond
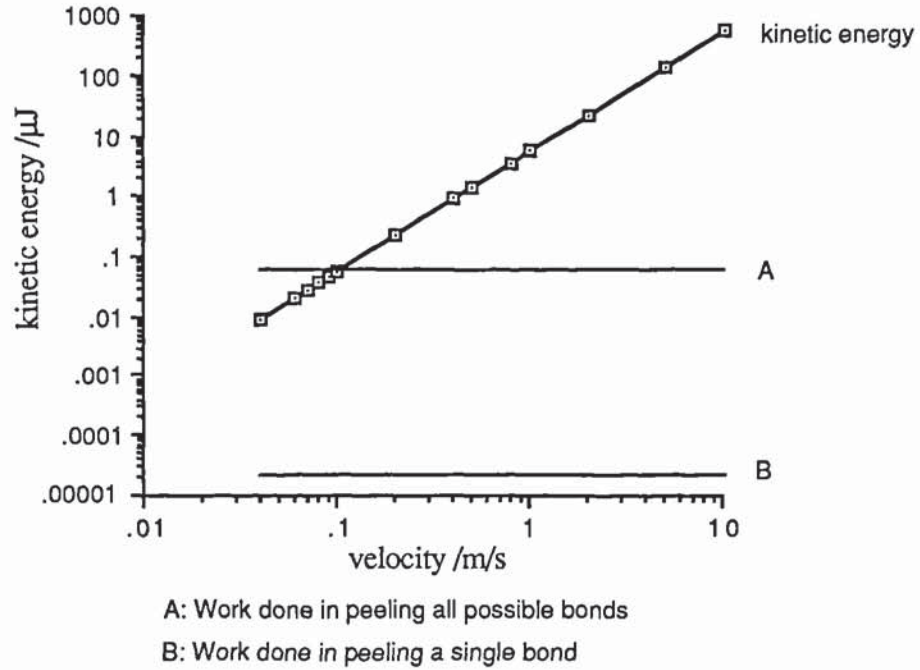
Figure 5.21 Initial kinetic energy

Figure 5.21 shows that, for the range of impact velocities applied to the strong agglomerate ($\gamma = 3.0$ Jm^{-2}), the initial kinetic energy input varies from 8.88e-3 μJ to 5.55e+2 μJ. The work required to break a single bond is 2.27e-5μJ which is far less than the input energy corresponding to an impact velocity of 0.04 m/s which produced no externally visible initial damage. The work required to break all the initial 2735 bonds is 6.21e-2μJ. This value is far less then the input energy required to produce shattering. The large difference between the work input and the work required to break bonds is primarily due to the large amount of energy dissipated in sliding at contacts during the plastic deformation stage.

It was shown in Section 5.4 that if the impact velocity is higher than the threshold velocity then two types of damage may result. High impact velocities produce shattering and moderate velocities result in semi-brittle fracture. From a detailed

156

examination of the computer graphics information, it was observed that the transition from shattering to semi-brittle behaviour occurred over a small range of velocities. From these visual observations it was possible, for each agglomerate, to select a value of velocity to represent the transition from shattering to semi-brittle behaviour. Figure 5.22 shows that the relationship between the transition velocity and the surface energy is exponential. The empirical relationship between the transition velocity and the surface energy is given by the equation

$$V_t = 0.003 \exp (1.23\gamma) \tag{5.7}$$

where

V_t is the transition velocity and γ the surface energy.
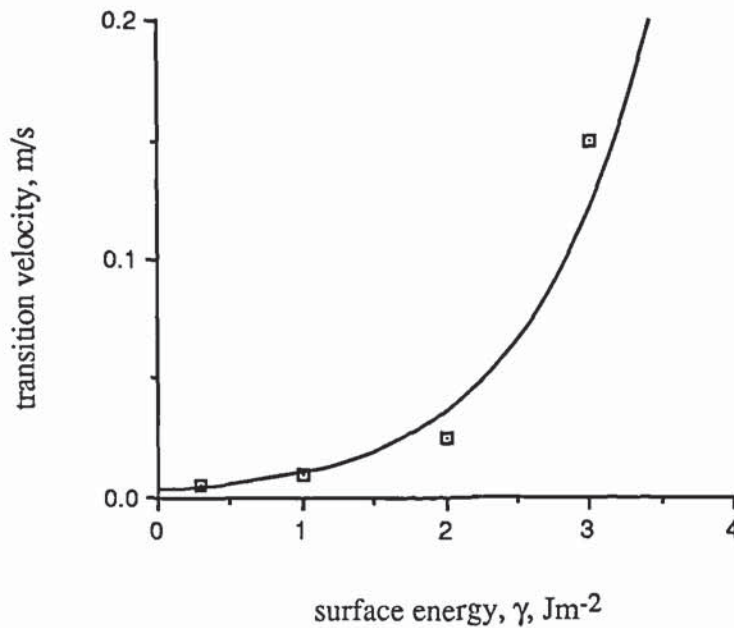
Figure 5.22 Ductile to semi brittle transition

The relationship shown in figure 5.22 has been combined with figure 5.20 to provide the information shown in figure 5.23. Figure 5.23 illustrates, for the 2D monodisperse

agglomerate, the combinations of velocity and surface energy that lead to the three different regimes of behaviour.
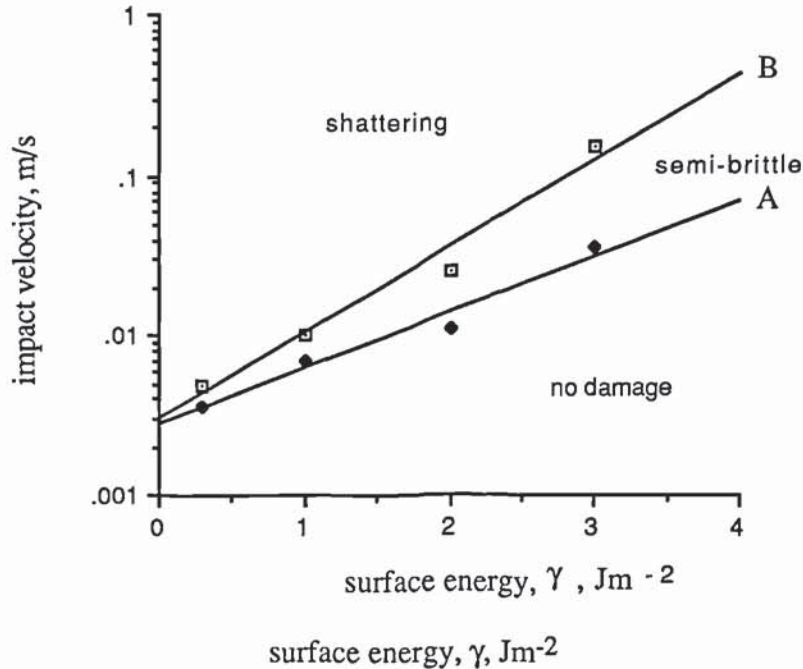
Figure 5.23 Plot of impact velocity against surface energy, indicating the various regimes of behaviour

Two slopes are shown in figure 5.23 with line A representing the threshold velocity and line B identifying the transition velocity. No damage will occur if the impact velocities are below line A. Semi-brittle behaviour will result if the impact velocities are between line A and B while shattering will occur if the velocities are above line B. In industry, this is very useful as it may aid in avoiding attrition by using velocities lower than line A or encouraging comminution by imposing velocities greater than line B.

5.5.3 Fragmentation

It was shown in the previous section that, agglomerate breakage is usefully quantified by the damage ratio which was defined as the number of bonds broken divided by the total number of bonds existing before the impact. With computer simulation this data is

readily available. In real experiments, however, it is not possible to accurately assess the number of bonds broken since the total number includes bonds which may be part of an internal crack. It is more convenient in real experiments to measure the sizes of the different fragments produced by the impact. Hence, it is relevant to examine the computer simulated data in terms of fragmentation.
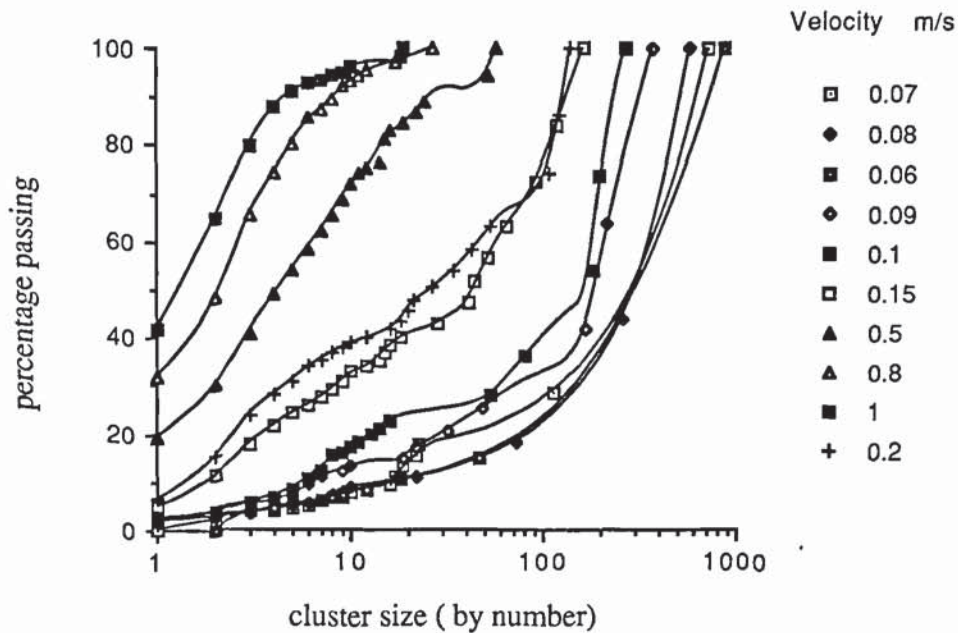
Figure 5.24 Grading curve of agglomerate, surface energy 3.0 Jm^{-2}

Figure 5.24 shows the grading curves obtained for an agglomerate of surface energy 3.0 Jm^{-2} under a series of impact velocities ranging from 0.06 to 1.0 m/s. The cluster size is defined by the number of primary particles in the cluster and may be considered to be analogous to the sieve sizes used for conventional grading curves. Figures 5.24 shows, for the different cluster sizes, the percentage of primary particles that belong to clusters of sizes less than the specified size. Since the assembly is monodisperse this is equivalent to the percentage by mass passing a given sieve size. The figure shows that the curvature of the grading curve reverses as the impact velocity is increased. High velocity impacts which result in shattering are characterised by grading curves whose gradient increases with decrease in cluster size. Moderate velocity impacts that produce

159

semi-brittle fracture are characterised by grading curves whose gradient decreases with decrease in cluster size.

Figure 5.25 shows how the number of clusters larger than or equal to a specified size varies with cluster size plotted on logarithmic scales. Three typical velocities were selected to illustrate how the relationship changes as the impact velocity of impacts is varied. The two extremes of behaviour are complete shattering and no damage which correspond to gradients of minus infinity and zero respectively. From figure 5.25, an approximate linear relationship is established for each of the three typical velocities selected. The negative gradient is increased for higher velocities indicating more production of fines (single particles) as shown by the abscissa.
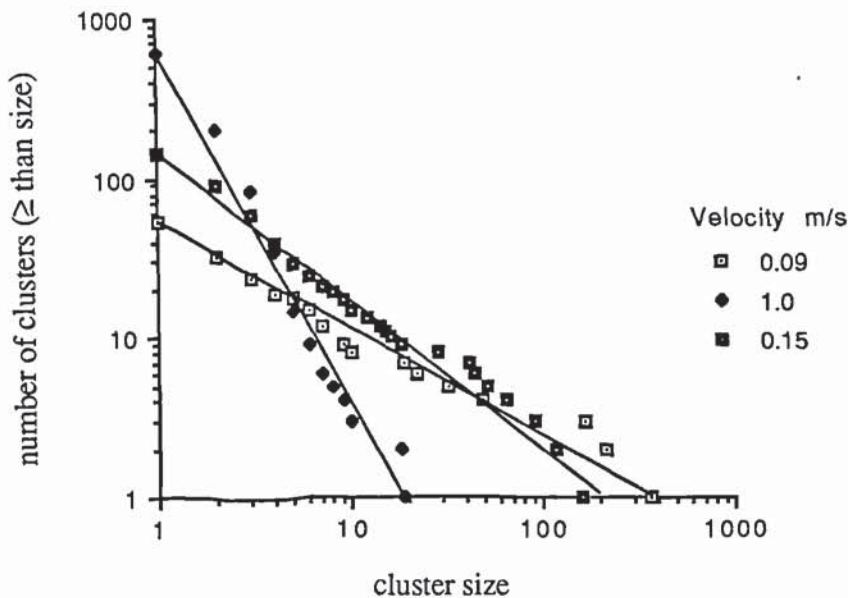
Figure 5.25 Frequency count against cluster size

In the context of comminution, a possible way of characterising the fragmentation is to use the gradient shown in figure 5.25 for the range of cluster sizes between 2 to 10 primary particles. If the gradient is defined as $-\beta$ then β may be plotted against impact velocity, as shown in figure 5.26.
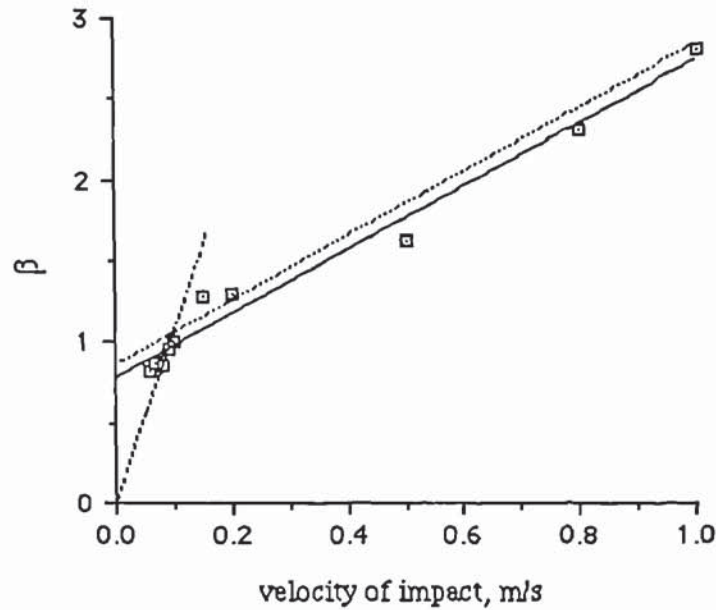
Figure 5.26 β against velocity of impact

Figure 5.26 shows the relationship between β and the velocity of impact for an agglomerate of surface energy 3.0 Jm^{-2}. Although a linear relationship may be established as shown by the solid line in figure 5.26 the gradient, -β, must be zero for zero velocity. Consequently, the interpretation of the data is that there are two linear relationships as shown by the dashed lines in figure 5.26. It may be noted that the intersection of these lines occurs at a velocity of about 0.1 m/s which approximates to the transition velocity, as defined previously.

As previously discussed, equation (5.3) showed the relationship between the amount of damage produced for a given impact velocity. A further connection may be made between the damage ratio and β. Figure 5.27 shows a semi-logarithmic plot of damage ratio, D, against β.

161
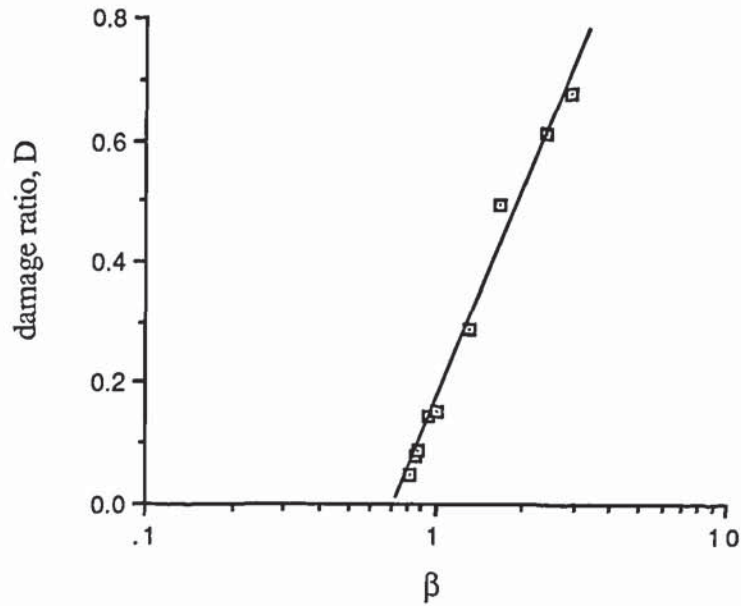
Figure 5.27 Damage ratio, D, against β

It can be seen from figure 5.27, that the damage done is linearly related to β which qualitatively corresponds to the relationship indicated by equation (5.3). For a value of β less than or equal to 1, only 20 per cent or less of the 0.2 damage ratio can be attributed to fines (clusters of sizes $\leq$ 10 primary particles) if reference to the grading curve of figure 5.25 is made. In other words, most of the breakage is in the form of large fragments.
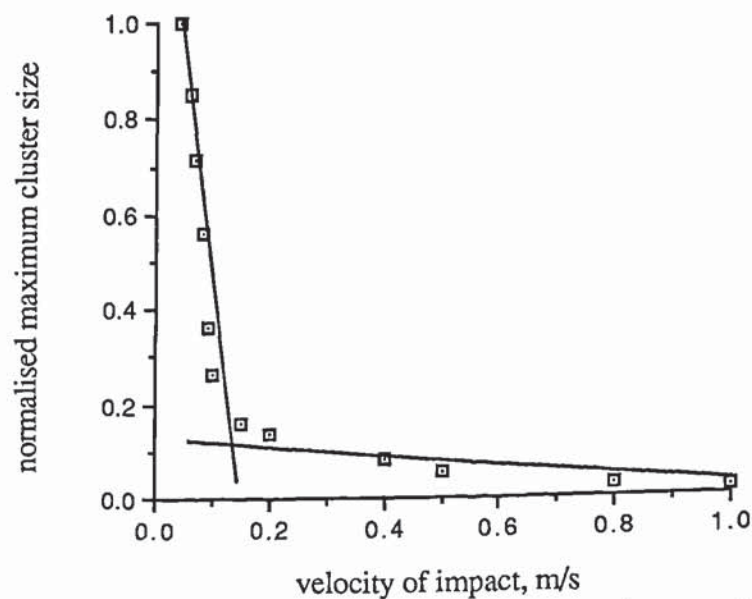
Figure 5.28 Normalised maximum cluster size to impact velocity

162

Figure 5.28 shows the normalised maximum cluster size plotted against the impact velocity for the agglomerate of surface energy 3.0 Jm^{-2}. The largest individual fragment for each simulation was recorded and normalised by dividing by the total number of particles (1000) in the original agglomerate. The best interpretation of the results is given by the two straight lines shown in figure 5.28. The intersection point occurs at a velocity of about 0.1 m/s agreeing with the interpretation of figure 5.27 and providing further support for the existence of a rapid transition from ductile to semi-brittle failure.

In contrast to plotting the largest cluster fragment, it is also relevant to present an alternative plot with emphasis on the number of fines produced. Figure 5.29 shows the percentage of singlets created by impacting the agglomerate on to the wall. As observed from the figure, high speed impacts are likely to create more fines than a lower velocity. Although there is not sufficient data to clearly show the trend between impact velocities of 1.0 m/s and 5.0 m/s, it is clear that at low velocities, the percentage of single particles produced increases linearly with increase in velocity.
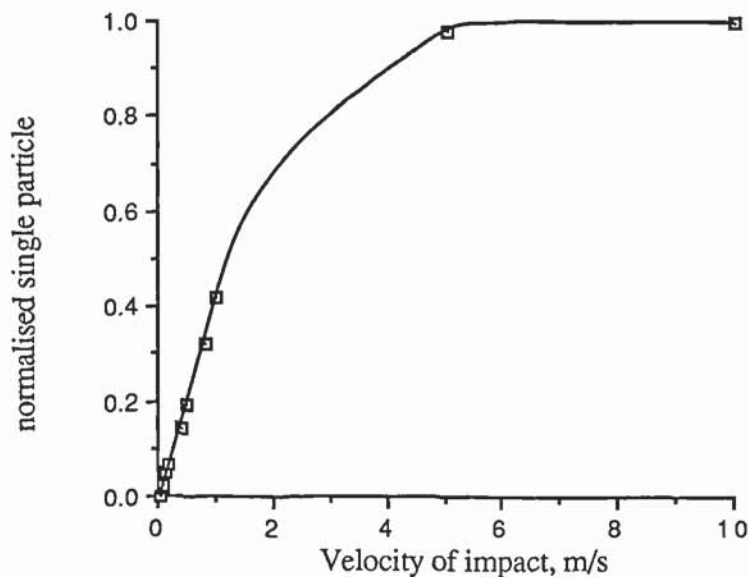
Figure 5.29 Percentages of single particles produced

163

Though confined to a 2D agglomerate of only one specific surface energy, the results presented in this section provide a simple guide to process engineering problems such as comminution and attrition.

5.6 Additional Remarks
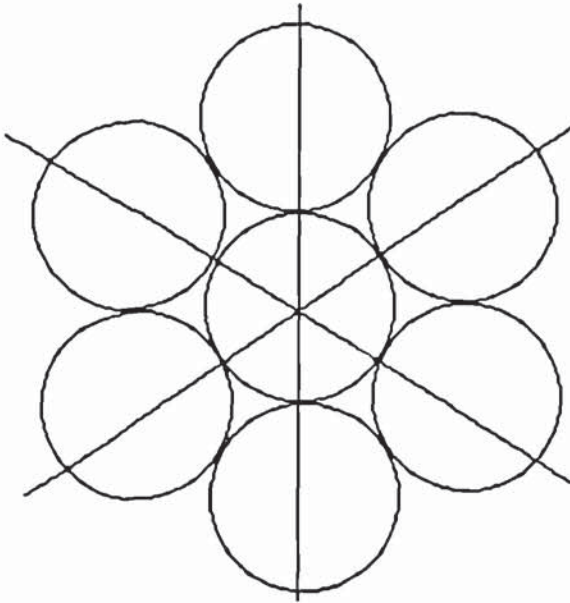
Figure 5.30a Initial alignment of packing   Figure 5.30b Plastic deformation
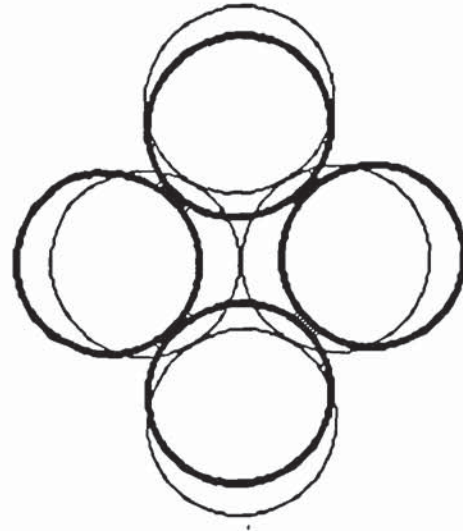
Figure 5.30 (a and b) shows the pure shear deformation mechanism of particulate material in which two of the three close packed rows of particles rotate an equal amount but in opposite directions, Rowe (1962) and Thornton (1977). This mode of deformation is only possible by breakage of contacts along the third row of close packed particles. In order for these contacts to break, sliding must occur at the interparticle contacts along the other two close packed rows.

The mechanism described above was observed, figure 5.4 (a to c), during the initial loading stage for the case of an impact velocity of 1.0 m/s. The main direction in which the maximum compressive force propagates is slightly off to the right of a vertical line. All contacts that are to the right of this line were seen to break in the direction normal to the compressive wave front. The same was observed for the case of those lying on the

164

left of the line of maximum compressive force. Figure 5.31 shows a schematic representation of the initial orientation of the particle system by showing two typical clusters of four particles within the agglomerate before the plastic deformation mechanism occurred. The contact arrangement forms a diamond shape connection between each of the four particles. The exact location of these clusters within the agglomerate and the velocity of impact determine whether plastic deformation will occur. A group of particles will only deform plastically if it lies well within the zone of initial deformation provided that the impact velocity is high enough to provide the energy needed to cause irrecoverable deformation.
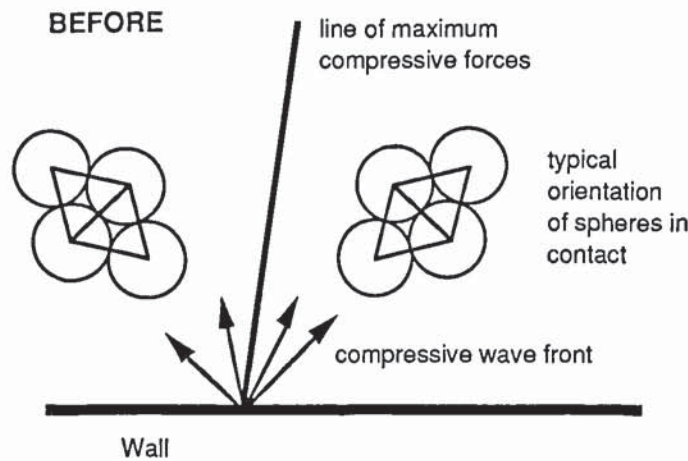
Figure 5.31 Schematic diagram of pre-plastic deformation
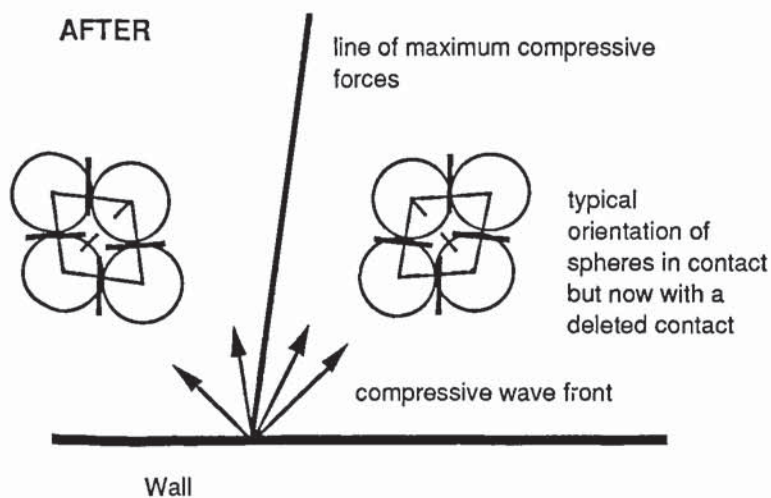
Figure 5.32 Schematic diagram of the plastic deformation mechanism

165

As the radial wavefront traverses the agglomerate it will break contacts that are immediately orthogonal to it. Figure 5.32 shows how the contacts are broken as the radial wavefront passes through the agglomerate. In figure 5.32 the broken lines indicate contact deletion while the short bold lines indicate sliding contact. During the initial plastic deformation stage of the computer simulated experiments, only the contacts orthogonal to the radial wavefront were deleted, while rigid body sliding was observed to take place at the other contacts in the deformed region, see figures 5.3 (a to c) and 5.4 (a to c). This process was observed behind the radial wavefront as it propagated through the agglomerate. Further contact breaking occurred as the tail end of the wave passed through the assembly. This second stage of contact breaking led to shattering within the plastic deformation zone due to local structural instability. This phenomenon is illustrated by figure 5.33 (a to l) where each plot indicates new contacts breaking with respect to the preceeding plot.

Having considered the mechanism of plastic deformation, it is also necessary to comment on crack initiation and propagation. It has been established, from detailed examination of the computer simulated data, that cracks are initiated at the boundary of the plastic deformation zone and propagate during the unloading stage when the wall force is decreasing. Figure 5.9 (a to f) show the evolution of a crack during the unloading stage. A detailed examination of the agglomerate impacted at a velocity of 0.09 m/s, revealed that the crack propagates by following the " path of lowest resistance", that is it chooses from the next available contacts the one with the smallest normal force. Crack initiation was examined for the range of impact velocities which produced semi-brittle behaviour. Figures 5.34 (a to d) show, for impact velocities of 0.06, 0.07, 0.08 and 0.09 respectively, when the initial damage has been established. It is clear from the figures that, although the crack direction is sensitive to the impact velocity, the major crack always originates from a point close to the intersection of the maximum compressive force and the plastic deformation zone boundary.
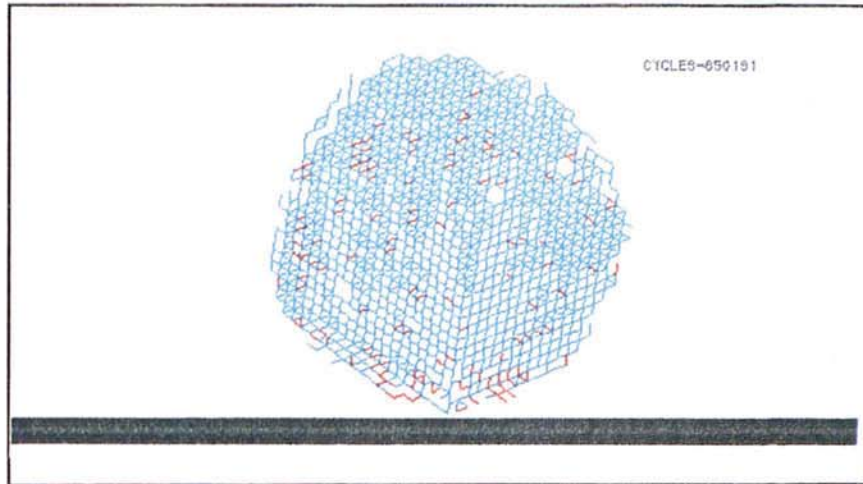
Figure 5.33a Equivalent space lattice indicating contact breaking due to tail end effect, t = 9.6 μs
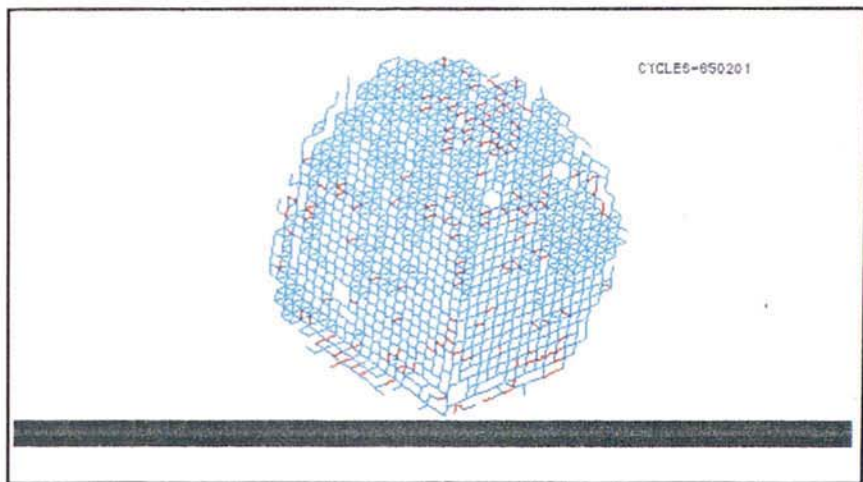
Figure 5.33b Equivalent space lattice indicating contact breaking due to tail end effect, t = 10.6 μs
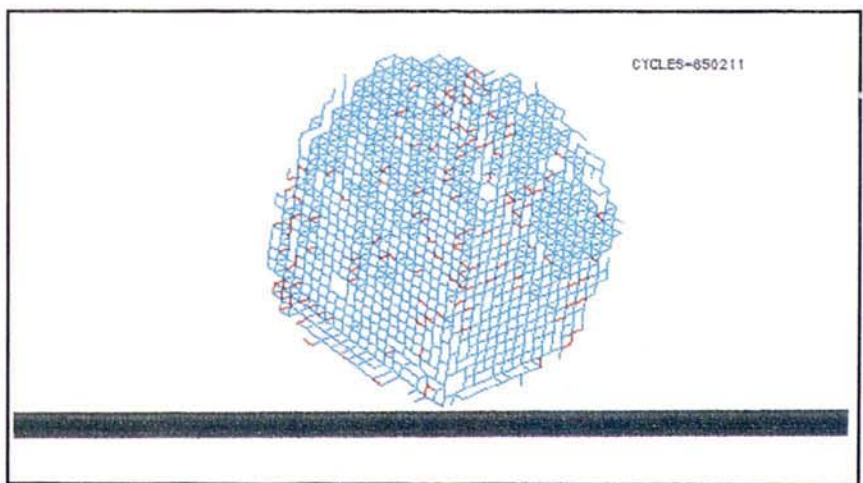
Figure 5.33c Equivalent space lattice indicating contact breaking due to tail end effect, t = 11.7 μs
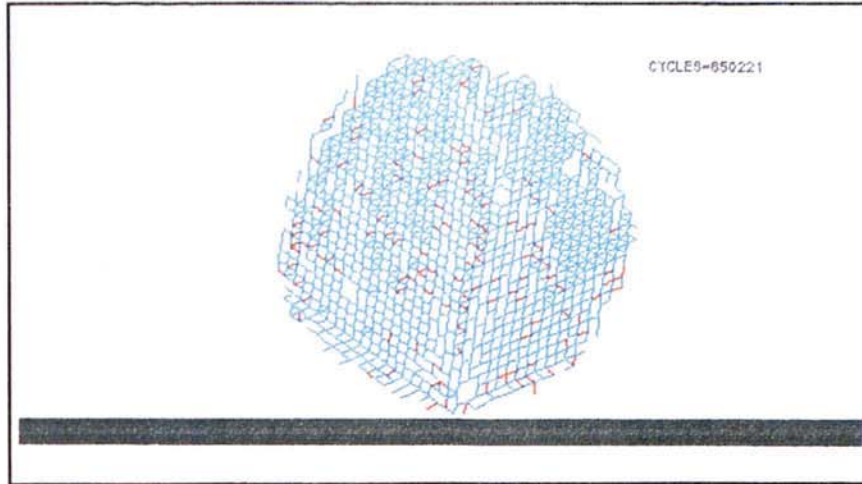
Figure 5.33d Equivalent space lattice indicating contact breaking due to tail end effect, t = 12.7 µs
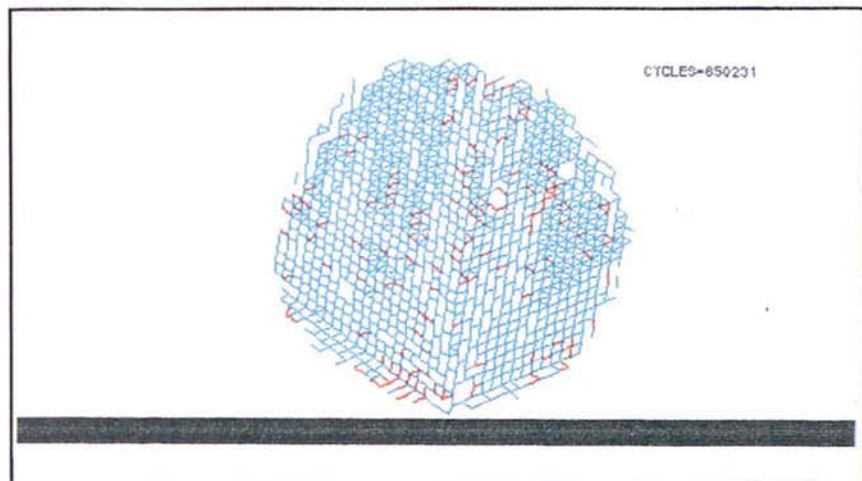
Figure 5.33e Equivalent space lattice indicating contact breaking due to tail end effect, t = 13.8 µs
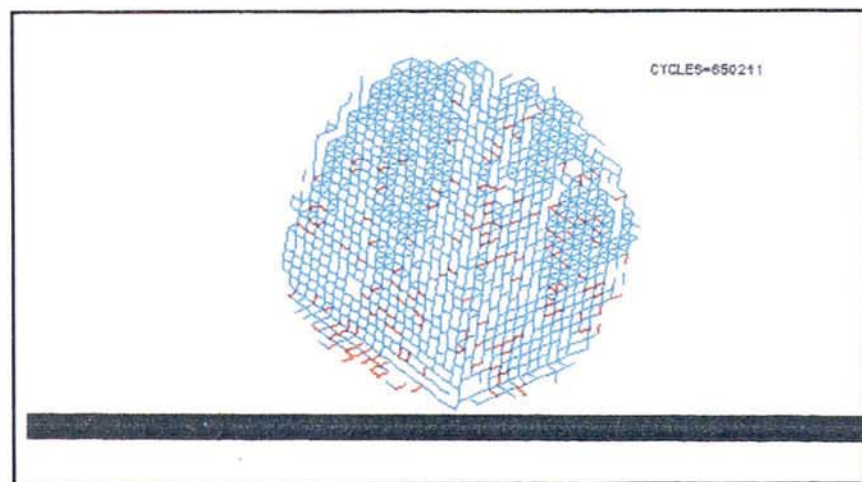
Figure 5.33f Equivalent space lattice indicating contact breaking due to tail end effect, t = 14.9µs
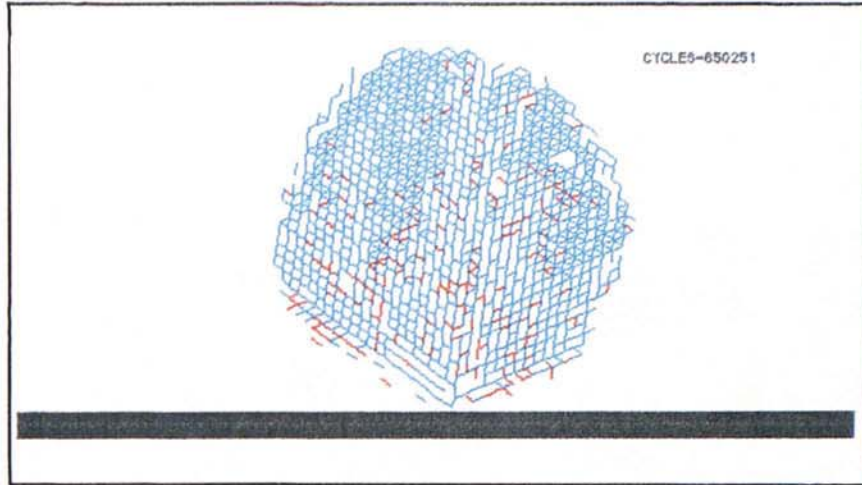
Figure 5.33g Equivalent space lattice indicating contact breaking due to tail end effect, t = 16.0μs
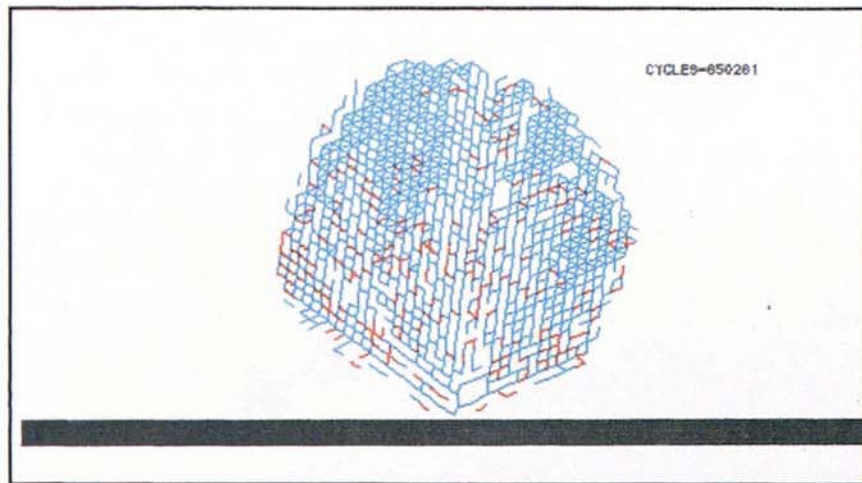
Figure 5.33h Equivalent space lattice indicating contact breaking due to tail end effect, t = 17.0μs
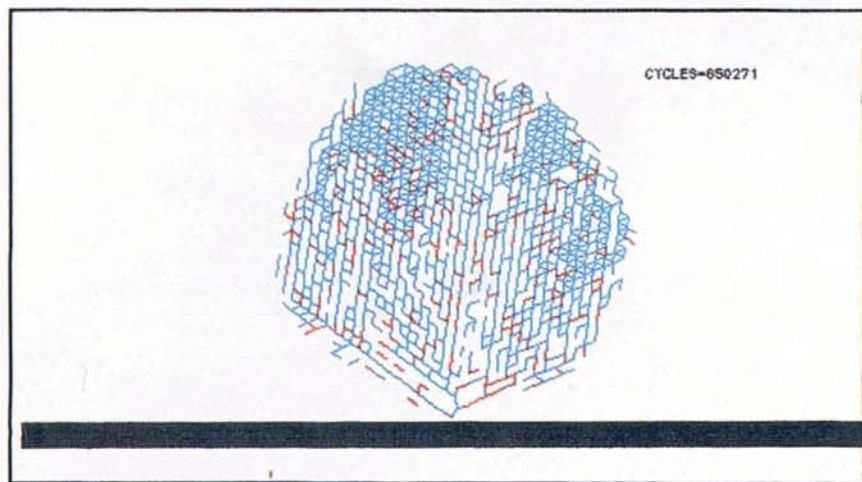
Figure 5.33i Equivalent space lattice indicating contact breaking due to tail end effect, t = 18.1μs

169
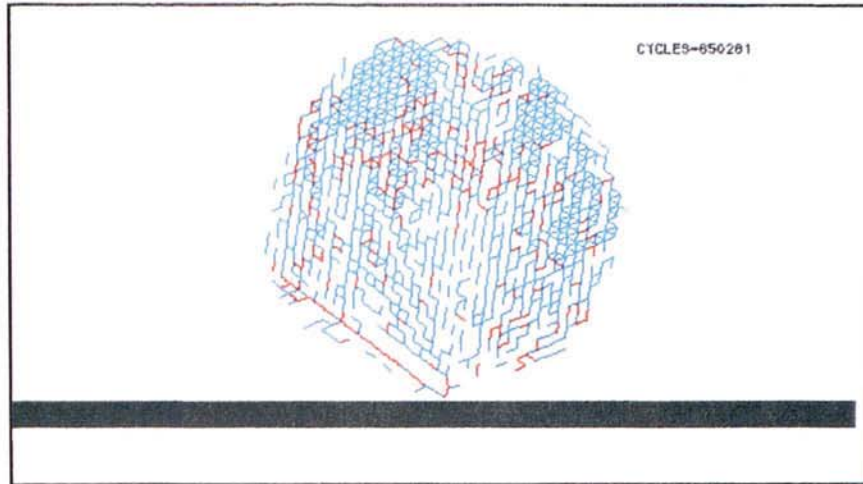
Figure 5.33j Equivalent space lattice indicating contact breaking due to tail end effect, t = 19.2µs
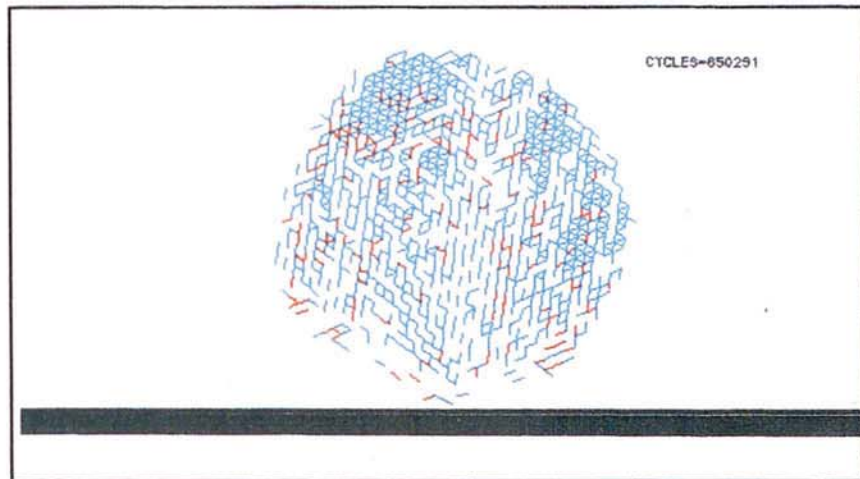
Figure 5.33k Equivalent space lattice indicating contact breaking due to tail end effect, t = 20.2µs
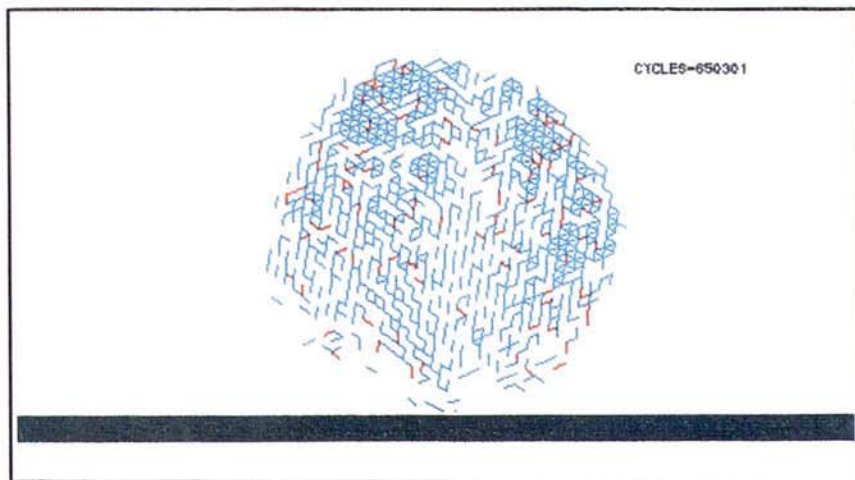
Figure 5.33l Equivalent space lattice indicating contact breaking due to tail end effect, t = 21.3µs
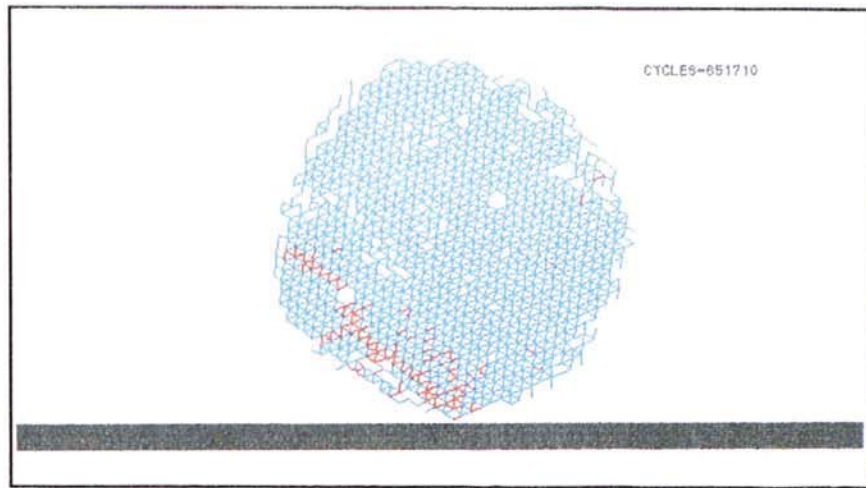
Figure 5.34a   Equivalent space lattice indicating the position of crack initiation
V = 0.06 m/s
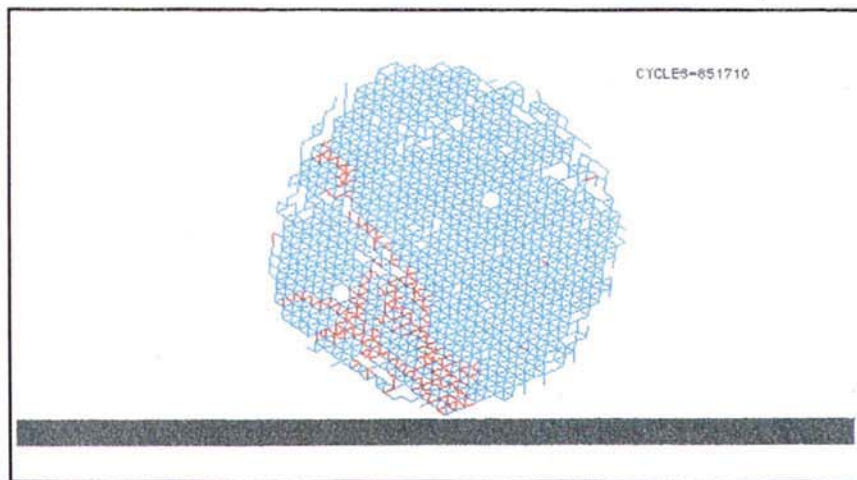
Figure 5.34b   Equivalent space lattice indicating the position of crack initiation
V = 0.07 m/s
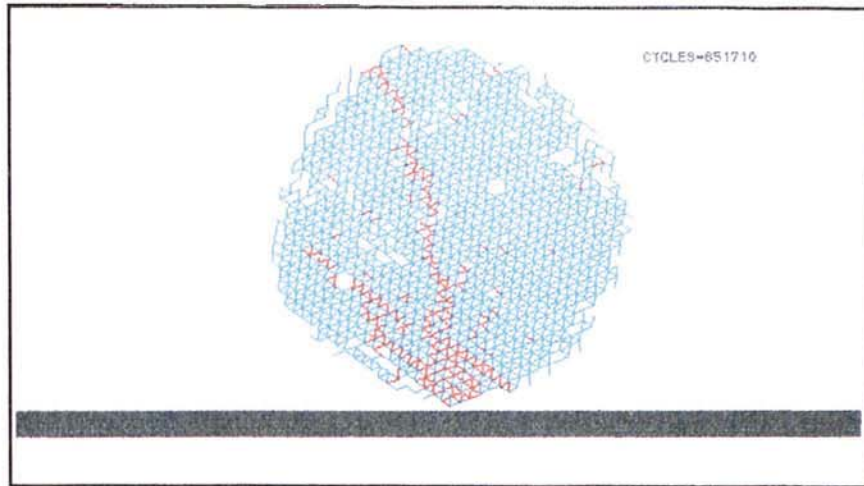
Figure 5.34c   Equivalent space lattice indicating the position of crack initiation V = 0.08 m/s
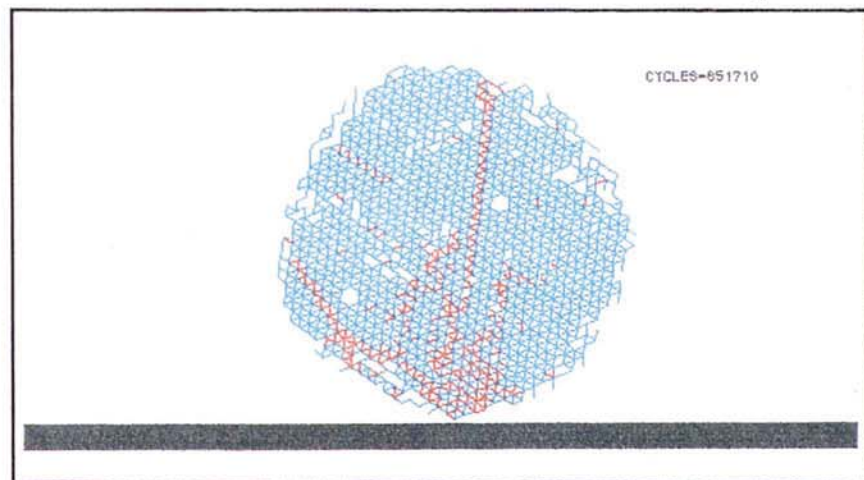
Figure 5.34d   Equivalent space lattice indicating the position of crack initiation for V = 0.09 m/s

The extent of the plastic deformation zone is controlled by the attenuation of the force propagating through the agglomerate. Figure 5.35 shows, for an impact velocity of 0.09 m/s and $\gamma = 3.0$ Jm^{-2}, the evolution of the normal contact force at each of the contacts lying along the line of maximum force propagation. The maximum force generated decreases with distance from the wall, as expected.
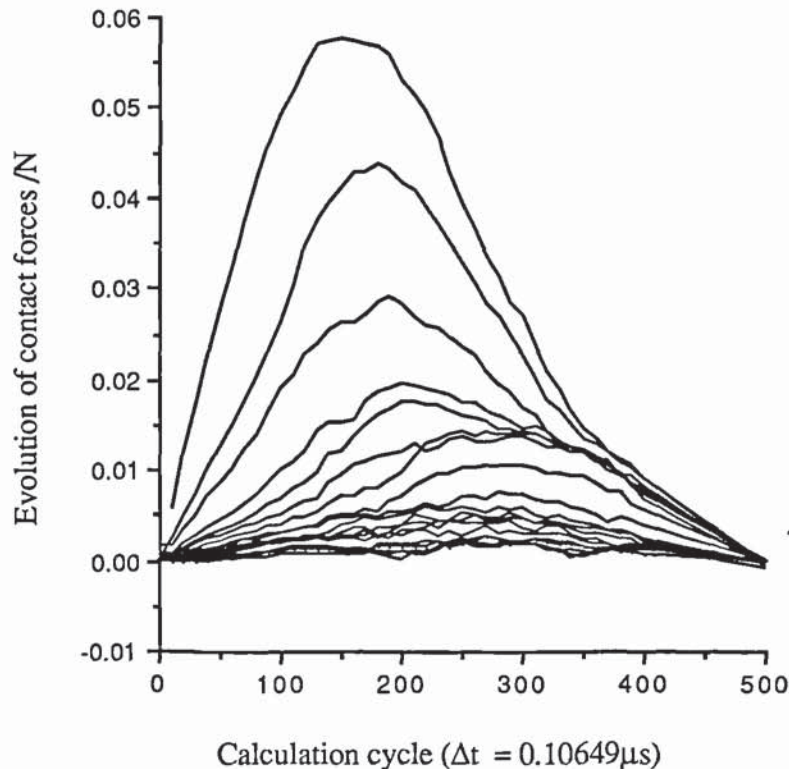
Figure 5.35 Evolution of interparticle contact forces along the line of maximum force propagation

The rate at which the contact force attenuates along the line of maximum force transmission is shown in figure 5.36 (a to c). It can be seen that the rate of attenuation is approximately exponential. Superimposed on figure 5.36 (a to c) is the critical maximum normal contact force necessary to ensure breakage of contacts due to adhesive peeling according to the theory of Johnson et al (1971), figure 5.36 (a to c). As defined in Chapter 3, there is a critical velocity of impact below which two impacting particles will stick together. Associated with this critical velocity is a

173
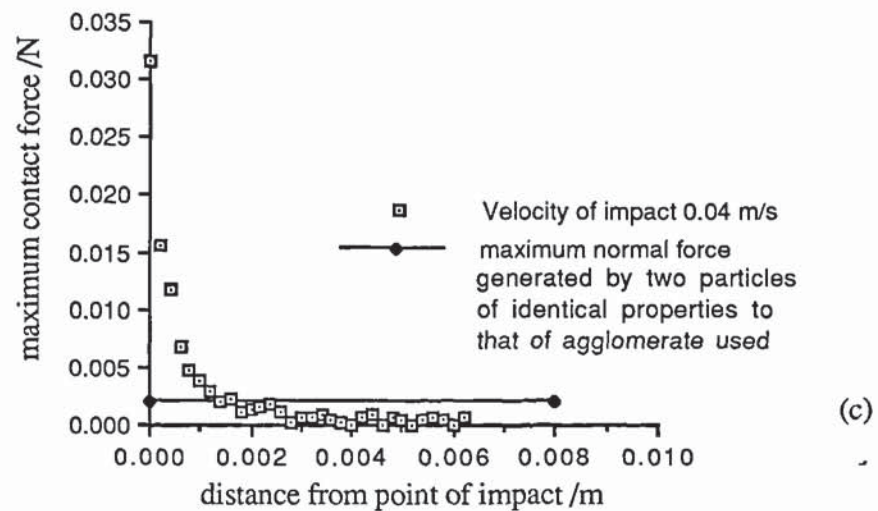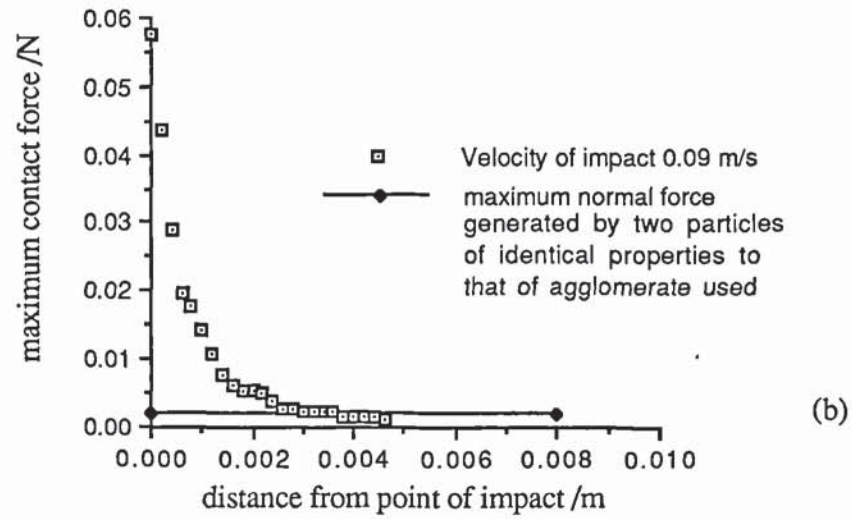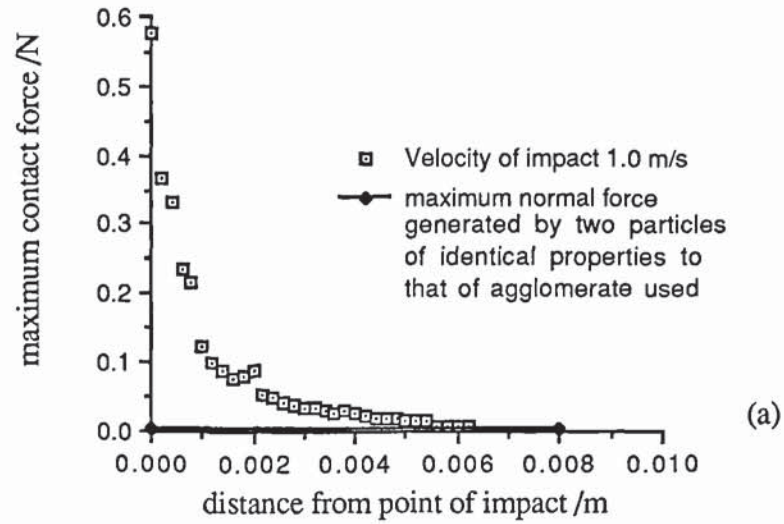
Figure 5.36 Rate of attenuation along line of maximum force transmission, (a) 1.0 m/s,

(b) 0.09 m/s, and (c) 0.04 m/s

174

maximum normal contact force which, due to the complexities of JKR theory, cannot be calculated. Therefore, the impact of two single particles, with identical properties to the primary particles of the agglomerate, was simulated using the corresponding critical relative velocity of impact. From this additional simulation the critical maximum normal force was determined and its value has been superimposed on figure 5.36 (a to c). If the maximum force generated at a contact is less than this value then the contact between these two particles will not be broken. Consequently, in figure 5.36 (a to c), the distance where the horizontal line intersects the attenuation curve indicates the maximum possible extent of the plastic deformation zone. Comparison with the computer simulated results indicate that this is a good way of predicting the extent of the plastic deformation zone.

5.7 Summary

A comprehensive series of simulations of agglomerate impact has been reported in this chapter. The work has been restricted to a 2D monodisperse agglomerate consisting of 1000 primary particles impacting orthogonally with a wall. Any conclusion drawn from the work carried out is strictly only applicable to the 2D behaviour of dense monodisperse systems. However, it is believed that the observation will also be qualitatively correct for real 3D agglomerates.

It has been shown that there is a threshold velocity below which no significant damage occurs. This threshold is dependent on the strength of the interparticle bonds and is an exponential function of the surface energy of the primary particles. Above the threshold velocity there are two regimes of behaviour. High velocity impacts result in shattering of the agglomerate whereas moderate velocities produce semi-brittle fracture. The velocity at which the transition from shattering to semi-brittle fracture occurs is also related to the surface energy of the primary particles by an exponential relationship. Consequently, as illustrated in figure 5.23, it is possible to identify the three regimes of

behaviour (shattering, semi-brittle, and no damage) corresponding to the various possible combinations of impact velocity and bond strength.

The contact forces generated within the agglomerate depend on the spatial distribution of the contacts between adjacent particles. Chains of 'aligned' contact points are able to absorb and transmit relatively large forces due to their relative positions with respect to the surrounding particles. Simulation results show that the wave propagation process increases the area of contacts in the propagation direction. If the generated contact forces are sufficiently large, the change in the particle configuration is an irreversible process and can lead to rearrangement of the load transfer paths. Classical crack pattern evolution in a discontinuous media is very different from that observed in solids which are explained by a continuum approach. The tortuous crack pattern is the result of the geometric configuration of the individual particles.

The effect of the compression wave propagating through the agglomerate, as observed in the computer simulated experiments, agrees with the observations of dynamic force transmission through photoelastic disc assemblies, as reported by Rossmanith et al (1982). Qualitatively, the observed way in which agglomerate breakup occurred in the computer simulated tests is similar to that observed for the cement-mortar spheres, Arbiter et al (1969), and for the urea prills, Ghadiri (1991)

6. Agglomerate Strength

The experiment may be considered a success if no more than 50% of the observed measurements must be discarded to obtain a correspondence with the theory.

6.1 Introduction

In order to assess the ability of an agglomerate to resist attrition or comminution it is conventional to consider the strength of the agglomerate. The strength of particulate solids can be represented in several ways. The choice depends on the application, e.g. the crushing or compressive strength of concrete for load bearing problems, the shear strength of soils or rocks for problems involving the stability of their respective masses, and the tensile strength for the fracture of highly brittle materials. For reasons given in section 6.2, it is the tensile strength that is generally considered to be relevant to agglomerate degradation.

There are, at present, a series of techniques used experimentally to determine the tensile strength of materials. These include the direct pull test, the flexure test, the ring test, uniaxial tensile test and the diametrical compression test. The diametrical compression or Brazilian test (also known as the split cylinder test in concrete technology) provides an indirect measure of a material's tensile strength by generating tensile stresses through compressive loading. Favoured highly for its simplicity, the diametrical compression test is often used in preference to the uniaxial tensile test which is difficult to perform to an acceptable standard for brittle materials. However, although simple to perform, the interpretation of the data obtained from diametrical compression tests on particulate solids has created confusion especially when it comes to the prediction of the 'true' failure mechanism.

In the first part of this chapter, a review of the published literature on the diametrical compression test and the theoretical and experimental interpretation of the indirectly obtained tensile strength is provided. This will then be followed by consideration of the significance of the failure criteria relevant to fracture initiation and propagation. Finally, for the same 1000 particle monodisperse 2D agglomerate used in the impact

177

simulations reported in Chapter 5, results of computer simulated diametrical compression tests will be reported and discussed.

6.2 Brief Literature Review

An acceptable and popularly used method of predicting the theoretical tensile strength, σ_T, of an agglomerate was developed by Rumpf (1962). Rumpf (1962) gave a detailed derivation of the theoretical tensile strength, σ_T, based on his mono-sized spheres or disc model and mathematically predicted

$$\sigma_T = [\, 9\,H\,(\,1 - \varepsilon\,)\,] / 8\,\varepsilon\,d^2 \qquad\qquad (6.1)$$

where, ε is the porosity, H is the bonding force per unit contact point and d is the diameter of a single sphere. Since H is the bonding force per unit contact point, it is dependent on the nature of the bond between the particles and their distance apart. Rumpf (1962) analysed different types of bond independently and attributed to each case an 'arbitrary' value. Rumpf's model of an agglomerate is based on an assembly of mono-sized spheres with interparticle bonds distributed, on average, uniformly in position and orientation through a cross-section. It was assumed that the macroscopic cross-section was homogenous and that the agglomerate failure plane could then be described in terms of a macroscopic cross-section through the agglomerate. However, in real agglomerates, stress concentrations will occur at flaws such as cracks or packing irregularities, and the granules will fail by a progressive mechanism involving crack initiation and propagation. Although the Rumpf (1962) analysis applies to the simplified case of a granule being broken by simultaneous rupture of bonds in a failure plane, the real failure mechanism in an agglomerate is not as straightforward as predicted by Rumpf.

Atkins et al (1985), proposed two categories of deformation mechanisms: deformation with and without flow and with and without cracking. Ductile materials tend to exhibit gross plastic flow before failure and brittle materials have little or no tendency to flow plastically. Failure by cracking with no plastic flow is termed as elastic fracture. An

alternative approach to the prediction of the strength of agglomerates has been proposed separately by Adams et al (1985, 1989) and Kendall et al (1986), in which the materials fail by propagation of cracks. A fracture mechanics approach is used in which the conditions for failure by crack propagation are considered in terms of the energy needed for propagation of a crack. The fundamental principle governing both approaches follows the Griffith (1920) theory, introduced in chapter 5.

Hondros (1959) gave a full mathematical analysis of the stresses along the principal planes upon biaxial loading, following the elastic theory of Timoshenko (1934), for both plane stress (discs) and plane strain (cylinders). Since the diametrical compression test is only valid when primary fracture occurs along the loading diameter, the stress distribution along that diameter is of greatest interest. Hondros (1959) considered the stress distribution along the two principal planes for a circular element supported by a short strip loading, figure 6.1.
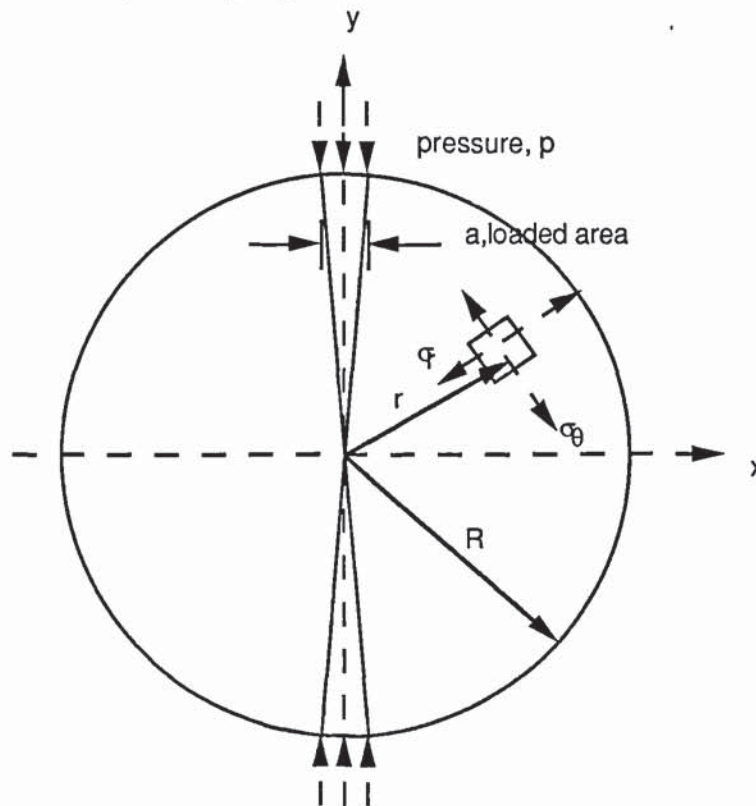
Figure 6.1 The Brazilian test. Notation for polar stress components in a disc compressed by two diametrically opposite short strip loadings, Hondros (1959).

179

The corresponding stresses along these principal planes through OY and OX were calculated and the results indicated relatively large compressive stresses at the boundary of the disc, figure 6.2. Stresses at the centre were expressed in terms of the applied load, and given as

$$\sigma_{\theta y} = \sigma_{rx} = -2P/\pi Dt \qquad\qquad (6.2)$$

$$\sigma_{\theta x} = \sigma_{ry} = 6P/\pi Dt \qquad\qquad (6.3)$$

The distribution of stresses at the centre of the disc in these expressions agree with Wright's (1955) analysis using point loads. Colback (1966) also mapped graphically the magnitudes and directions of the principal stresses for the case of line loading.
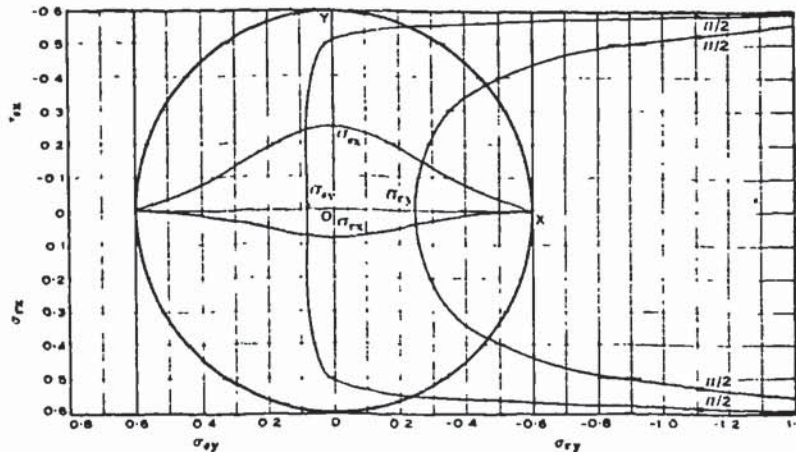
Figure 6.2 Theoretical stress distribution along the vertical and horizontal diameters, $2p/\pi = 1$

According to Mellor et al (1971), indirect tensile tests, which induce non-uniform stress fields controlled partly by the properties of the test material can never fully substitute for the direct uniaxial tensile test. However, the Brazilian test is capable of giving a very good measure of uniaxial tensile strength for Griffith-type materials when it is carefully performed, with special attention paid to control of contact stresses, to accurate load readout, loading rate, application of load, specimen dimension and

specimen preparation. There are some materials, reported by Mellor et al (1971), like ice, for which the standard Brazilian test gives consistent but wholly erroneous results. Ice has a low compressive to tensile strength and so, does not conform to the Griffith's failure criterion as proposed by Mellor et al (1971). According to this criteria, failure occurs when,

$$\sigma_1 = \sigma_T \text{ if } 3\sigma_1 + \sigma_3 > 0 \qquad\qquad (6.4)$$

where σ_1 and σ_3 can be derived from the Hondros (1959) equations. Also, according to this criteria, failure will initiate from the centre only for materials with large compressive to tensile strength ratios. Although this criterion was valid for most of the experiments of Mellor et al (1971) they did not show conclusive evidence of the source of crack initiation and propagation but presumed that crack propagation occurred from the centre outwards.

Materials like rock consist of grains with inherent pore and crack micro-structures, so that they can only be considered homogeneous in volumes that are large compared with the dimensions of these micro-structures. There is also a characteristic distribution of these defects in structures such that the probability of encountering larger, and therefore more critical defects increases with increasing sample volume. While the most severe stress conditions may exist at a certain point in the specimen, the most critical defects in small specimens may lie at some distant point where the combination of stress and defects occurs. This effect on the diametrical compression test results have been investigated theoretically by Fairhurst (1964).

An analysis of the diametrical compression test was also reported by Rudnick et al (1963), in which the two cases of line and distributed loading were compared analytically. Figures 6.3 and 6.4 showed the similarities and differences in accounting for the different type of loadings. It was pointed out that, in the case of ideal line loading, the high shear and compressive stresses near the ends of AB are the cause of failure modes in shear and compression and that tensile failure will not occur. The

maximum compressive stresses occur at the specimen surface immediately beneath the loads. Failure from these compressive stresses would therefore be expected to appear as local crushing, figure 6.3. If this local crushing is not extensive, it may only increase the area over which the load is applied, so that ultimate failure may be either in shear or tension. Padding was suggested by Rudnick et al (1963) to uniformly distribute the load and hence induce a tensile failure along the loaded diameter. Figure 6.4 gives the stress redistribution as the result of introducing paddings. Note that the choice of introducing proper padding is to curb the infinitely high compressive stresses beneath the loading area. Compressive stresses are reduced significantly but in doing so, the horizontal stresses across the loading planes are now compressive while the centre's stress distribution remained unchanged as pointed out earlier. This issue will be discussed in the concluding remarks of this chapter. If, as pointed out by Rudnick et al (1963), the introduction of padding can reduce the compressive stresses and also reduce the shear stress to nil at the points of loading, then surely this does not imply directly that the tensile crack will be induced at a later stage. Rudnick et al (1963) also reported different failures modes, each attributed to the significance of reducing the high compressive stresses beneath the loading area. None of the failure modes obtained or suggested agreed with the prediction of a tensile crack initiated from the centre and propagating towards the loaded platens. If there was genuinely a controlled tensile failure, then surely they must start from the centre. Instead Rudnick et al (1963) attributed the choice of failure modes to the statistical concept of strength of brittle materials put forward by Weibull (1952).

Peltier (1954) calculated the stress distribution in a Brazilian test for various assumed pressure distributions. He reported that the induced tensile stresses are essentially uniform over a reasonable proportion of the loaded diameter if the width of the pads are to within one-fifth or less the specimen diameter. Fairhurst (1964), however, reported that the size of the padding will grossly affect the true tensile strength of the materials to be tested.

Beside the shear and tensile failure modes, there is also the triple-cleft-type fracture which was first reported by Mitchell (1961), who suggested that this behaviour was wholly due to shear stresses. With this finding, he further suggested the limited range of materials to which the Brazilian test technique is applicable. Rudnick et al (1963), however, proved that the triple-cleft-type failure can also be due to tensile stresses developing across the loaded platens Their study indicated that the triple-cleft-type fracture initiates along the the loaded diameter, causing a central break, the load causing fracture is the highest and the outer fracture surfaces are developed subsequent to the central crack under the influence of the remaining load. Figure 6.5 gives a visual appreciation of the types of fracture obtained by Rudnick et al (1963).

6.3 Simulation Technique

A series of simulations were performed in order to study the strength of the agglomerate when subjected to biaxial loading. As in the cases reported in the preceeding chapter, the range of surface energies adopted was the 'same, $\gamma = 0.3$, 1.0, 2.0 and 3.0 J/m^2, for the 1000 mono-sized particle agglomerate.

The initial setup for the diametrical compression is shown schematically in figure 6.6. Both platens have the same elastic properties as the agglomerate and, in order to induce loading on the agglomerate, are attributed with equal and opposite initial velocities. In this setup, the question of having a loading pad to uniformly distribute the loads will not be considered. The main assumption is that the walls come into point contact with the uppermost and the lowest particles from which load is transferred to the rest of the agglomerate.

The strain rate, dε/dt can be calculated as,

$$d\varepsilon/dt = V/D \tag{6.5}$$

where V is the relative velocity of the approaching platens and D is the diameter of the agglomerate (approximately 7mm).

Figure 6.3 Stress distribution across loaded diameter for two line loads, Rudnick et al (1963)

Figure 6.4 Stress distribution across loaded diameter (assuming contact width of 1/10 diameter and uniform contact pressure, Rudnick et al (1963)

Aston University

Illustration removed for copyright restrictions

Figure 6.5 Fracture modes commonly obtained with the diametrical compression test, Rudnick et al (1963)

185
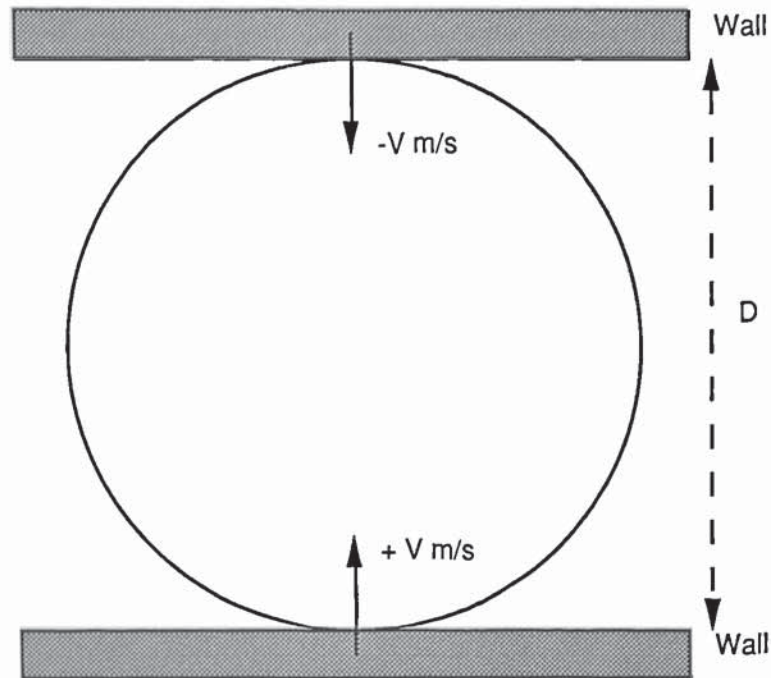
Figure 6.6 Schematic representation of initial agglomerate setup

The diametrical strain of the agglomerate will be expressed in terms of engineering strain, where

$$\varepsilon = \Delta D / D \qquad (6.6)$$

6.4 Computer Simulated Brazilian Tests

From the series of simulations performed under different loading rates, a selection of two typical cases was adopted to provide a detailed analysis. The choice in the selection of these cases was governed by the knowledge that the local deformation is a function of the loading rate which significantly affects the failure mode. For convenience the agglomerate with a surface energy of $3.0 \ Jm^{-2}$ is used to illustrate the typical cases, as in chapter 5. It will be shown that a relatively low strain-rate of $15 \ s^{-1}$ results in semi-brittle behaviour with a very localised zone of plastic flow directly under the loading areas. In contrast, a high strain rate of $150 \ s^{-1}$ leads to extensive plastic deformation and crushing of the agglomerate.

186

6.4.1 Low Strain-rate Test Results

In this simulation, both platens approached each other at a relative velocity of 0.1 ms^{-1} with the agglomerate setup as in figure 6.6. Figure 6.7(a to e) show the force distribution within the agglomerate at different stages of diametrical strain and with the same colour coding as used in the previous chapter, (The initial forces distribution can be seen in figure 5.1c). Figure 6.7a (0.03% strain) shows clearly the compressive wave extending radially under the influence of a biaxial loading. The total number of contacts, however, remained almost unchanged during this initial stage, with most of the previously tensile contacts now in compression. The tensile forces remaining are approximately orientated at right angles to the loaded diameter, as indicated in figure 6.7a, with the exception of particle contacts near the boundary which are essentially undisturbed by the propagating compressive waves. The orientation of tensile contacts in the centre of the agglomerate clearly indicate a horizontal tensile stress state. In figure 6.7b (0.045% strain), tensile contacts have been broken along the main loaded diameter as can be seen from the presence of a longitudinal void area. At the two loading points large compressive forces are still present at this stage. Once the main crack has been formed, further cracks are initiated, figure 6.7(c to e). During this stage the platens loads are decreasing but there is still sufficient energy input to produce further minor fractures of the cracked agglomerate. It is interesting to note that one of the secondary cracks merges with the original crack. Consequently, at the end of the test, a clear fracture would not be observed by the conventional experimentalist.

Figures 6.8(a to e) show the current locations of sliding contacts. The maximum number of sliding contacts is shown by figure 6.8b, when the loads on the platens are at their respective maximums. As previously discussed in chapter 5, regions of high concentration of sliding contacts suggest the formation of plastic deformation zones. Figure 6.8b shows large numbers of sliding contacts adjacent to the loading areas indicating significant plastic deformation. For the rest of figures 6.8, the amount of sliding reduces as the loads on the platens decrease.

187
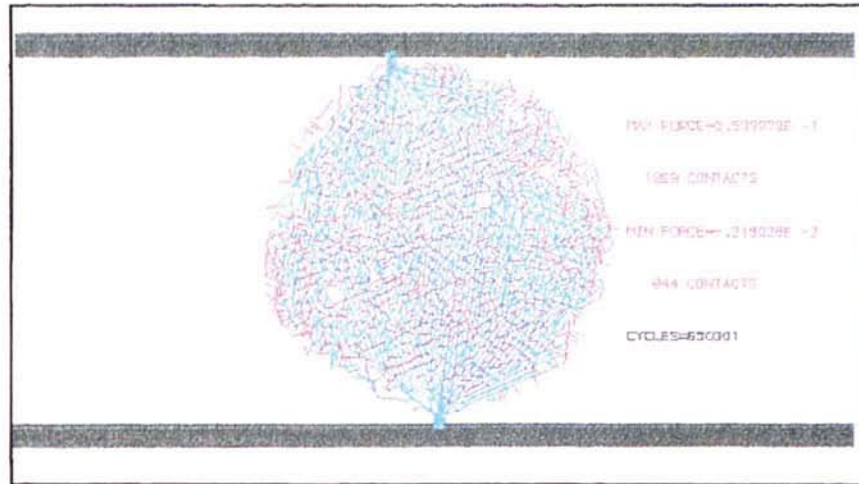
Figure 6.7a Distribution of contact forces at 0.03% strain
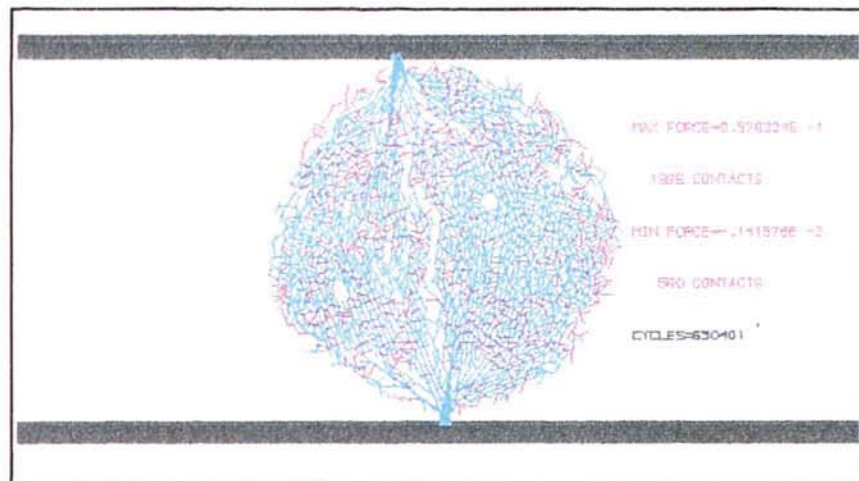
Figure 6.7b Distribution of contact forces at 0.045% strain with a clear longitudinal void area along the loaded diameter
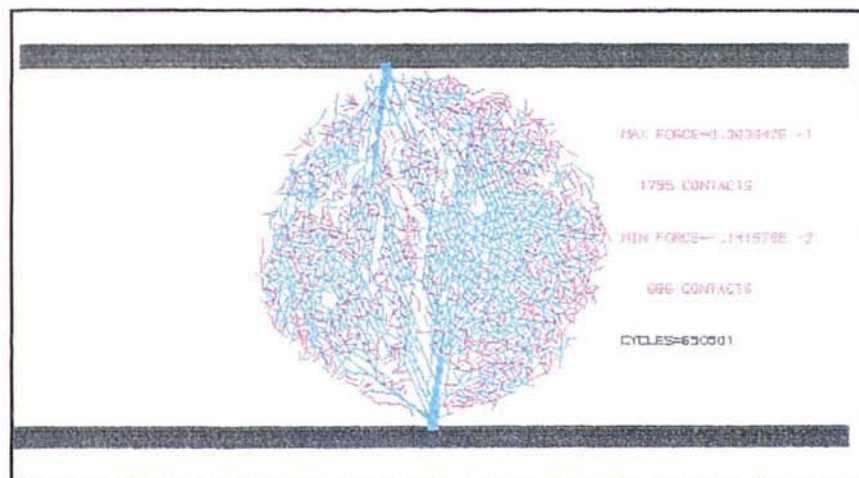
Figure 6.7c Distribution of contact forces at 0.06% strain with development of secondary cracks
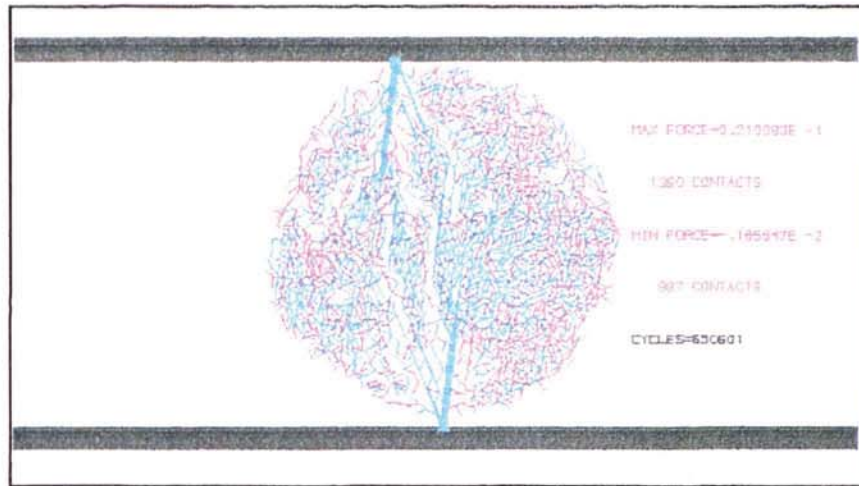
Figure 6.7d Distribution of contact forces at 0.076% strain
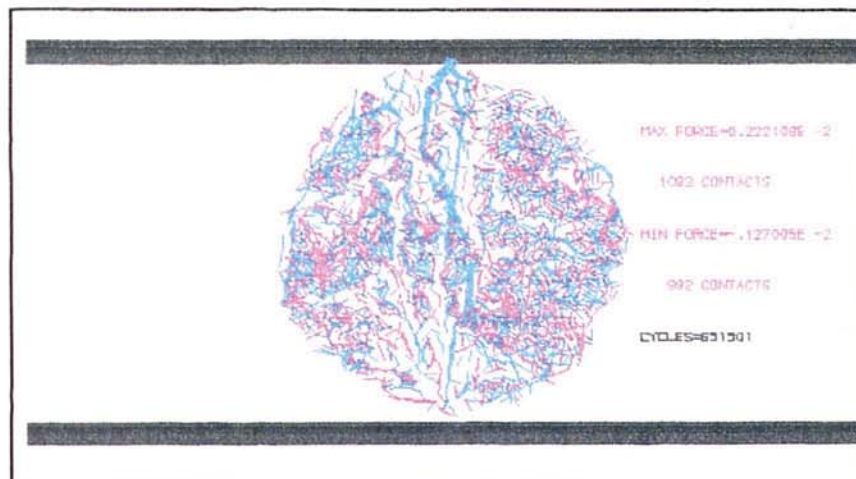
Figure 6.7e Distribution of contact forces at 0.213% strain

189

Figure 6.8a Sliding contacts at 0.03% strain

Figure 6.8b Sliding contacts at 0.045% strain
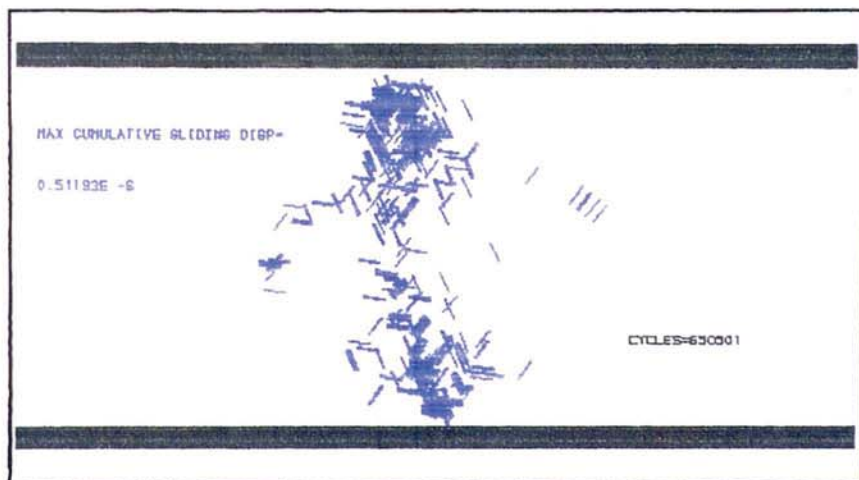
Figure 6.8c Sliding contacts at 0.06% strain
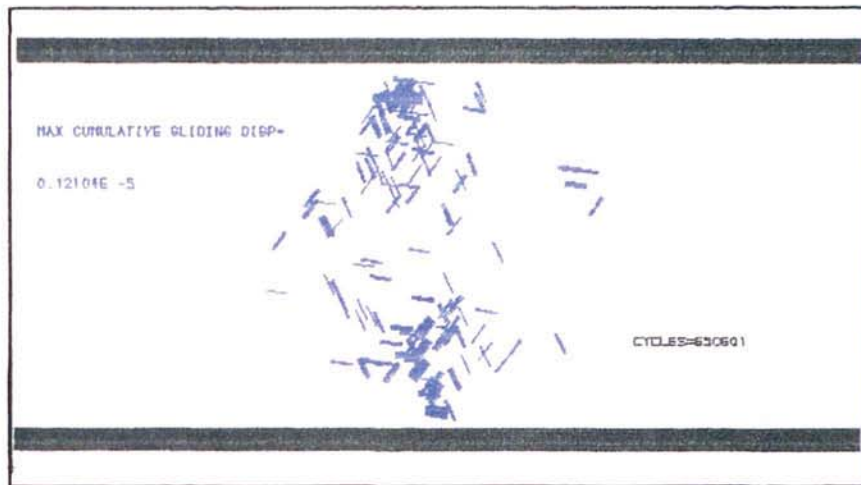
Figure 6.8d Sliding contacts at 0.076% strain
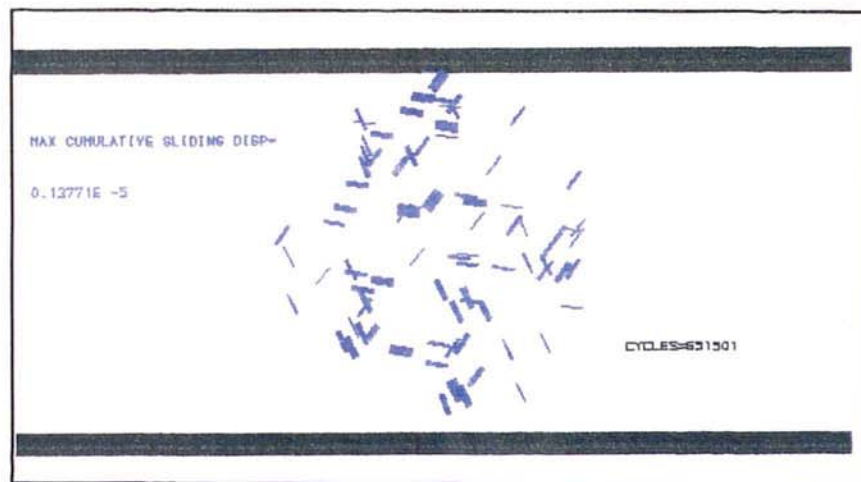
Figure 6.8e Sliding contacts at 0.213% strain

191

The corresponding space lattice plots of the assembly are shown in figures 6.9 (a to e). When the strain is approximately 0.03%, figure 6.9a shows that damage originates at the platens. Figure 6.9b shows that plastic deformation is contained to small regions near the platens and cracks propagate from the zones toward the centre of the agglomerate. Figure 6.9b (0.045% strain) shows the eventual connection of the two main crack paths. Further secondary crack formation is clearly shown in figure 6.9 (c to e) which confirm the previous observations based on the force distribution plots.

The ball plots represented by figures 6.10 (a to e) show clearly a longitudinal gap along the diameter of the agglomerate which widens as the strain is increased gradually. Although figure 6.9b shows a clear crack at around a strain of 0.045%, no gap can be seen in the ball plot due to the micron-sized separation at this stage. Figure 6.10a shows the agglomerate orientation at a strain of 0.47% when a small crack at the centre of the agglomerate can be identified. At a strain of 0.77%, the visible gap has widened and extended in the vertical direction, figure 6.10b. As explained earlier, the crack had already been established at a strain of 0.045% but only after a long period of gap widening was it visible on the ball distribution plots. Figures 6.10(c to e) show the apparent failure mechanism that would be observed in a conventional experimental diametrical compression test. At the location of the loading points, there is evidence of fines in the form of singlets due to local crushing and the central gap is observed to widen from the centre point towards each of the platens. It is significant to note that plastic deformation leading to local crushing adjacent to the platens has already occurred at a strain of 1.69%, at which stage there is no significant overall change in the shape of the agglomerate. The corresponding velocity plots of figures 6.11 (a to e) show two major uniformly distributed regions which clearly indicate the post failure separation mechanism.
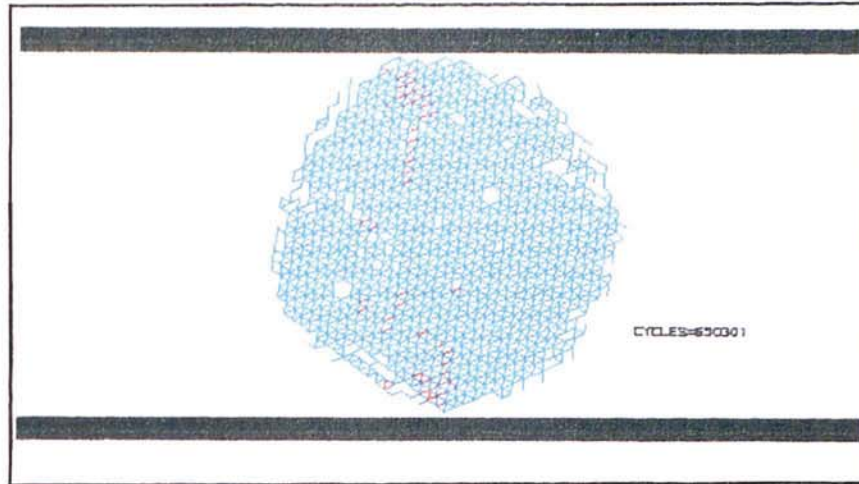
Figure 6.9a Equivalent space lattice at 0.03% strain
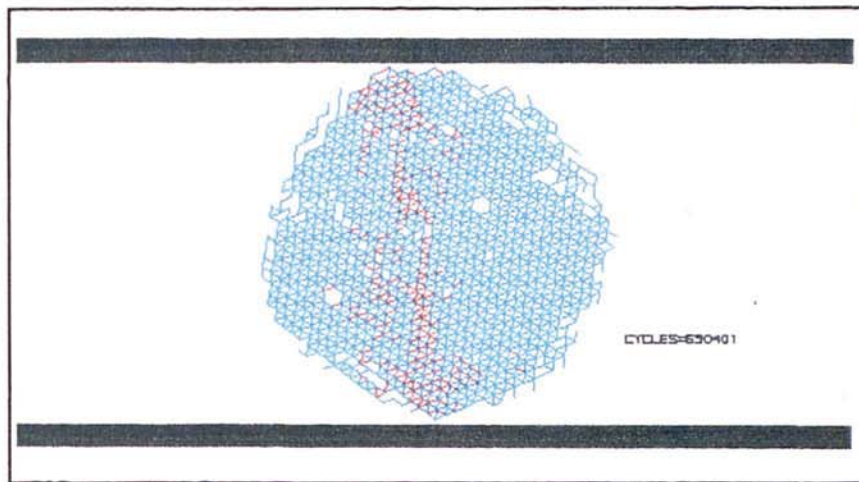
Figure 6.9b Equivalent space lattice at 0.045% strain with the main crack path established
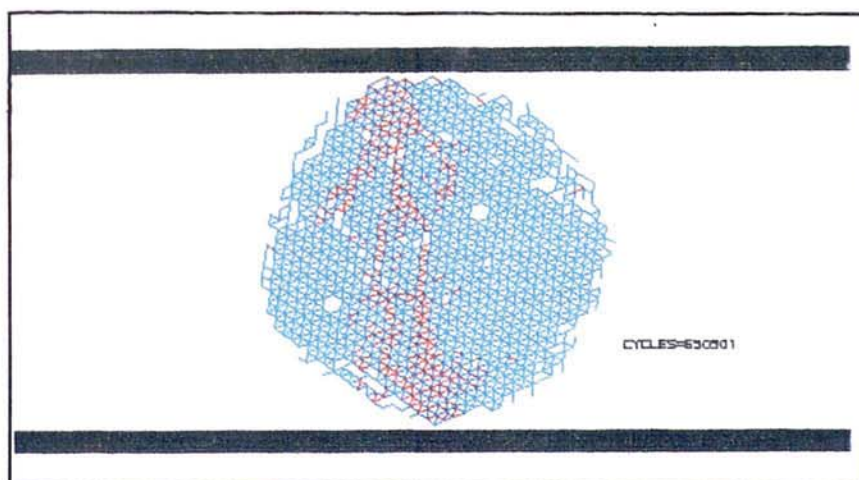
Figure 6.9c Equivalent space lattice at 0.06% strain with formation of a second crack path
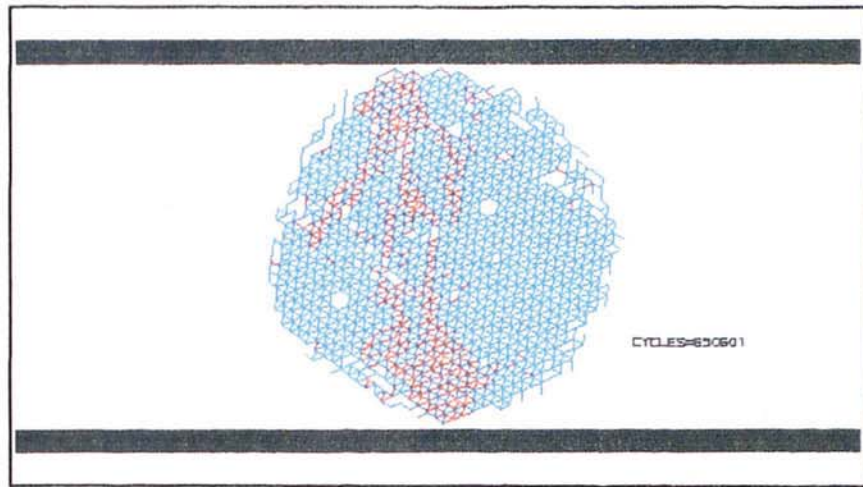
Figure 6.9d Equivalent space lattice at 0.076% strain
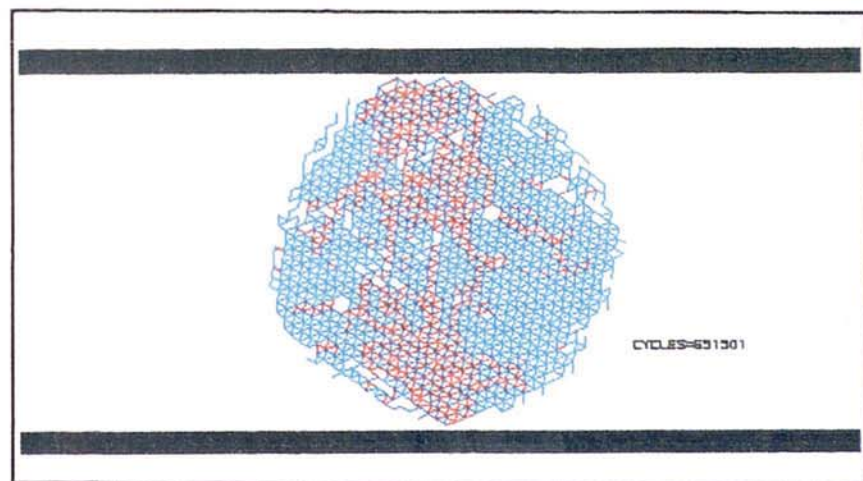
Figure 6.9e Equivalent space lattice at 0.213% strain

194
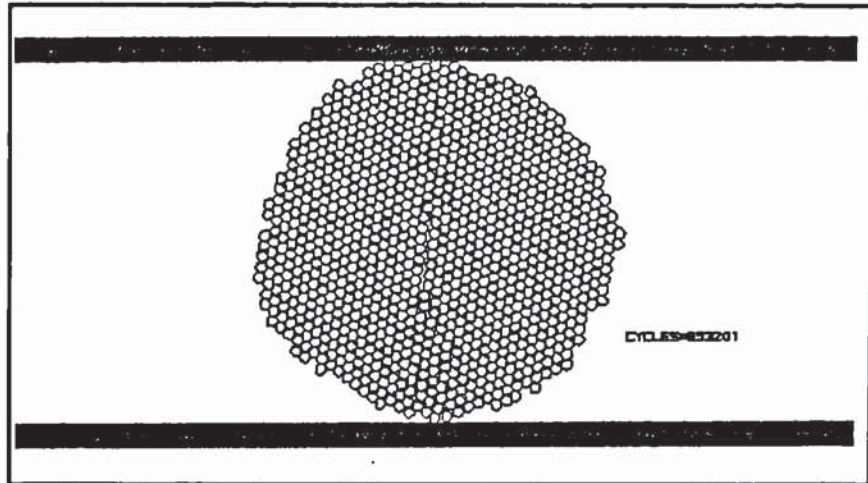
Figure 6.10a Particle layout at 0.47% strain with a fine longitudinal void area along the loaded diameter
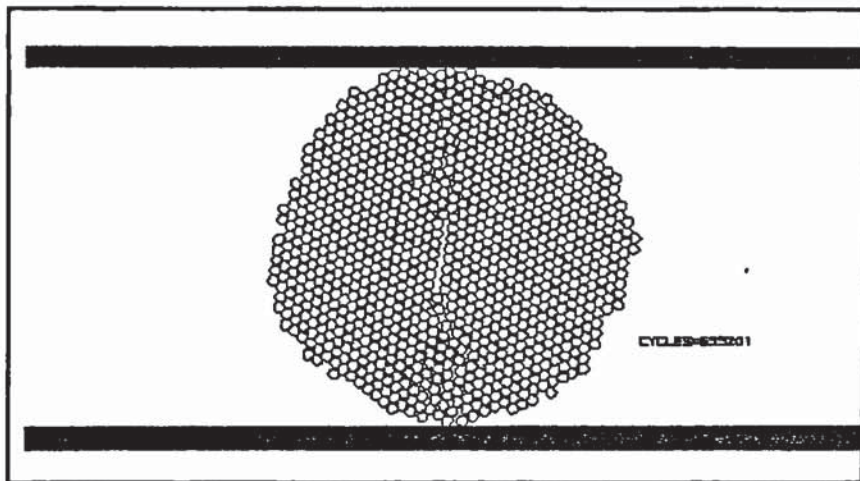
Figure 6.10b Particle layout at 0.77% strain with the longitudinal void area extending towards the platens and widening
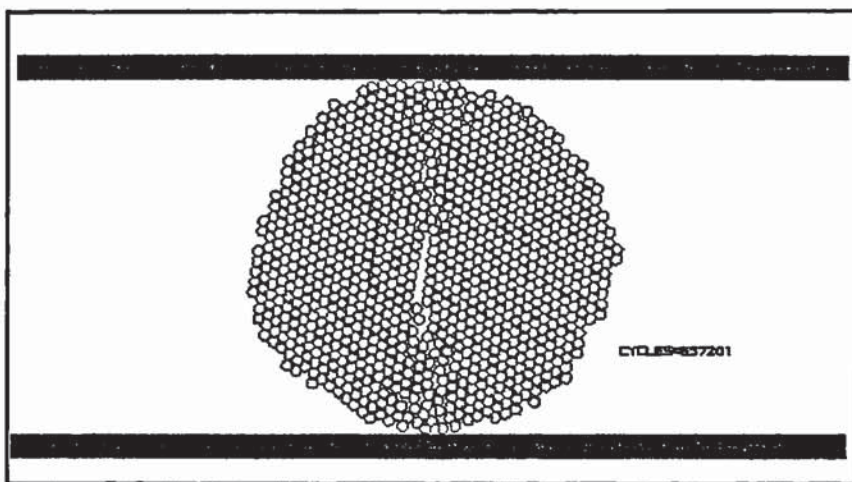
Figure 6.10c Particle layout at 1.08% strain with a central void core

195
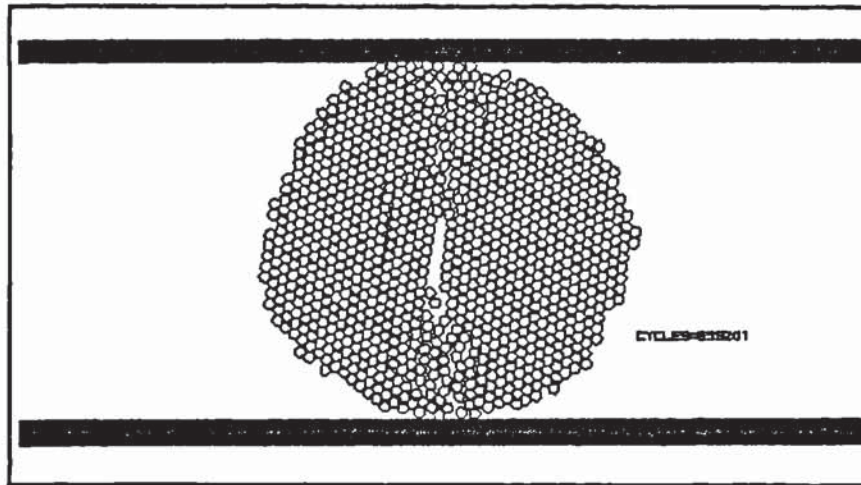
Figure 6.10d Particle layout at 1.38% strain with localised crushing near the platens and a central void area
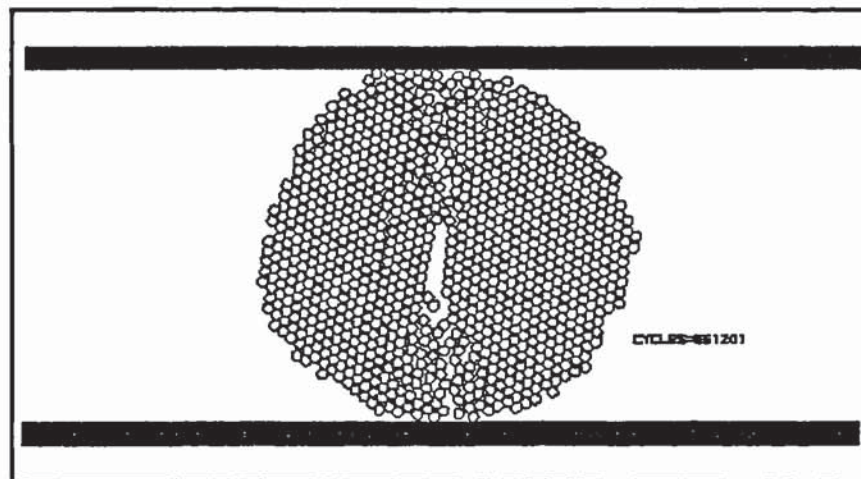
Figure 6.10e Particle layout at 1.69% strain with further increment in the central void area
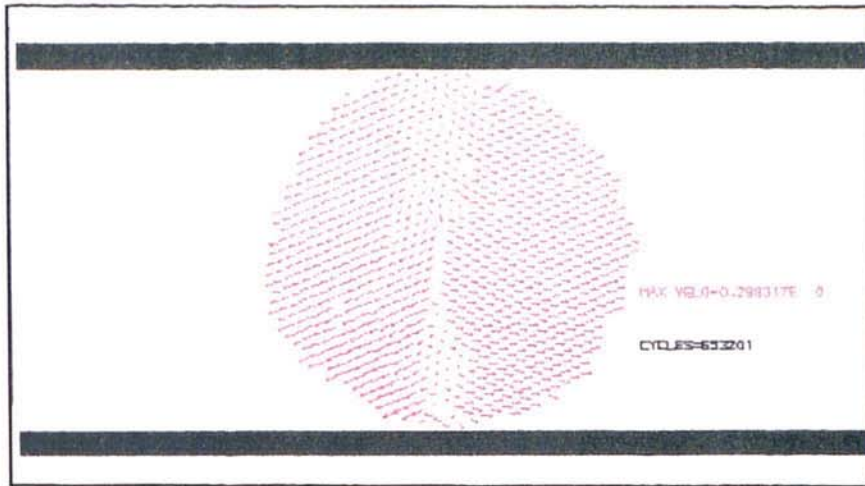
Figure 6.11a Velocity distribution at 0.47% strain
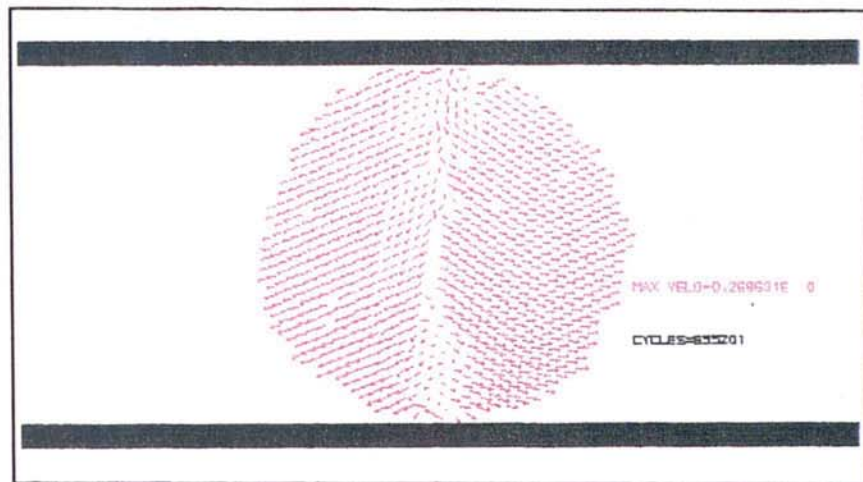
Figure 6.11b Velocity distribution at 0.77% strain
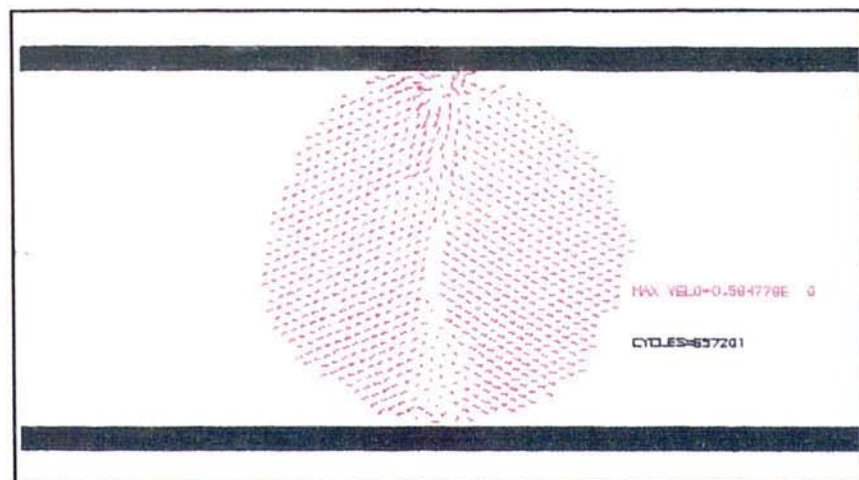
Figure 6.11c Velocity distribution at 1.08% strain
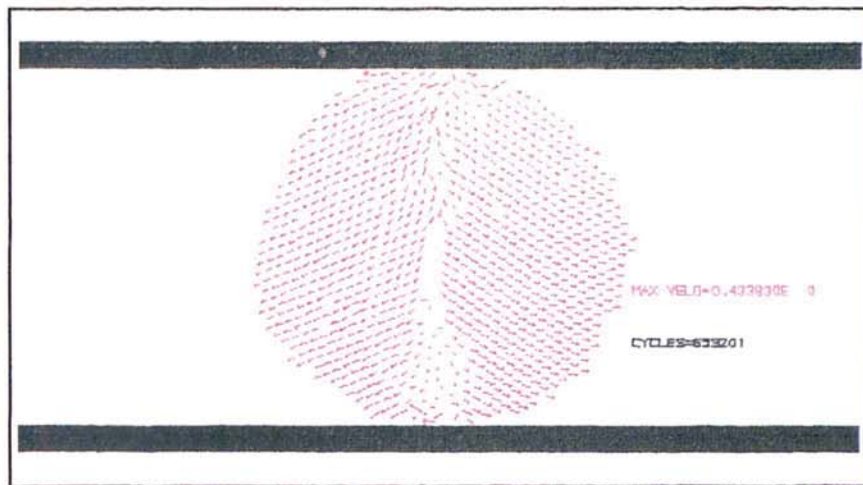
Figure 6.11d Velocity distribution at 1.38% strain
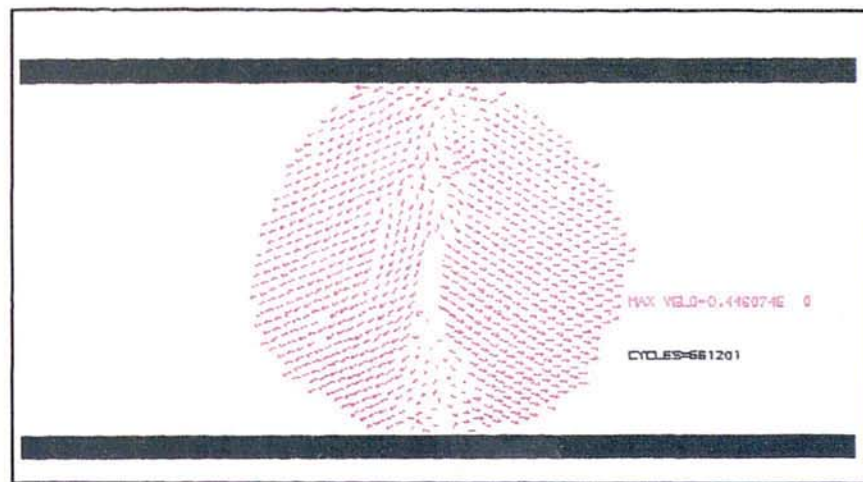
Figure 6.11e Velocity distribution at 1.69% strain

Figure 6.12a shows the evolution of the forces generated at the platens. The force evolution is similar for both the upper and lower platens. During the loading stages, as described in the previous chapter, the formation of localised plastic deformation zones is observed as shown by figure 6.9a. When the maximum platen loads are reached at a strain of 0.045%, a short crack is observed to have formed at the centre of the agglomerate. Though not shown in any of the figures provided in the thesis, detailed examination of the computer graphics showed that for all values of γ cracks always propagated from the plastic deformation zones towards the centre. As the load on the platens decrease, a central crack connecting each of the plastic deformation zones is clearly visible, figure 6.9c.

The total work done by both platens is observed to increase at a decreasing rate until a maximum is reached at approximately 0.25% strain, figure 6.12b, where the platen loads have reduced to zero. The evolution of work done is similar for both platens, the difference in the maximum work done being of the order of 5%. This is due to local differences in the structure of the agglomerate due to the initial random arrangement.

Figure 6.12c shows the evolution of contacts under the influence of diametrical loading. During the initial stages, the compressive contacts increase with a corresponding decrease in the number of tensile contacts, therefore maintaining the total number of contacts present. The number of compressive contacts effectively start to decrease gradually after the maximum force has been attained and the reverse is also seen for the tensile contacts. The initial damage ratio, as defined in chapter 5, is taken as the final number of contacts deleted divided by the initial number of contacts.

6.4.2 High Strain-rate Results

When a high strain-rate of $150s^{-1}$ was used the behaviour was different from that reported in the previous section. For the high strain-rate case, both platens approached each other at a relative velocity of 1.0 m/s. Figure 6.13 (a to e) shows the force
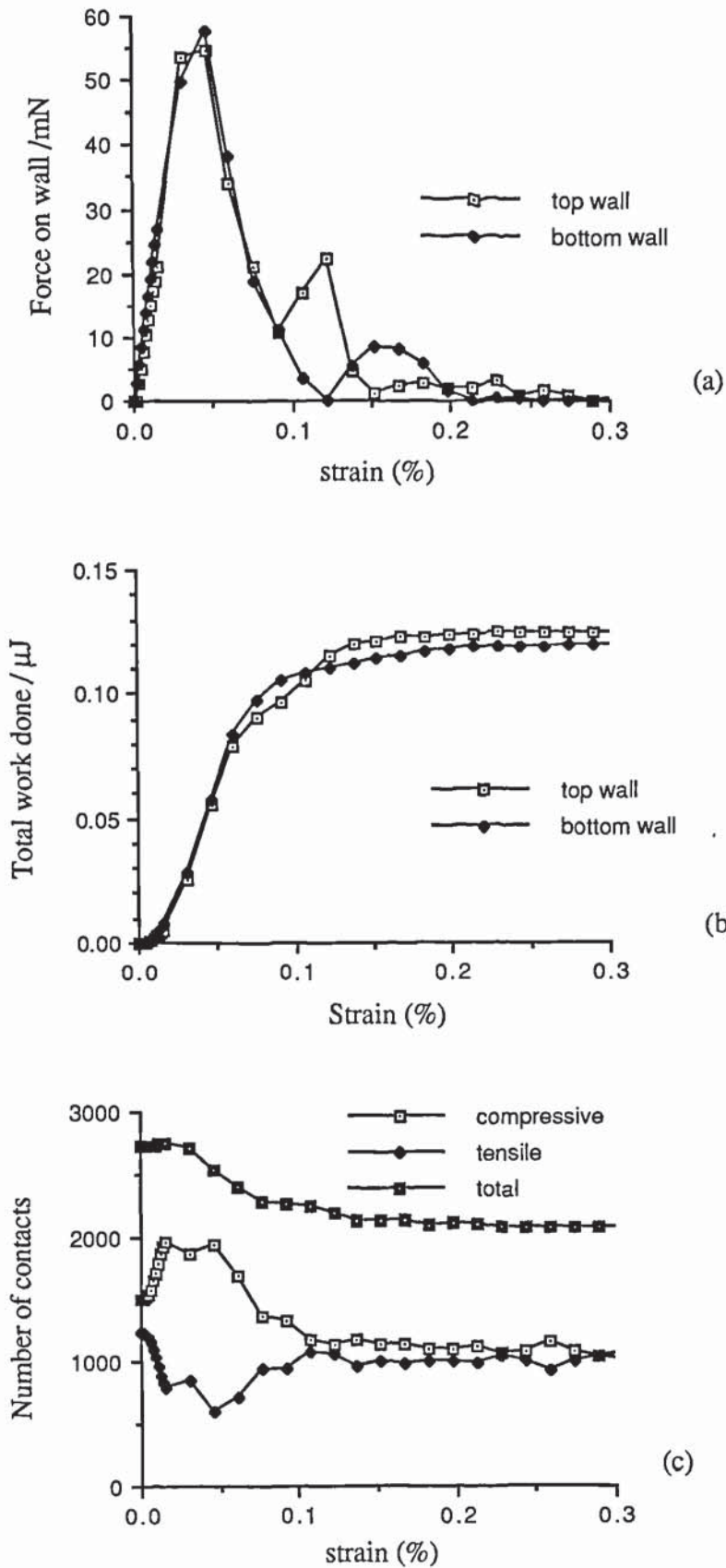
Figure 6.12 Evolution of a) force on platens, b) total work done by platens, and c)number of contacts

distribution under the influence of the two loading platens for the different stages of diametrical strain. Figure 6.13a shows the development of two fan shaped compressive zones as the wave from each platen propagates through the agglomerate. Figure 6.13b shows that, at a strain of 0.06%, the two fan shaped compressive zones have almost met. More contacts have been broken as a result of the higher compressive wave amplitude but there is still no evidence of any clear crack path as observed in figure 6.7c. Figure 6.13 (c and d) show a higher proportion of compressive to tensile contacts, 87% and 88% for strains of 0.106% and 0.152% respectively. This high proportion of compressive contacts within the assembly suggest that, if the mechanism is the same as observed in the impact tests, there are a large number of sliding contacts and significant plastic deformation has occurred. The tensile contacts remaining are approximately orientated at right angles to the loaded diameter of the agglomerate. The last figure, figure 6.13e shows the force distribution just before the loading of the platens had ceased.

Figure 6.14 (a to e) show the current locations of sliding contacts. In the initial stage, figure 6.14a shows that, at a strain of 0.03%, two very localised zones of sliding have occurred within the compressive regions shown in figure 6.13a. As the strain is increased, the regions of sliding locations increase with the propagation of the compressive wavefronts, figure 6.14b. Outside these well defined zones there is no evidence of sliding, suggesting that the initial propagation of these waves has not yet extended to cover the entire agglomerate. At a strain of 0.106%, sliding locations dominate the entire loaded diameter, figure 6.14c, suggesting extensive plastic deformation zones. When the wall loading is a maximum, most contacts are sliding, figure 6.14d. Subsequently, sliding is observed to decline gradually as the wall forces decrease, figure 6.14e.

The corresponding space lattice plots of the assembly are shown in figures 6.15 (a to e). When the strain is approximately 0.03%, figure 6.15a shows two regions of plastic
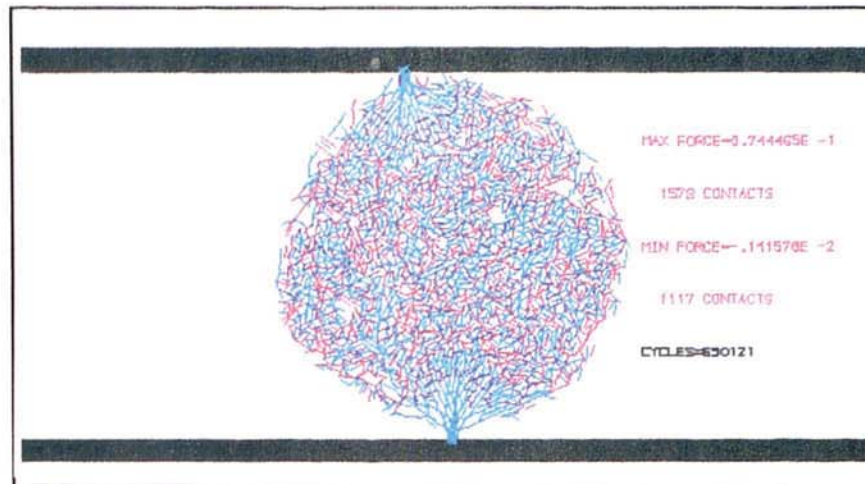
Figure 6.13a Distribution of contact forces at 0.03% strain with two fan shaped compressive zone
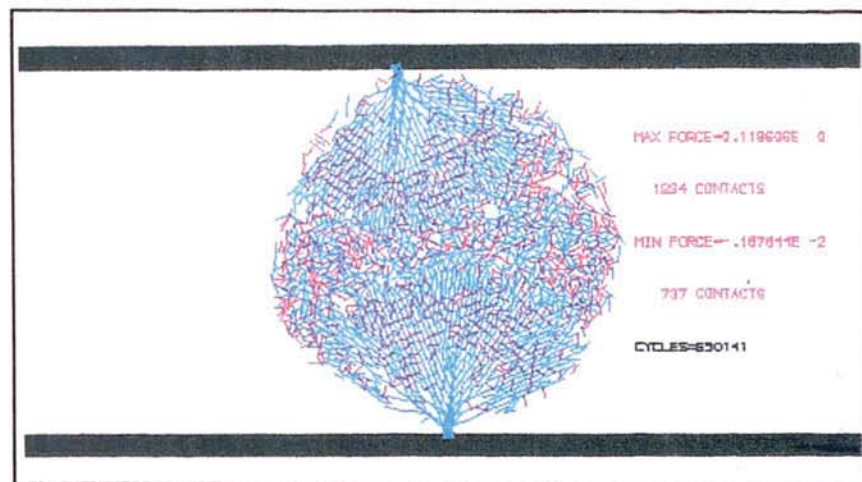
Figure 6.13b Distribution of contact forces at 0.06% strain as compressive wave is propagating
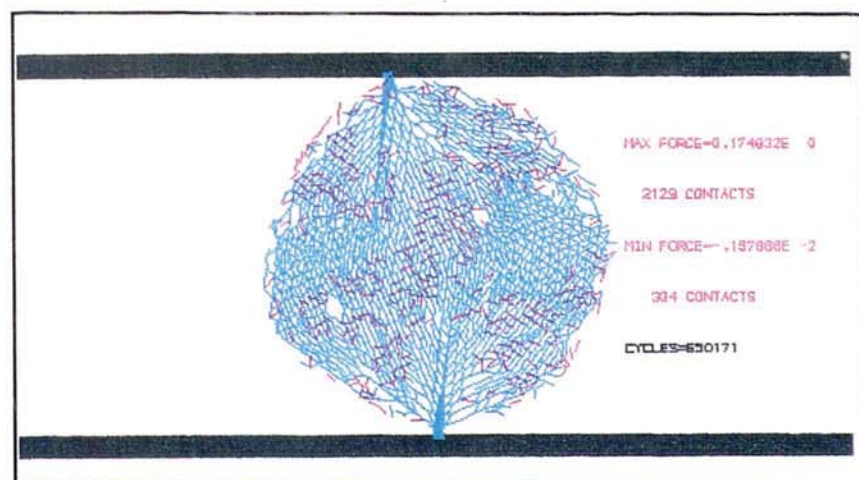
Figure 6.13c Distribution of contact forces at 0.106% strain, mainly compressive
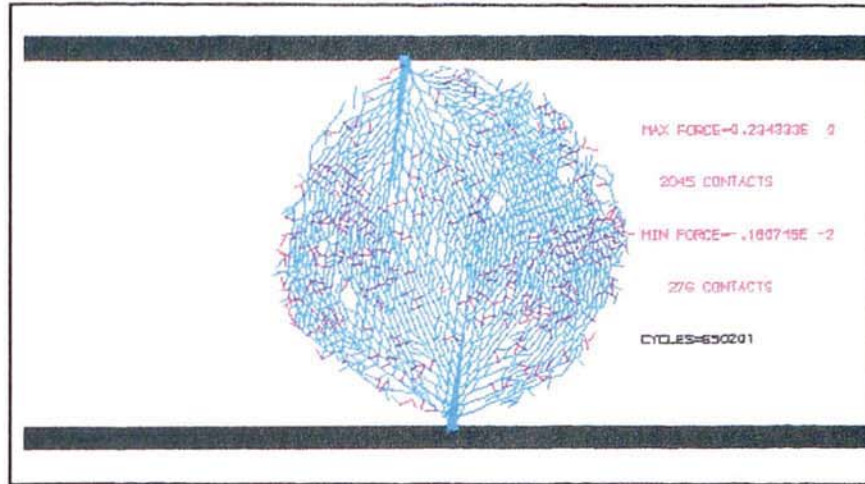
Figure 6.7d Distribution of contact forces at 0.152% strain
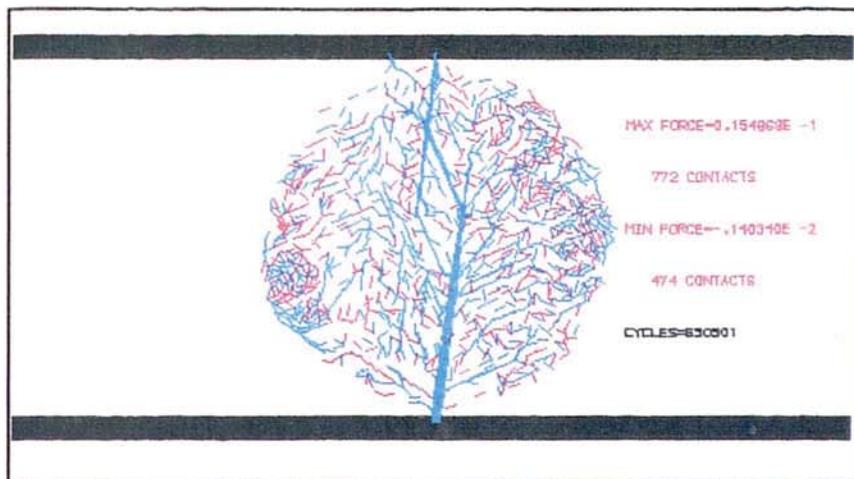
Figure 6.13e Residual contact forces at 0.609% strain
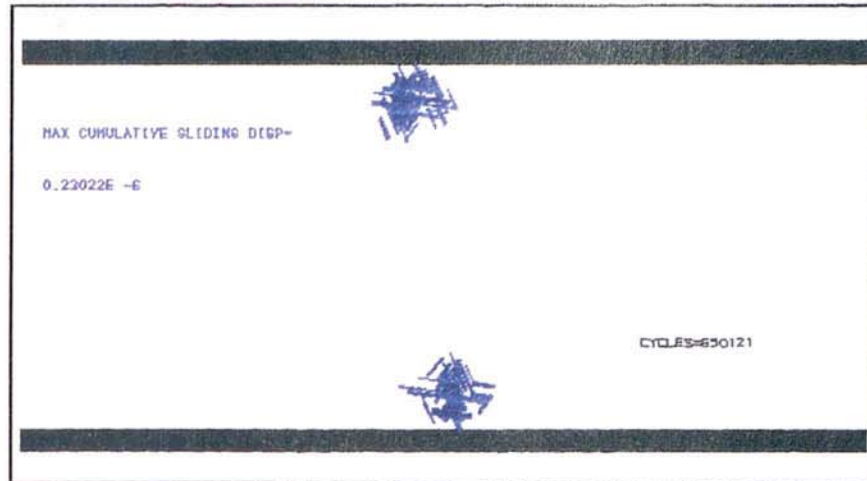
Figure 6.14a Sliding contacts at 0.03% strain
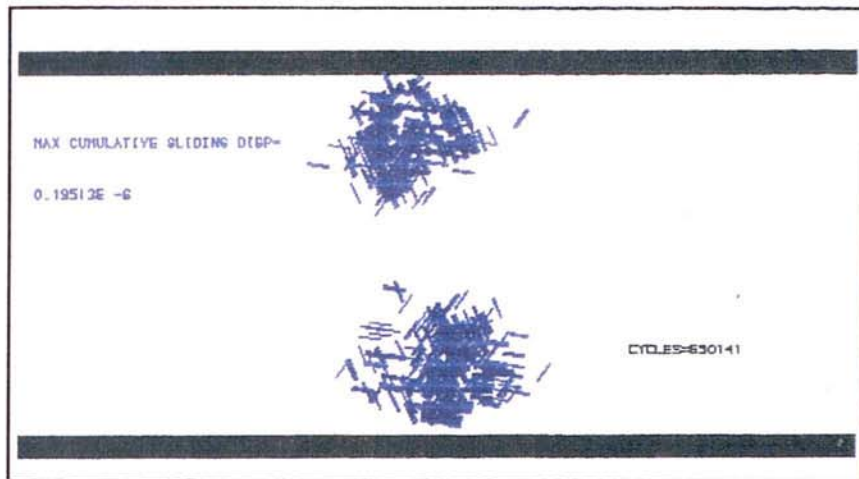
Figure 6.14b Sliding contacts at 0.045% strain
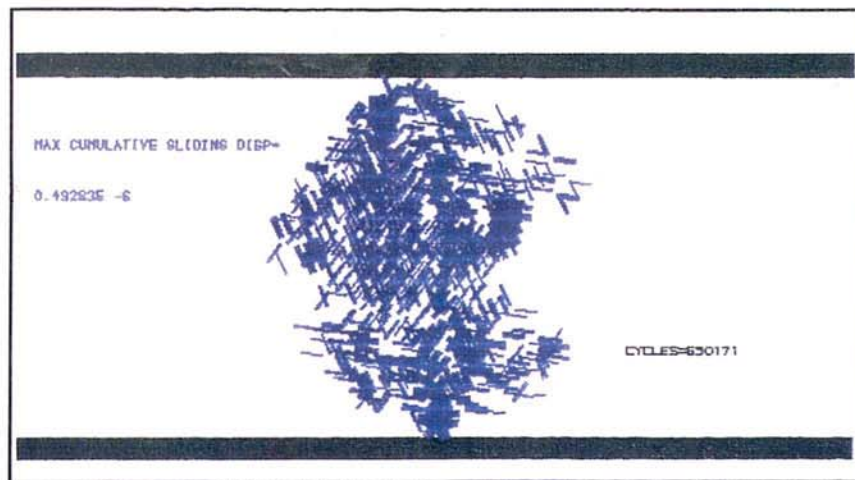
Figure 6.14c Sliding contacts at 0.106% strain
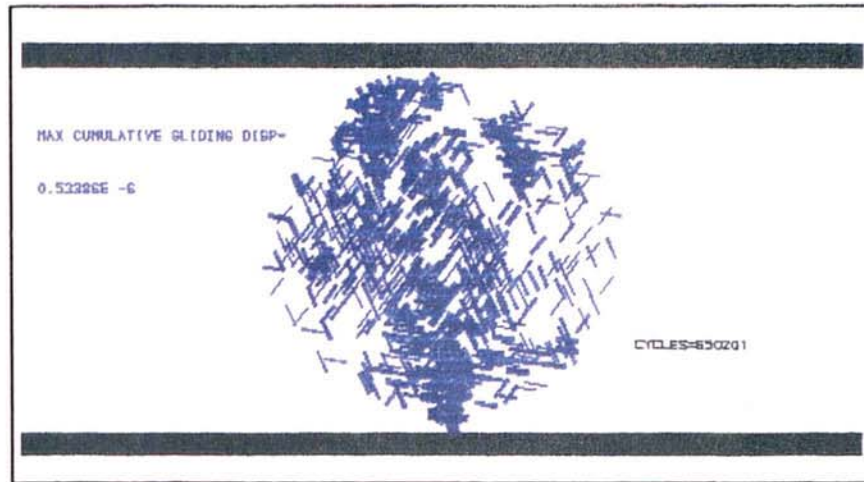
Figure 6.14d Sliding contacts at 0.152% strain
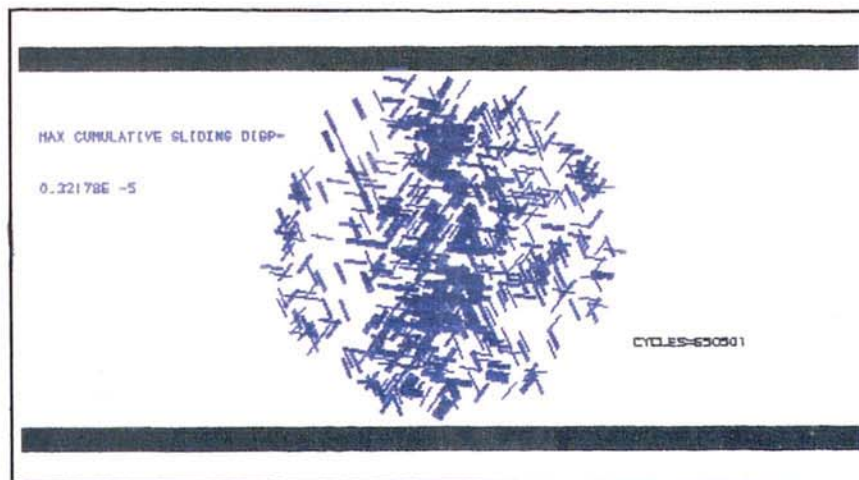
Figure 6.14e Sliding contacts at 0.609% strain

deformation located adjacent to each of the loading platens. Further increments of strain lead to the enlargement of these plastic deformation zones, figure 6.15b, without any evidence of crack formation. The rest of figures 6.15 show the merging of the two plastic deformation zones as straining continues. High strain-rate loading produced extensive plastic deformation zones, figure 6.15e, suggesting the likelihood of crushing rather than tensile failure.

The ball plots, figures 6.16 (a to e) give a visual appreciation of the behaviour of the agglomerate in the final stages of the simulation. At a strain of 0.609%, figure 6.15e, there is a large number of contact deletions and therefore at a strain of 2.434%, figure 6.16a, most of the contacts will inevitably be broken. Due to the initial formation of extensive plastic deformation zones, most particles are now in the form of singlets and are free to move when subjected to further strain. Local crushing adjacent to the platens is observed at this stage. A few fracture lines are also visible through the ball plot. Figures 6.16 (b and c) show significant flattening of the agglomerate adjacent to the platens and the gaps in the centre of the agglomerate have widened. Figures 6.16 (d and e) illustrate the subsequent crushing of the agglomerate. It can be seen from figure 6.16e that in addition to further flattening adjacent to the platens the agglomerate is grossly distorted. The asymmetric shape observed in figure 6.16e may be attributed to the initial asymmetry of the main load transfer paths, as seen in figure 6.13. The corresponding velocity plots are shown in figures 6.17(a to e). In all these figures, the velocity vectors are reasonably uniformly distributed in two separate regions and clearly illustrate a vertical fracture zone.

Figure 6.18 shows the evolution of the forces generated at the platens, the external work done and the number of contacts in the agglomerate. The results are qualitatively similar to the low strain-rate test results, figure 6.12. A quantitative comparison between the two figures, however, indicates that, in the high strain-rate test, the maximum platen force generated was 4 times higher, the maximum external work done

206
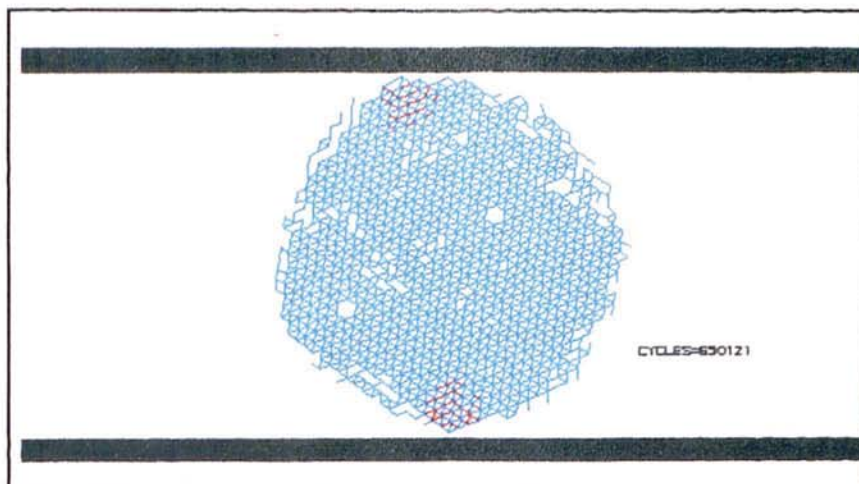
Figure 6.15a Equivalent space lattice at 0.03% strain
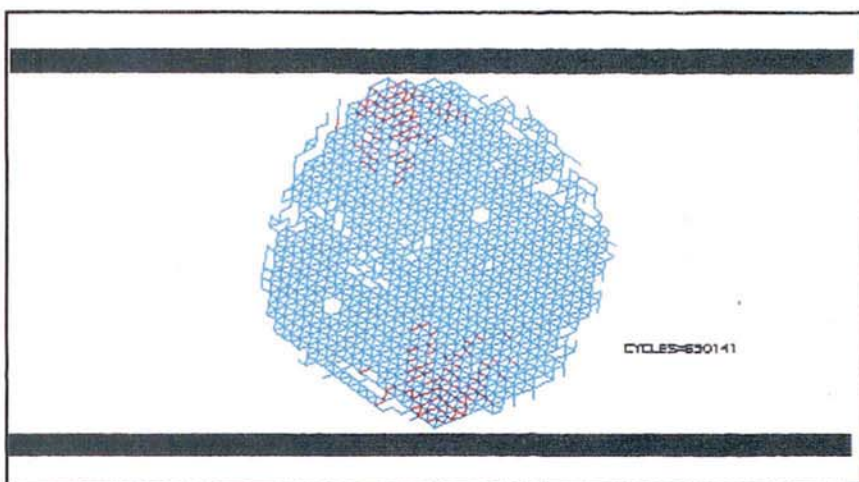
Figure 6.15b Equivalent space lattice at 0.06% strain
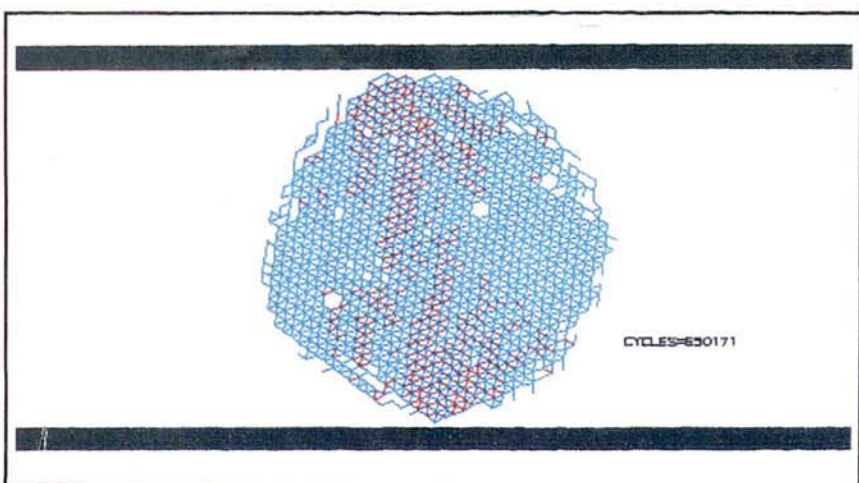
Figure 6.15c Equivalent space lattice at 0.106% strain
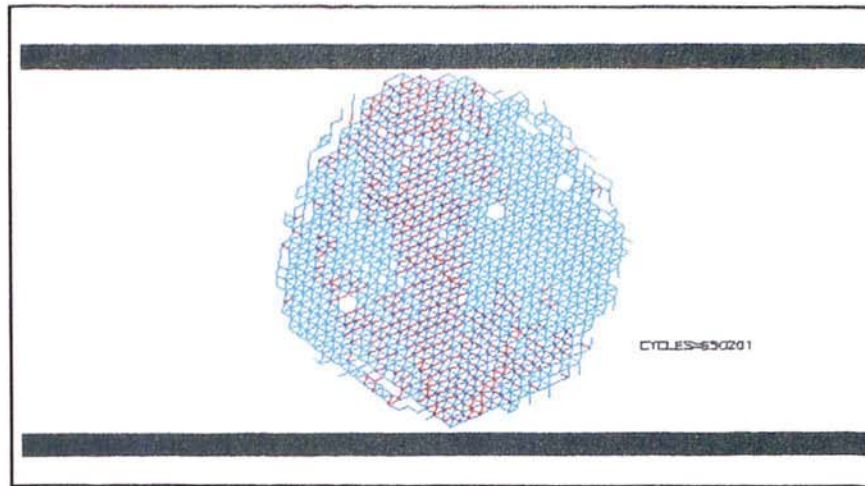
Figure 6.15d Equivalent space lattice at 0.152% strain
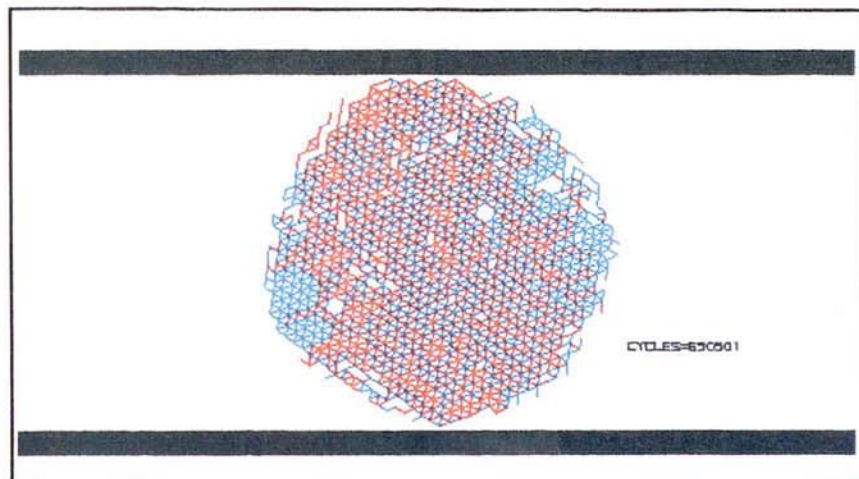
Figure 6.15e Equivalent space lattice at 0.609% strain
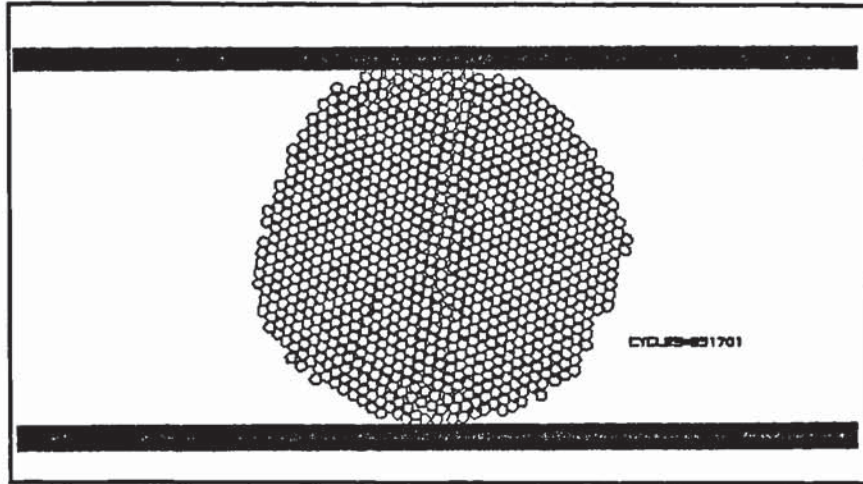
Figure 6.16a Particle layout at 2.434% strain
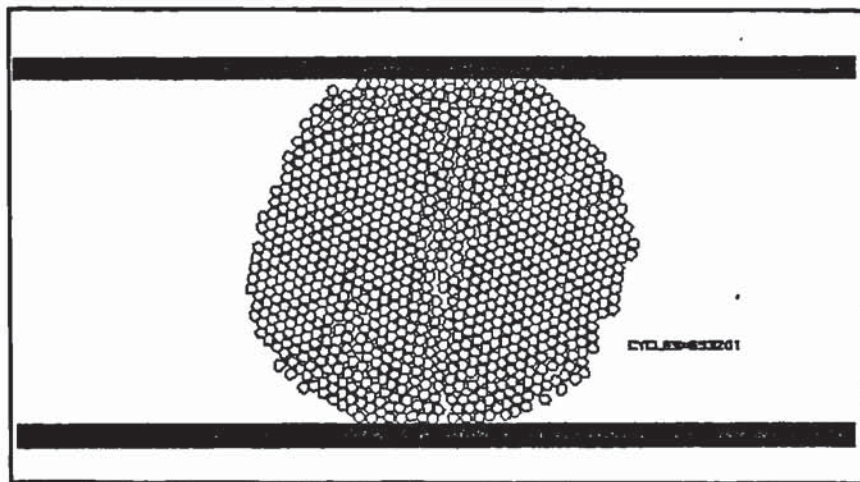
Figure 6.16b Particle layout at 3.195% strain
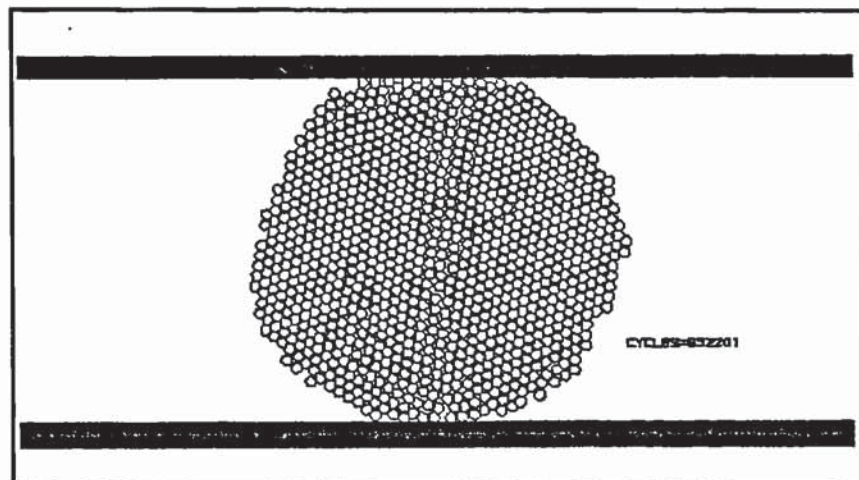
Figure 6.16c Particle layout at 4.716% strain
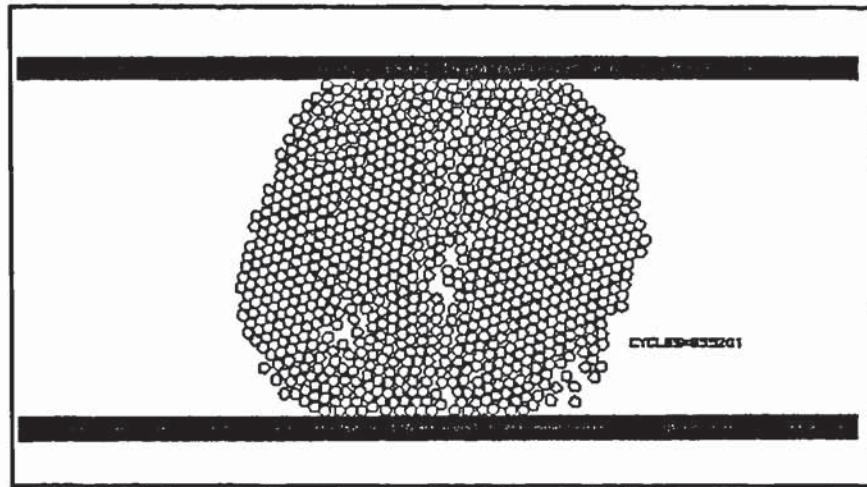
Figure 6.16d Particle layout at 6.237% strain with the agglomerate approaching geometrical distortion
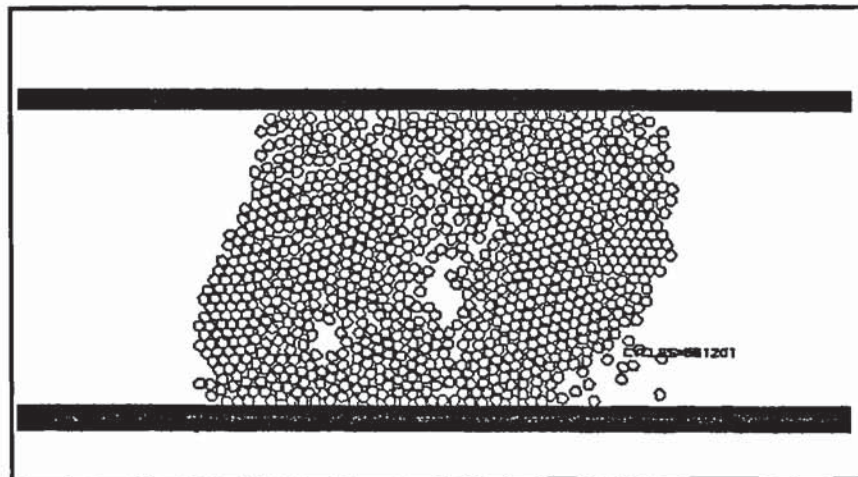
Figure 6.16e Particle layout at 16.886% strain with the agglomerate essentially distorted
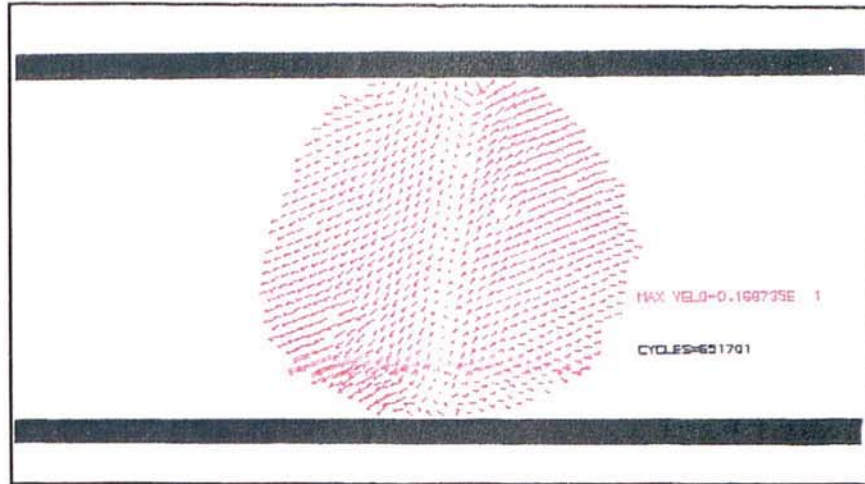
Figure 6.17a Velocity distribution at 2.434% strain
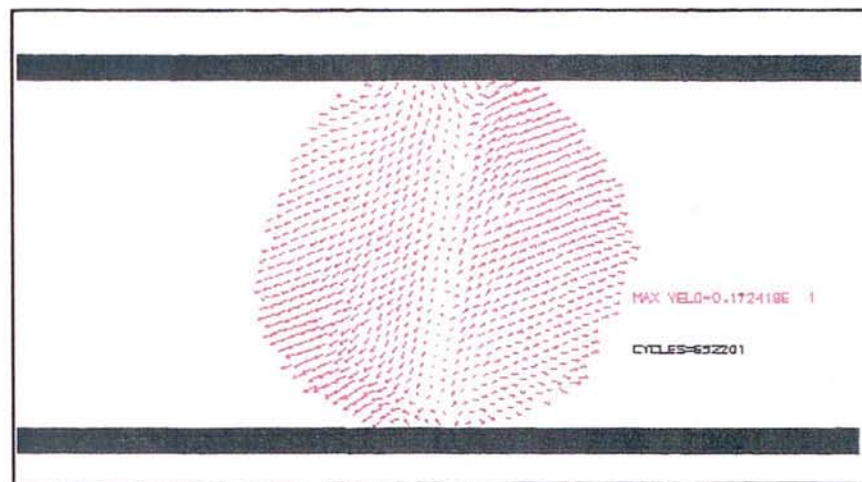
Figure 6.17b Velocity distribution at 3.195% strain
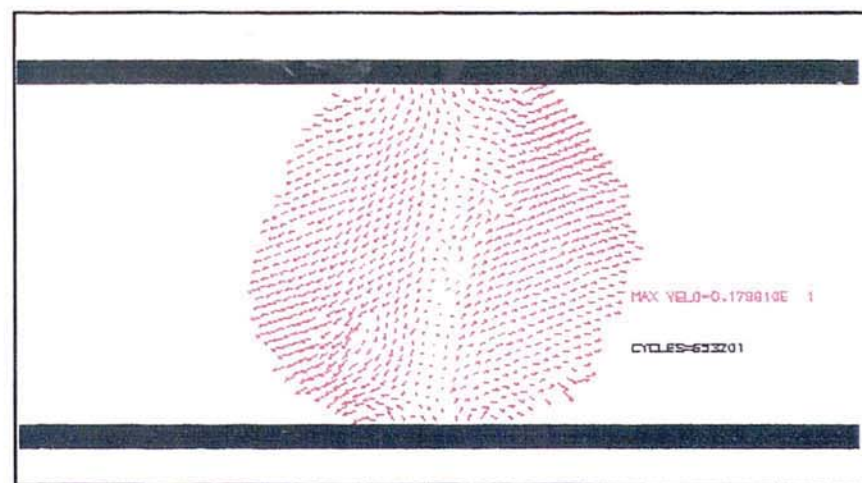
Figure 6.17c Velocity distribution at 4.716% strain
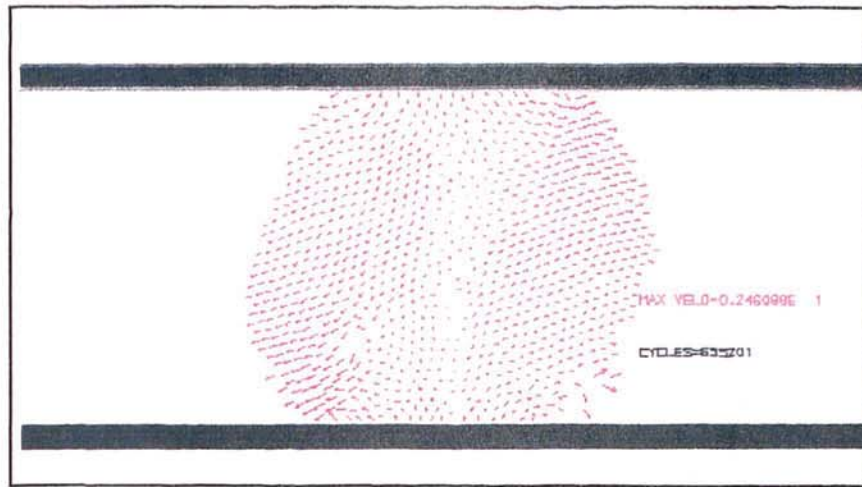
Figure 6.17d Velocity distribution at 6.237% strain
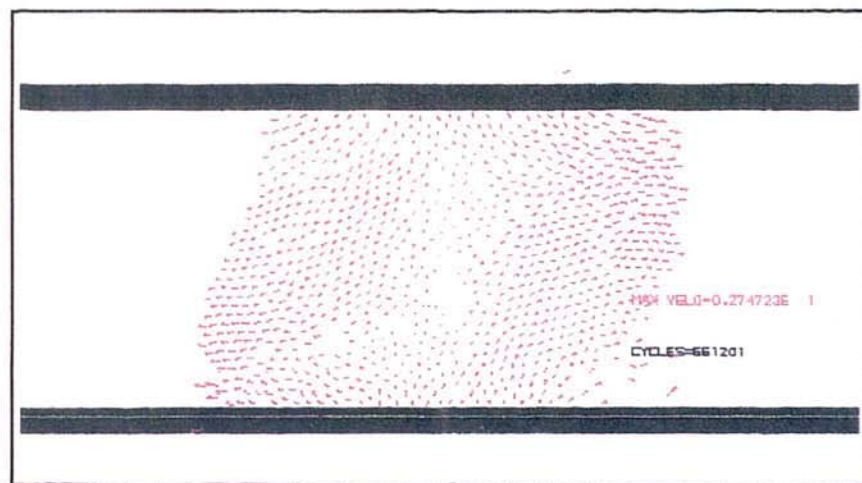
Figure 6.17e Velocity distribution at 16.886% strain
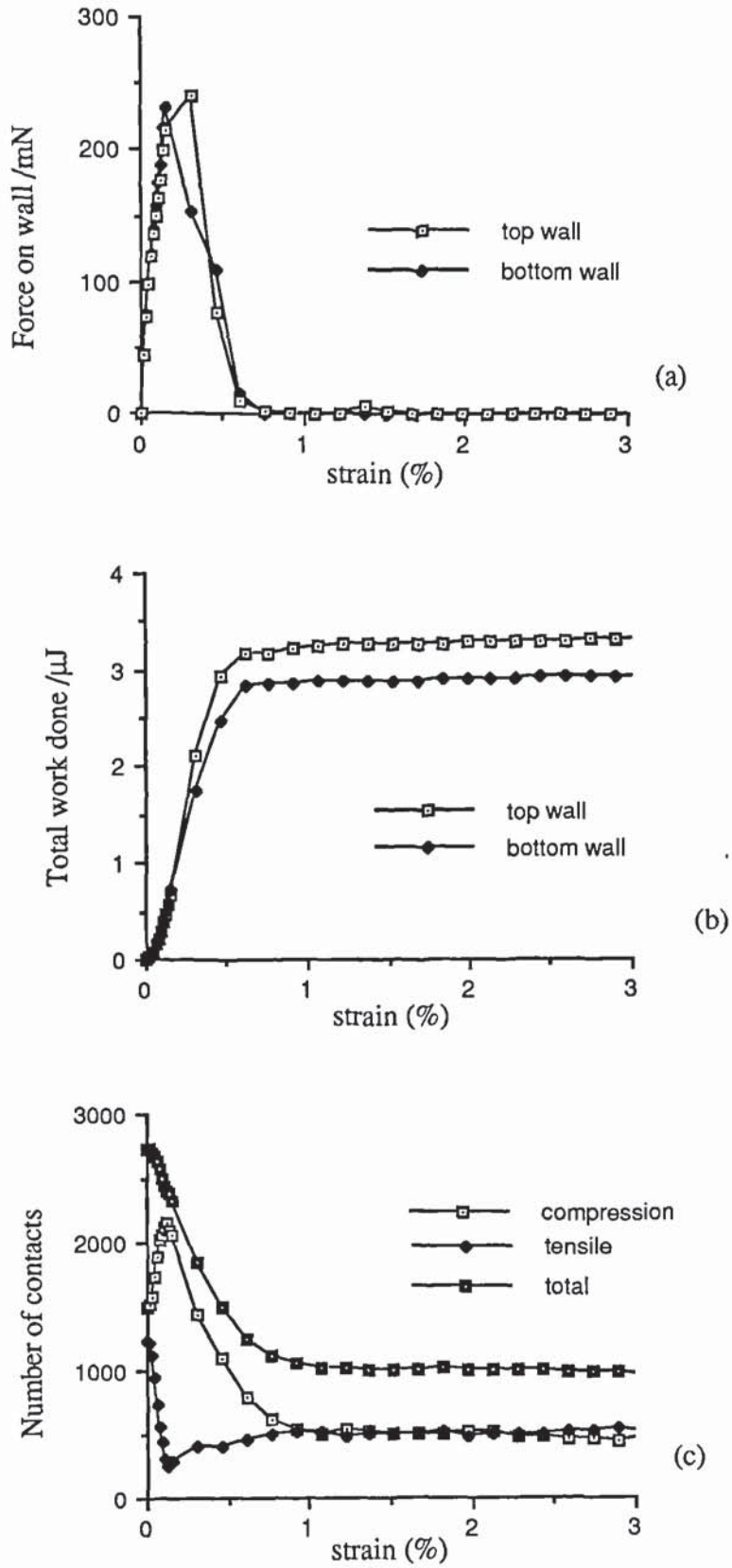
Figure 6.18 Evolution of a) force on platens, b)total work done by platens, and c) number of contacts

was 25 times higher and approximately 3 times the number of contacts were broken. It is clearly the much higher forces propagating through the agglomerate that lead to extensive plastic deformation and subsequent crushing of the agglomerate
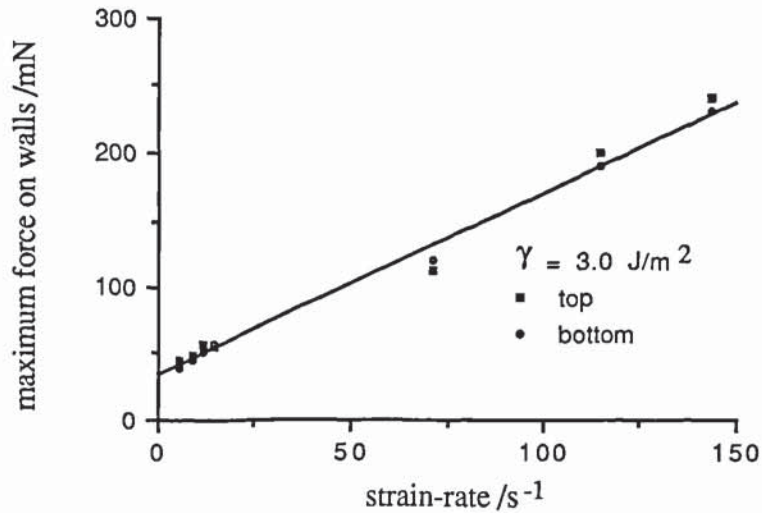
Figure 6.19 Effect of strain-rate on maximum platen force

From the series of simulations performed at different strain-rates, the maximum load at each of the platens was obtained and plotted against the imposed strain-rates, figure 6.19. It can be seen that higher strain-rates generate higher platen forces and the relationship is linear. As described in the preceeding section, high strain-rates result in extensive plastic deformation within the agglomerate and subsequent crushing. This type of failure mechanism does not conform to the tensile failure assumed in the traditional interpretation of the diametrical compression test. Consequently, the conventional calculation of the tensile strength, Hondros (1959)

$$\sigma_T = 2P/\pi Dt \qquad (6.7)$$

is not appropriate for high strain-rate diametrical compression tests. The alternative interpretation of Rumpf (1962) given by equation (6.1) assumes an instantaneous tensile crack is formed and, therefore, is also not relevant to the interpretation of the high strain-rate results. Even at low strain-rates, which produce semi-brittle failure,

214

figure 6.19 shows that the maximum forces developed at the platens are strain-rate dependent. Consequently, if the results of the low strain-rate tests are analysed using equation (6.7), this would imply that the tensile strength of the agglomerate was strain-rate dependent. It should be noted that none of the computer simulated diametrical compression tests induced a true tensile failure in the agglomerate. Consequently it is necessary to consider an alternative method of relating the observed behaviour in the diametrical compression tests to the observations of agglomerate impacts described in chapter 5.

Results obtained for the surface energies of 0.3, 1.0 and 2.0 Jm^{-2} exhibited the same strain-rate dependence as shown in figure 6.19. Appendix C provides details of all the diametrical compression test carried out in this research project. For all cases the space lattice plots at maximum wall force and at zero wall force are provided together with the evolutions of wall forces, work done and number of contacts in the agglomerate.

6.5 Damage Analysis

In the previous chapter results of the computer simulated agglomerate impacts were reported. It was shown that the initial damage produce by an agglomerate collision could be quantified by the damage ratio defined as the ratio of the number of contacts broken to the total number of contacts existing before the impact. In a similar way a damage ratio can be determined for the simulations of diametrical compression using the number of contacts broken when the external work done has reached a constant value and the forces generated at the platens have decreased to zero.

Figure 6.20 shows the dependence of the damage ratio on the work input obtained from agglomerate impact tests and diametrical compression tests. In the case of the impact tests the work input is the initial kinetic energy, while for the diametrical compression tests the work input is the total work done by the forces on the platens. As observed

215

from figure 6.20, the results are in good agreement with each other except for the results shown for the case of $\gamma = 0.3$ Jm^{-2} for which the agreement is not quite as good.

An alternative way of comparing the data obtained from the two different types of test is shown in figure 6.21. In the figure the results of the impact tests are plotted against impact velocity and the Brazilian test results are plotted against the relative velocity of the platens. It can be seen that there is good agreement between both sets of simulations for all three cases.

More computer simulation need to be performed, using different agglomerates, before it is clear which of the two comparisons shown in figures 6.20 and 6.21 is more reliable. Similar laboratory experiments on real agglomerates also need to be carried out to test the validity of the computer simulated results. In real experiments the platen velocities are easily obtained but careful testing is necessary to accurately determine the total work done. The major problem in laboratory diametrical compression tests is the inability to accurately assess the damage ratio as defined in this thesis. However, it was shown in Chapter 5 that the fragmentation data obtained from the impact simulations, e.g. grading curve, largest cluster size, percentage of singlets, can be related to the damage ratio. It may be possible in real experiments to relate Brazilian test data to impact data by replacing the damage ratio parameter used in figures 6.20 and 6.21 by an equivalent parameter obtained from the particle size distribution curves of the broken agglomerates.
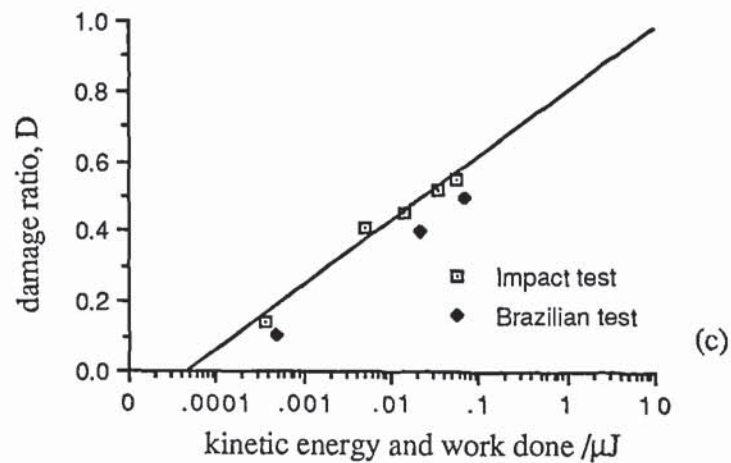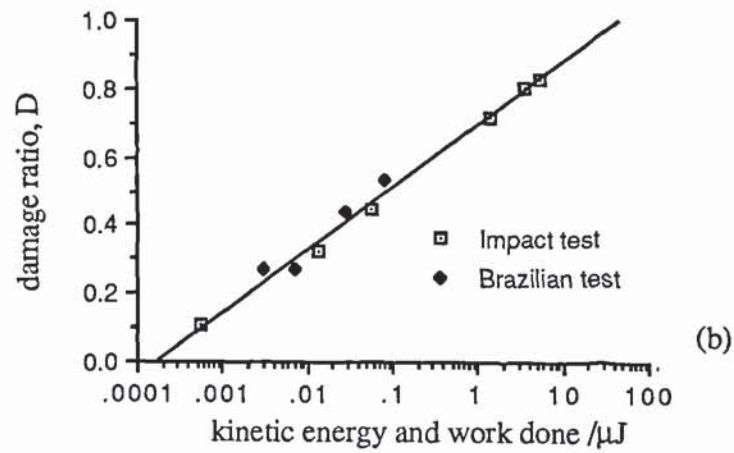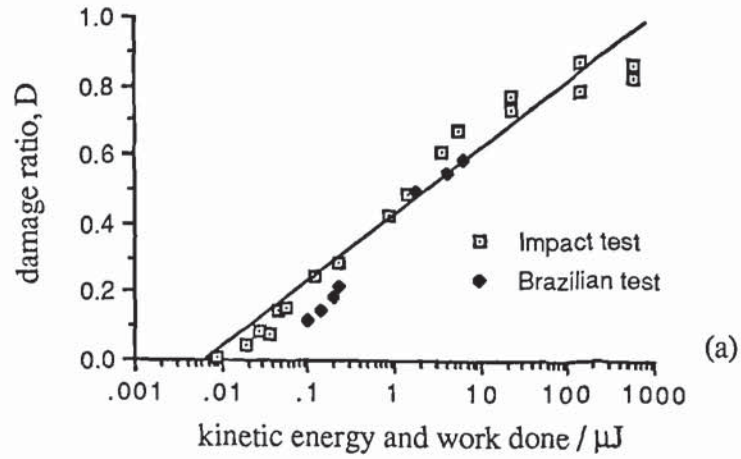
Figure 6.20 Damage ratio, D, against work input for agglomerate of surface energy a) 3.0Jm^{-2}, b) 1.0Jm^{-2}, and c) 0.3Jm^{-2}
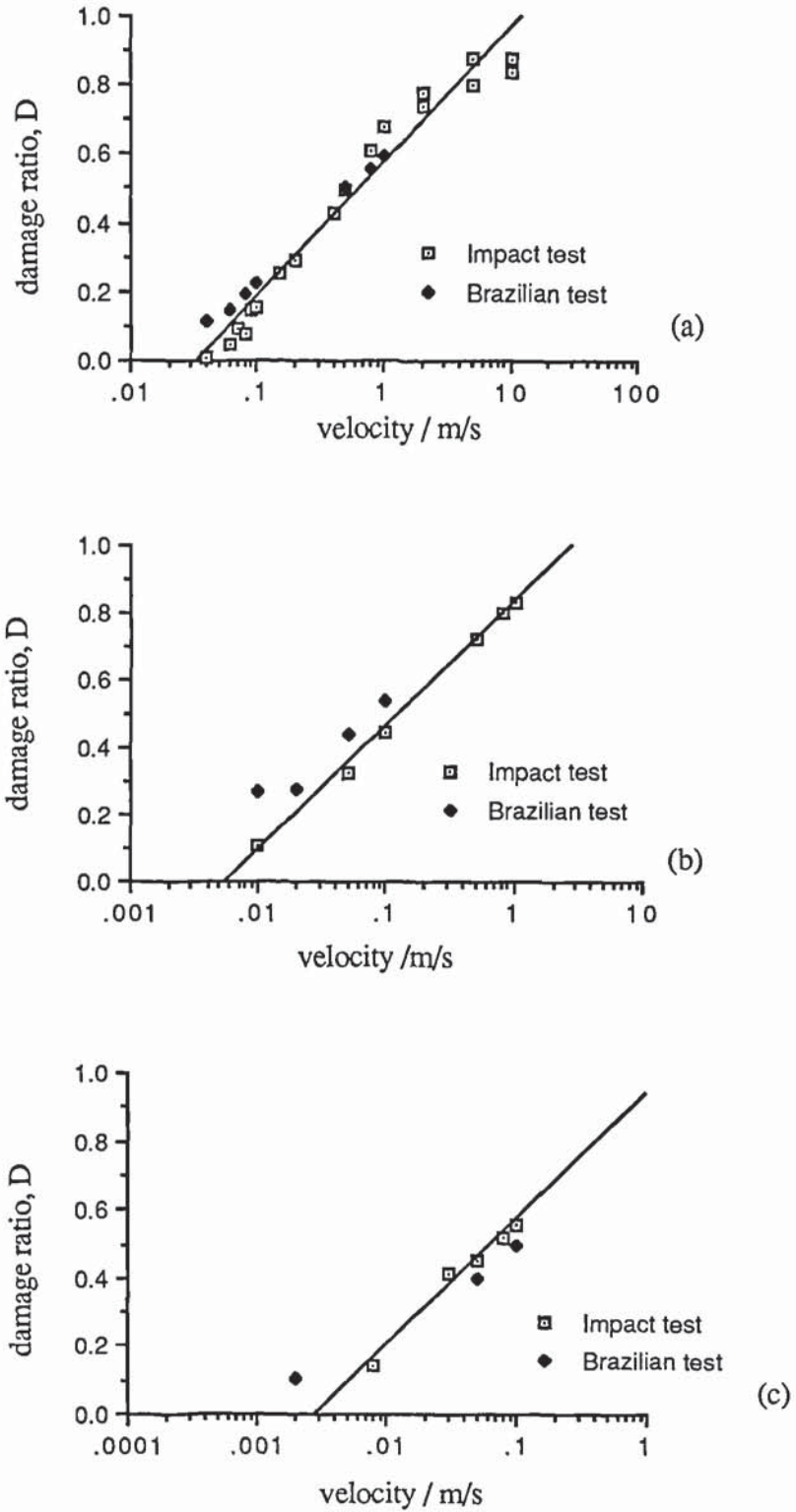
Figure 6.21 Damage ratio, D, against velocity for agglomerate of surface energy a) 3.0 Jm^{-2}, b) 1.0 Jm^{-2}, and c) 0.3 Jm^{-2}

7. Concluding Remarks

Enough research will tend to support your theory

7.1 Introduction

A conclusion is made when the author gets tired of analysing and a final attempt is made to resolve any previous contradictory comments or questions that may be expected. The delicate task of trying to develop a concluding chapter is further complicated by having to support, believe and defend computer simulated behaviour. In itself, presenting computer simulation results to a world of cynics is like trying to explain the term 'quarks' or forwarding the theory of quantum mechanics in its early days. Of course, nobody can doubt that putting computer simulation on equal par with the theory of quantum mechanics is a preposterous analogy but few can deny the problems faced by both, in their attempt to gain recognition and general confidence.

The following section attempts to summarise the main findings and achievements of the research programme. This is followed by a consideration of the current limitations and possible future work. Some concluding remarks are added to complete the chapter.

7.2 Summary

In order to simulate an agglomerate it was necessary to adapt the program BALL to model the effect of adhesion at the interparticle contacts. New interaction laws were developed to model the normal contact stiffness according to the theory of Johnson et al (1971) and the tangential contact stiffness according to the theories of Savkoor and Briggs (1977) and Thornton (1991). These theories were described in Chapter 3 and a description of the main alterations to the computer code was provided in Chapter 4. The application of the program to oblique impacts between two identical spheres, with and without adhesion, was demonstrated in Chapter 3 and Chapter 2 respectively.

It has been shown that, following an oblique impact, the rebound angle, velocity and particle spin are all functions of the total history of the impact duration. The energy

dissipated and changes in both linear and rotational kinetic energy are significant and are complex functions of the impact angle. The computer simulation results also show that, although adhesion has some effect on the dissipation and redistribution of energy for all angles of impact, the effect is most pronounced when tangential peeling is only completed at the end of the impact. The angles of impact at which this occurs depend on the impact velocity. For all impact angles, if the impact velocity is not large enough to complete the peeling process when the normal force is increasing, then the particles will either stick together or rebound back along the initial impact trajectory. This observation needs to be checked by real experiments.

Computer simulated results have been presented of a 2D monodisperse agglomerate consisting of 1000 primary particles impacting orthogonally with a wall. Although the conclusions drawn from the work carried out are strictly applicable only to the 2D behaviour of a dense monodisperse system, it is believed that the observations drawn will also be qualitatively correct for real 3D agglomerates.

A threshold velocity exists for a specific agglomerate below which no significant damage occurs. This threshold velocity is an exponential function of the surface energy of the primary particles. Above the threshold velocity there are two regimes of behaviour. High velocity impacts result in shattering of the agglomerate while moderate velocities produce semi-brittle behaviour. The velocity transition from semi-brittle to plastic behaviour is exponentially dependent on the surface energy of the primary particles. A possible way of relating the various combinations of impact velocity and bond strength to the possible shattering, semi-brittle fracture, or quasi-elastic rebound behaviour has been presented.

Crack initiation and propagation is preceeded by the formation of a local plastic deformation zone. If this zone is extensive as in the case of in high velocity impacts, no clear crack formation will result. Instead, fragmentation into a large proportion of

220

singlets will result as demonstrated by the grading curve. The initial distribution of contact forces within the agglomerate is random due to the spatial distribution of contacts between adjacent particles. Therefore, it is difficult to predict the direction of any crack line that may develop during moderate velocity impacts. However, crack initiation (as far as the main crack is concerned) is observed to take place between the intersection of the boundary of plastic deformation and the chain of particles in line with the angle of impact. The tortuous crack pattern is the result of the geometric configuration of the individual particles.

The effects of the compressive wave propagating through the agglomerate observed in this research study agree with the observations of dynamic force transmission through photoelastic disc assemblies of Rossmanith et al (1982). Qualitatively, the simulated graphics show good agreement with the results obtained from the impact of cement-mortar spheres by Arbiter et al (1969) and of urea prills, Ghadiri (1991).

Results of computer simulated diametrical compression tests have also been reported. It was shown that the maximum wall load and the mode of breakage of the agglomerate were dependent on the nominal rate of diametrical strain. High strain-rates produced no evidence of cracks and resulted in crushing of the agglomerate. Low strain-rates produced the same type of semi-brittle fracture as observed in the moderate velocity impact simulations. Ghadiri (1990) described this type of fracture mechanism as "indentation fracture" and is similar to the failure mechanism assumed by Chen (1975) in his upper bound solution for the diametrical compression test. None of the computer simulated diametrical compression tests induced a true tensile failure according to the assumptions of the more traditional theories due to Hondros (1959) or Rumpf (1962).

An attempt has been made to compare the results of both the impact test and the Brazilian test simulations. Reasonable agreement was obtained by comparing the damage obtained in terms of both input energy and applied velocity. The latter case

221

may be more useful because it is easier to measure the velocity of the platens than to determine the work done in real experiments.

7.3 Limitations

Although the Distinct Element Method (DEM) is able to simulate the behaviour of granular materials, the main disadvantage is the amount of computing time or CPU time needed for each simulation. The amount of time is linearly proportional to the number of individual primary particles that make up the total system. Better statistical averages and more accurate spatial variations would be obtained if the number of particles were larger but that would require much greater CPU time. The program runs currently on a VAX 8650 (6.5 MIPS) along with other users on a time-share basis. When using a large complex program like BALL on a time-sharing system it is very difficult to predict how long it will take, in real time, to complete a planned series of simulations. Furthermore, due to the original half bit cells in the main array, the current program is incapable of handling information stored for anything more than 1000 particles (current maximum limit which takes up 57000 of a possible 65536 memory cells). However, this is not critical as half bit cells can be easily expanded to full bit cells, hence providing the maximum limit of 2.1 giga memory cells. There is however a crucial need for better computing 'power' preferably in a single user environment.

There are problems with graphical output. At present, the output relies on two colour plotters available in the university. The Digital LCG01 is an old plotter and although it provides better resolution, the colour is inconsistent and the rotating drum technique takes a long time to produce a single file (5 minutes). The second plotter, a Tektronix Colorquick, provides faster output but poorer resolution and smaller plot size. The graphics routines are supported by the GINO library but the capability of providing better graphics commands is limited. It is strongly recommended that such graphics commands to be fully converted to UNIRAS for the reasons of flexibility and the availability of support staff to provide advice on problems encountered. In addition,

222

UNIRAS allows free device drivers which will inevitably reduce the financial budget and provides a source code to facilitate any output command that is deemed necessary for further enhancement in graphics quality.

The new algorithms developed to simulate contact adhesion are based on the contact mechanics theories described in Chapter 3. These theories contain approximations and assumptions which are not strictly correct. It has been assumed that they provide a reasonable model for the contact behaviour. There is a need for more real experiments to be done to check this assumption e.g. oblique impacts of micron-sized spheres.

7.4 Further Work

An obvious extension to the research reported in this thesis is to carry out 3D agglomerate simulations. This is being done currently by other members of the research group. There is, however, a continuing need to perform 2D simulations because they provide clear visual informations and a larger number of primary particles can be used.

Using the existing 1000 particle monodisperse agglomerate, the surface energy should be increased further to produce a very strong agglomerate. Internal contacts may be selected to have zero adhesion in order to simulate a small existing crack. Brazilian test simulations should then be carried out to determine whether or not failure occurs by crack propagation outwards from the "flaws", in agreement with the assumption of classical linear elastic fracture mechanics.

The current work has been restricted to a monodisperse system. It would be logical to follow this by a similar project but using a polydisperse agglomerate. By comparing the results of the two projects a better understanding of the effect of particle arrangement on plastic deformation, crack initiation and crack propagation may be obtained.

More particles are recommended in order to obtain more detailed information about agglomerate degradation. A more detailed analysis should be carried out of the local micromechanics in the plastic zones and along crack lines. This will require better computing facilities and new analysis subroutines. Current computers such as IBM RISC 6000 Model 320H workstations are capable of handling approximately 100,000 particles at a processing speed of 7 times (41 MIPS) the VAX 8650 and are dedicated machines. It is recommended that this type of workstation is used in future projects for 2D simulations of very large particle systems.

Lastly, but not least, other possible types of particle-particle interactions, e.g. capillary or solid bridges, electro-static forces, could be considered and the computer code modified accordingly.

7.5 Final Concluding Remarks

A methodology originally developed in understanding the micromechanics of sand has been transformed to examine process engineering problems. The problem of agglomerate degradation has been examined in this thesis. In principle, the methodology can also be applied to many other process engineering problems. Cynics are unavoidable where computer simulation results are concerned but this should not deter further developements and wider applications of the computer simulation program.

Knowledge is based on the building blocks of ideas which are generated from various origins. This research has laid its first building block towards a better understanding of agglomerate degradation. Much more work needs to be done. It is hope that future work will develop from this first attempt and make computer simulation an indispensable tool to complement the traditional real experiments.

REFERENCES

Adams, M.J (1985). The strength of particulate solids. Journal of Powder and Bulk Solids Technology. Vol. 9; 15-20

Adams, M.J., Muiller, M.A., Seville, J.P.K., Williams, J.G (1989). A fracture mechanics approach to the breakage of agglomerated particulate solids. Powder and Grains. Eds. Biarez and Gourves. Balkema, Rotterdam.; 105-110

Adamson, A.W (1967). Physical Chemistry of surfaces. London, Interscience. 317.

Arbiter, N., Harris, C.C., Stambolitzis, G.A (1969). Single fracture of brittle spheres. Trans. SMEI Aime. Vol. 244; 118-133

Atkins, A.G., Mai, Y.W (1985). Elastic and Plastic Fracture. John Wiley, New York.

Barker, L.M., Hollenbach, R.E (1965). Interferometer technique for measuring the dynamic mechanical properties of materials. The Review of Scientific Instruments. Vol. 36; 1617-1620

Barnes, D.J (1985). Ph.D thesis, Aston University.

Bowden, F.P., Tabor, D (1950). Friction and Lubrication of Solids Part I London O.U.P.

Bowden, F.P., Tabor, D (1964). Friction and Lubrication of Solids Part II London O.U.P.

Bradley, R. S (1932). Philosophical Magazine. Vol. 13; 853

Briscoe, B.J., Kremnitzer, S.L (1979). A study of the friction and adhesion of polyethylene-terephthalate monofilaments. Journal of Physics.D. Applied Physics. Vol. 12;103-516.

Budgett, H. M (1911). The adherence of flat surfaces. Proceeding of Royal Society London. A86; 25-35.

Campbell, C.S., Brennen, C.E (1982). Computer simulation of chute flows of granular materials. IUTAM Conference on deformation and failure of granular Materials. Delft; 515.

Cattaneo, C (1938). Sul contatto di due corpi elastici: distribuzione locale degli sforzi. Rendiconti dell' Accademia nazionale dei Lincei.

Chen, W.F (1970). Double punch test for tensile strength of concrete. ACI Journal. December; 993-995.

Chen, W.F (1975). Limit Analysis and Soil Plasticity (Ch. 11). Elsevier Scientific Publishing Company.

Cheng, D.C.H (1968). The tensile strength of powders. Chemical Engineering Science. Vol. 23; 1405-1419.

Colback, P.S.B (1966). An analysis of brittle fracture initiation and propagation in the Brazilian test. Proceedings of the Congress of International Society of Rock Mechanics. 1st Lisbon. 385-391.

Cundall, P. A (1971). A computer model for simulating progressive, large scale movements in blocky rock systems. Proceedings of the Symposium of International Society of Rock Mechanics. Nancy. Article 8.

Cundall, P. A (1978). Ball - a program to model granular media using the distinct element method. Technical Note, Advanced Technology Group, Dames and Moore, London.

Cundall, P. A (1983). Modelling of microscopic mechanisms in granular material. Mechanics of Granular Materials: New Models and constitutive Relations. Eds. J.T. Jenkins and M. Satake. Elsevier Science Publisher. Amsterdam.

Cundall, P.A., Drescher, A., Strack, O.D.L (1982). Numerical experiments on granular assemblies: measurements and observations. IUTAM Conference on deformation and failure of granular Materials. Delft; 355-370.

Cundall, P.A., Strack, O.D.L (1979a). A discrete numerical model for granular assemblies. Geotechnique. Vol. 29, 1 ; 47-65.

Cundall, P.A., Strack, O.D.L (1979b). The distinct element method as a tool for research in granular media, Part II, Dept. Civ. Min. Engrg. Univ. Minnesota.

Darvell, B.W (1990). Uniaxial compression tests and the validity of indirect tensile. Journal of Material Science. Vol.25; 757-780.

De Bruyne, N. A (1947). The Physics of adhesion. Journal of Science Instruments Vol. 24; 29-35.

Deresiewicz, H (1968). A note on Hertz impact. Acta Mechanica. Vol. 6; 110-112.

Deryaguin, B.V., Muller, V.M.,Toporov, Y.P (1975). Effect of contact deformations on the adhesion of particles. Journal of Colloid and Interface Science. Vol. 53; 314-379.

Drescher, A (1979). Application of photoelasticity to investigation of constitutive laws for granular materials. Proceedings of IUTAM Symposium on Optical methods in solid mechanics. Poitiers, France.

Drescher, A., de Josselin de Jong, G (1972) Photoelastic verification of mechanical model for the flow of granular media. Journal of Mechanics and Physics of Solids. Vol 20; 337-351.

Eley, D.D (1961). Adhesion. Oxford University Press.

Fairhurst, C (1964). On the validity of the Brazilian test for brittle materials. International Journal of Rock Mechanics and Mining Science. Vol. 1; 535-546.

Fox, H.W., Zisman, W.A (1950). The spreading of liquids on low energy surfaces. Journal of Colloid Science. Vol.5; 514-531

Ghadiri, M (1990). Formation of particle by size reduction. Particulate Technology Summer School. Bradford University.

Ghadiri, M (1991) Private communication.

Ghadiri, M., Zhang, Z (1990). Impact attrition of particulate solids. International Fine Particle Research Institute.

Gilman, J.J (1969). Micromechanics of flow in solids. McGraw-Hill Book Company.

Goldsmith, W (1960). Impact. Edward Arnold (Publisher) Ltd.

Graham, G.A.C (1973). A contribution to Hertz's theory of elastic impact. International Journal of Engineering Science. Vol. 11; 409-413.

Greenwood, J.A., Johnson, K.L (1981). The mechanics of adhesion of viscoelastic solids. Philosophical Magazine. Vol. 43; 697-711.

Griffith, A.A (1920). The phenomenon of rupture and flow in solids. Phil. Trans. Royal Society. Vol. 221; 163-198.

Hart, R.D (1991). An introduction to distinct element modelling for rock engineering. 7th International Congress on Rock Mechanics. Aachen, Germany.

Hondros, G (1959). The evaluation of Poisson's ratio and the modules of materials of a low tensile resistance by the Brazilian test with particular reference to concrete. Australia Journal of Applied Science. Vol. 10; 243-268.

Horn, R.G., Israelachvili, J.N., Pribac, F (1987). Measurement of the deformation and adhesion of solids in contact. Journal of Colloid and Interface Science. Vol. 115; 480-491.

Hopkins, M.A (1987). Particle Simulation : Volume I. Department of Civil and Environmental Engineering, Clarkson University, New York.

Hughes, D.S., Gourley, L.E., Gourley, M.F (1961). Shock wave compression of Iron and Bismuth. Vol. 32; 624-629.

Hunter, S.C (1957). Energy absorbed by elastic waves during impact. Journal of Mechanics and Physics of Solids. Vol. 5; 162.

Inglis, C.E (1913). Stresses in a plate due to the presence of cracks and sharp corners. Trans. Institute of Naval Architect. Vol. 55; 219.

Irwin, G.R (1957). Analysis of stresses and strains near the end of a crack traversing a plate. Journal of Applied Mechanics. Vol. 24; 361-364.

Irwin, G.R (1958). Fracture. In Handbuch der Physik. Springer-verlag, Berlin. Vol. 6; 551.

Jaeger, J.C (1969). Elasticity, Fracture and Flow with Engineering and Geological applications. Methuen and Company Ltd.

Jayatilaka, A.D.S (1979). Fracture of Engineering Brittle Materials. Applied Science Publishers Ltd.

Johnson, K.L (1982). One hundred years of Hertz contact. Proceeding of Insitute of Mechanical Engineers. Vol. 196; 363-377.

Johnson, K.L (1958). A note on the adhesion of elastic solids. British Journal of Physics. Vol. 9; 199-200.

Johnson, K.L (1976). Adhesion at the contact of solids. Theoretical and Applied Mechanics, Proceeding of 4th IUTAM Congress. (eds. W.T. Koiter); 133-143.

Johnson, K.L (1985) Contact Mechanics. Cambridge University Press.

Johnson, K.L., Kendall, K., Roberts, A.D (1971). Surface energy and the contact of elastic solids. Proceedings, Royal Society. A324; 301-313.

Johnson, W (1972). Impact Strength of Materials. Edward Arnold.

Jones, O.E., Neilson, F.W., Benedick, W.B (1962). Dynamic yield behaviour of explosively loaded metals determined by a quartz tranducer technique. Journal of Applied Physics. Vol. 33; 3224.

Kelly, A., Macmillan, N.H (1986). Strong Solids. Clarendon Press.

Kendall, K (1986). Inadequacy of Coulomb's friction law for particle assemblies. Nature. Vol.319;203.

Kendall, K., Alford, N. McN., Birchall, J.D (1986). The strength of green bodies. Institute of Ceramics Proceeding Special Ceramics., No.8. Institute of Ceramics, Stoke-on-Trent; 255-266.

Kolsky, H (1953). Stress waves in Solids. Oxford University Press (340)

Kuznetsov, V.D (1957). Surface Energy of Solids. Department of Scientific and Industrial Research. (Russian translation).

Lawn, B.R., Wilshaw, T.R (1974). Fracture of Brittle Solids. Cambridge University Press.

Lifshitz and Kolsky, H (1964). Some experiments on an elastic rebound. Journal of Mechanics and Physics Solids. Vol. 12; 35-43.

Marsh, S.P., McQueen, R.G (1960). Investigation of the Hugonist elastic limit in Armco Iron by optical reflection measurements. Bulletin, American Physical Society. Vol. 50; 506.

Maw, N., Barber, J.R., Fawcett, J.N (1976). The oblique impact of elastic spheres. Wear. Vol. 38; 101-113.

Maw, N., Barber, J.R., Fawcett, J.N (1981). The role of tangential compliance in oblique impact. Journal of Lubrication Technology, Trans. ASME Series F. Vol. 103; 74-80.

McFarlane, J.S., Tabor, D (1950). Adhesion of solids and the effect of surface fims. Proceeding of the Royal Society of London. Series A, Vol. 202; 224-243.

Mellor, M., Hawkes, I (1971). Measurement of tensile strength by diametrical compression of discs and annuli. Engineering Geology. Vol. 5; 173-225.

Mindlin, R.D (1949). Compliance of elastic bodies in contact. Trans. ASME, Series E, Journal of Applied Mechanics. Vol. 16; 259-268.

Mindlin, R.D., Deresiewicz, H (1953) Elastic spheres in contact under varying oblique forces. Trans. ASME, Series F, Journal of Applied Mechanics. Vol . 20; 327-344.

Minshall, S (1955). Properties of elastic and plastic waves determined by pin contractors and crystals. Journal of Applied Physics. Vol. 26; 463-469.

Mitchell, N.B (1961). The indirect tension test for concrete. Material Research and Standards. Vol. 1; 780-788.

Mott, N.F (1948). Brittle fracture in weld steel plates. Engineering. Vol. 24; 820.

Muller, V.M., Yushchenko, Deryaguin, B.V (1980). On the influence of molecular forces on the deformation of an elastic sphere and its sticking to a rigid plane. Journal of Colloid and Interface Science. Vol. 77; 91-101.

Orowan, E (1955). Energy criteria of fracture. Weld. Res. Supp. Vol. 34; 157.

Prasher, C.L (1987). Crushing and Grinding Process Handbook. John Wiley and Sons Ltd.

Peltier, R (1954). Theoretical investigation of the Brazilian test. Union of Testing and Research Laboratories for Materials and Structures. Vol; 19.

Puttick, K.E., Badrick, A.S.T (1987). The mechanical breakdown of sodium chloride crystals. Chemical Engineering Science. Vol. 42; 855-869.

Randall, C.W (1989). Ph.D thesis, Aston University.

Reed, J (1987). Impact adhesion of particles. Tribology in particulate technology. eds. Briscoe, B.J and Adams, M.J. 123-130.

Rice, M.H (1961). Capacitor technique for measuring the velocity of a plane conducting surface. The Review of Scientific Instruments. Vol. 32; 449-451.

Rossmanith, H. P., Shukla, A (1982). Photoelastic Investigation of Dynamic Load Transfer in Granular Media. Acta Mechanic. Vol. 42;211-225.

Rowe, P.W (1962). The Stress-dilatancy relation for static equilibrium of an assembly of particles in contact. Proceeding of Royal Society London. A. Vol.269; 500-527.

Rudnick, A.; Hunter, A.R.; Holden, F.C. (1963). An analysis of the diametrical compression test. Material Research and Standard. April; 283-289.

Rumpf, H (1961). The strength of granules and agglomerates- Agglomeration. Ed. Knepper, W. A. Interscience Publishers.

Samuels, J., Roberts, S.G (1986). The brittle to ductile transition in silicon. Institute of Ceramics Proceeding Special Ceramics., No.8. Institute of Ceramics, Stoke-on-Trent; 267-272.

Sanders, B.E., Ackermann,N.L (1986). Two dimensional gravity driven granular flow: experimental data. Society of Engineering Sciences 23rd Annual Meeting, State University, Buffalo, New York.

Savkoor, A.R., Briggs, G.A.D (1977). The effect of tangential froce on the contact of elastic solids in adhesion. Proceeding of Royal Society London. A356; 103-114.

Shinohara, K., Capes, C.E., Fouda, A.E (1982). A theoretical model of the effect of distributed loading on the tensile strength of agglomerates as measured in the diametrical compression test. Powder Technology. Vol. 32; 163-171.

Stone, W (1930). Some phenomena of the contact of solids. Philosophical Magazine. Vol. 9; 610-620

Swalwinski, C.M (1985) Flexibility of a contact area of an isotropic elastic body. Journal of Applied Mechanics. Vol. 52; 62-66.

Tabor, D (1978). On the role of molecular forces in contact deformations. Journal of Colloid and Interface Science. Vol. 67; 380.

Tabor, D., Winterton, R.H.S (1969). The direct measurement of normal and retarded van der Waals forces. Proceeding of Royal Society. A312; 435-450.

Taylor, J.W (1965). Dislocation dynamics and dynamics yielding. Journal of Applied Physics. Vol. 36; 3146-3150.

Thornton, C (1977). Deformation of a single particulate model. Proceedings of Specialty Session 9, IX ICSMFE, Tokyo.

Thonton, C (1991). Interparticle sliding in the presence of adhesion. Journal of Physics. D: Applied Physics. Vol. 24; 1942-1946.

Thornton, C., Randall, C.W (1988). Applications of theoretical contact mechanics to solid particle system simulation, Micromechanics of Granular Materials (eds. M Satake and J T Jenkins) Elsevier (1988) Amsterdam; 133.

Thornton, C., Yin K.K (1991). Impact of elastic spheres with and without adhesion. Powder Technology. Vol. 65; 153.

Timoshenko, S., Goodier, J.N (1934, 1951, 1970). Theory of Elasticity. McGraw-Hill, New York.

Tomlinson, G. A (1928). Molecular cohesion. The Philosophical Magazine. Vol. 6; 695-712.

Tsai, Y.M (1968). Note on the surface waves produced by Hertzian impact. Physics of Solids. Vol. 16; 133-136.

Venables, D (1964) Phermex: A pulse high energy radiographic machine emitting X rays. Physics Today. Vol. 17; 19-22.

Walton, O. R (1982). Explicit Particle-Dynamics Model for granular materials. 4th International conference on Numerical Methods in Geomechanics, Edmonton.

Walton, O. R (1983) Particle-dynamics calculations of shear flows. Mechanics of Granular Materials: New Models and constitutive Relations. Eds. J.T. Jenkins and M. Satake. Elsevier Science Publisher. Amsterdam.

Walton, O. R., Braun, R.L (1985). Viscosity, granular temperature and stress calculations for shearing assemblies of inelastic, frictional disks. Journal of Rheology. Vol. 30; 949.

230

Weibull, W (1952). A survey of 'statistical effect' in the field of material failure. Applied Mechanics Review. Vol. 5; 449-451.

Wilkins, M. L (1964). Calculation of elastic plastic flow. Methods in Computational Physics. Vol. 3; 211-263.

Williams, J.R., Hocking, G., Mustoe, G.G.W (1985). The theoretical basis of the discrete element method. Proceedings of the NUMETA 1985 Conference, Swansea.; 897-906.

Wright, P.J.F (1955). Comments on an indirect tensile test on concrete cylinders. Magazine of Concrete Research. July; 87-96.

Yuriger, K.R., Ghadiri, M., Clift, R (1987). Impact attrition of sodium chloride crystals. Chemical Engineering Science. Vol. 42; 843-854.

Zimon, A.D (1982). Adhesion of Dust and Powder. Consultants Bureau, New York. (Russian translation).

Appendix A

SUBROUTINE FORD(C,IC,B1,B2)

```
C==============================================================
C  The purpose of this subroutine is to update the contact forces
C  Both normal and tangential interaction rules are based on contact mechanics theories
C  The relevant theoretical background is provided by the theories of
C  Hertz, see Johnson (1985)
C  Mindlin (1949)
C  Mindlin and Deresiewicz (1953)
C  Johnson, Kendall and Roberts (1971)
C  Savkoor and Briggs (1977)
C  Thornton (1991)
C  see also Thorton and Randall (1988), Thornton and Yin (1991)
C  The contact information is stored in C(I)
C
C  C(1) Contact radius
C  C(2) Cumulative sliding displacement
C  C(3) normal force
C  C(4) tangential force
C  C(5) pointer to particle addresses
C  C(6) pointer to next contact address
C  C(7) critical tangential peeling force
C  C(8) tangential force from which unloading commenced
C  C(9) tangential force from which reloading commenced
C  C(10) DD - see Ph.D thesis of Randall (1989)
      LOGICAL WFLAG
      INTEGER IL,ITYP1,ITYP2,ICALL,IAD,LINK,BP1,BP2
      INTEGER IAL,IA,IAC
      INTEGER NCYTOT,BPOINT
      INTEGER CDF,THE1,UFL
      REAL*4 MN
      REAL*4 DD,AMUE,DFN,DFS,FNT,FST,DN,DS,SUMDN,SUMDS,PEQ,DSC, THETAR
      REAL*4 MSTAR,FND,FSD,RRMIN,EXTOVLP,MOVER1,MOVER2,DX1,DX2,DY1,DY2,TDE
      INCLUDE 'COMMONCONTIN.FOR'
      COMMON /FOR/ICALL,IAD,WFLAG,ITYP1,ITYP2,N10,NN
      DIMENSION C(10),IC(10),B1(13),B2(22),IA(1),IL(2)
      COMMON /TH1/DS,AMUE,DFN,CDF,DFS,GSTAR,RCON,DSC,UFL,FAD,PEQ
      EQUIVALENCE (IA(1),A(1))
      AMUE=0.0
      DD=0.0
      CDF=0
C    UFL IS -VE IF SYSTEM IS UNLOADING
      UFL=1
C ==============
C TEST FOR CONTACT
    9 IF(WFLAG) THEN
      XDIF=B1(1)+B1(11)-B2(3)-B2(20)
      YDIF=B1(2)+B1(12)-B2(4)-B2(21)
      XR=XDIF*B2(10)+YDIF*B2(9)
      YR=YDIF*B2(10)-XDIF*B2(9)
      IF(XR.GT.B2(2).OR.XR.LT.B2(1)) GO TO 110
      RRMIN=R1
      ELSE
      XDIF=B2(1)+B2(11)-B1(1)-B1(11)
      YDIF=B2(2)+B2(12)-B1(2)-B1(12)
      ENDIF
      D=SQRT(XDIF*XDIF+YDIF*YDIF)
      SA=YDIF/D
      CA=XDIF/D
      IF(WFLAG) THEN
      R1=R(ITYP1)
      ELSE
      R1=R(ITYP1)
      R2=R(ITYP2)
      ENDIF
      IF(WFLAG) THEN
      RDIF=YR-R1
```

```
      ELSE
      RDIF=D-R1-R2
      ENDIF
      IF(RDIF.GT.0.0.AND.C(1).LE.0.0) GO TO 100
C     CALCULATE CONTACT PROPERTIES
      IF(WFLAG) THEN
      MSTAR=AMASS(ITYP1)
      RSTAR=R1
      ELSE
      RSTAR=R1*R2/(R1+R2)
      MSTAR=AMASS(ITYP1)*AMASS(ITYP2)/(AMASS(ITYP1)+AMASS(ITYP2))
      ENDIF
      COAV=(COH(ITYP1)+COH(ITYP2))*0.5
      PI=4.0*ATAN(1.0)
      FAD=3.0*COAV*PI*RSTAR
   10 ESTAR1=YMOD(ITYP1)/(1.0-PRAT(ITYP1)*PRAT(ITYP1))
      ESTAR2=YMOD(ITYP2)/(1.0-PRAT(ITYP2)*PRAT(ITYP2))
      ESTAR=ESTAR1*ESTAR2/(ESTAR1+ESTAR2)
      G1=0.5*YMOD(ITYP1)/(1.0+PRAT(ITYP1))
      G2=0.5*YMOD(ITYP2)/(1.0+PRAT(ITYP2))
      GSTAR1=G1/(2.0-PRAT(ITYP1))
      GSTAR2=G2/(2.0-PRAT(ITYP2))
      GSTAR=GSTAR1*GSTAR2/(GSTAR1+GSTAR2)
      RCONC3=0.75*RSTAR*FAD/ESTAR
      RCONC=RCONC3**(1.0/3.0)
      ALFC3=0.1875*FAD*FAD/(ESTAR*ESTAR*RSTAR)
      ALFC=ALFC3**(1.0/3.0)
      RCONI=(0.75**(-2.0/3.0))*RCONC
      IF(RDIF.GT.ALFC) GO TO 100
C     CALCULATE RELATIVE NORMAL AND TANGENTIAL DISPLACEMENT INCREMENTS
      IF(WFLAG) THEN
      XDR=B2(6)-B1(3)
      YDR=B2(7)-B1(4)
      ELSE
      XDR=B1(3)-B2(3)
      YDR=B1(4)-B2(4)
      ENDIF
C     ALLOW FOR CONTINUUM STRAIN IF APLLIED
      IF(CFLAG)THEN
      XDR=XDR+CEDA(1,1)*XDIF+CEDA(1,2)*YDIF
      YDR=YDR+CEDA(2,2)*YDIF+CEDA(2,1)*XDIF
      END IF
      IF(WFLAG) THEN
      DN=(YDR*B2(10)-XDR*B2(9)+XR*B2(8))*TDEL
      DS=(XDR*B2(10)+YDR*B2(9)-R1*B1(5))*TDEL
      ELSE
      DN=(XDR*CA+YDR*SA)*TDEL
      DS=(XDR*SA-YDR*CA-B1(5)*R1-B2(5)*R2)*TDEL
      ENDIF
C     UPDATE NORMAL FORCE
      IF(FAD.GT.0.0) GOTO 51
      IF(FAD.LE.0.0.AND.RDIF.GE.0.0) GOTO 80
      IF(FAD.LE.0.0.AND.C(3).EQ.0.0.AND.C(7).LE.0.0) THEN
      DN=-RDIF
      DFN=4.0*ESTAR*SQRT(RSTAR*DN*DN*DN)/3.0
      STIFN=0.0
      GOTO 12
      ELSE
      STIFN=2.0*ESTAR*C(1)
      DFN=DN*STIFN
      GOTO 12
      END IF
   51 IF(RDIF.GE.ALFC) GO TO 100
      IF(-RDIF.LE.(-ALFC*0.4223653229)) THEN
      ABC=-1.0
      ELSE
      ABC=1.0
      END IF
      IF(C(1).LE.0.0) THEN
      C(3)=-8.0*FAD/9.0
      DRCON=DN/((2.0*RCONI/RSTAR)-SQRT(PI*COAV/(ESTAR*RCONI)))
      DFN=DRCON*((4.0*ESTAR*RCONI*RCONI/RSTAR)
     *-(6.0*SQRT(PI*COAV*ESTAR*RCONI)))
      ELSE
      RCON3=C(1)*C(1)*C(1)
      RACA3=SQRT(RCONC3/RCON3)
```

233

```
      IF(C(7).LE.0.0) THEN
        STIFN=2.0*ESTAR*C(1)*((3.0-3.0*RACA3)/(3.0-RACA3))
      ELSE
        STIFN=ABC*2.0*ESTAR*C(1)
      END IF
      DFN=DN*STIFN
      END IF
C   UPDATE NORMAL FORCE
   12 FN=C(3)+DFN
      IF(FAD.LE.0.0.AND.FN.LT.0.0) GOTO 80
      IF(FN.LE.-0.998*FAD) THEN
      FN=-0.998*FAD
      END IF
      C(3)=FN
C      ADD DAMPING CONTRIBUTION
C    CONTACT DAMPING F=KX + DX', D=BETA*DCRIT,
C    DCRIT=2*SQRT(MASS*STIFFNESS)
      IF(WFLAG) THEN
      FND=2.0*BETAW*SQRT(MSTAR*ABS(STIFN))*DN/TDEL
      ELSE
      FND=2.0*BETA*SQRT(MSTAR*ABS(STIFN))*DN/TDEL
      END IF
      FNT=FN+FND
C   CALCULATION OF RELATIVE PROPERTIES
C
C      UPDATE RADIUS OF CONTACT AREA
      IF(FAD.LE.0.0) THEN
        RCON=(0.75*RSTAR*C(3)/ESTAR)**(1.0/3.0)
      GOTO 13
      END IF
      PP=4.0*(C(3)*FAD+FAD*FAD)
      PEQV=C(3)+2.0*FAD+ABC*SQRT(PP)
      PEQ=PEQV*((2.0*PEQV+C(3))/(3.0*PEQV))**1.5
      IF((C(7).GT.0.0).AND.(C(3).LT.-0.3*FAD)) GOTO 32
      IF(C(7).GT.0.0) THEN
      PONE=C(3)+2.0*FAD
      ELSE
      PP=4.0*(C(3)*FAD+FAD*FAD)
      TEG=0.25*C(4)*C(4)*ESTAR/GSTAR
      IF(PP.GT.TEG)THEN
      PONE=C(3)+2.0*FAD+ABC*SQRT(PP-TEG)
      ELSE
      PONE=C(3)+2.0*FAD
      TSTAR=2.0*SQRT(PP*GSTAR/ESTAR)
      C(7)=ABS(TSTAR)
      END IF
      END IF
   32 IF((C(7).GT.0.0).AND.(C(3).LT.-0.3*FAD)) THEN
        RCON=(0.75*PEQ*RSTAR/ESTAR)**(1.0/3.0)
      ELSE
        RCON=(0.75*PONE*RSTAR/ESTAR)**(1.0/3.0)
      END IF
   13 C(1)=RCON
C DEAL WITH FRICTIONLESS CONTACTS
      AMUE=AMIN1(AMU(ITYP1),AMU(ITYP2))
      IF(AMUE.EQ.0.0)THEN
      DFS=0.0
      FS=0.0
      FST=0.0
      GOTO 25
      END IF
C   DETERMINE THE TANGENTIAL LOADING CASE
      IF(C(8).GT.0.0) GOTO 34
      IF((C(8).EQ.0.0) .AND. (C(4).LT.0.0)) GOTO 33
      IF((C(8).EQ.0.0) .AND. (C(4).GT.0.0)) GOTO 34
      IF((DS.GE.0.0) .AND. (C(8).GE.0.0)) GOTO 34
   33 CDF=-1
      GOTO 37
   34 CDF=1
C   THE CALCULATION OF TANGENTIAL FORCE INCREMENT
C   CALLING FUNCTION THETA, HAVING PASSED THE CURRENT VALUE OF DS.
C   FOR NO TANGENTIAL DISPLACEMENT
   37 IF(DS.EQ.0.0)THEN
      DFS=0.0
C    FS=C(4)
C    GOTO 20
```

```
      GOTO 25
      END IF
   50 IF(C(7).LE.0.0.AND.FAD.GT.0.0) THEN
      THETAR=1.0
      ELSE
      THETAR=THETA(C)
      END IF
C     ***********************************************************
      DFS=CDF*(THETAR*(8.0*GSTAR*RCON*DS*CDF-AMUE*DFN*UFL)+AMUE*DFN*UFL)
C     ***********************************************************
C     FS=C(4)+DFS
      IF(FAD.LE.0.0) GOTO 99
      IF(C(7).GT.0.0) THEN
      GO TO 99
      ELSE
      TEG=0.25*(C(4)+DFS)*(C(4)+DFS)*ESTAR/GSTAR
      END IF
      IF(TEG.LT.PP) THEN
      GO TO 75
      ELSE
      TSTAR=2.0*SQRT(PP*GSTAR/ESTAR)
      C(7)=ABS(TSTAR)
C     WRITE(6,1300) C(7)
      GO TO 50
      END IF
C   TO ENSURE THAT ON INCREASING AND DECREASING N VALUES THAT
C   WHEN DS<DSC THE AMOUNT THAT DFS IS SMALLER THAN AMUE*DFN
C   IS MONITORED AND STORED UNDER 'DD'. THIS IS TO ENSURE THAT
C   EQUATIONS FOR DS>DSC ARE NOT USED UNTIL THE VALUE OF 'DD'
C   HAS BEEN REDUCED TO ZERO.
C   TO CHECK WHETHER THE LAST INCREMENT OF DS HAS COUNTERED
C   THE PREVIOUS VALUE OF DD.
C   IF N IS DECREASING, DECREASE DD
C   THE SIGN OF DSC IS DEPENDANT ON DFN
C   DD IS ALWAYS +VE
   99 DD=C(10)
      IF(DFN.LT.0.0) THEN
      DD=DD+DSC
      END IF
C   IF N IS INCREASING AND DFS<AMUE*DFN INCREASE DD
      IF((DFN.GT.0.0) .AND. (ABS(DFS).LT.AMUE*DFN)) THEN
      DD=DD+(DSC-ABS(DS))
      END IF
C
C   IF N IS INCREASING AND DFS>AMUE*DFN DECREASE DD
      IF((DFN.GT.0.0) .AND. (ABS(DFS).GT.AMUE*DFN)) THEN
      DD=DD-(ABS(DS)-DSC)
      END IF
C   TO ENSURE DD IS NEVER NEGATIVE, AND THUS IF LAST DECREMENT OF
C   DD HAS COUNTERED ITS VALUE
      IF(DD.LT.0.0) THEN
      DD=0.0
      END IF
      C(10)=DD
C   ON INITIAL LOADING TONE AND TTWO ARE SET TO ZERO, ONCE
C   A REVERSAL HAS OCCURRED TONE IS SET TO THE PREVIOUS T
C   VALUE, AND IS ALWAYS TMAX FOR THE DURATION OF THE CONTACT
C   ,OR INCREASED/DECREASED BY AMUE*DFN WHEN T<TONE. TTWO
C   IS SET TO T ON THE SECOND REVERSAL, IE WHEN T IS INCREASING
C   AGAIN, AND IS THEN ALWAYS TMIN FOR THE DURATION OF THE
C   CONTACT, OR INCREASED/DECREASED BY AMUE*DFN WHEN T>TTWO.
C   FOR DS INCREASING, TONE WITH A VALUE AND TTWO ZERO
C   (THUS A SECOND REVERSAL, THIS WILL SET TTWO TO T AT PT OF SECOND
C   REVERSAL ONLY (BEFORE T IS UPDATED)).
      IF((DS*CDF.GT.0.0) .AND. (C(8).NE.0.0) .AND.
     .   (C(9).EQ.0.0)) THEN
      C(9)=C(4)
      END IF
C   FOR T DECREASING, TONE WITH NO VALUE, AND TTWO WITH
C   NO VALUE (THUS FIRST REVERSAL, THIS WILL SET TONE TO T
C   AT PT OF FIRST REVERSAL ONLY BEFORE T IS UPDATED).
      IF((DS*CDF.LT.0.0) .AND. (C(8).EQ.0.0) .AND.
     .   (C(9).EQ.0.0)) THEN
      C(8)=C(4)
      END IF
   25 FS=C(4)+DFS
```

235

```
C     SLIDING TEST
      IF(FAD.LE.0.0) THEN
      FSMAX=AMUE*FN
      GOTO 26
      END IF
      IF((C(7).GT.0.0).AND.(C(3).LT.-0.3*FAD)) THEN
      FSMAX=AMUE*PEQ
      ELSE
      FSMAX=AMUE*(FN+2.0*FAD)
      END IF
   26 IF(ABS(FS).LE.FSMAX) GO TO 20
C     MUST BE SLIDING
   15 FS=SIGN(FSMAX,FS)
C     CUMULATIVE SLIDING DISPLACEMENT
      IF(AMUE.NE.0.0) C(2)=C(2)+ABS(DS)
      GO TO 20
C   IF TANGENTIAL DAMPING REQUIRED USE:
C     (DFS/DS)=STIFFS
   75 IF(C(7).LE.0.0) THEN
      FS=C(4)+DFS
      END IF
   20 IF(DS.EQ.0.0) GOTO 21
      IF(WFLAG) THEN
      FSD=2.0*BETAW*SQRT(MSTAR*ABS(DFS/DS))*DS/TDEL
      ELSE
      FSD=2.0*BETA*SQRT(MSTAR*ABS(DFS/DS))*DS/TDEL
      END IF
      FST=FS+FSD
   21 C(4)=FS
C     TO UPDATE TONE C(8) AND TTWO C(9) SUCH THAT THE SYSTEM IS ON
C     THE CORRECT EQUIVALENT NORMAL FORCE CONSTANT CURVE.
C     PROVIDED T IS NOT EQUAL TO TONE, AND FOR THE OTHER
C     CONDITION T IS NOT EQUAL TO TTWO.
C     THIS WILL UPDATE TONE FOR ALL UNLOADING N VARYING CASES
C     EXCEPT AT REVERSAL PTS.
   22 IF((C(4).NE.C(8)) .AND. (C(8).NE.0.0)) THEN
      C(8)=C(8)+CDF*AMUE*DFN
      END IF
C     THIS WILL UPDATE TTWO FOR ALL RELOADING N VARYING CASES
C     EXCEPT AT REVERSAL PTS.
      IF((C(4).NE.C(9)) .AND. (C(9).NE.0.0)) THEN
      C(9)=C(9)-CDF*AMUE*DFN
      END IF
C     TO CHECK WHETHER VIRGIN LOADING HAS BEEN RE-ESTABLISHED
C     (IF ON UNLOADING OR RELOADING VIRGI_BN LOADING IS
C     RE-ESTABLISHED THEN TONE AND TTWO MUST BE RESET TO ZERO)
      IF((C(8).NE.0.0) .AND. (ABS(C(4)).GE.ABS(C(8))))
C     *(DFS.GT.0.0)) THEN
      *THEN
      C(8)=0.0
      C(9)=0.0
      END IF
C     SIMILARLY FOR THE RE-ESTABI ISHMENT OF VIRGIN UNLOADING,
C     WHEN TTWO MUST BE RESET TO ZERO
      IF((C(9).NE.0.0) .AND. (C(4)*CDF.LT.C(9)*CDF)) THEN
      C(9)=0.0
      END IF
C     NOW RESOLVE FORCES BACK INTO X,Y, THETA COMPONENTS
      IF(WFLAG) GO TO 180
      FX=FNT*CA+FST*SA
      FY=FNT*SA-FST*CA
      IF(FAD.LE.0.0) THEN
      FT1=FST*R1
      FT2=FST*R2
      GOTO 27
      END IF
      IF(C(7).GT.0.0) THEN
      FT1=FST*R1
      FT2=FST*R2
      ELSE
      FT1=0.0
      FT2=0.0
      END IF
C     ADD IN THIS CONTACTS CONTRIBUTION TO FORCE SUMS
   27 B1(6)=B1(6)-FX
      B1(7)=B1(7)-FY
```

```
      B1(8)=B1(8)+FT1
      B2(6)=B2(6)+FX
      B2(7)=B2(7)+FY
      B2(8)=B2(8)+FT2
      RETURN
C     DEAL WITH NON-TOUCHING BALLS
C     (DELETE THE CONTACT IF GAP>TOL)
   80 IF(COAV.EQ.0.0.AND.RDIF.LT.TOL) GOTO 120
  100 GAP=RDIF-ALFC
      IF(GAP.LT.TOL) GO TO 120
  110 ILSCGE=NEMC
      CALL ILS(1,ILSCGE,IAL)
      IC(1)=IAL
      IAL=IC(6)
      LINK=ILF(2,IAL)
      CALL IAUNPK(IL,IA(ICALL))
      IAL=IA(ICALL)
      NEMC=ILF(2,IAL)
      CALL ILS(2,LINK,IAL)
      IA(ICALL)=IAL
      IAD=ICALL-5
      RETURN
  120 C(1)=0.0
      C(2)=0.0
      C(3)=0.0
      C(4)=0.0
      C(7)=0.0
      C(8)=0.0
      C(9)=0.0
      C(10)=0.0
      RETURN
C FORCE-DISPLACEMENT LAW FOR BALL-TO-WALL CONTACT
C (NOTE ... B2 CORRESPONDS TO THE WALL ` B1 TO THE BALL)
  180 FX=FNT*B2(9)-FST*B2(10)
      FY=FST*B2(9)+FNT*B2(10)
      B1(6)=B1(6)-FX
      B1(7)=B1(7)+FY
      B1(8)=B1(8)+FST*R1
      B2(15)=B2(15)+FX
      B2(16)=B2(16)-FY
      B2(17)=B2(17)-FN*XR
      RETURN
      END
C     ----------------------
C     FUNCTION THETA(C)
C     ----------------------
      FUNCTION THETA(C)
C     THE PREVIOUS MAXIMUM VALUE OF TANGENTIAL FORCE 'TONE' IS
C     STORED UNDER C(8), THE PREVIOUS MINIMUM 'TTWO' IS STORED UNDER
C     C(9). FOR NORMAL FORCE INCREASING THE TANGENTIAL FORCE INCREMENT
C     MAY NOT BE SUFFICIENT TO REACH A POINT ON THE CORRESPONDING
C     N CONSTANT CURVE, AND THUS AS THE TANGENTIAL INCREMENT
C     NECESSARY TO REACH THE N CONSTANT CURVE =AMUE*DFN (WHERE AMUE
C     IS THE COEFFICIENT OF FRICTION) THEN AS:
C     DFS=AMUE*DFN =8.0*GSTAR*RCON*DS, THUS
C     DS=(AMUE*DFN)/(8.0*GSTAR*RCON). THIS VALUE OF DS WILL BE
C     CALLED DSC, THE CRITICAL DS VALUE NECESSARY FOR THE SYSTEM TO
C     BE REPRESENTED BY A POINT ON THE APPROPRIATE N CONSTANT CURVE.
C     HENCE FOR DS>DSC THEN THE SYSTEM PROGRESSES TOWARDS SLIP.
C     FOR DS<DSC THE INCREASE IN CONTACT AREA DUE TO THE INCREASE
C     IN NORMAL FORCE, IN RELATION TO THE INCREASE IN TANGENTIAL
C     DISPLACEMENT IS SUCH THAT THE SYSTEM IS FURTHER FROM FAILURE.
C     FOR DS<DSC THE AMOUNT THAT DS<DSC IS STORED UNDER 'DD' AND
C     USED TO ENSURE THAT UNTIL 'DD' IS DECREASED TO ZERO EQUATIONS
C     FOR DS>DSC WILL NOT BE USED.
C     NOTE THE DIRECTION OF LOADING IS STORED UNDER 'CDF'.
C     C(3)=NORM
C     C(3)=NORMAL FORCE, C(4)=TANGENTIAL FORCE, C(8)=TONE (TMAX),
C     C(9)=TTWO (TMIN), DS=TANGENTIAL DISPLACEMENT INCREMENT,
C     DFN=NORMAL FORCE INCREMENT, GSTAR=EQUIVALENT BULK MODULUS
C     AND RCON=RADIUS OF CONTACT.
C
C     THE FOLLOWING STATEMENTS ARE USED TO IDENTIFY THE VARIOUS
C     LOADING/UNLOADING/RELOAD AND RE-UNLOADING CASES, AND 'THE1'
C     WILL STORE THE TRIGGER FOR THE APPROPRIATE EQUATION FOR EACH  CASE.
      INTEGER*4 THE1,CDF,UFL
```

```
      DIMENSION C(10)
      REAL*4 DSC,DD,DFN,DS,AMUE,DFS,GSTAR,RCON
      COMMON /TH1/ DS,AMUE,DFN,CDF,DFS,GSTAR,RCON,DSC,UFL,FAD,PEQ
      DD=C(10)
C     CALCULATION OF 'DSC'
      DSC=(AMUE*DFN)/(8.0*GSTAR*RCON)
C           NORMAL FORCE INCREASING
C           ***********************
C     RELOADING, IE DFN>0, DS>0, DS>DSC+DD BUT C(4)<C(8)
      IF((DFN.GT.0.0) .AND. (DS*CDF.GT.0.0) .AND.
     .   (DS*CDF.GE.DSC+DD) .AND. (ABS(C(4)).LT.ABS(C(8)))) THEN
      THE1=3
      UFL=1
      GOTO 50
      END IF
C     VIRGIN LOADING, IE DFN>0, DS>0, DS>DSC+DD
      IF((DFN.GT.0.0) .AND. (DS*CDF.GT.0.0) .AND.
     .   (DS*CDF.GE.DSC+DD)) THEN
      THE1=1
      UFL=1
      GOTO 50
      END IF
C     OTHER LOADING CASES WITH DS<DSC+DD
      IF((DFN.GT.0.0) .AND. (DS*CDF.GT.0.0)) THEN
      THE1=4
      UFL=1
      GOTO 50
      END IF
C     RE-UNLOADING, IE DFN>0, DS<0, DS>DSC+DD BUT C(4)>C(9)
      IF((DFN.GT.0.0) .AND. (ABS(DS).GE.DSC+DD) .AND.
     .   (C(4)*CDF.GT.C(9)*CDF) .AND. (C(9).NE.0.0)) THEN
      THE1=3
      UFL=1
      GOTO 50
      END IF
C     UNLOADING, IE DFN>0, DS<0, DS>DSC+DD
      IF((DFN.GT.0.0) .AND. (ABS(DS).GE.DSC+DD)) THEN
      THE1=2
      UFL=-1
      GOTO 50
      END IF
C     OTHER UNLOADING CASES WITH DS<DSC+DD
      IF(DFN.GT.0.0) THEN
      THE1=4
C     IF C(9) EQUALS 0.0 THEN UNLOADING NOT RELOADING
      IF(C(9).EQ.0.0) THEN
      UFL=-1
      ELSE
      UFL=1
      END IF
      GOTO 50
      END IF
C           NORMAL FORCE DECREASING
C           ***********************
C     RELOADING, IE DFN<0, DS>0 BUT C(4)<C(8)
      IF((DFN.LT.0.0) .AND. (DS*CDF.GT.0.0) .AND.
     .   (ABS(C(4)).LT.ABS(C(8)))) THEN
      THE1=3
      UFL=1
      GOTO 50
      END IF
C     VIRGIN LOADING, IE DFN<0, DS>0
      IF((DFN.LT.0.0) .AND. (DS*CDF.GT.0.0)) THEN
      THE1=1
      UFL=1
      GOTO 50
      END IF
C     RE-UNLOADING, IE DFN<0, DS<0 BUT C(4)>C(9)
      IF((DFN.LT.0.0) .AND. (C(4)*CDF.GT.C(9)*CDF) .AND.
     .   (C(9).NE.0.0)) THEN
      THE1=3
      UFL=1
      GOTO 50
      END IF
C     UNLOADING, IE DFN<0, DS<0
      IF((DFN.LT.0.0)) THEN
```

238

```fortran
      THE1=2
      UFL=-1
      GOTO 50
      END IF
C          NORMAL FORCE CONSTANT
C          **********************
C    RELOADING, IE DFN=0, DS>0 BUT C(4)<C(8)
      IF((DS*CDF.GT.0.0) .AND. (ABS(C(4)).LT.ABS(C(8)))) THEN
      THE1=3
      UFL=1
      GOTO 50
      END IF
C    VIRGIN LOADING, IE DFN=0, DS>0
      IF((DS*CDF.GT.0.0)) THEN
      THE1=1
      UFL=1
      GOTO 50
      END IF
C    RE-UNLOADING, IE DFN=0, DS<0 BUT C(4)>C(9)
      IF(CDF*C(4).GT.CDF*C(9) .AND. (C(9).NE.0.0)) THEN
      THE1=3
      UFL=1
      GOTO 50
      END IF
C    UNLOADING, IE DFN=0, DS<0
      THE1=2
      UFL=-1
C TO CALCULATE THETA IN EACH CASE
   50 GOTO(10,20,30,40),THE1
   10 IF((C(7).GT.0.0).AND.(C(3).LT.-0.3*FAD)) THEN
      THETA=(1.0-(C(4)*CDF+AMUE*DFN)/(AMUE*PEQ))
      ELSE
      THETA=(1.0-(C(4)*CDF+AMUE*DFN)/(AMUE*(C(3)+2.0*FAD)))
      END IF
      IF(THETA.LT.0.0) THEN
      THETA=0.0
      ELSE
      THETA=THETA**(1.0/3.0)
      END IF
      RETURN
   20 IF((C(7).GT.0.0).AND.(C(3).LT.-0.3*FAD)) THEN
      THETA=(1.0-(C(8)*CDF-C(4)*CDF+2.0*AMUE*DFN)
     */(2.0*AMUE*PEQ))
      ELSE
      THETA=(1.0-(C(8)*CDF-C(4)*CDF+2.0*AMUE*DFN)
     */(2.0*AMUE*(C(3)+2.0*FAD)))
      END IF
      IF(THETA.LT.0.0) THEN
      THETA=0.0
      ELSE
      THETA=THETA**(1.0/3.0)
      END IF
      RETURN
   30 IF((C(7).GT.0.0).AND.(C(3).LT.-0.3*FAD)) THEN
      THETA=(1.0-(C(4)*CDF-C(9)*CDF+2.0*AMUE*DFN)
     */(2.0*AMUE*PEQ))
      ELSE
      THETA=(1.0-(C(4)*CDF-C(9)*CDF+2.0*AMUE*DFN)
     */(2.0*AMUE*(C(3)+2.0*FAD)))
      END IF
      IF(THETA.LT.0.0) THEN
      THETA=0.0
      ELSE
      THETA=THETA**(1.0/3.0)
      END IF
C    WRITE(6,1003) THETA
C 1003 FORMAT(3X,'THIS IS THE3=',1E12.5)
      RETURN
   40 THETA=1
C    WRITE(6,1004) THETA
C 1004 FORMAT(3X,'THIS IS THE4=',1E12.5)
      RETURN
      END
```

239

Appendix B

Appendix B provides a comprehensive layout on the series of impact simulations for agglomerate of surface energies 0.3, 1.0, 2.0 and 3.0 Jm-2. Graphics plots showing the forces, the equivalent lattice plots and the ball plots taken at the end of primary collision are first introduced. This will be followed by additional analyis figures of the evolution of wall force, kinetic energy and finally the number of contacts.
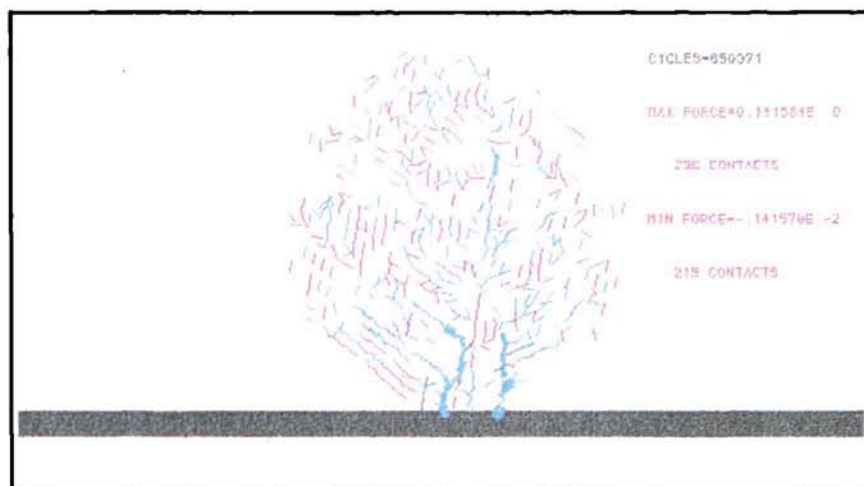
Force plot
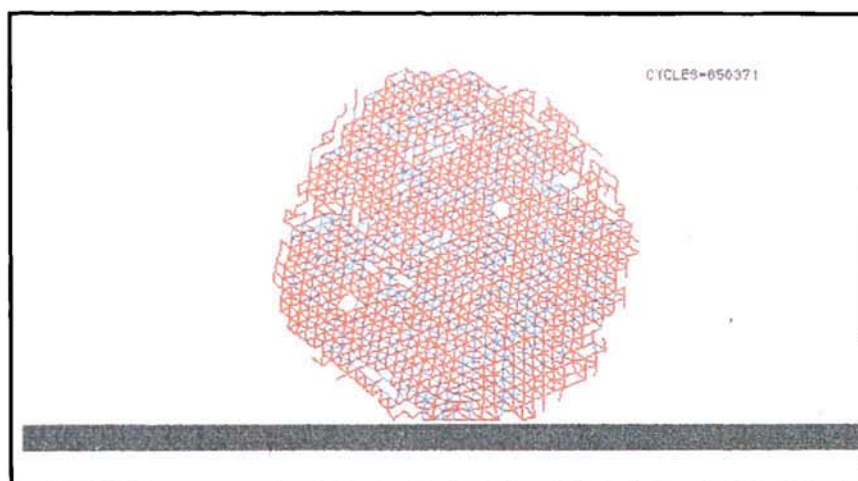
Lattice plot
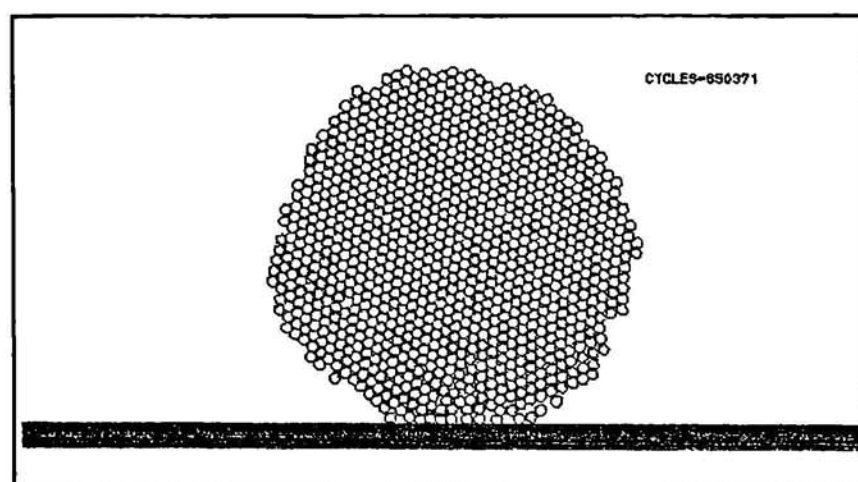
Ball plot

B1 Velocity of impact = 5.0 m/s, γ = 3.0 Jm^{-2}

(a)

(b)

(c)
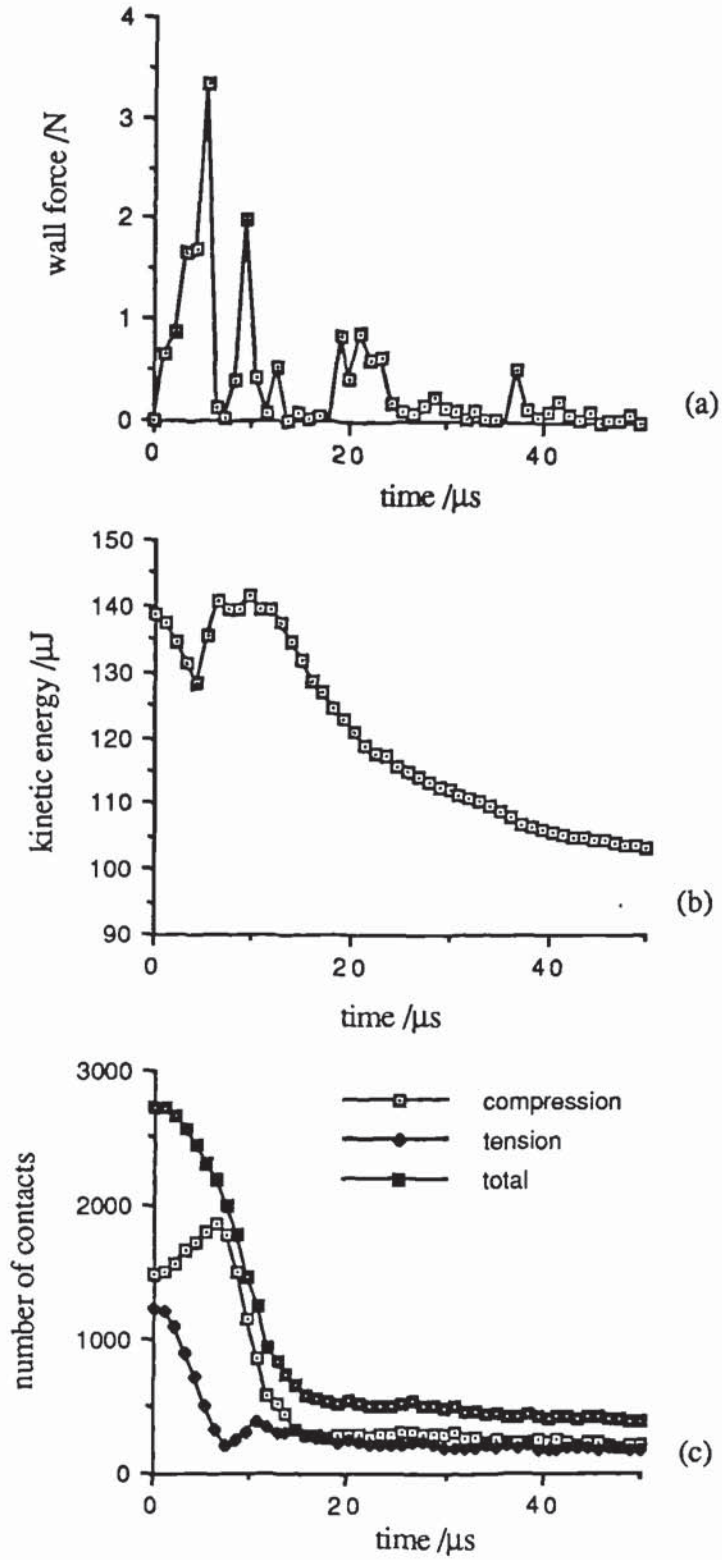
B2 Data for Velocity 5.0 m/s, $\gamma = 3.0$ Jm^{-2}

242
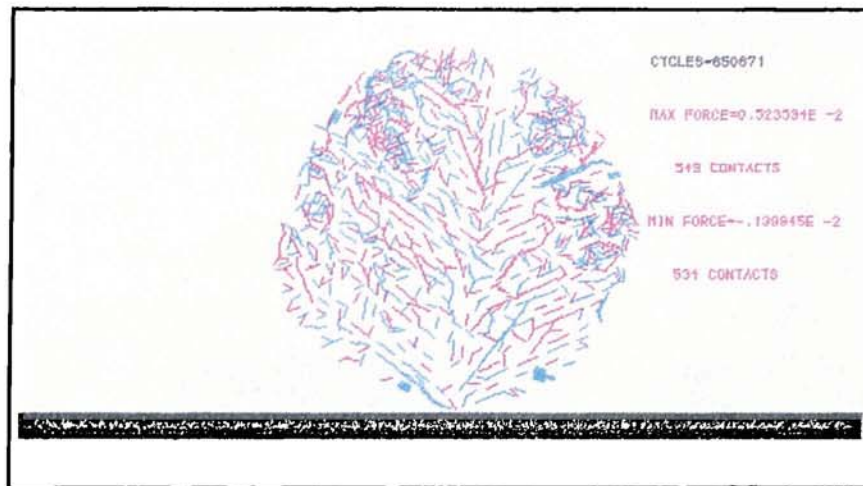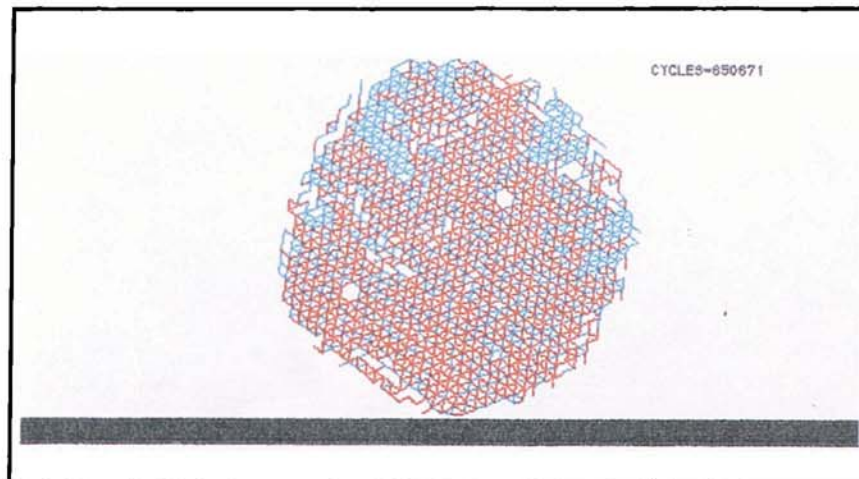
Force plot
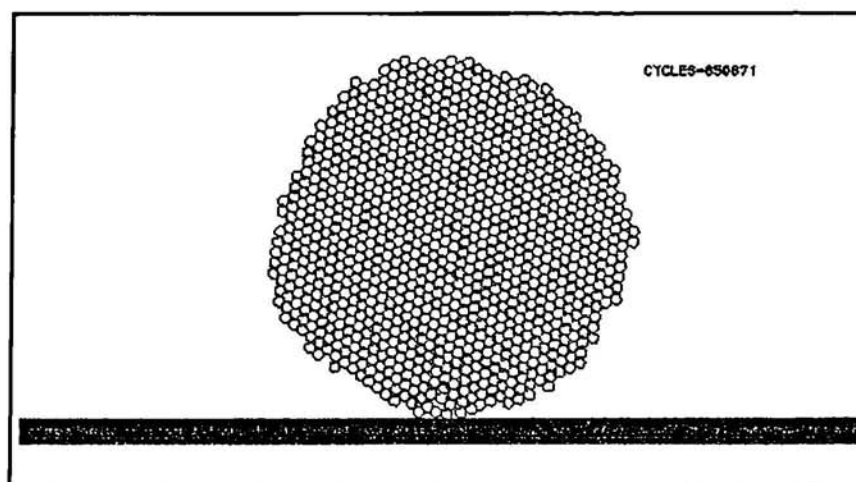
Lattice plot

Ball plot

B3 Velocity of impact = 0.8 m/s, γ = 3.0 Jm^{-2}
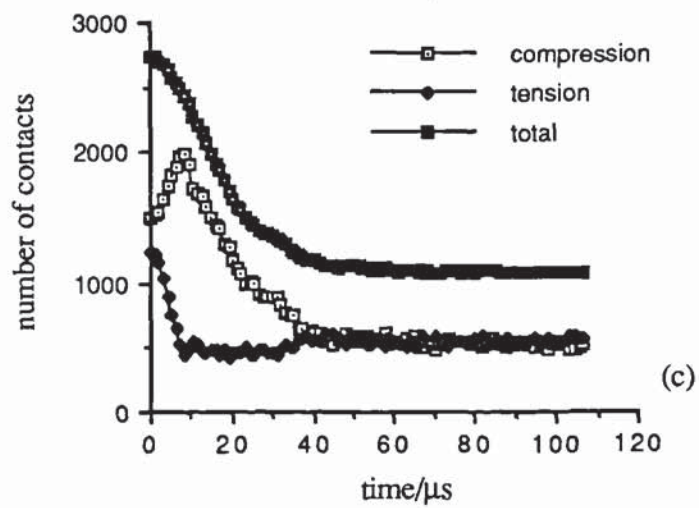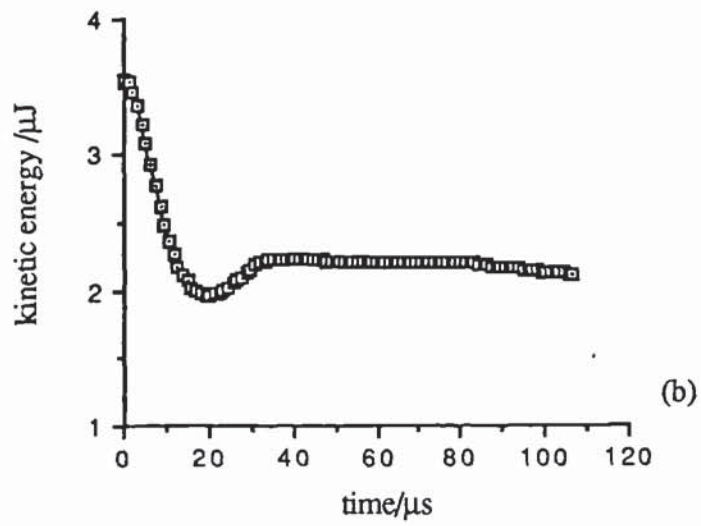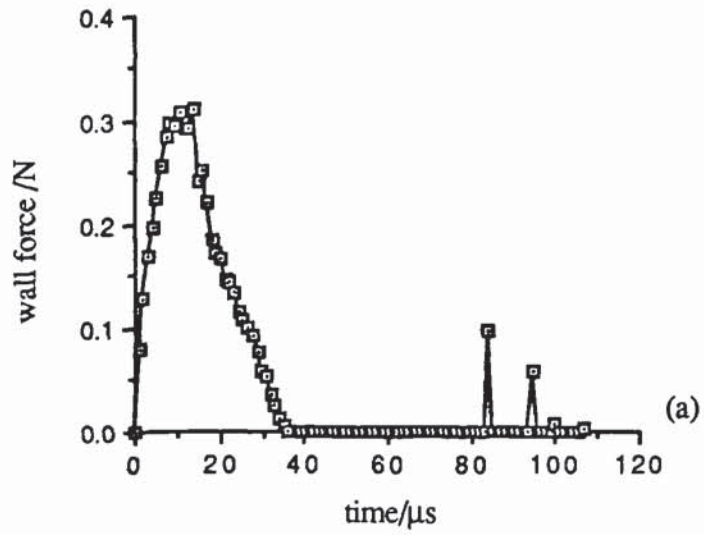
B4 Data for Velocity 0.8m/s, $\gamma = 3.0$ Jm^{-2}
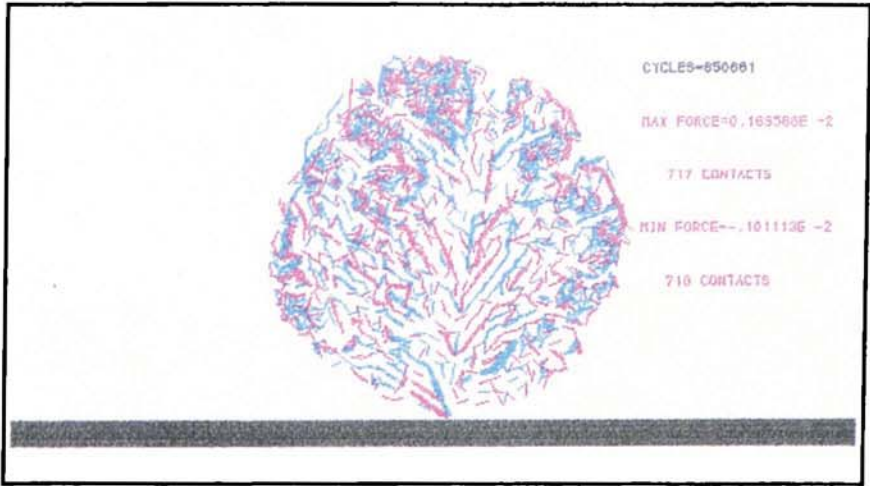
Force plot
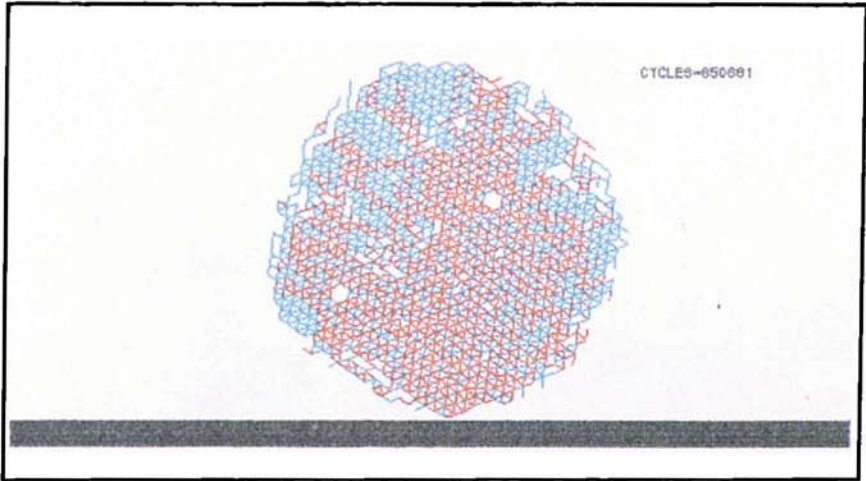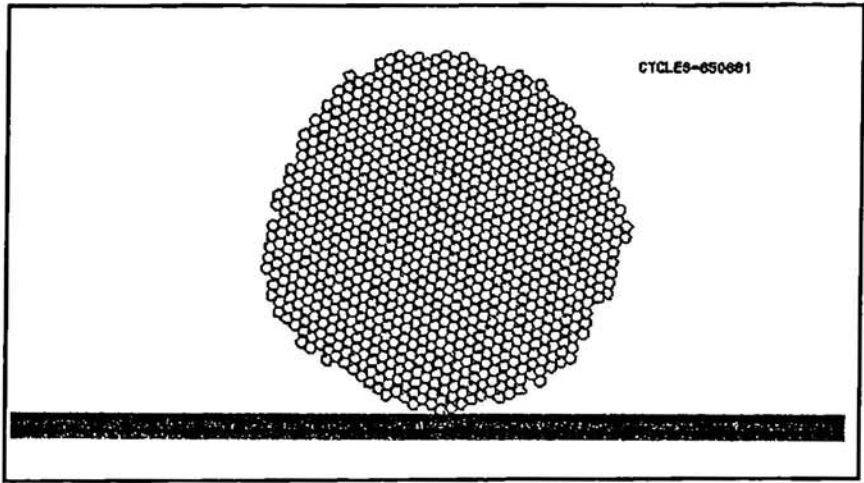
Lattice plot

Ball plot

B5 Velocity of impact = 0.5 m/s, γ = 3.0 Jm^{-2}

(a)

(b)

(c)
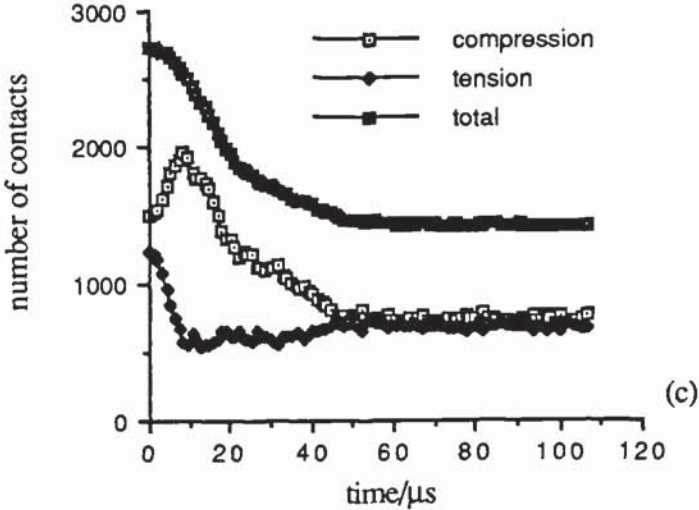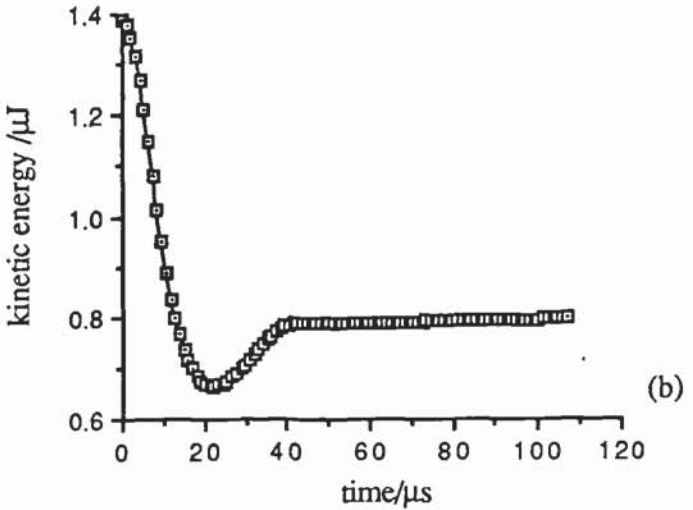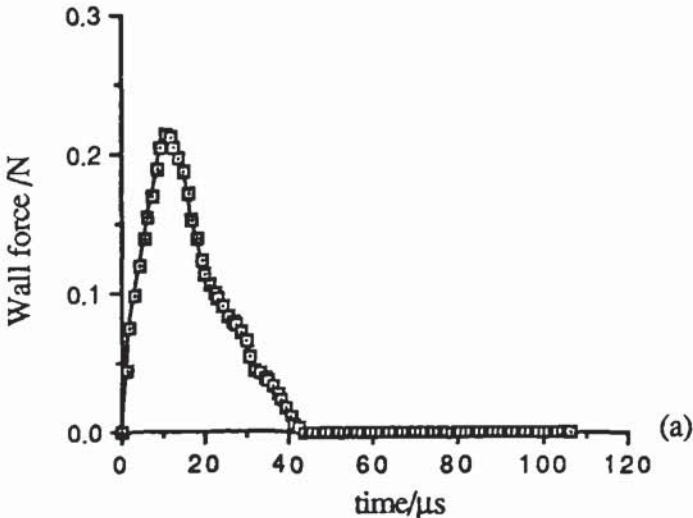
B6 Data for Velocity 0.5 m/s, $\gamma = 3.0$ Jm^{-2}
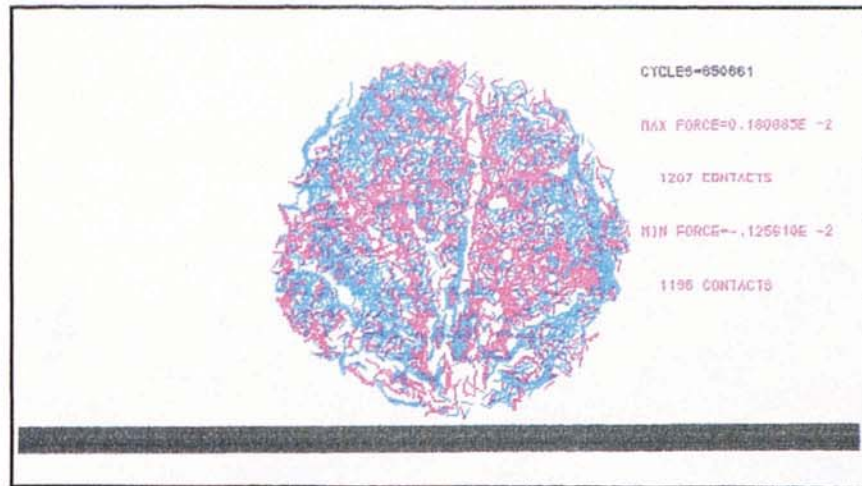
Force plot
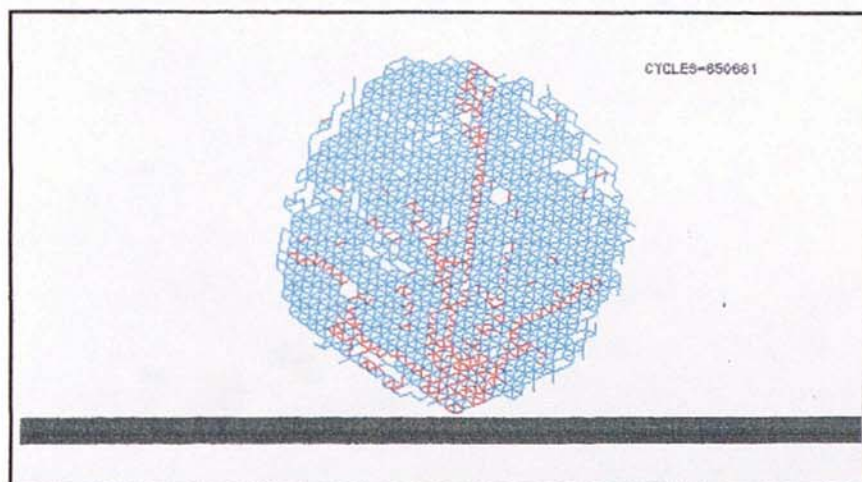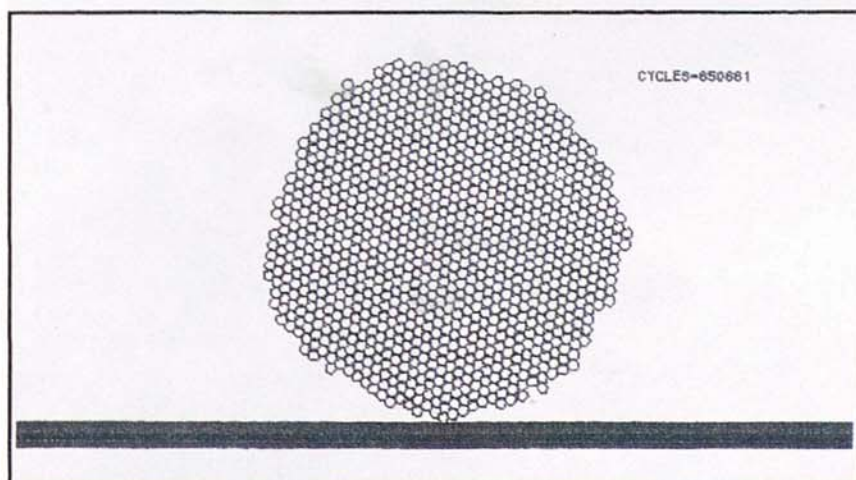
Lattice plot

Ball plot

B7 Velocity of impact = 0.09 m/s, γ = 3.0 Jm^{-2}
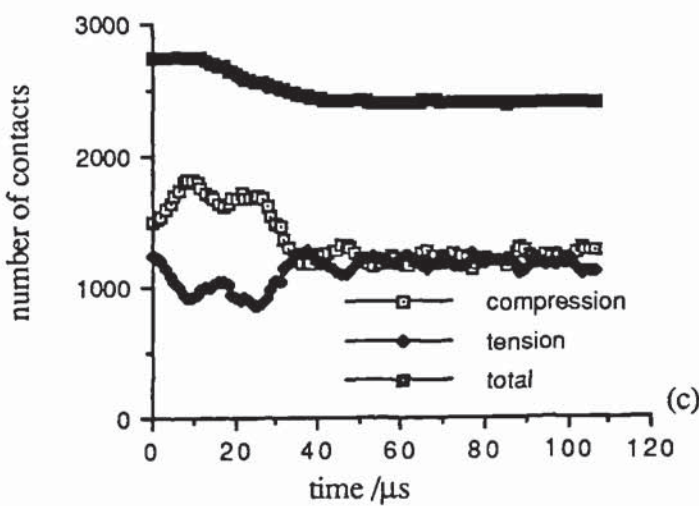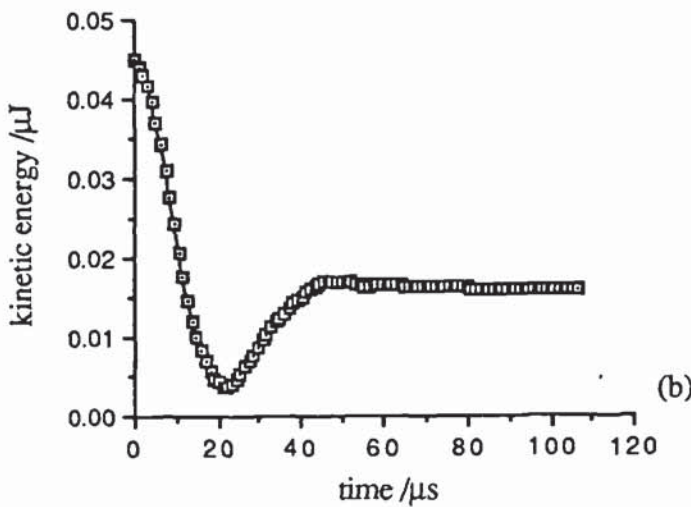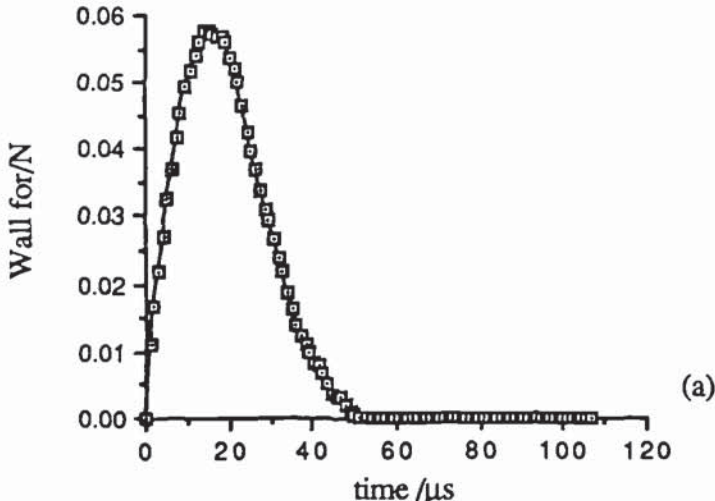
B8 Data for Velocity 0.09 m/s, $\gamma = 3.0$ Jm^{-2}

248
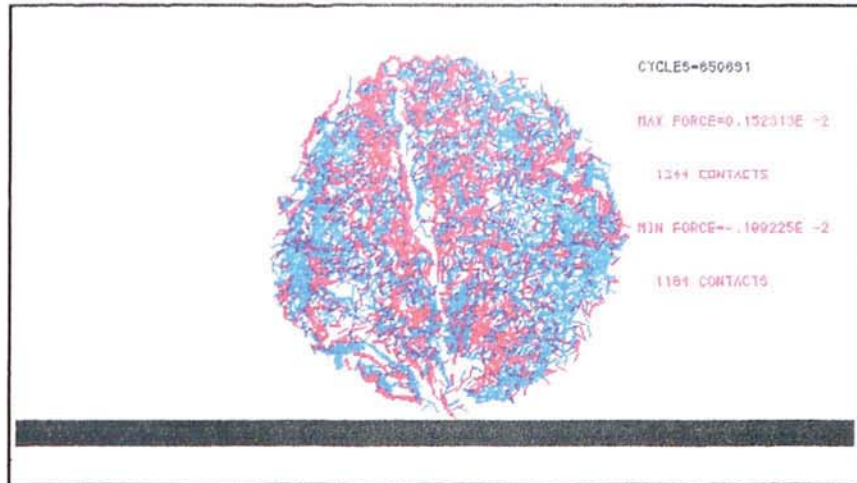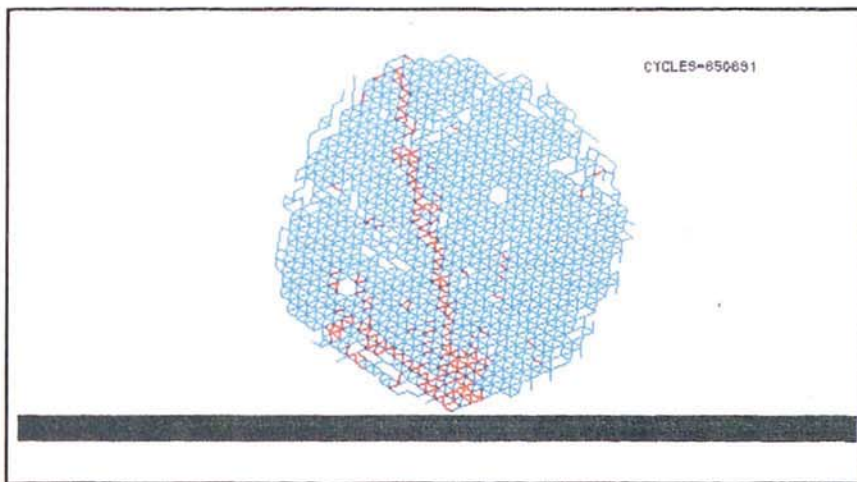
Force plot
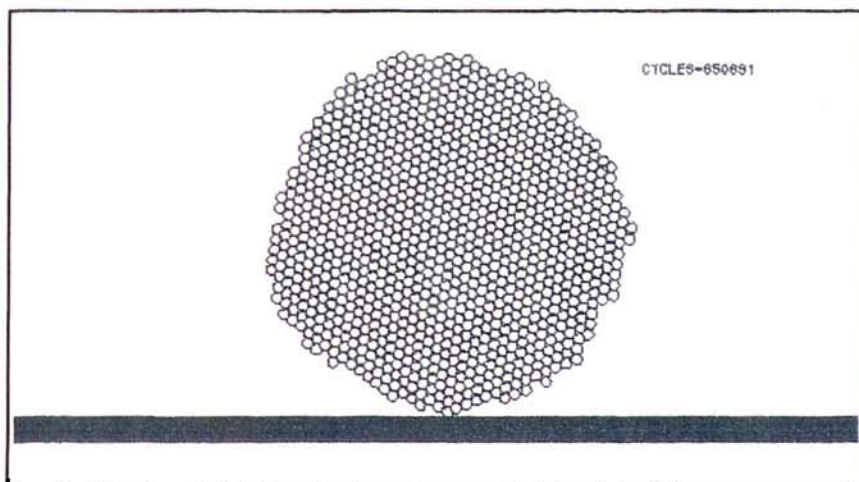
Lattice plot

Ball plot

B9 Velocity of impact = 0.08 m/s, $\gamma' = 3.0$ Jm^{-2}
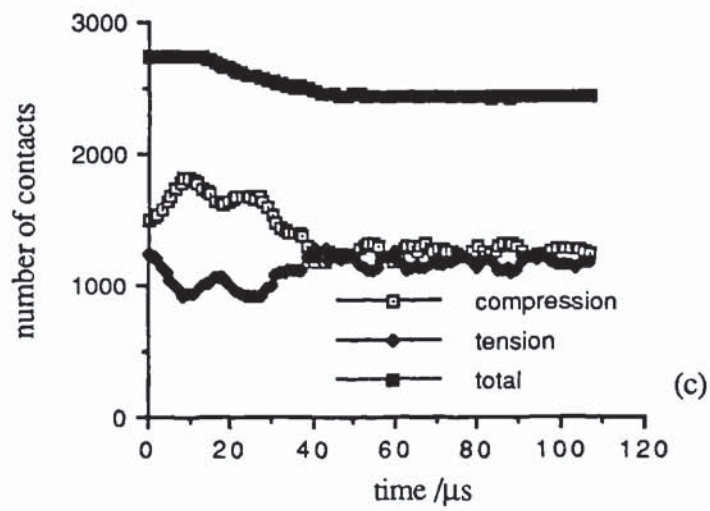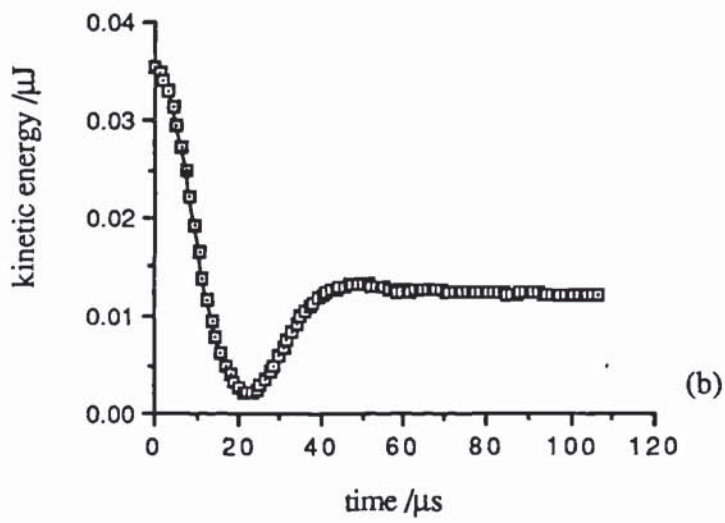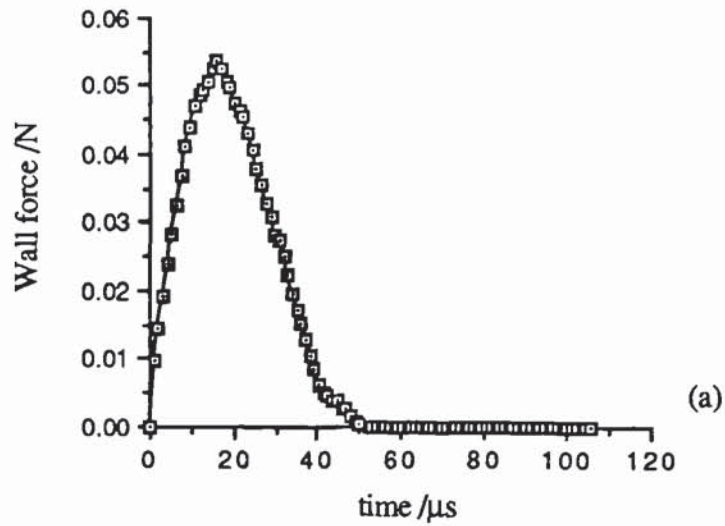
B10 Data for Velocity 0.08 m/s, $\gamma = 3.0$ Jm^{-2}
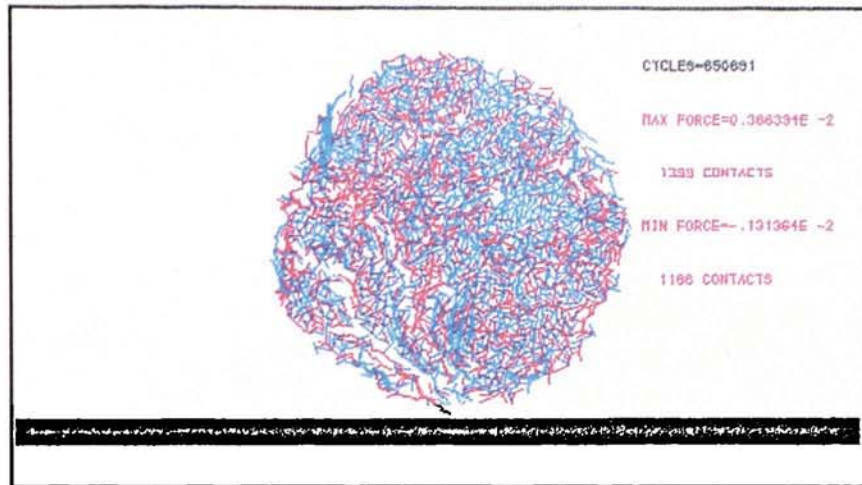
Force plot
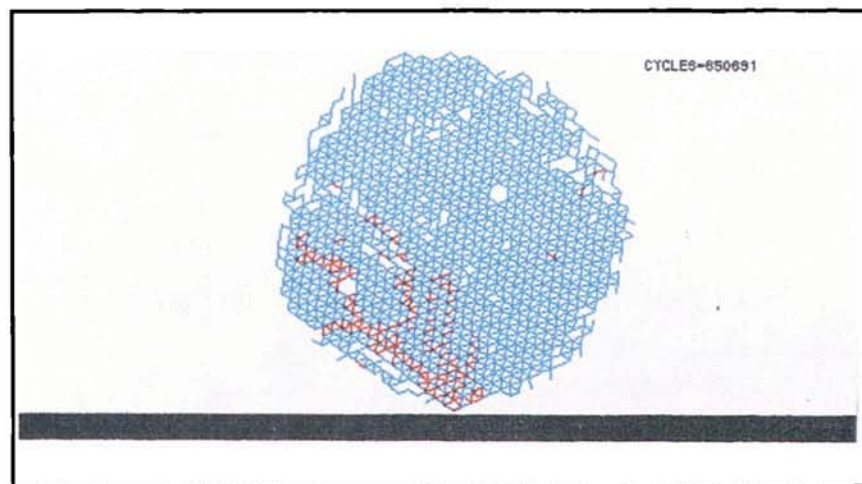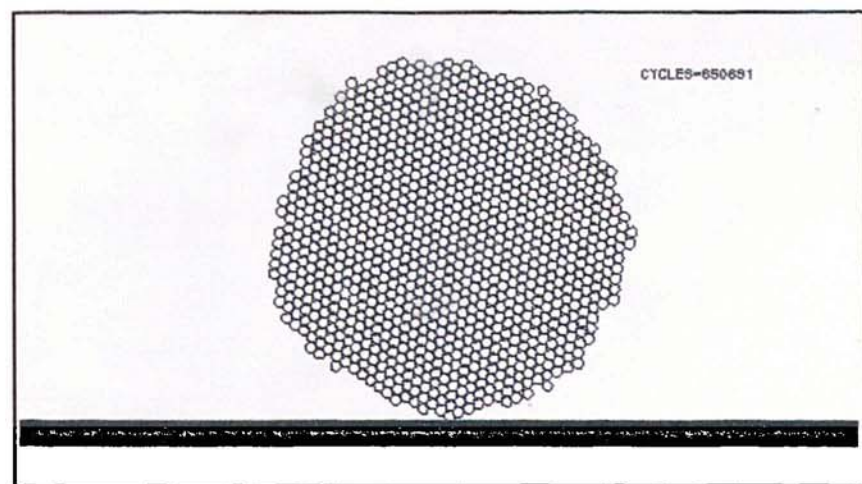
Lattice plot

Ball plot

B11 Velocity of impact = 0.07 m/s, $\gamma = 3.0$ Jm^{-2}
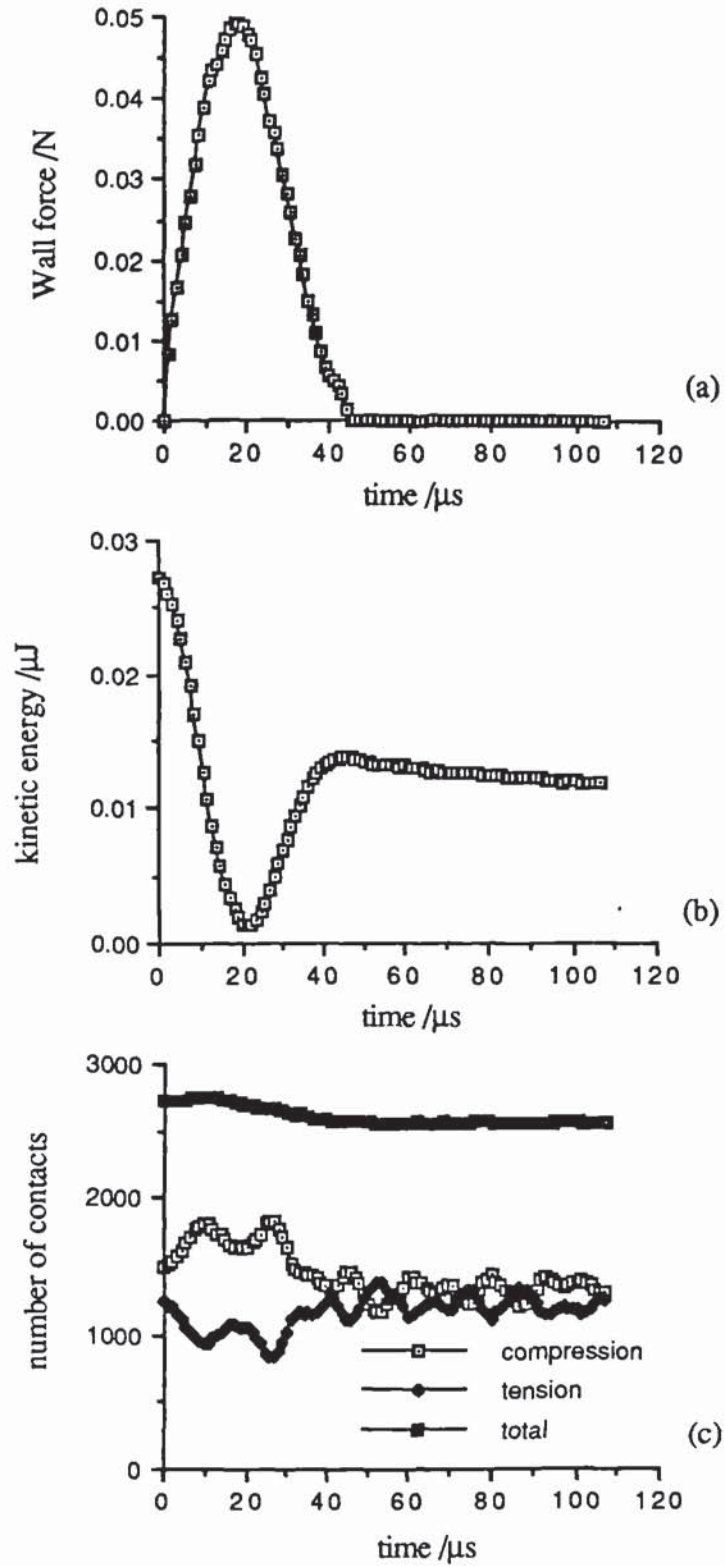
B12 Data for Velocity 0.07 m/s, $\gamma = 3.0$ Jm^{-2}
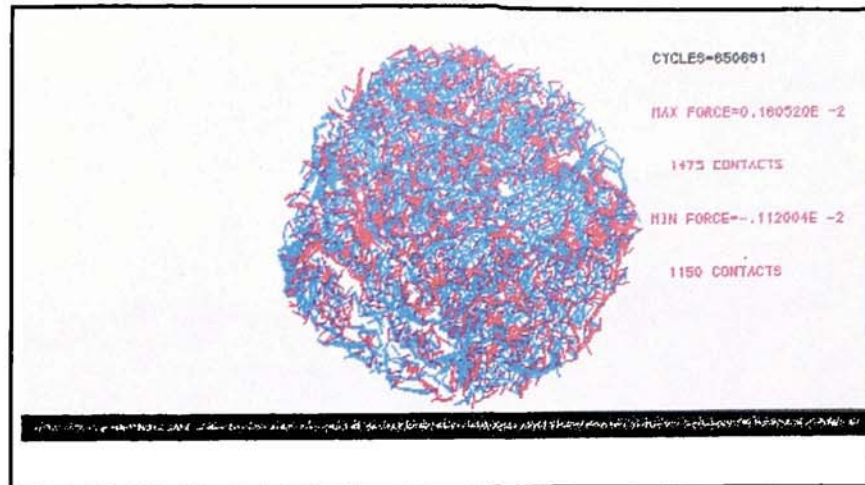
Force plot
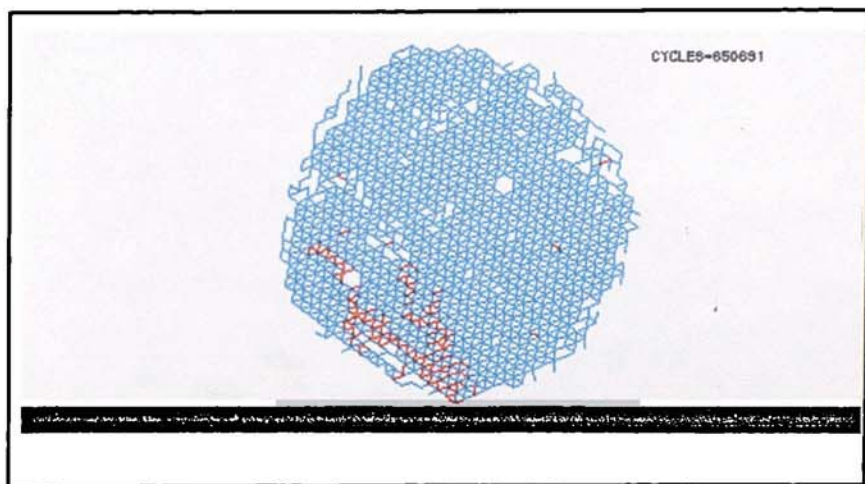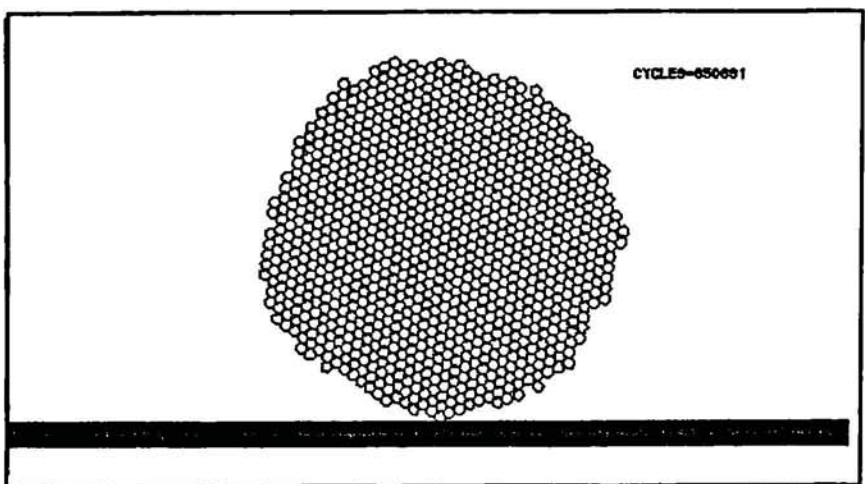
Lattice plot

Ball plot

B13 Velocity of impact = 0.06 m/s, γ = 3.0 Jm^{-2}
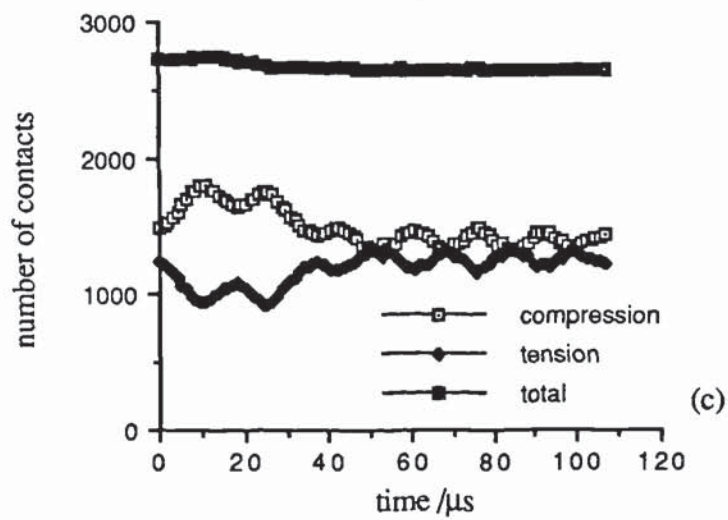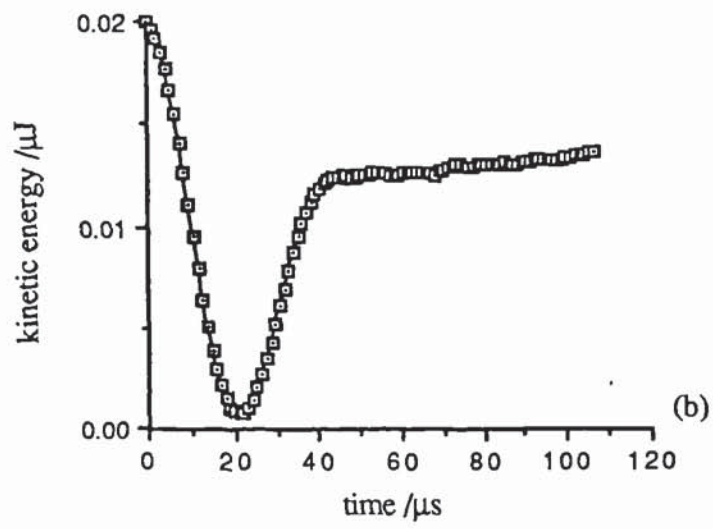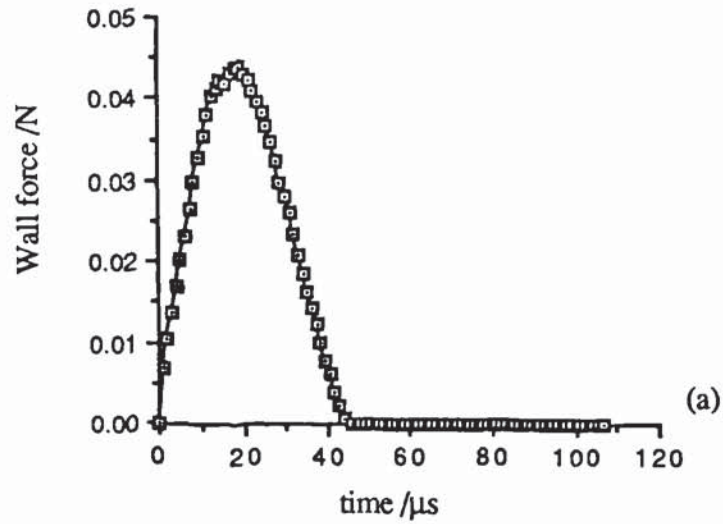
B14 Data for Velocity 0.06m/s, $\gamma = 3.0$ Jm^{-2}
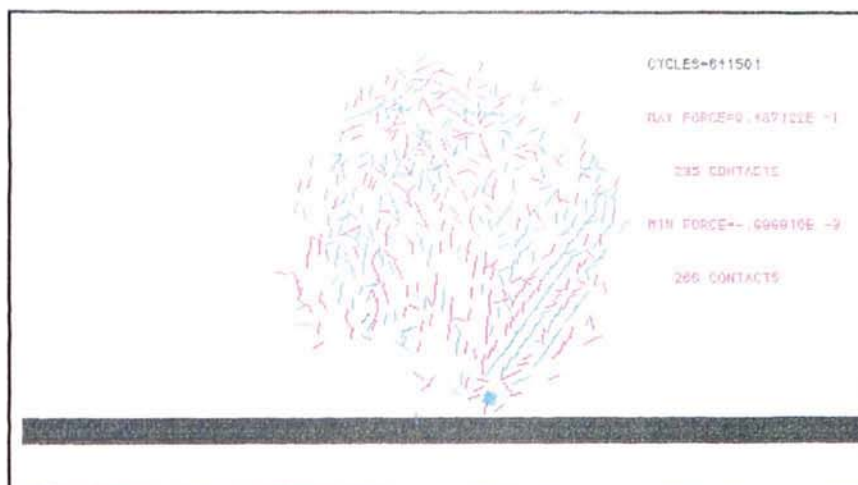
Force plot
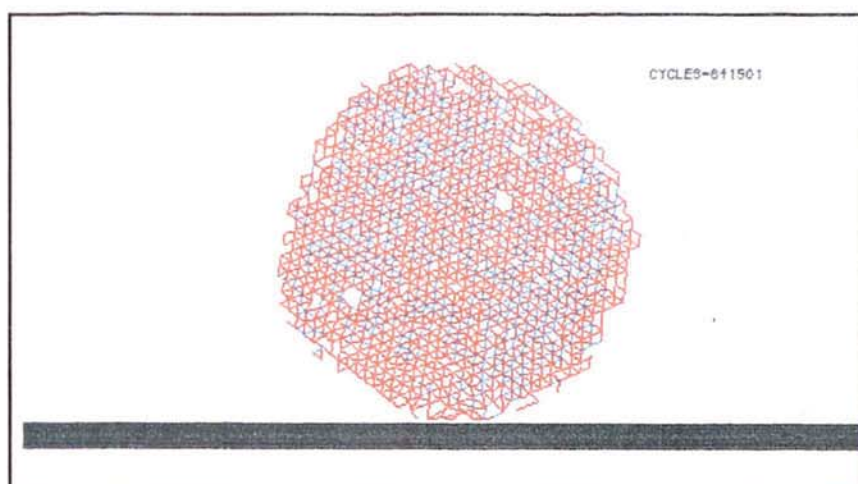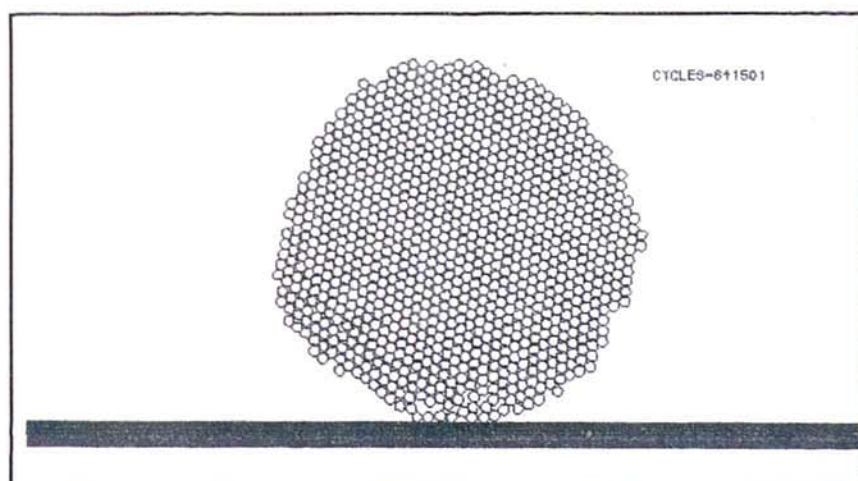
Lattice plot

Ball plot

B15 Velocity of impact = 1.0 m/s, γ^j = 2.0 Jm^{-2}
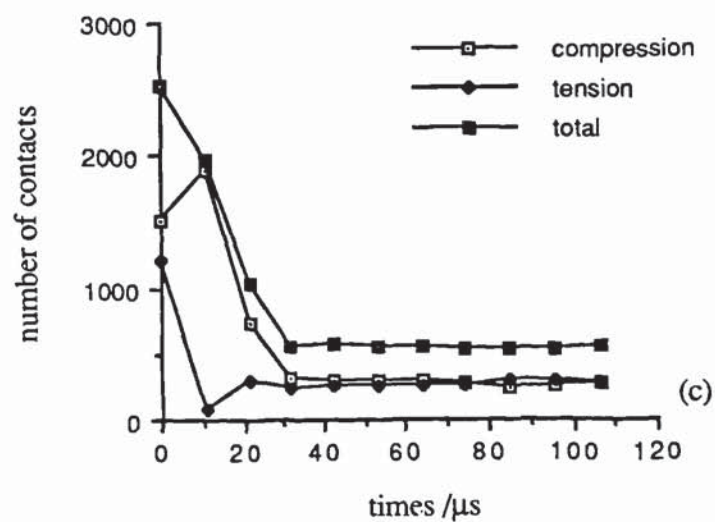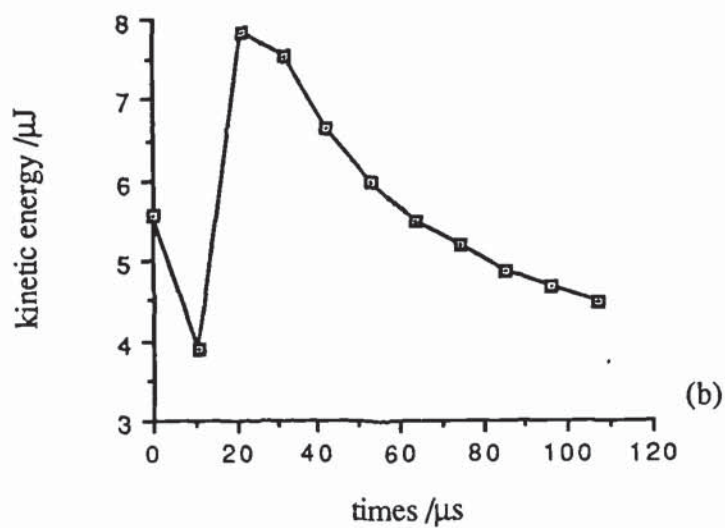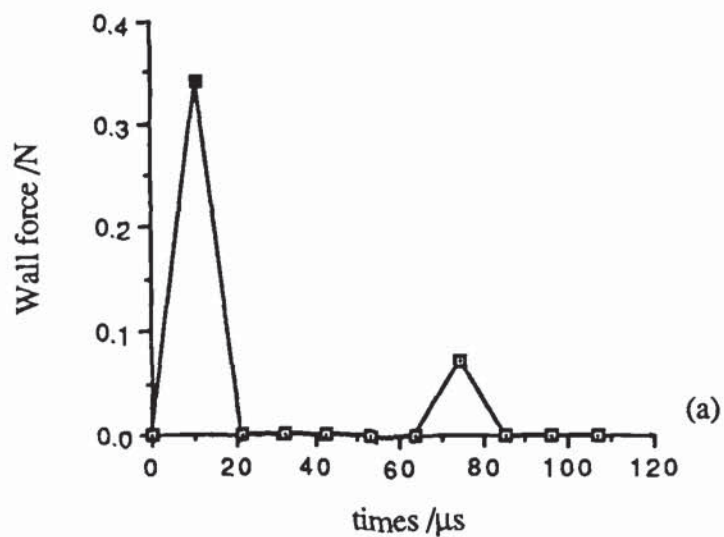
B16 Data for Velocity 1.0m/s, $\gamma = 2.0$ Jm^{-2}
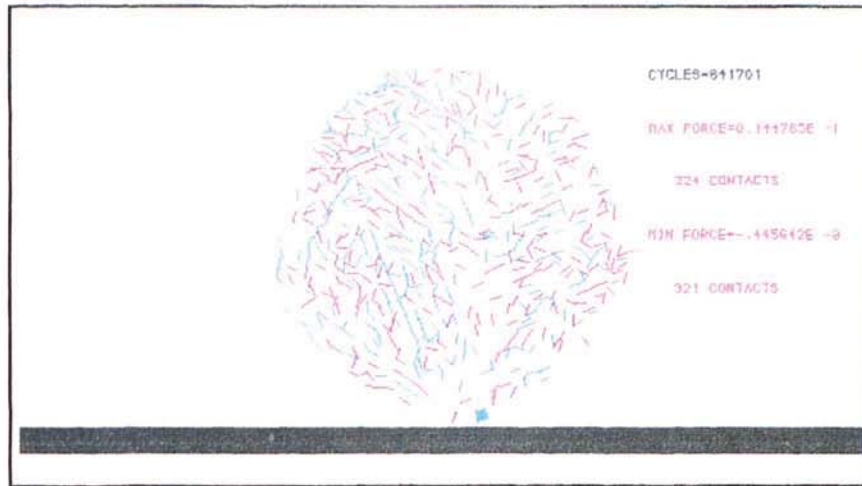
Force plot
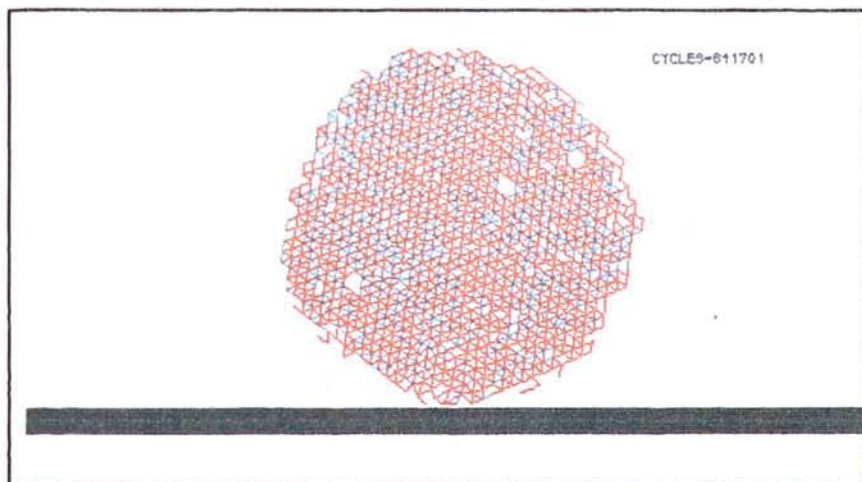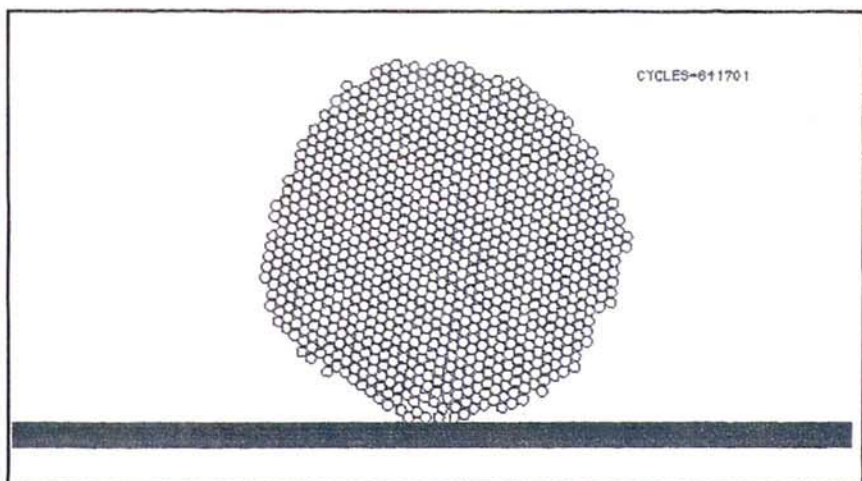
Lattice plot

Ball plot

B17 Velocity of impact = 0.8 m/s,γ= 2.0 Jm^{-2}

257
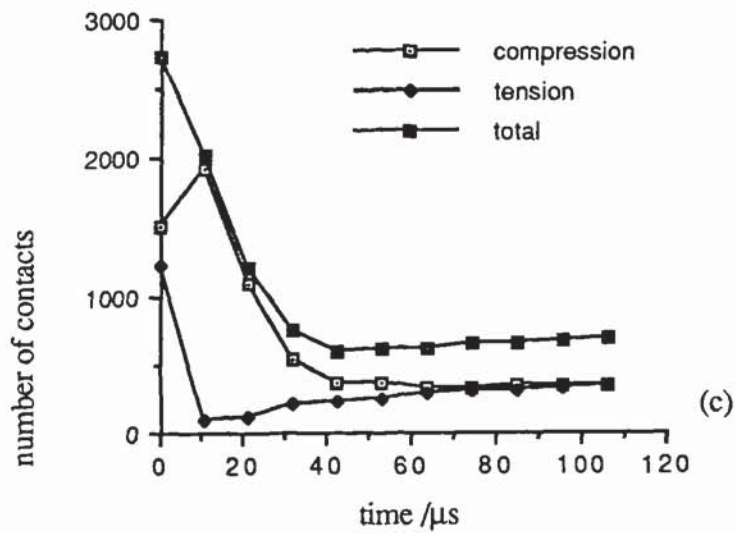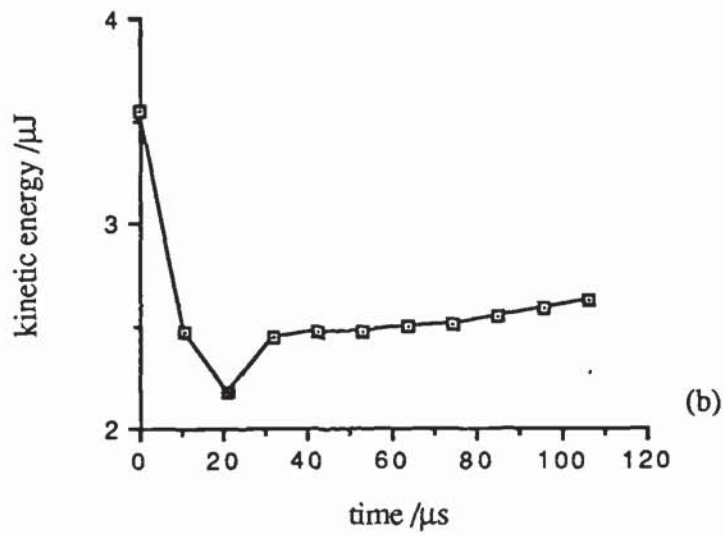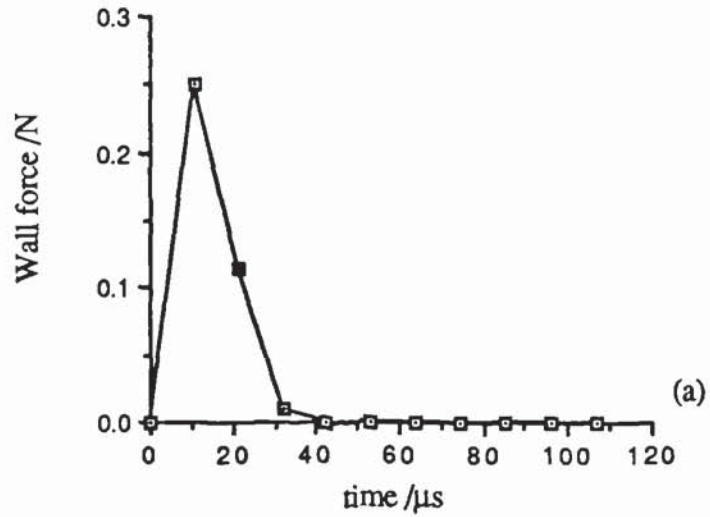
B18 Data for Velocity 0.8m/s, $\gamma = 2.0$ Jm^{-2}
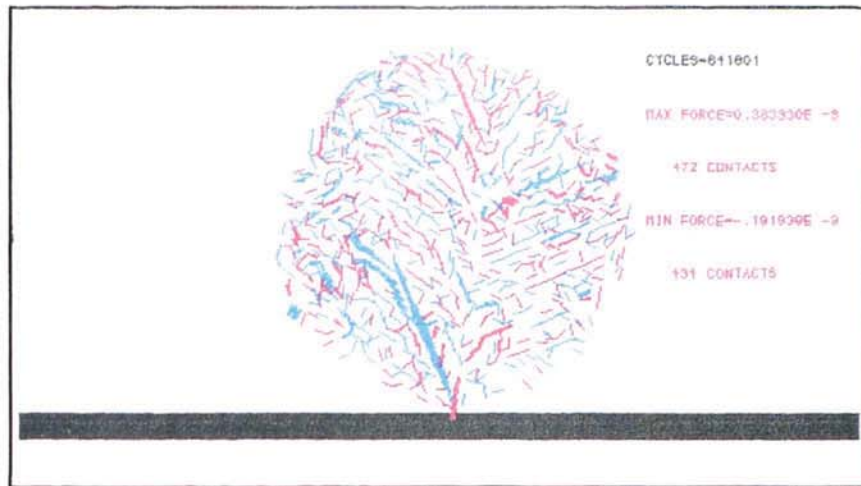
Force plot
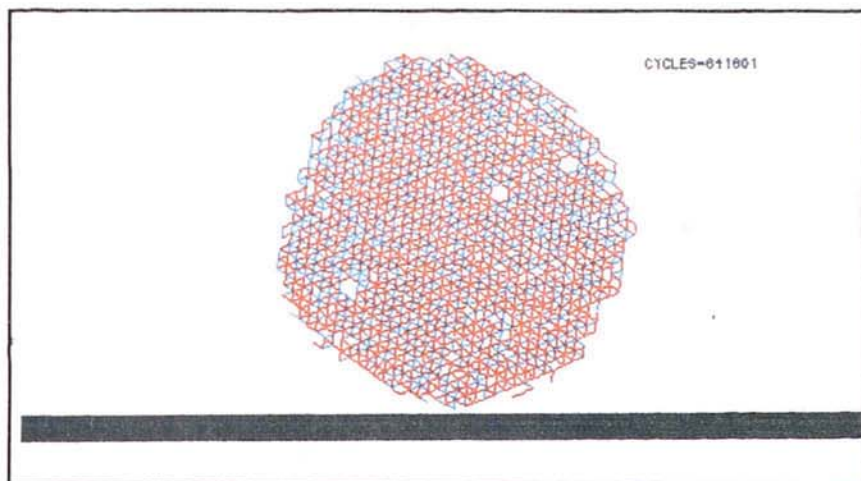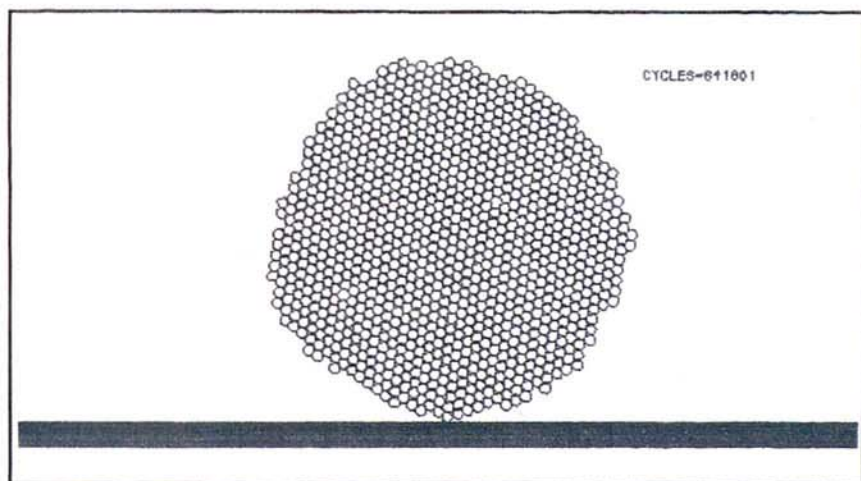
Lattice plot

Ball plot

B19 Velocity of impact = 0.5 m/s, γ = 2.0 Jm^{-2}

259

(a)

(b)

(c)
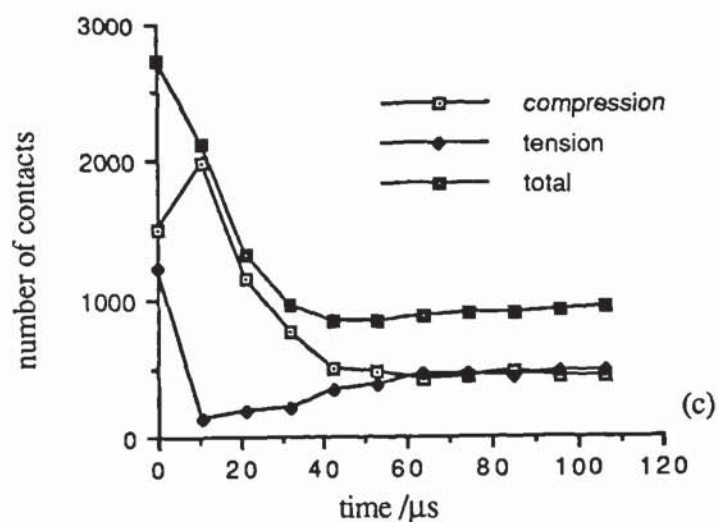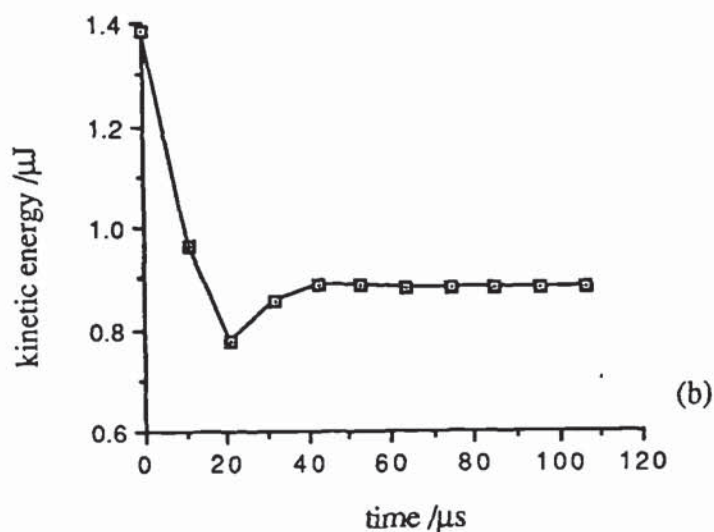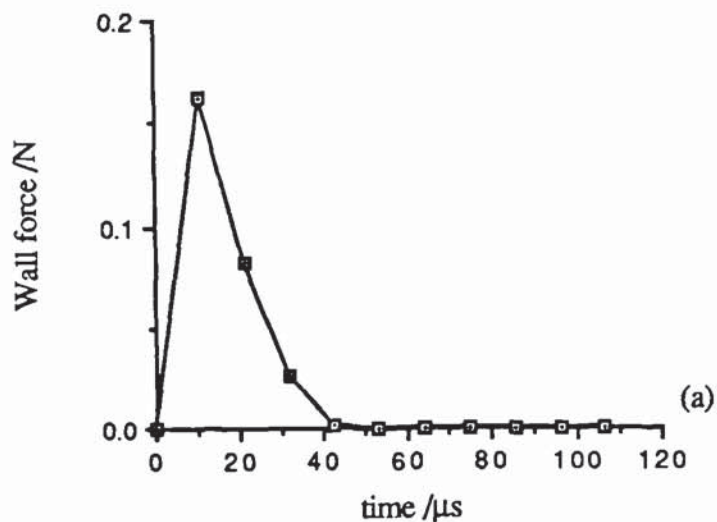
B20 Data for Velocity 0.5m/s, $\gamma = 2.0$ Jm^{-2}
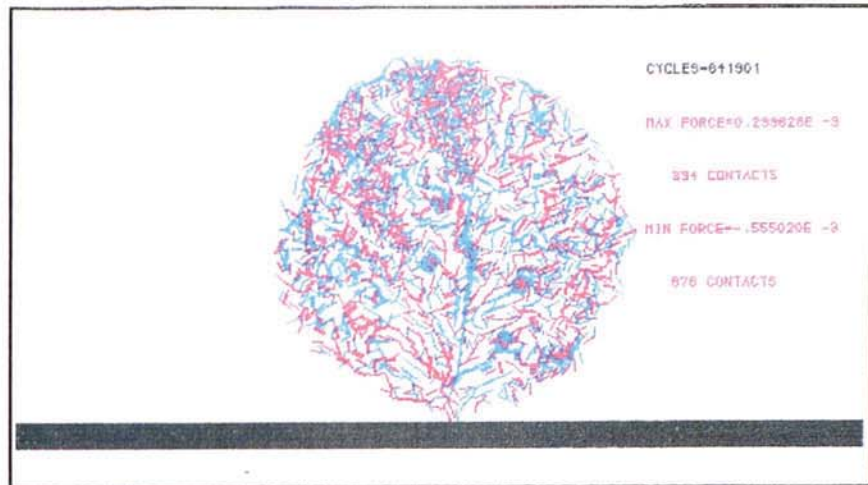
Force plot
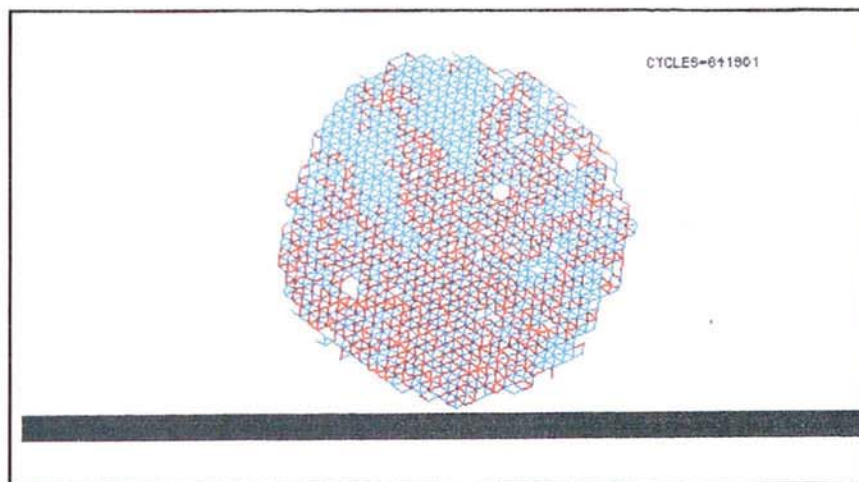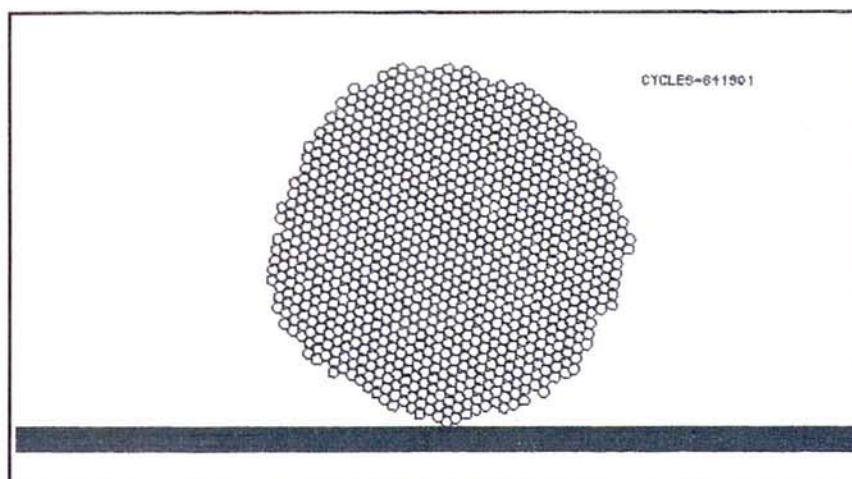
Lattice plot

Ball plot

B21 Velocity of impact = 0.1 m/s, γ = 2.0 Jm^{-2}

(a)

(b)

(c)
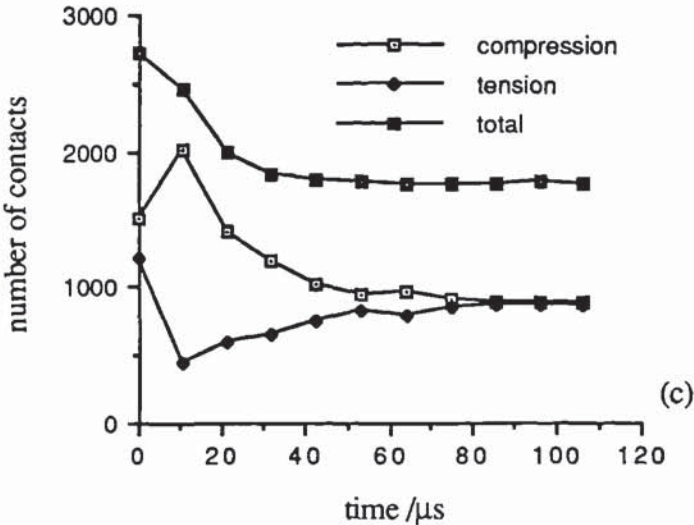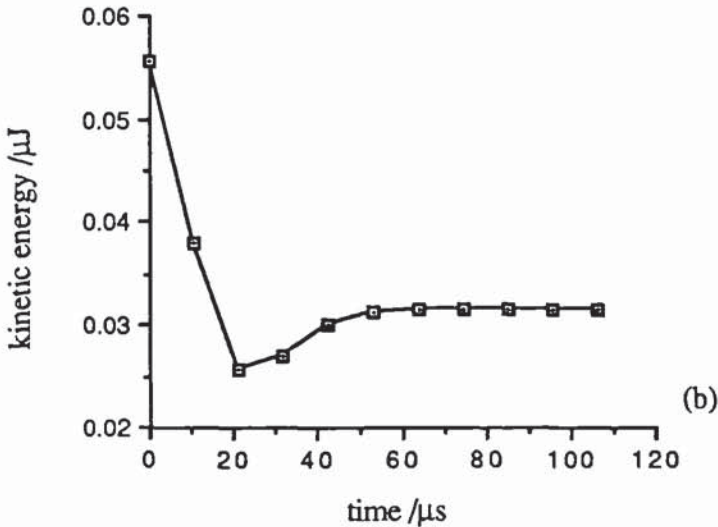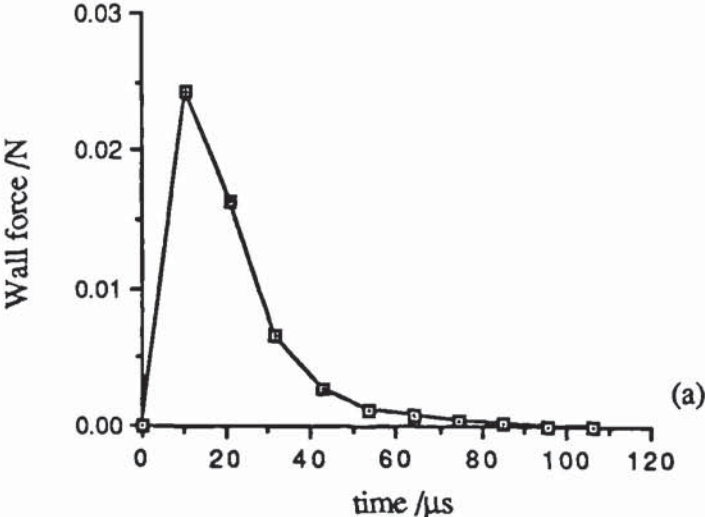
B22 Data for Velocity 0.1m/s, $\gamma = 2.0$ Jm^{-2}

CYCLES=641901

MAX FORCE=0.507664E -5

1105 CONTACTS

MIN FORCE=-.639157E -9

892 CONTACTS

Force plot

CYCLES=641901

Lattice plot

CYCLES=641901
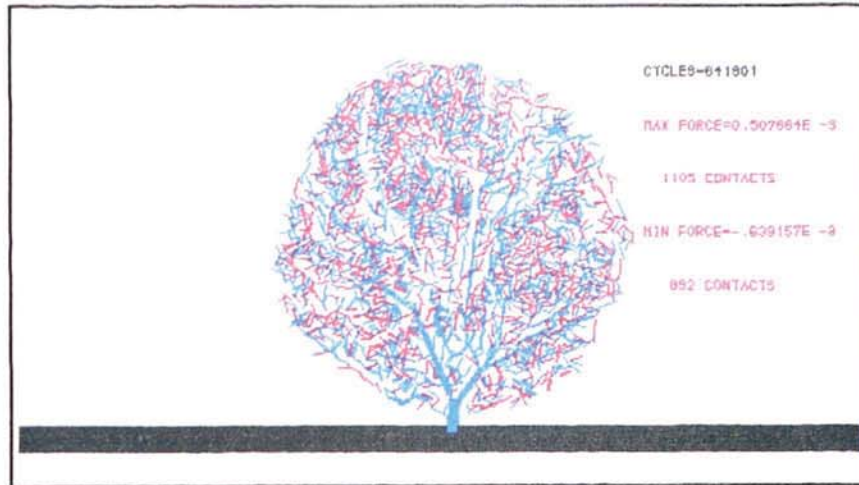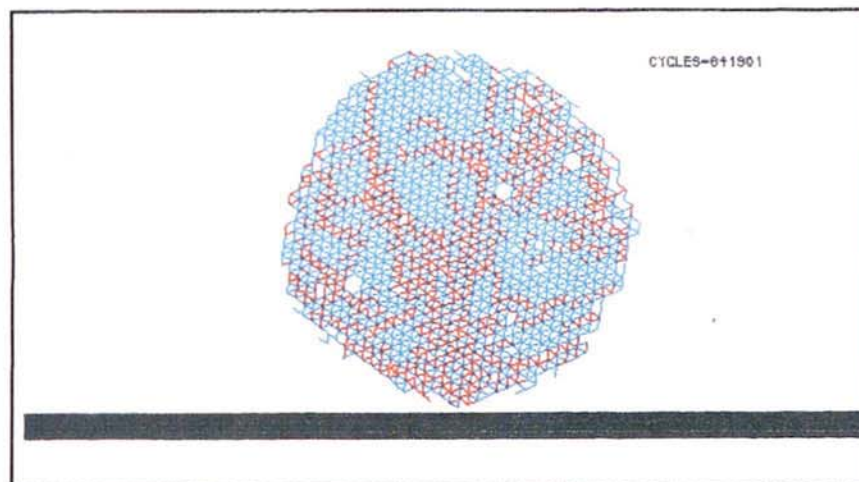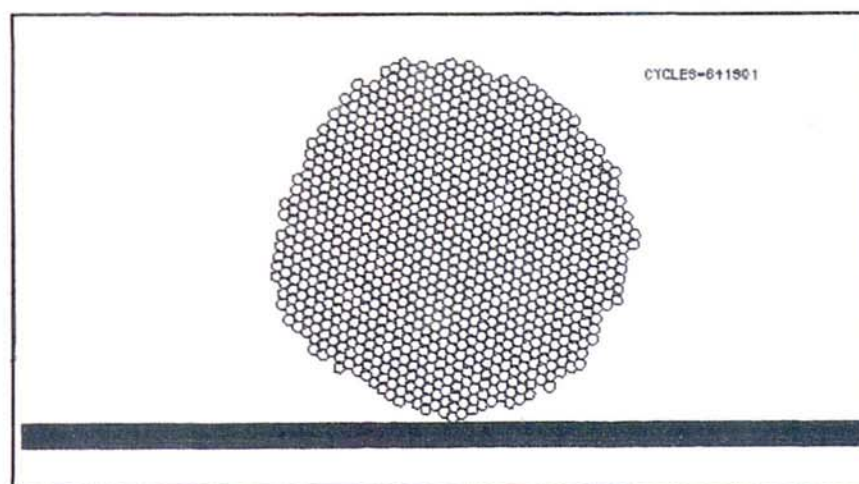
Ball plot

B23 Velocity of impact = 0.05 m/s, $\gamma = 2.0$ Jm^{-2}
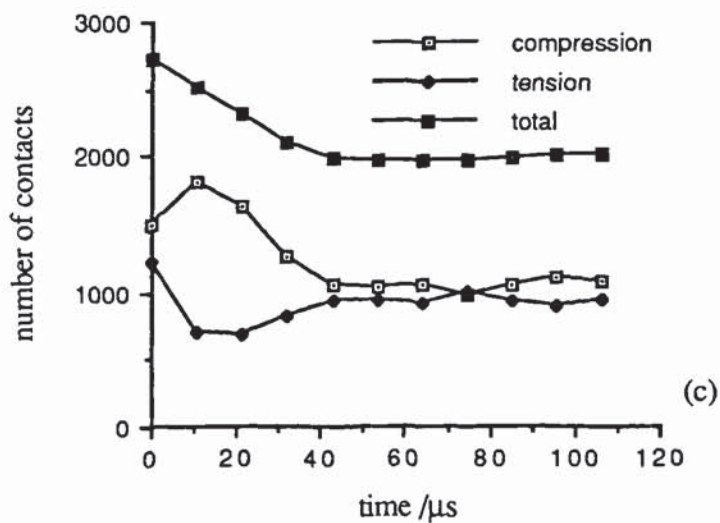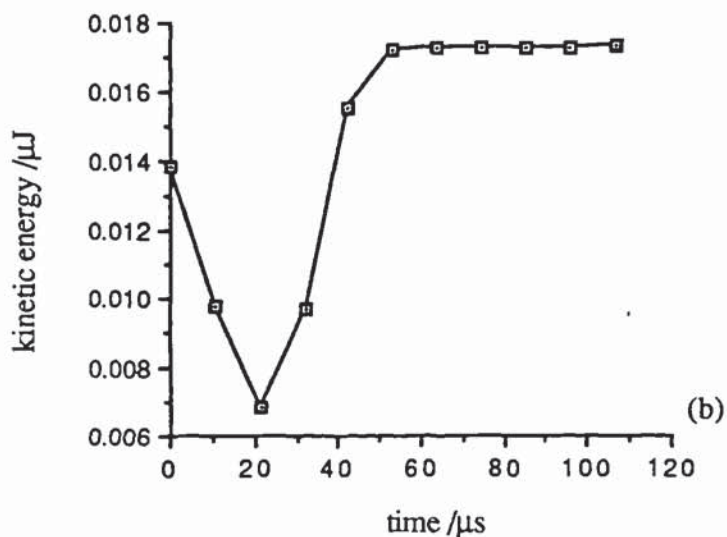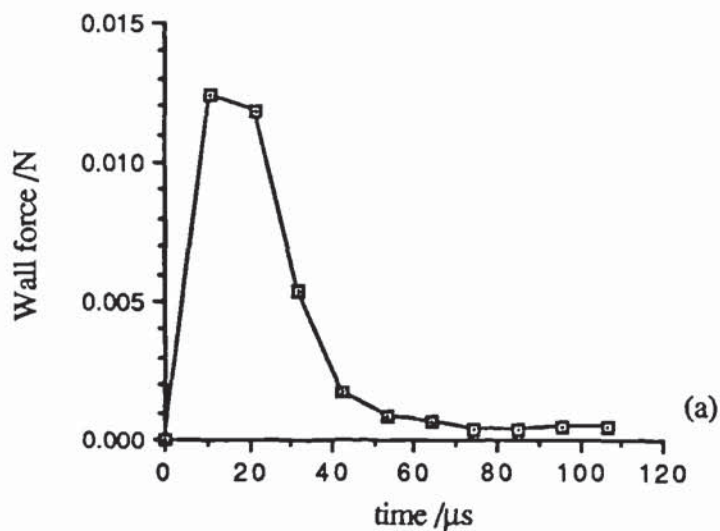
B24 Data for Velocity 0.05m/s, $\gamma = 2.0$ Jm^{-2}
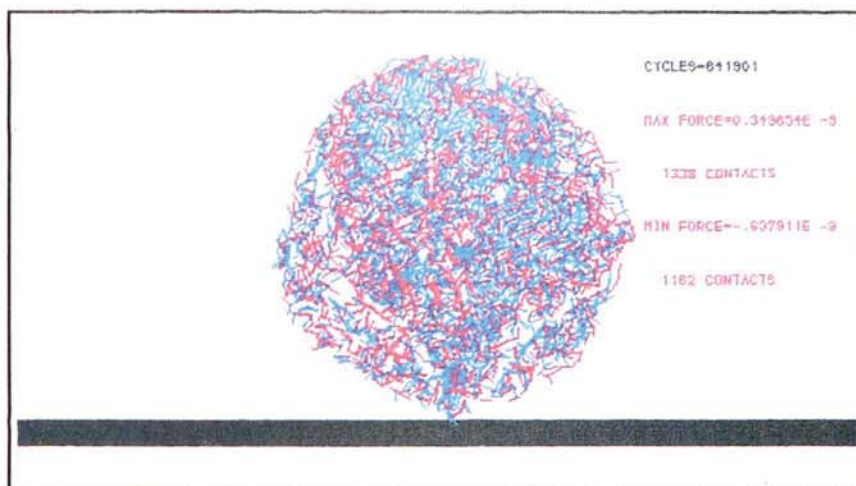
Force plot
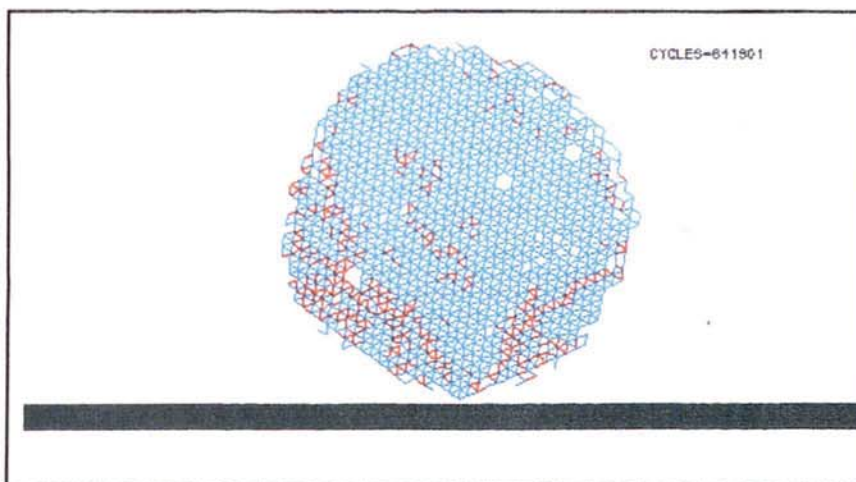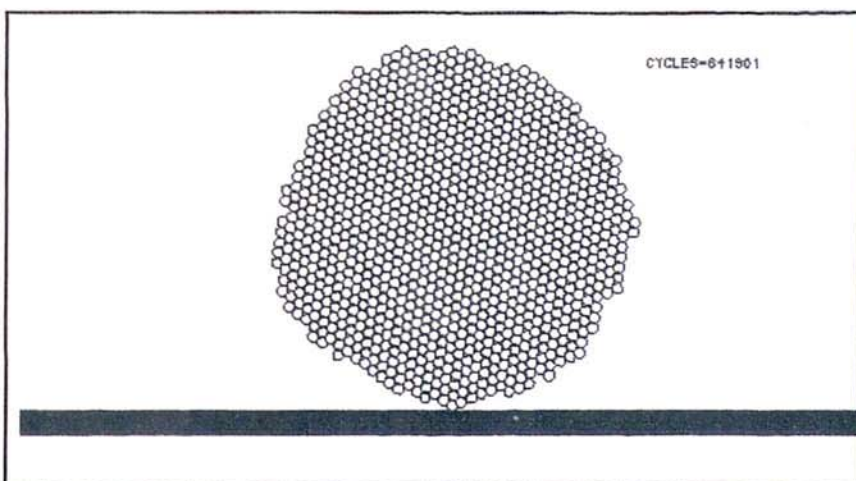
Lattice plot

Ball plot

B25 Velocity of impact = 0.01m/s, γ = 2.0 Jm^{-2}
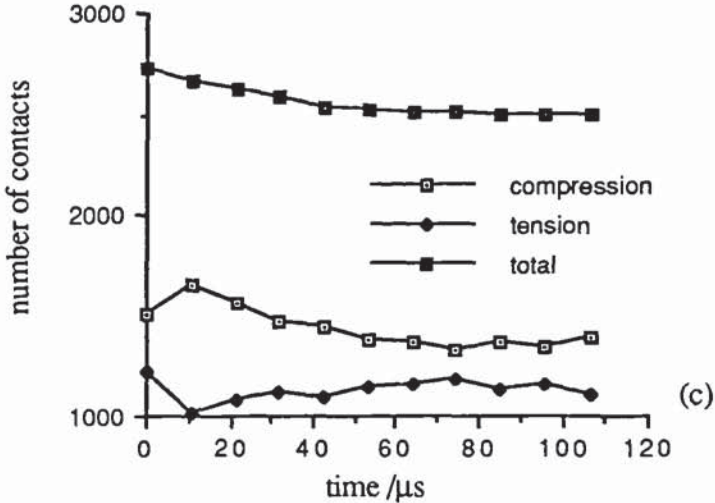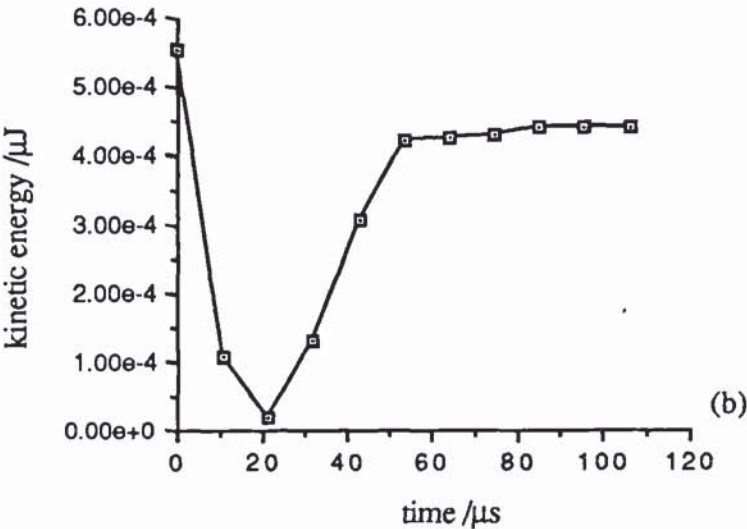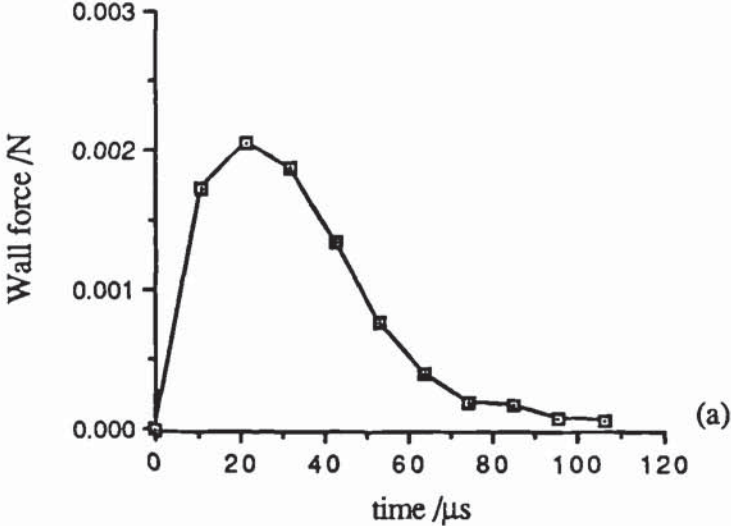
B26 Data for Velocity 0.01m/s, $\gamma = 2.0$ Jm^{-2}

266
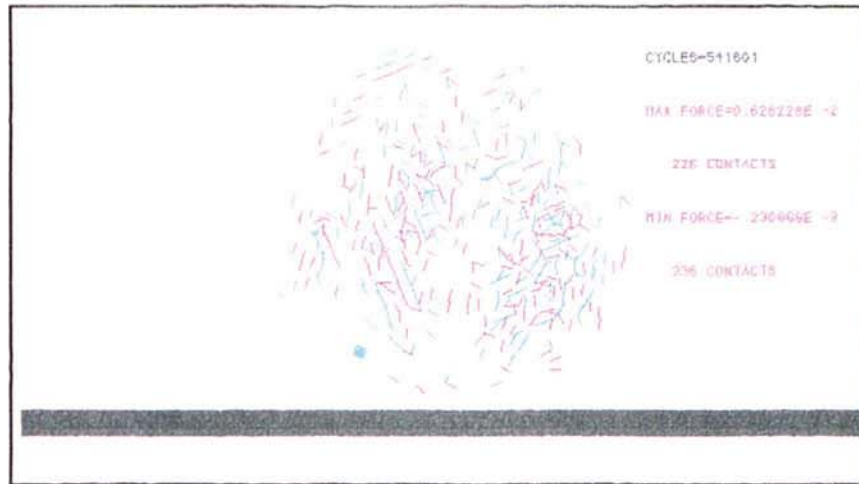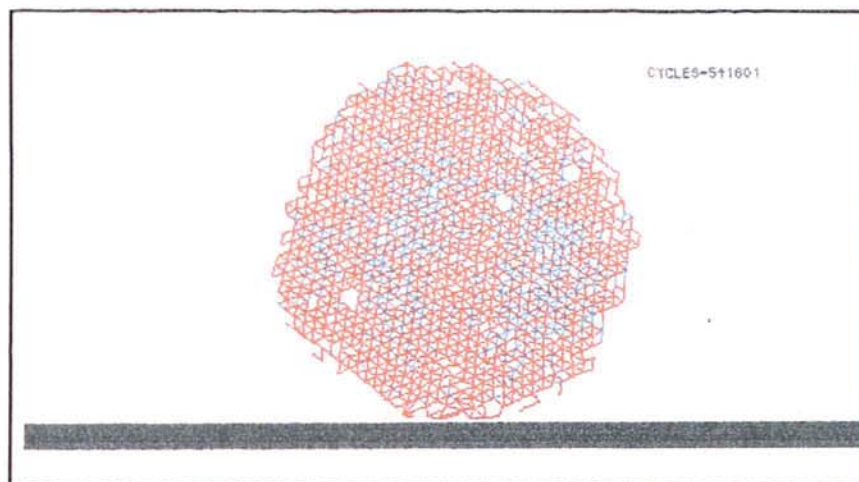
Force plot
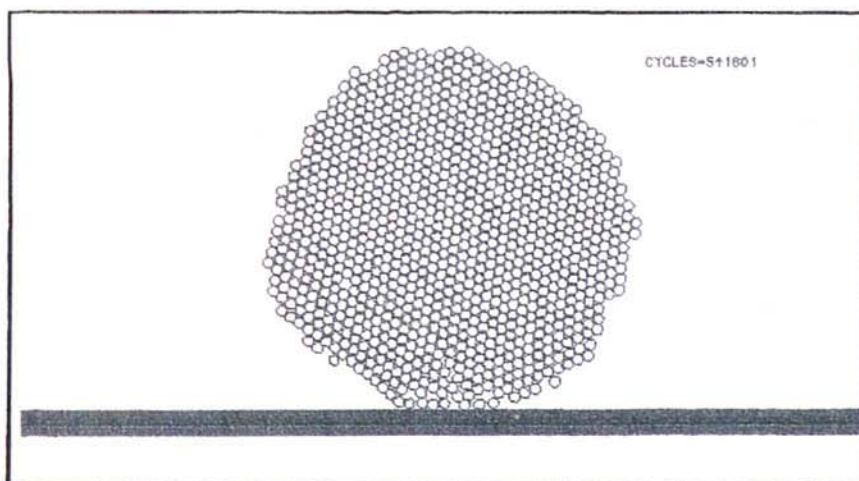
Lattice plot

Ball plot

B27 Velocity of impact = 1.0 m/s, γ = 1.0 Jm^{-2}
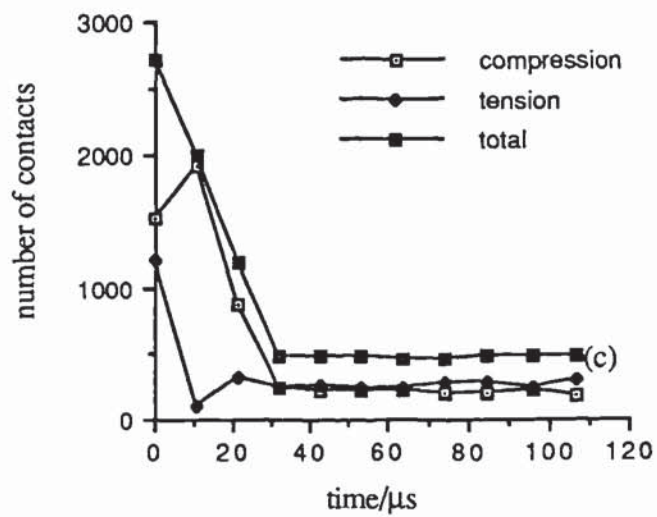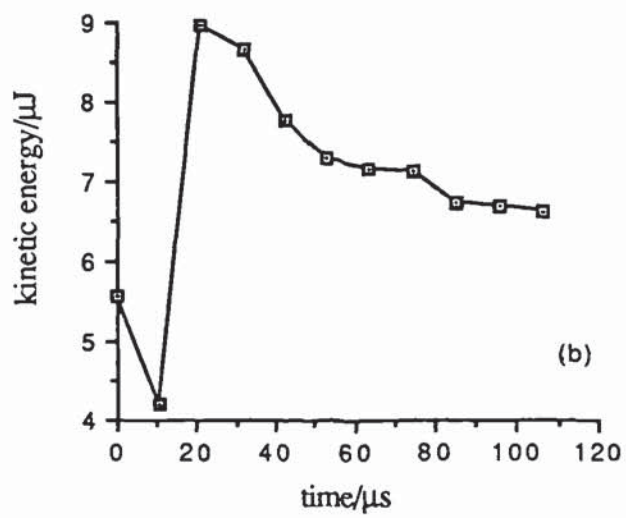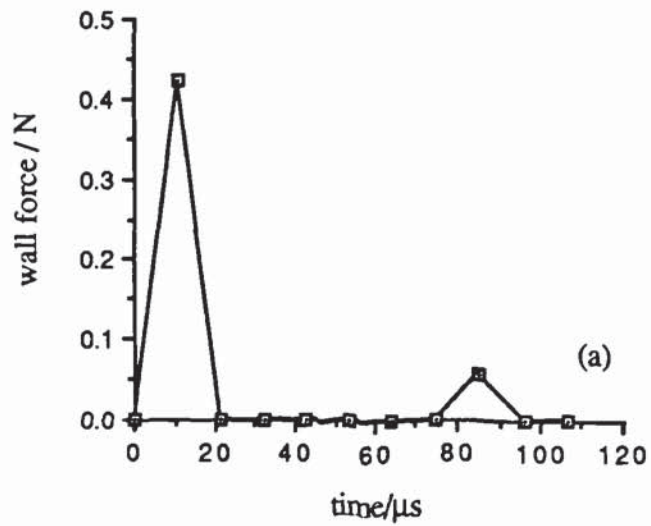
B28 Data for Velocity 1.0 m/s, $\gamma = 1.0$ Jm^{-2}
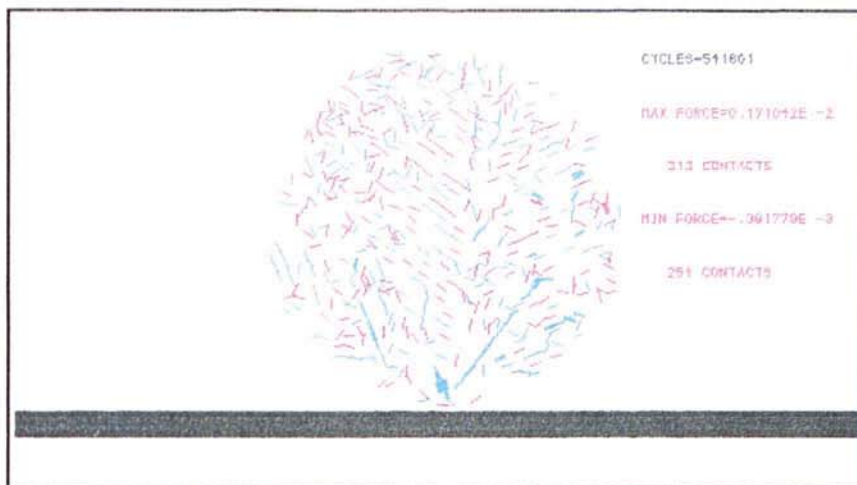
Force plot
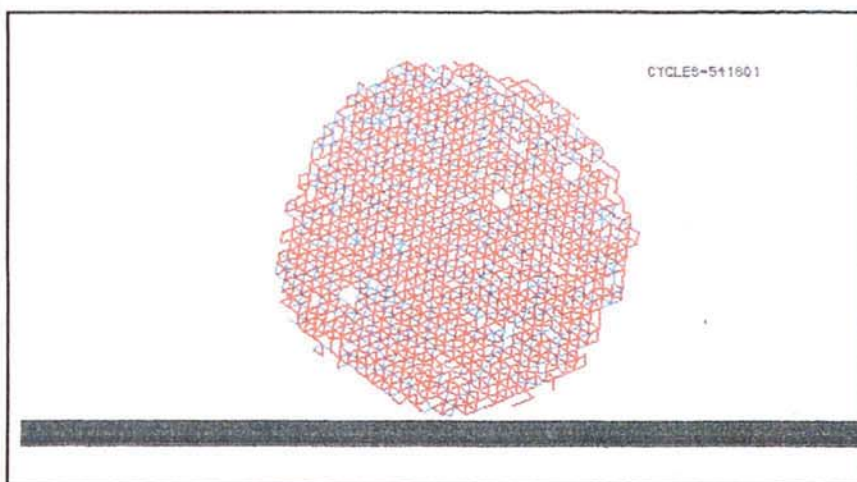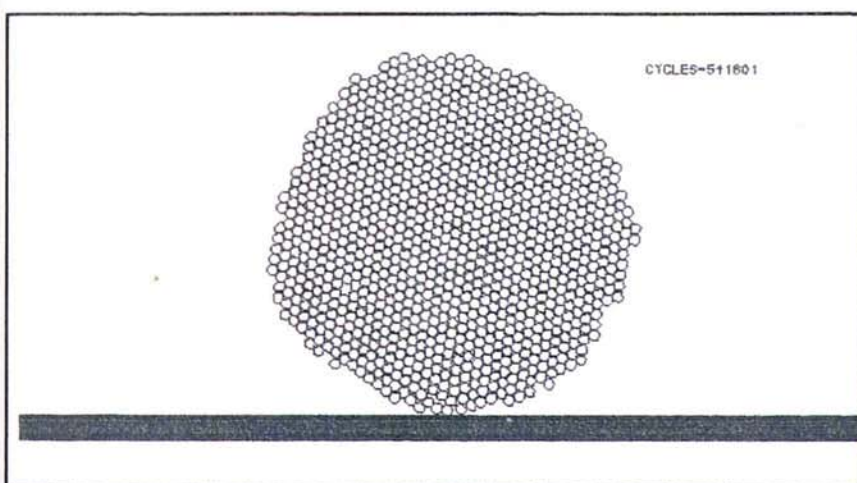
Lattice plot

Ball plot

B29 Velocity of impact = 0.8 m/s, $\gamma = 1.0$ Jm^{-2}
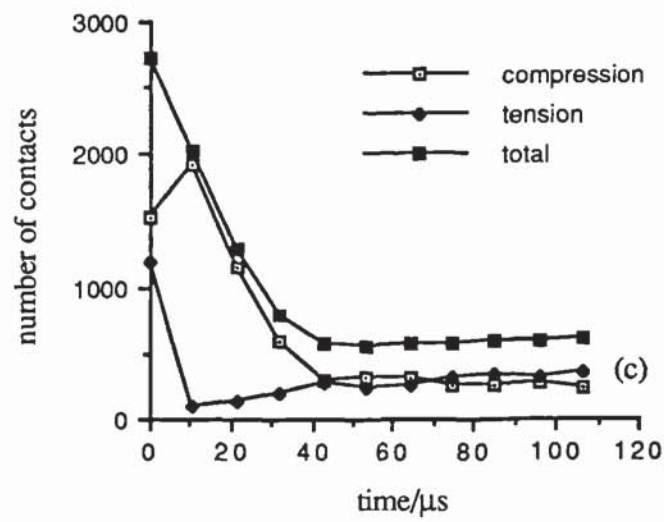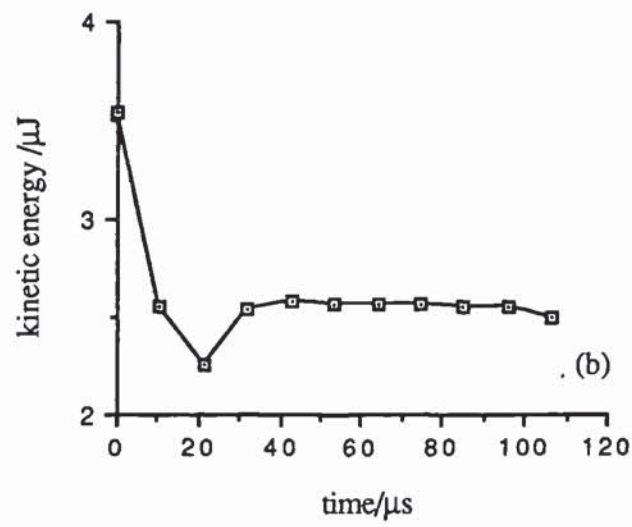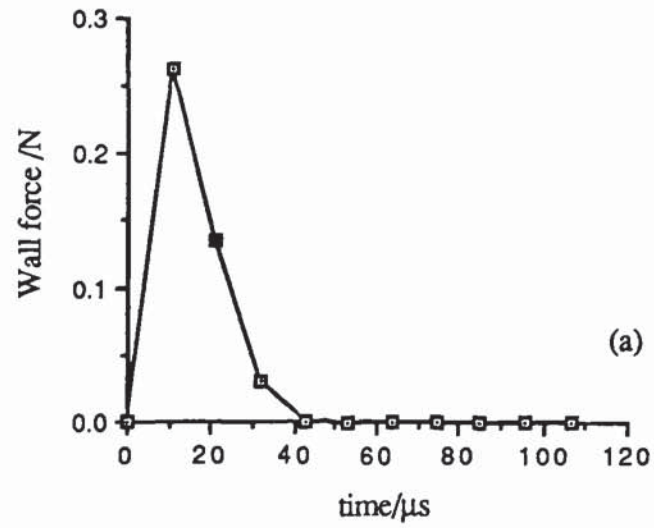
B30 Data for Velocity 0.8 m/s, $\gamma = 1.0$ Jm^{-2}

270
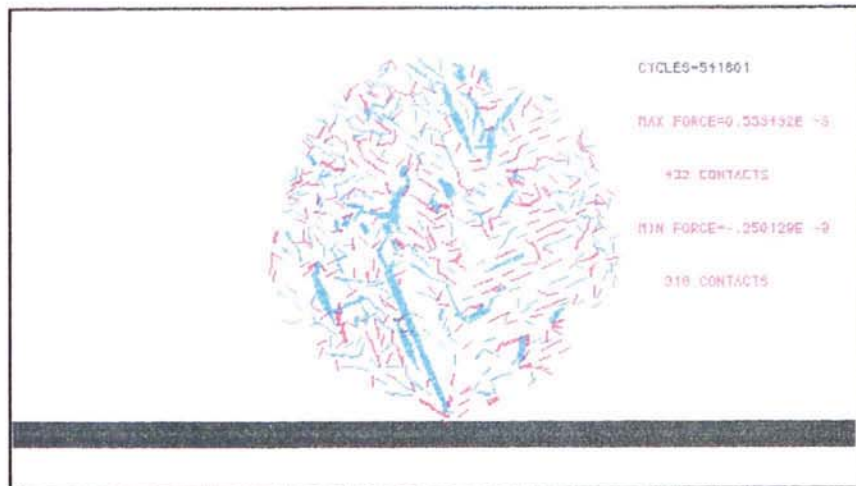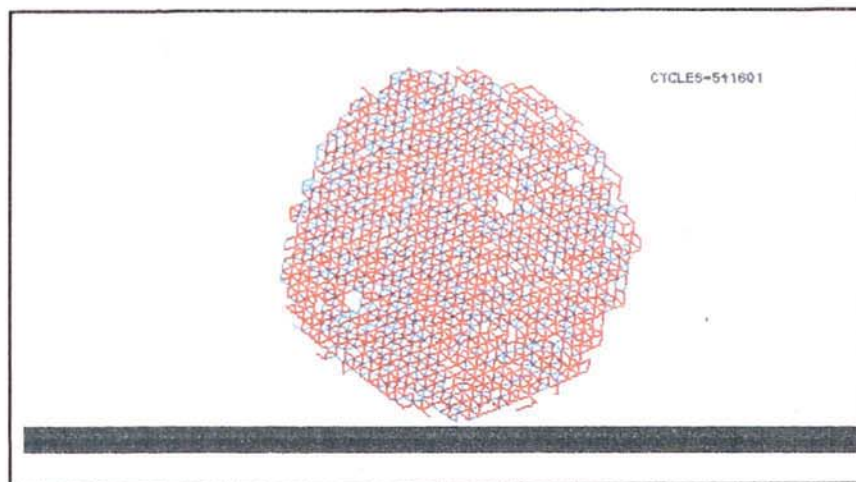
Force plot
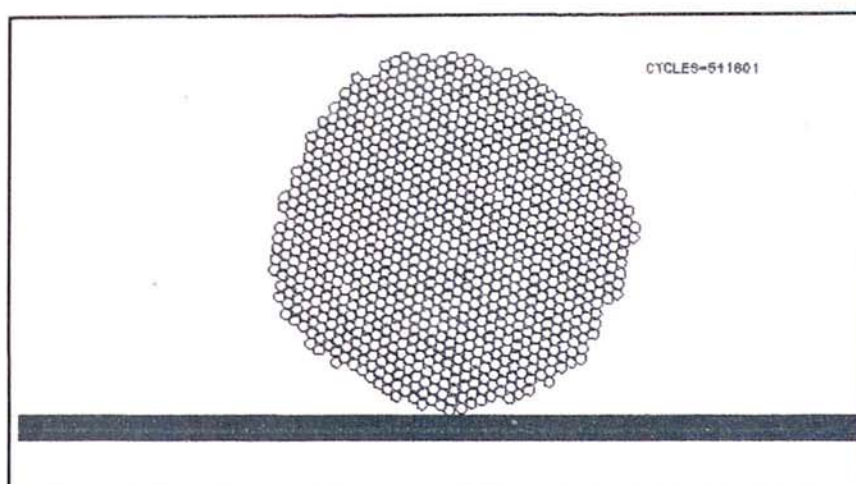
Lattice plot

Ball plot

B31 Velocity of impact = 0.5 m/s, $\gamma = 1.0$ Jm^{-2}
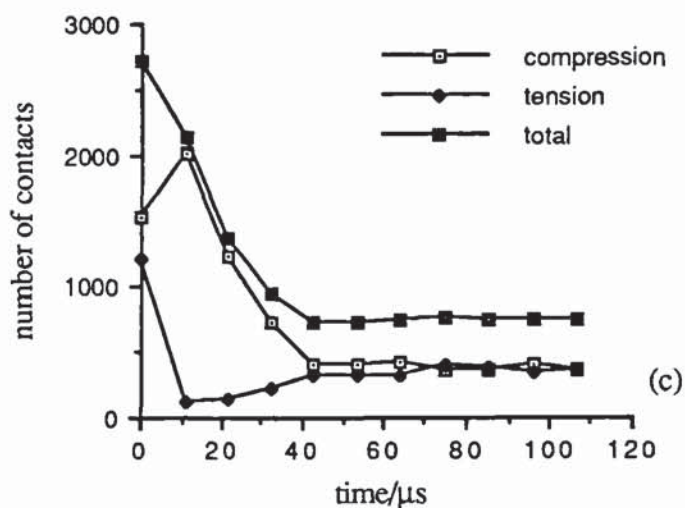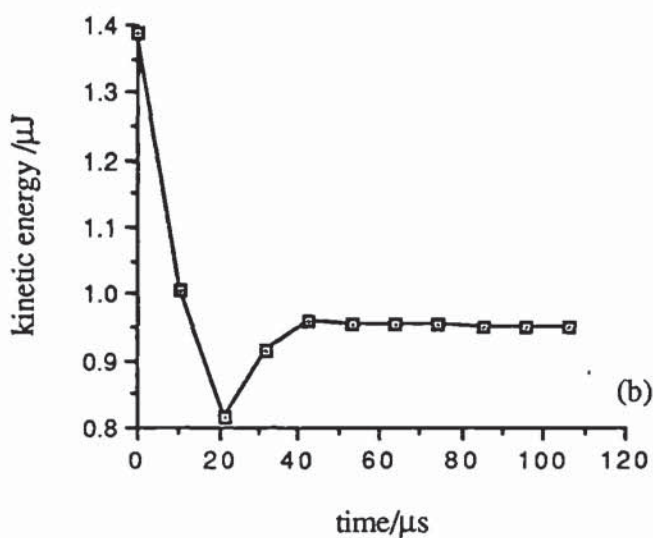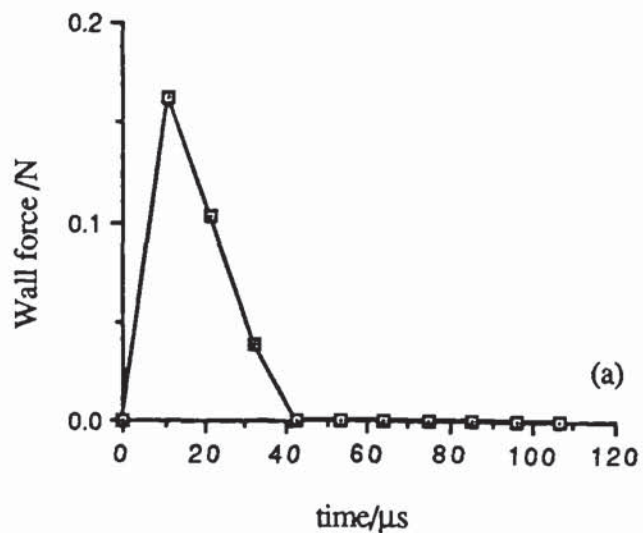
B32 Data for Velocity 0.5 m/s, $\gamma = 1.0$ Jm^{-2}
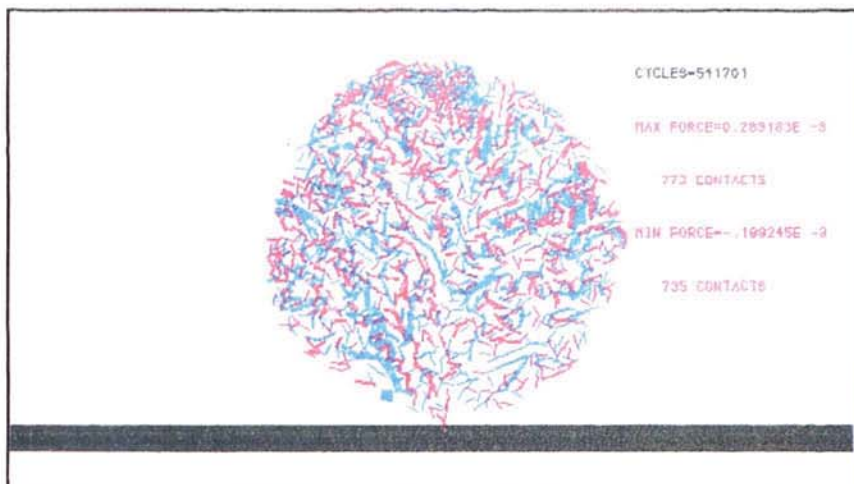
Force plot
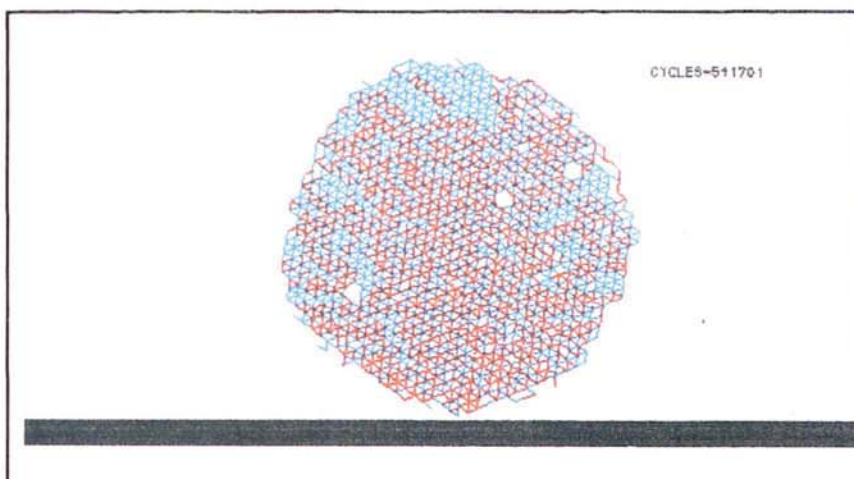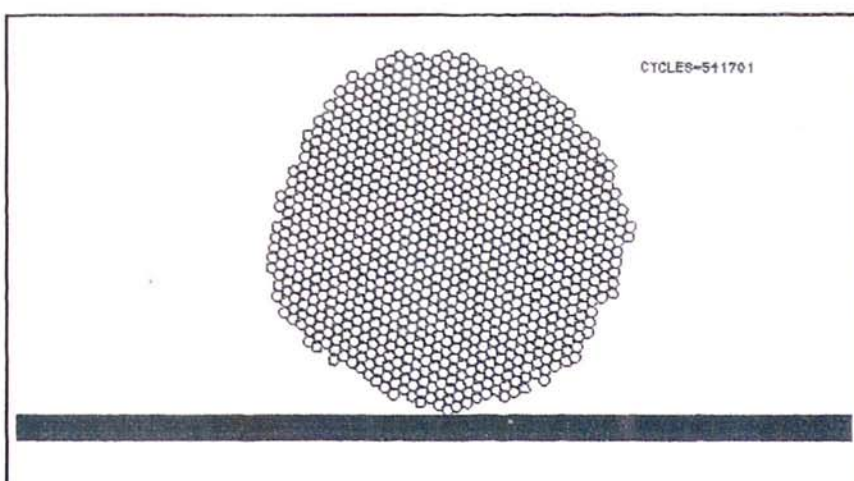
Lattice plot

Ball plot

B33 Velocity of impact = 0.1 m/s, Υ_{t} = 1.0 Jm^{-2}
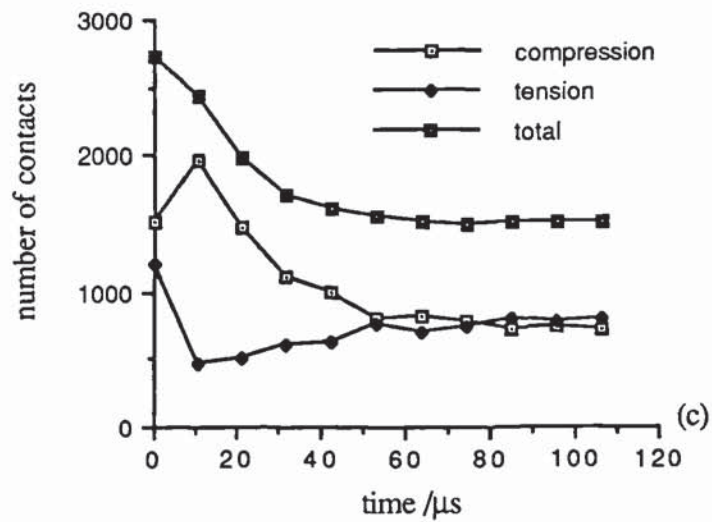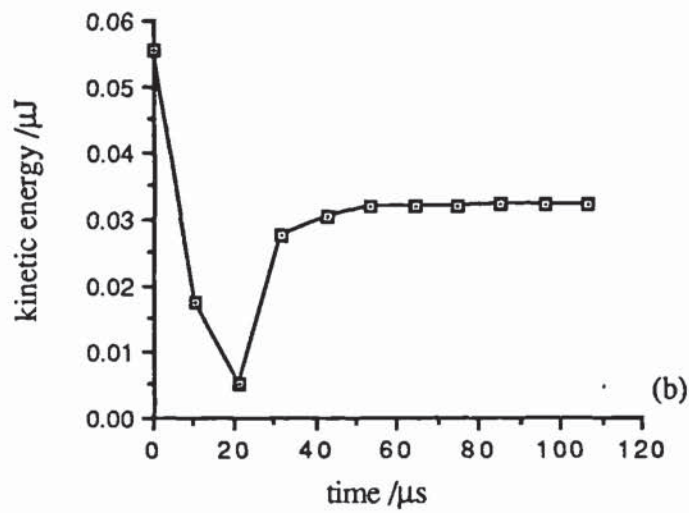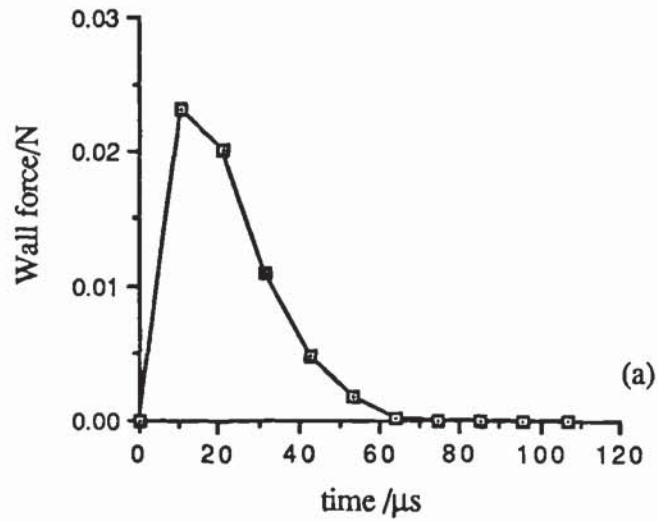
B34 Data for Velocity 0.1 m/s, $\gamma = 1.0$ Jm^{-2}
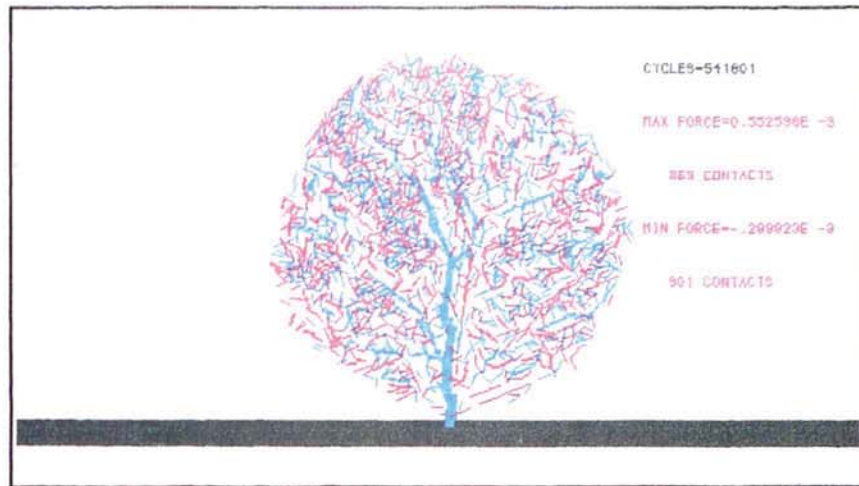
Force plot
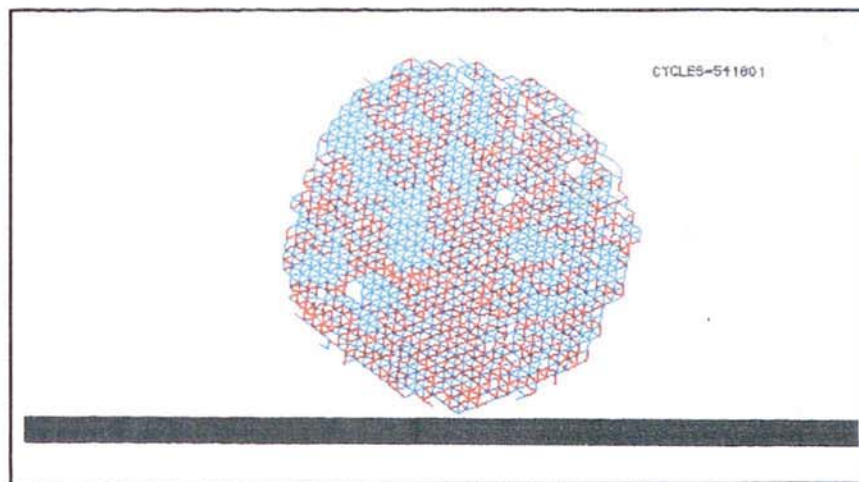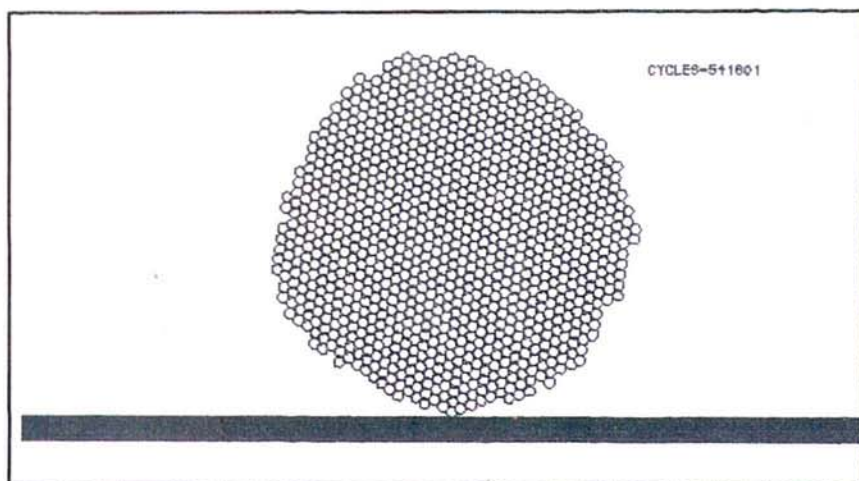
Lattice plot

Ball plot

B35 Velocity of impact = 0.05 m/s, $\gamma = 1.0$ Jm^{-2}
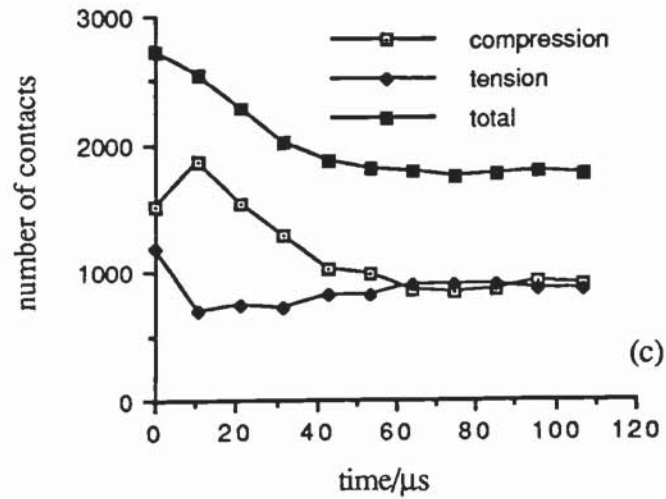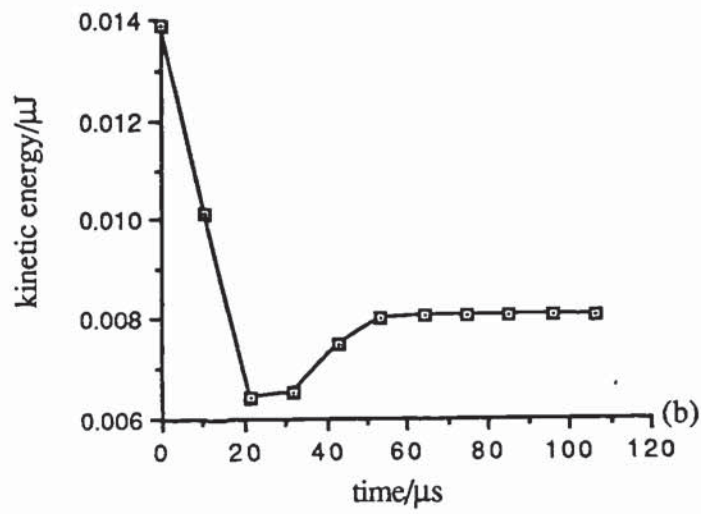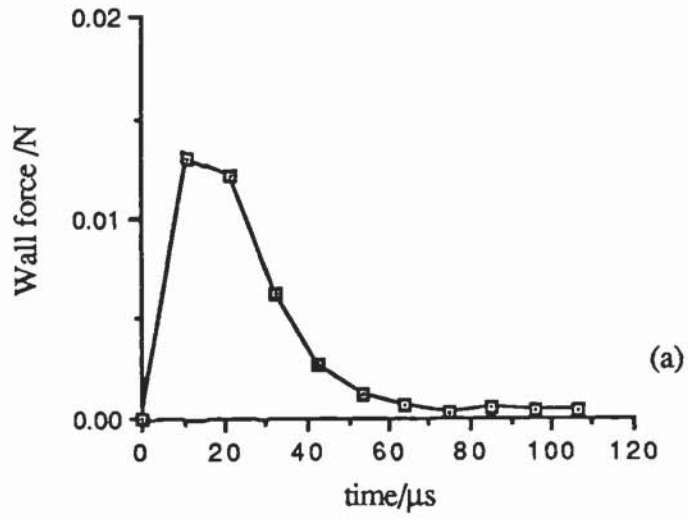
B36 Data for Velocity 0.05 m/s, $\gamma = 1.0$ Jm^{-2}

CYCLES=511601

MAX FORCE=0.228038E -5

1232 CONTACTS

MIN FORCE=-.339651E -2

1104 CONTACTS

Force plot

CYCLES=511601

Lattice plot

CYCLES=511601
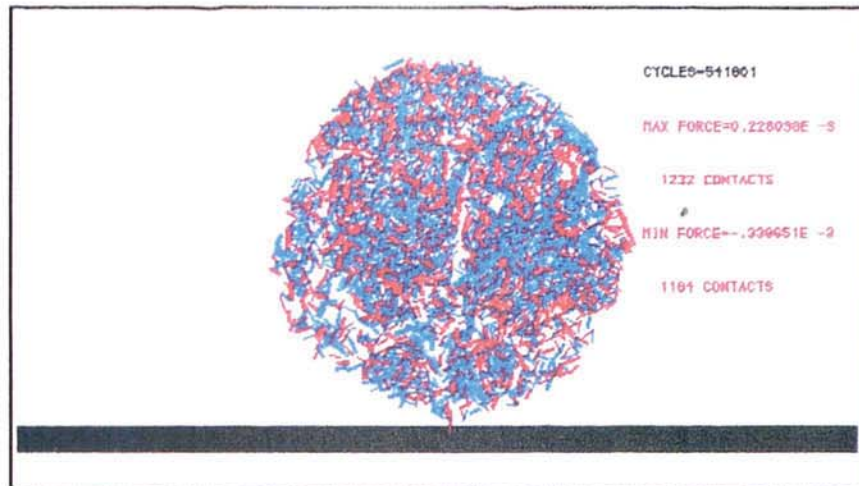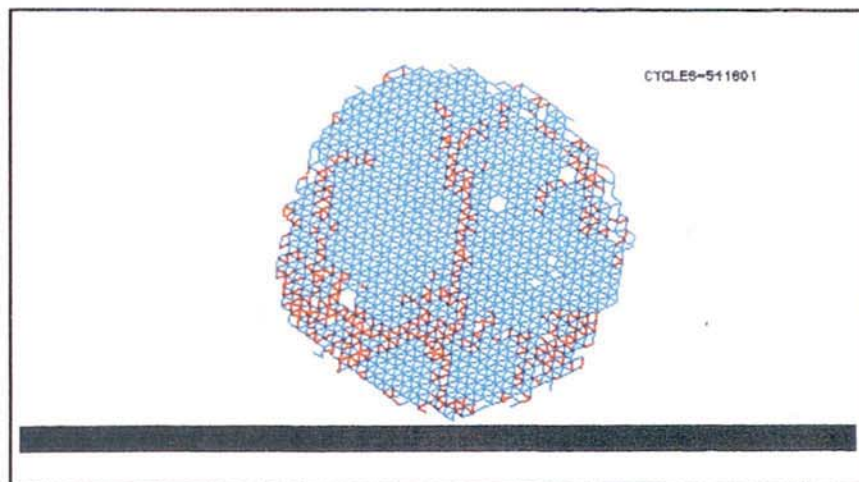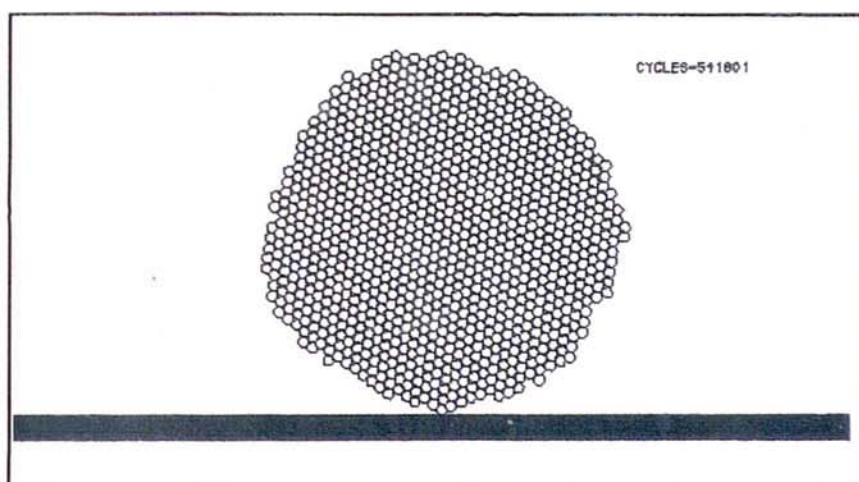
Ball plot

B37 Velocity of impact = 0.01 m/s, $\gamma' = 1.0$ Jm^{-2}
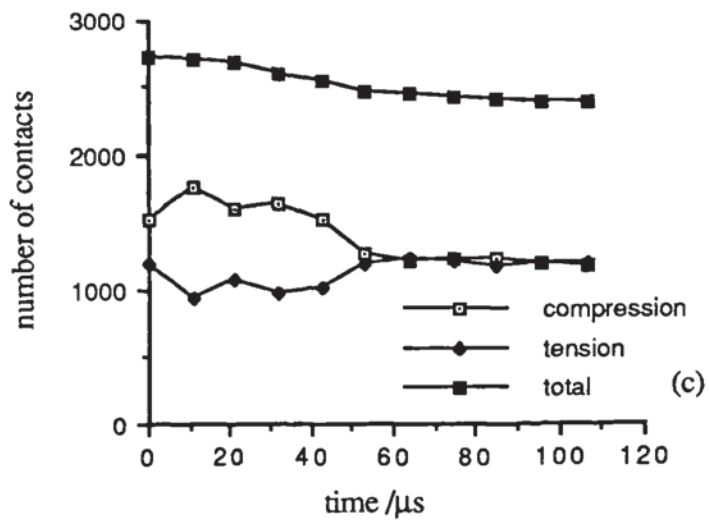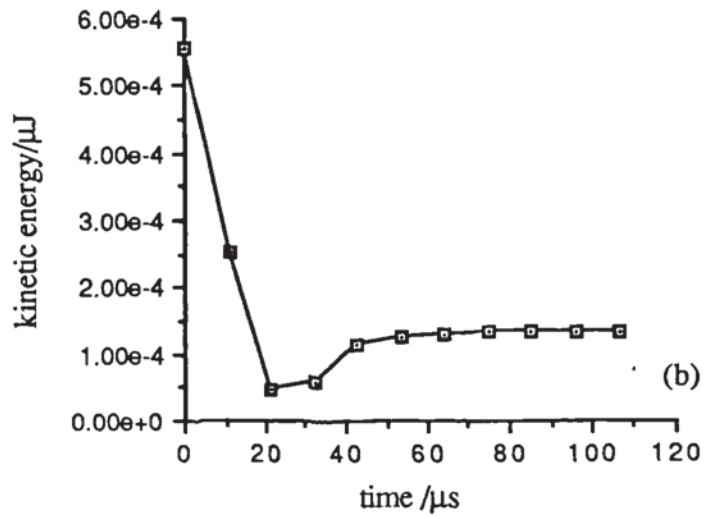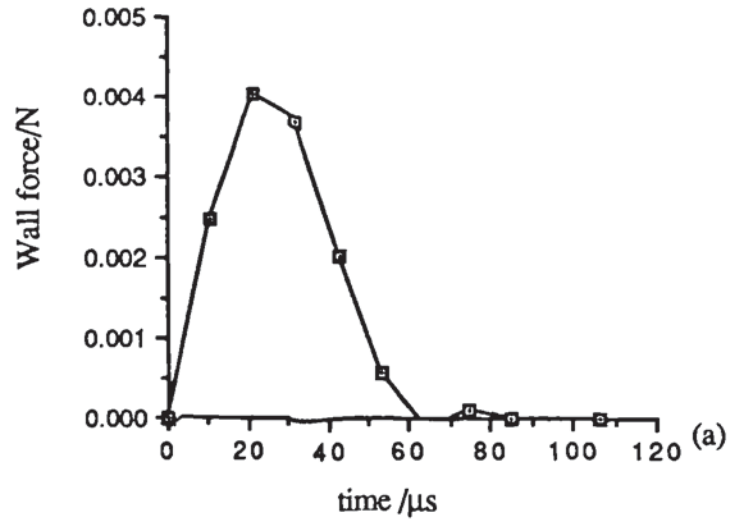
B38 Data for Velocity 0.01 m/s, $\gamma = 1.0$ Jm^{-2}
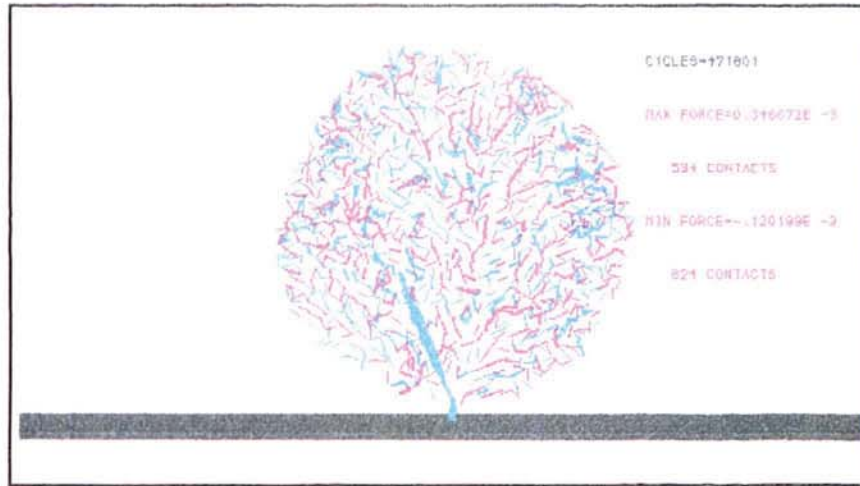
Force plot
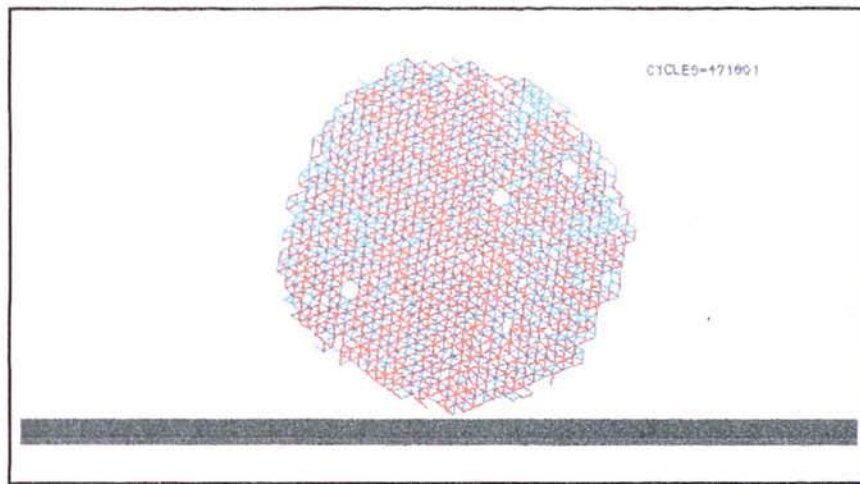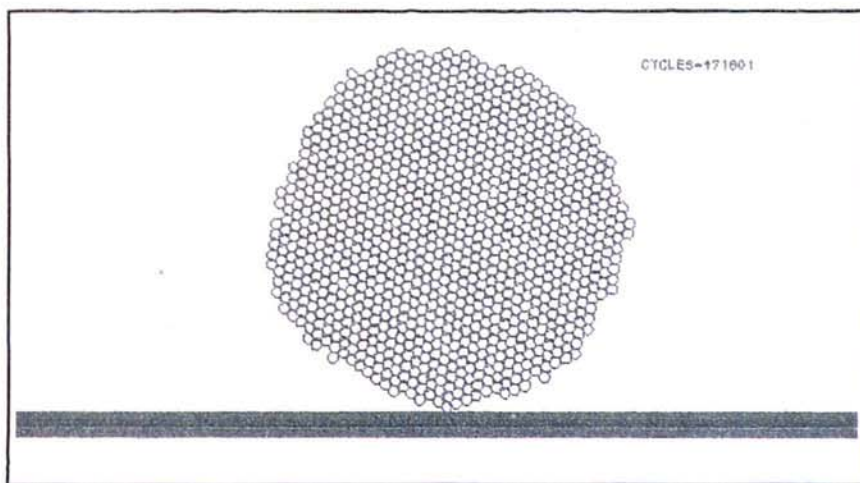
Lattice plot

Ball plot

B39 Velocity of impact = 0.1m/s, γ = 0.3 Jm^{-2}

279
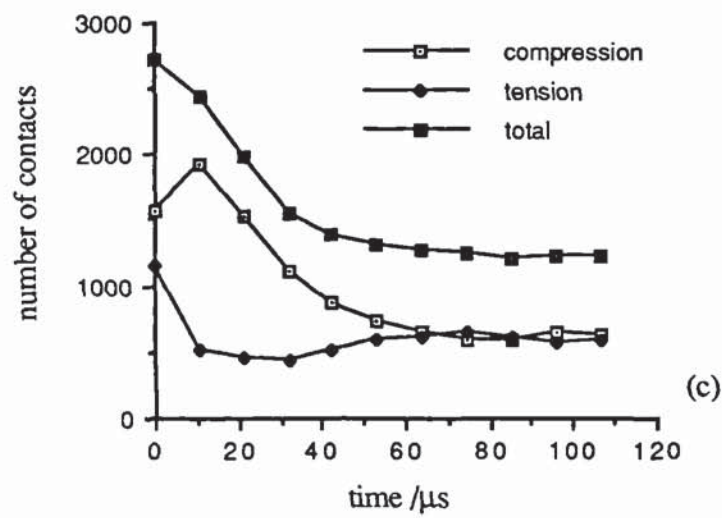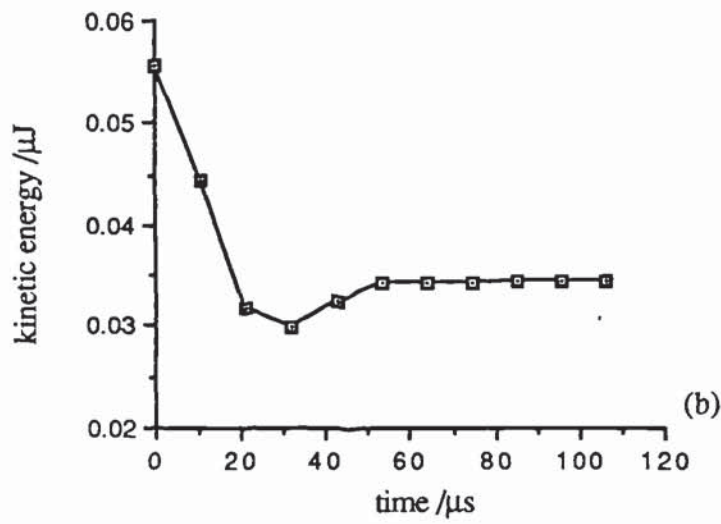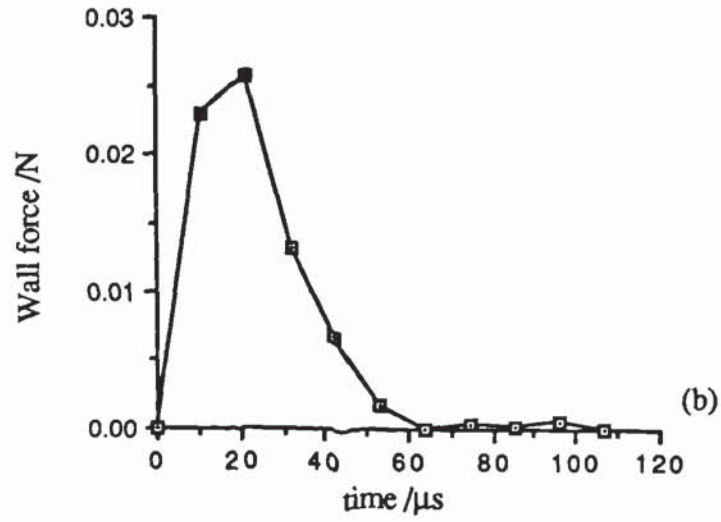
B40 Data for Velocity 0.1m/s, $\gamma = 0.3$ Jm^{-2}
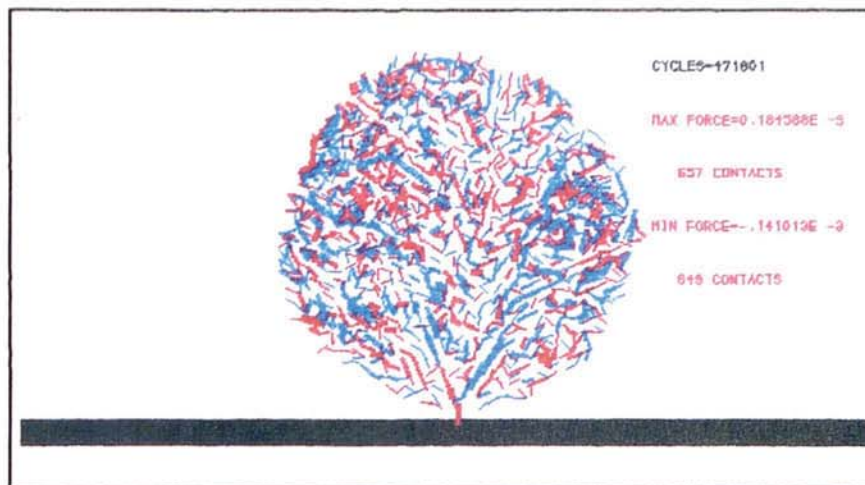
Force plot
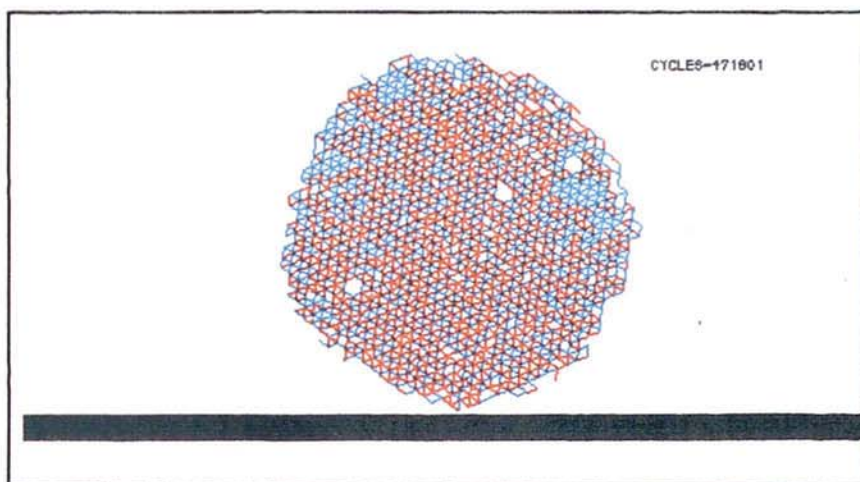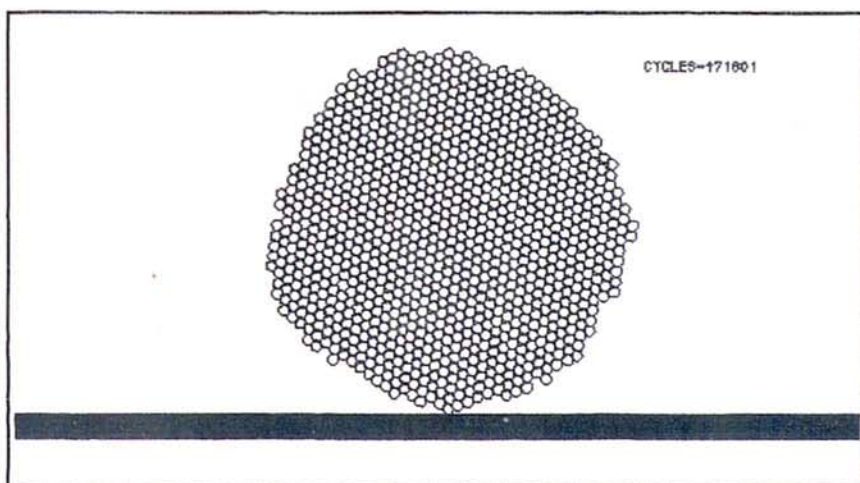
Lattice plot

Ball plot

B41 Velocity of impact = 0.08m/s, γ = 0.3 Jm^{-2}

(a)

(b)

(c)
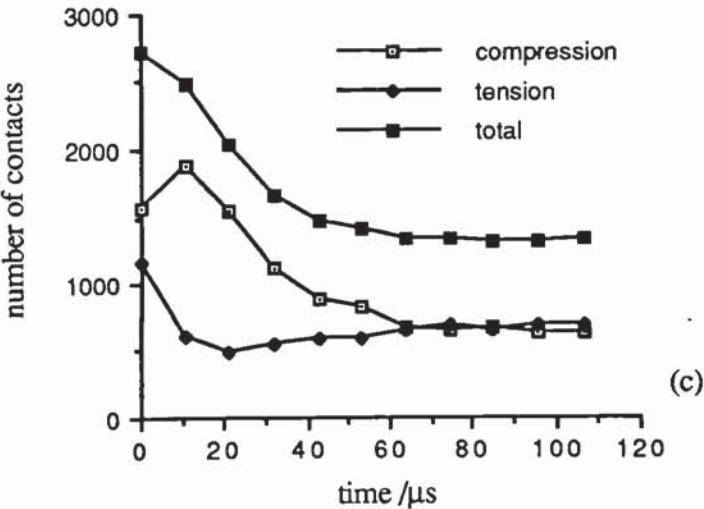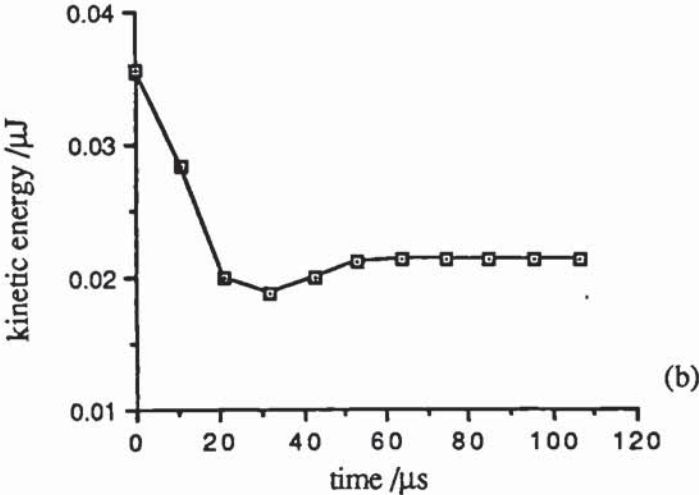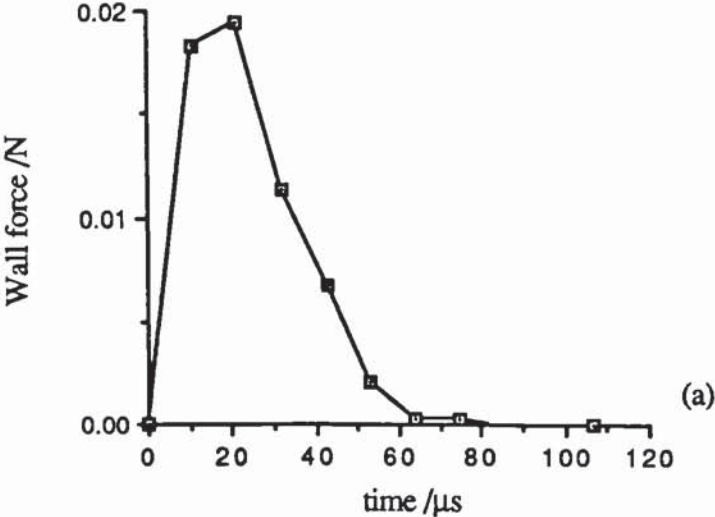
B42 Data for Velocity 0.08m/s, $\gamma = 0.3$ Jm^{-2}
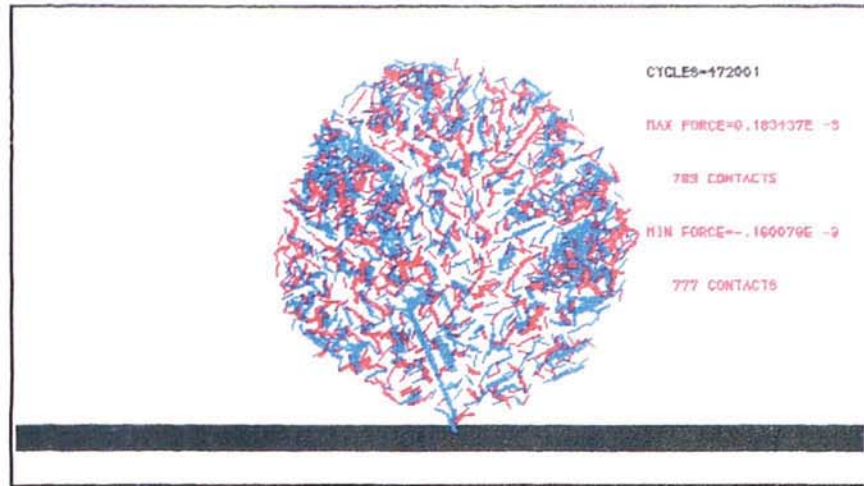
Force plot
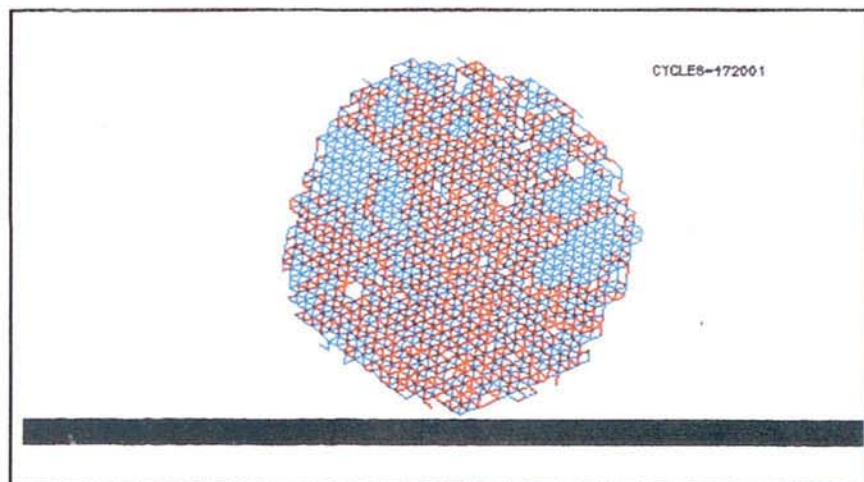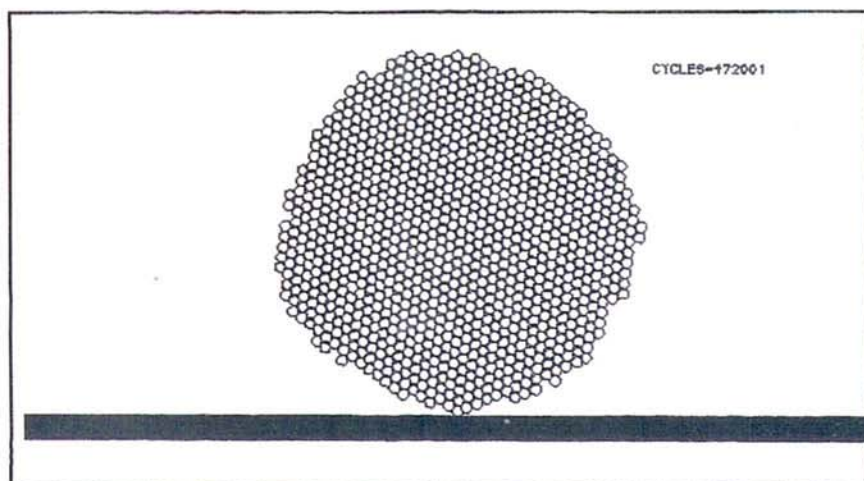
Lattice plot

Ball plot

B43 Velocity of impact = 0.05 m/s, γ = 0.3 Jm^{-2}

283

(a)

(b)

(c)
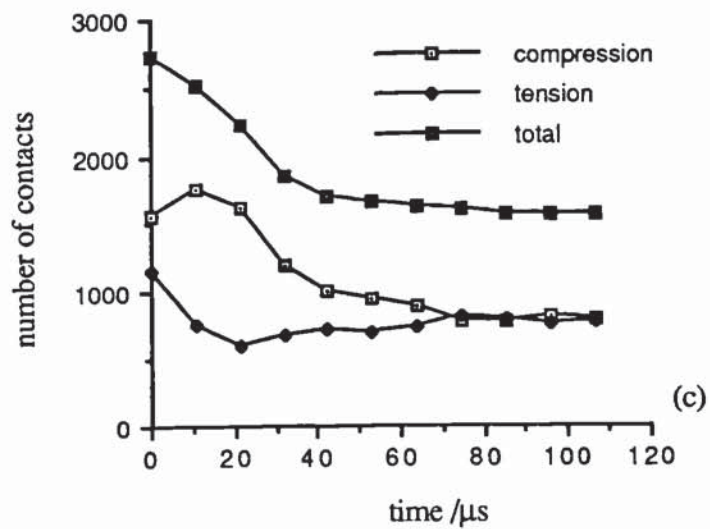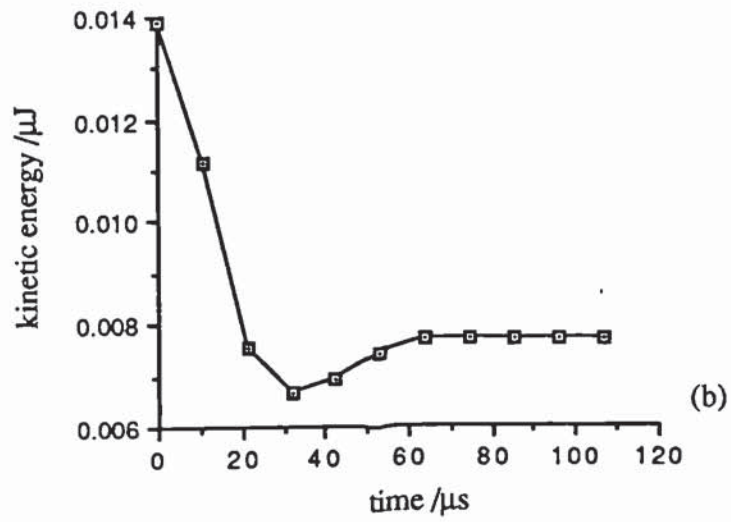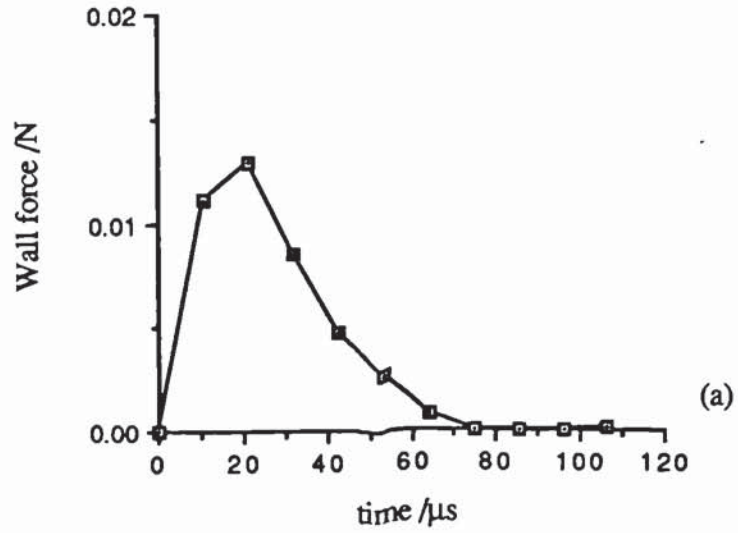
B44 Data for Velocity 0.05m/s, $\gamma = 0.3$ Jm^{-2}

(a)

(b)

(c)
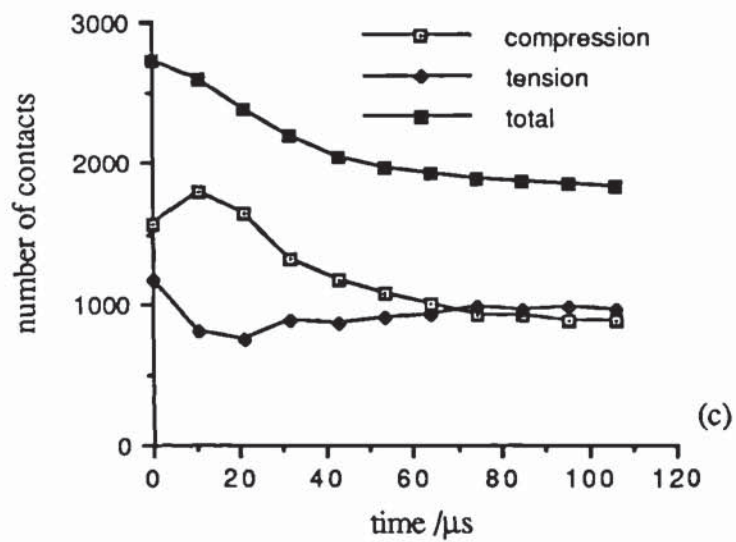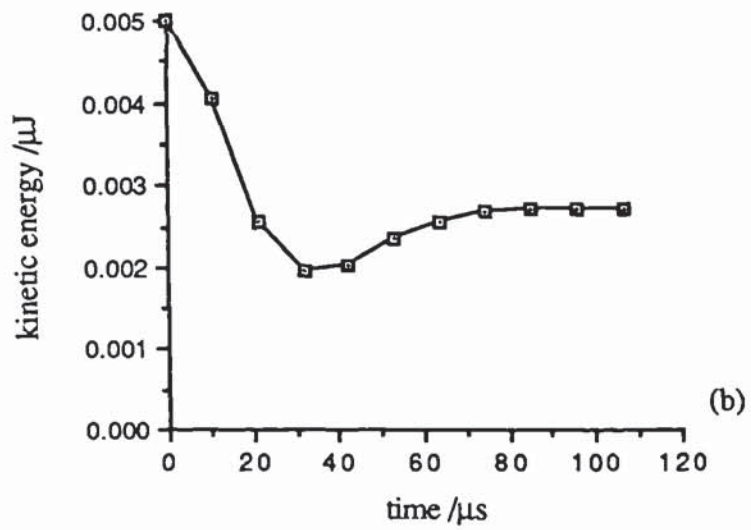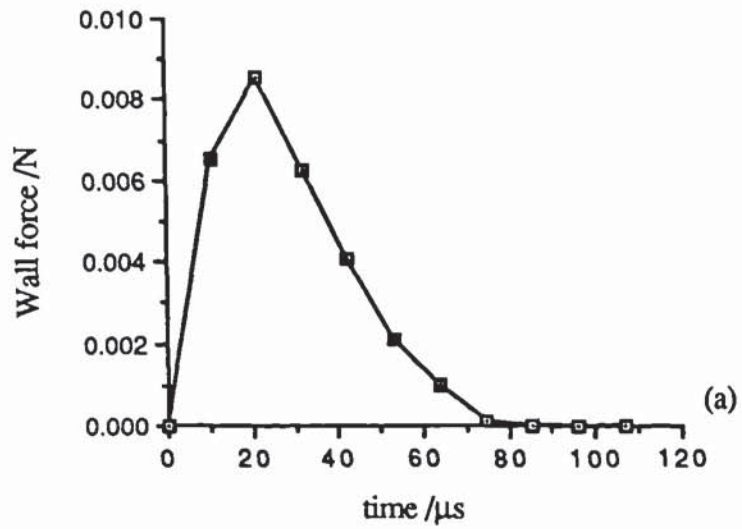
B46 Data for Velocity 0.03m/s, $\gamma = 0.3$ Jm^{-2}
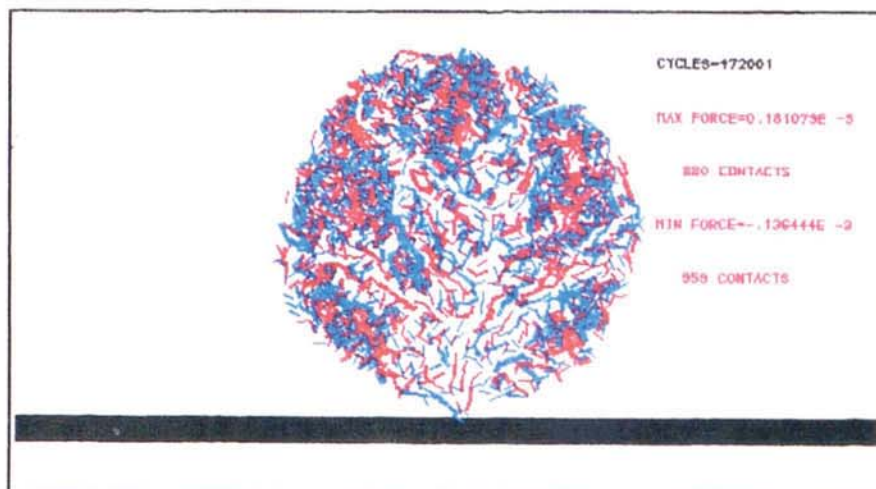
Force plot
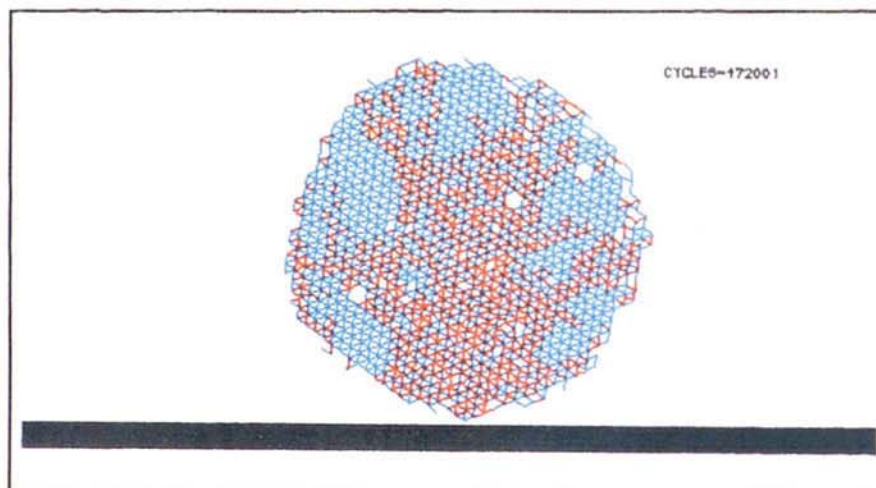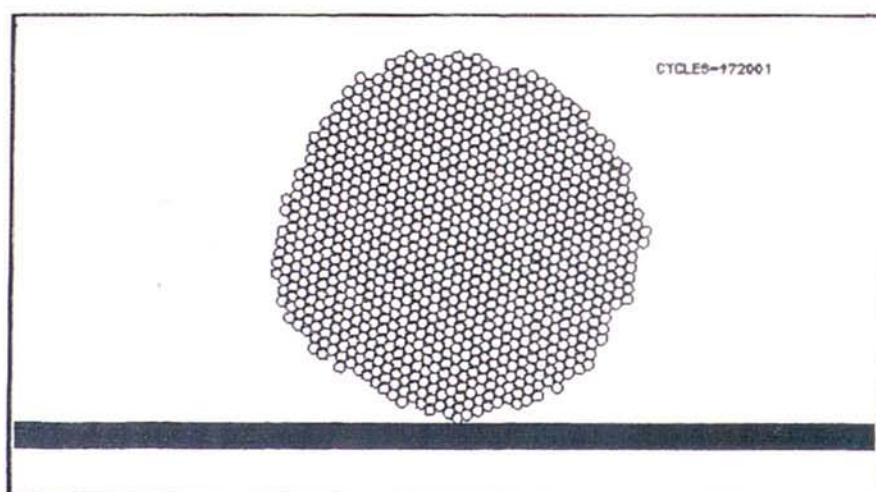
Lattice plot

Ball plot

B45 Velocity of impact = 0.03 m/s, $\gamma = 0.3$ Jm^{-2}

285
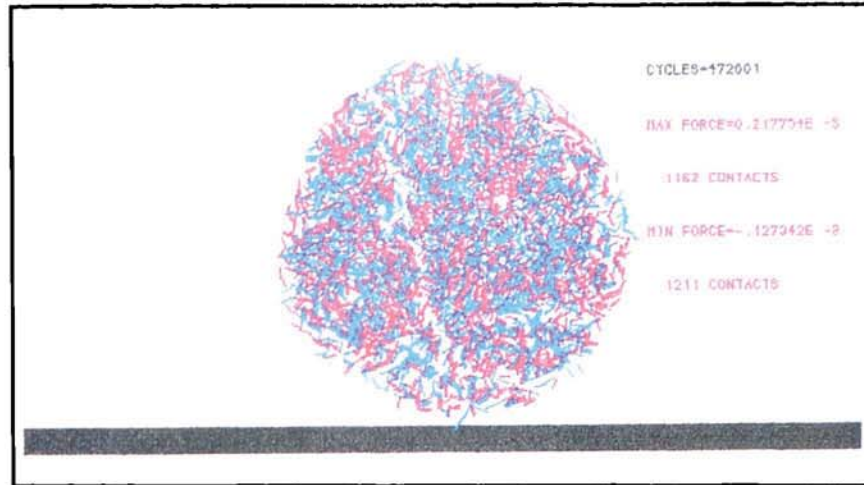
Force plot
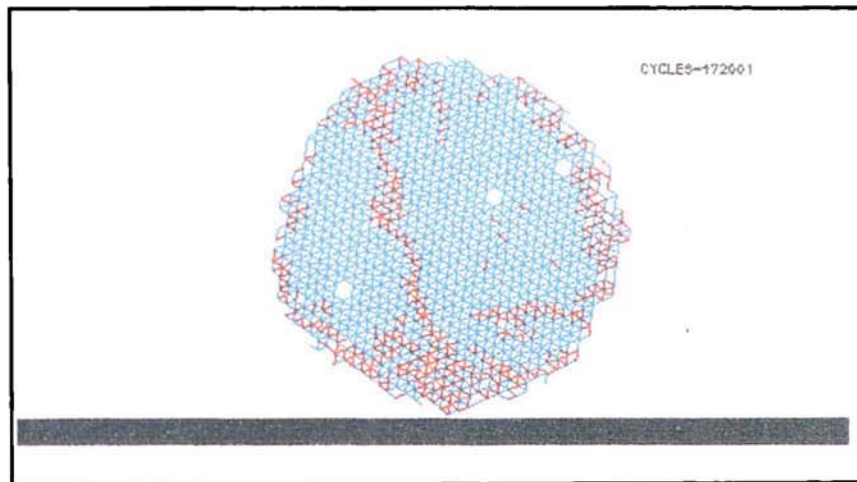
Lattice plot
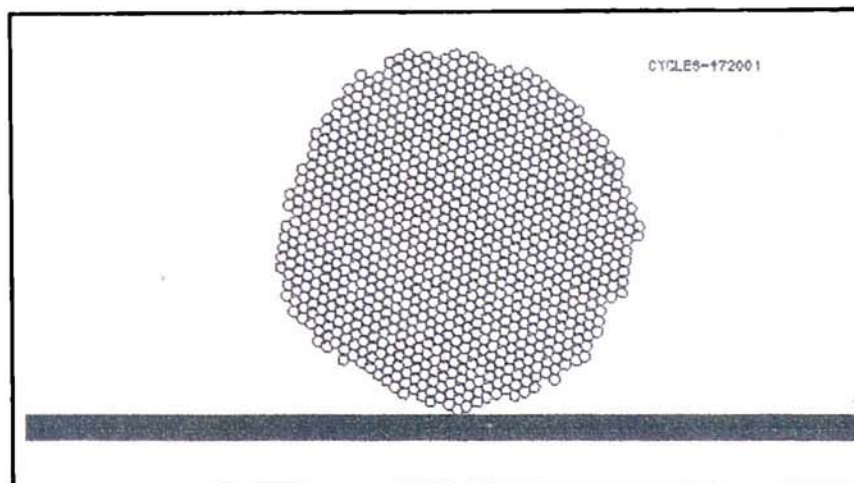
Ball plot

B47 Velocity of impact = 0.008 m/s, $\gamma = 0.3$ Jm^{-2}
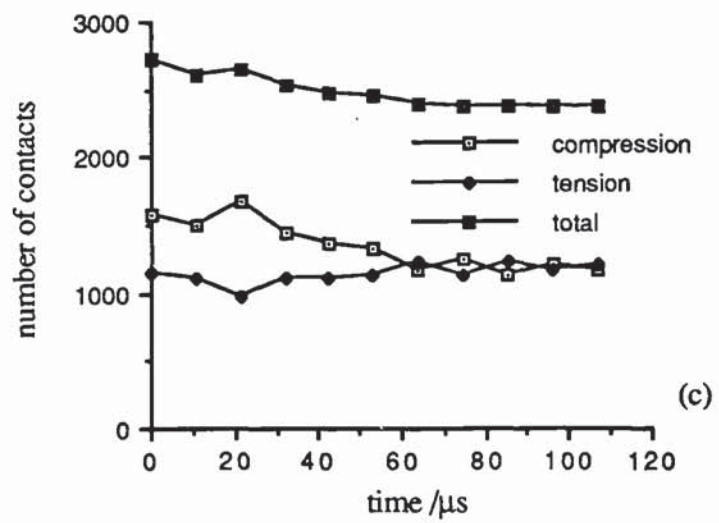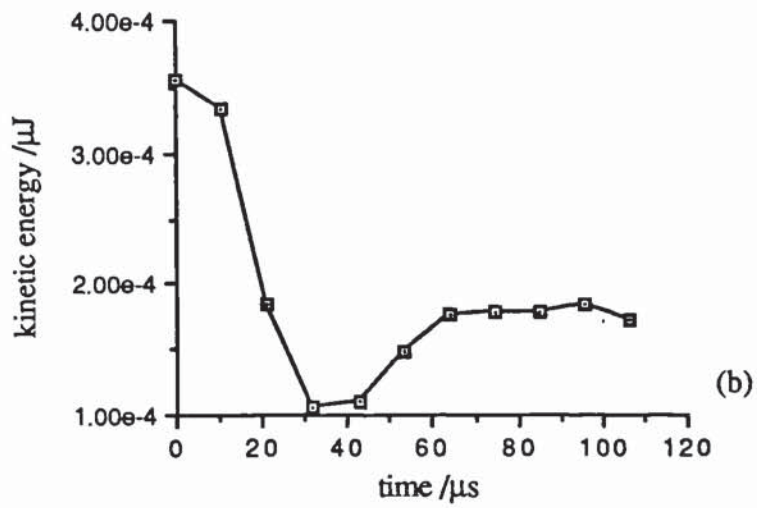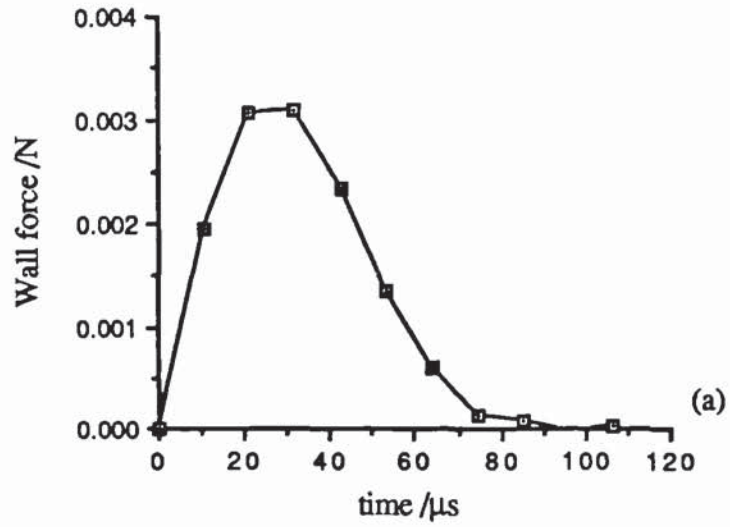
B48 Data for Velocity 0.008m/s, $\gamma = 0.3$ Jm^{-2}

Appendix C

Appendix C covers a comprehensive layout for the diametrical compression simulations on agglomerates of surface energies 0.3, 1.0, 2.0 and 3.0 Jm-2. The lattice plots show the connection diagrams when the forces on both wall are at maximum and at zero. Further quantitative figures on the evolution of (a)wall force, (b) total work done in straining and finally (c) number of contacts, for the appropriate connection diagrams.
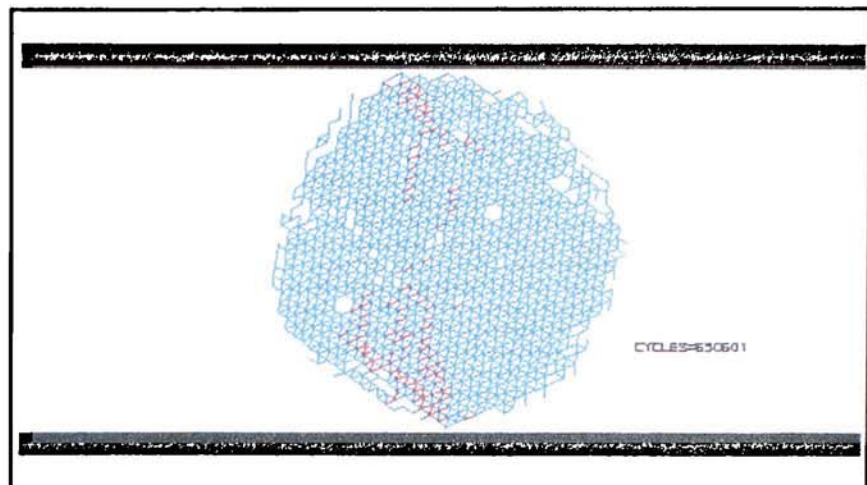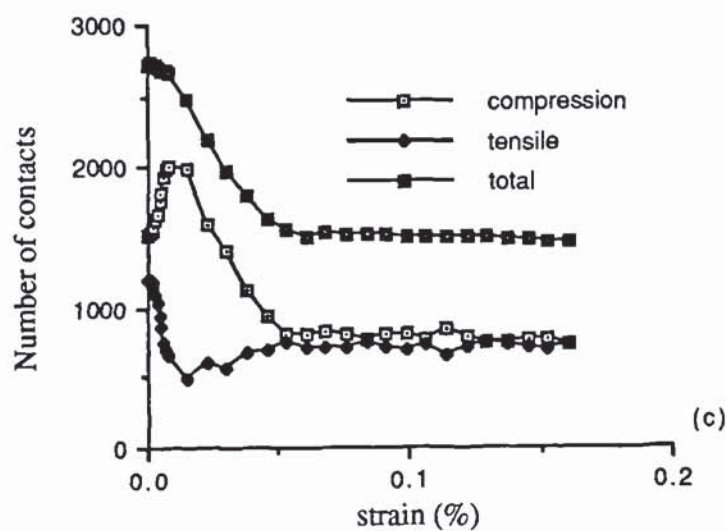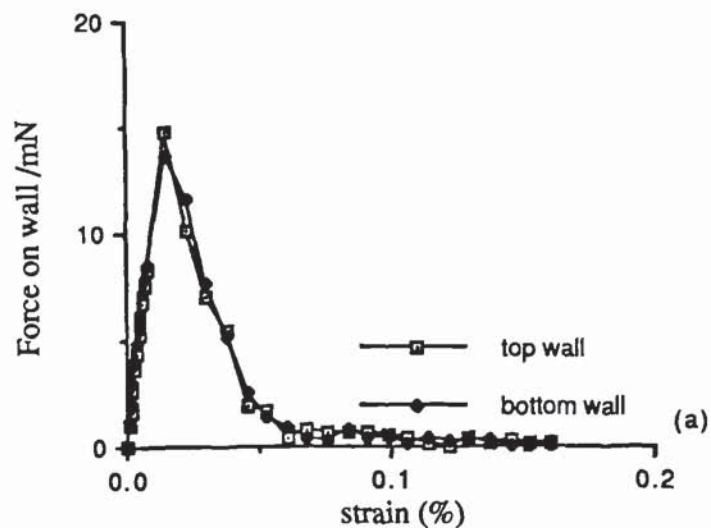
C 1a Lattice plot when wall force is maximum, γ = 3.0 J/m^{-2}, Velocity of walls = ±0.02m/s
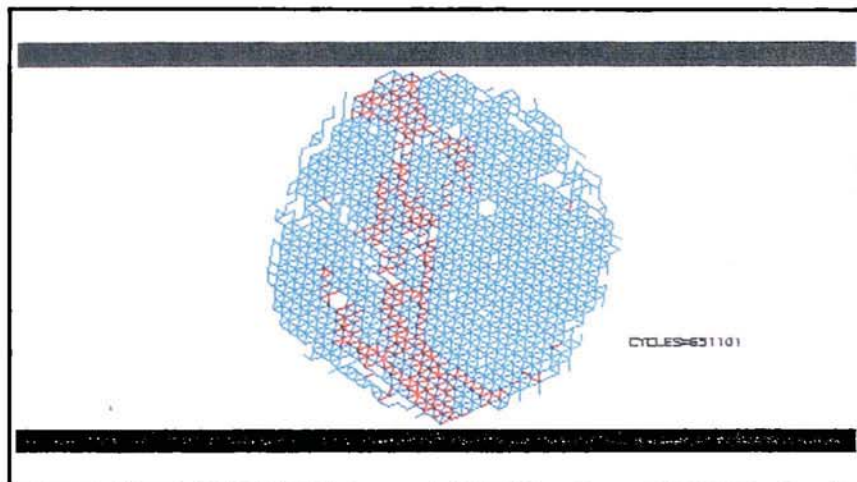
C 1b Lattice plot when wall force is zero, γ = 3.0 J/m-2, Velocity of walls = ±0.02m/s
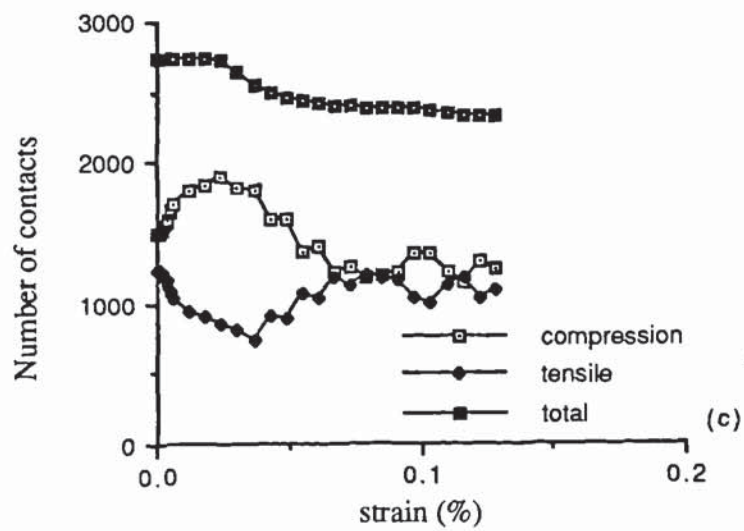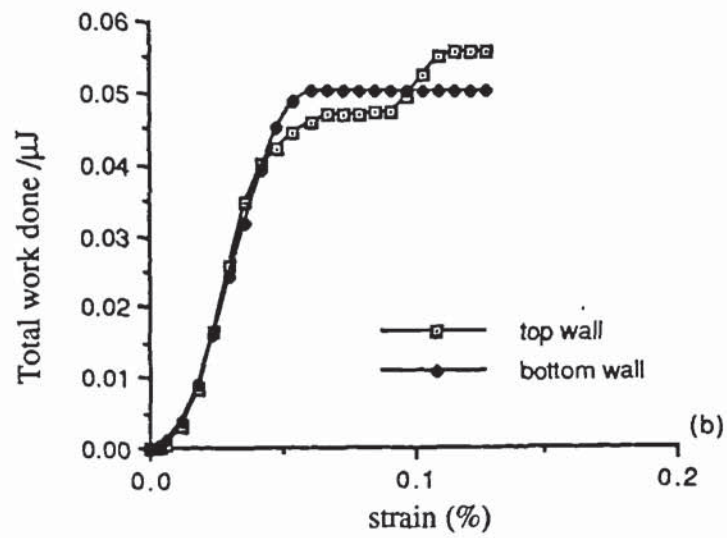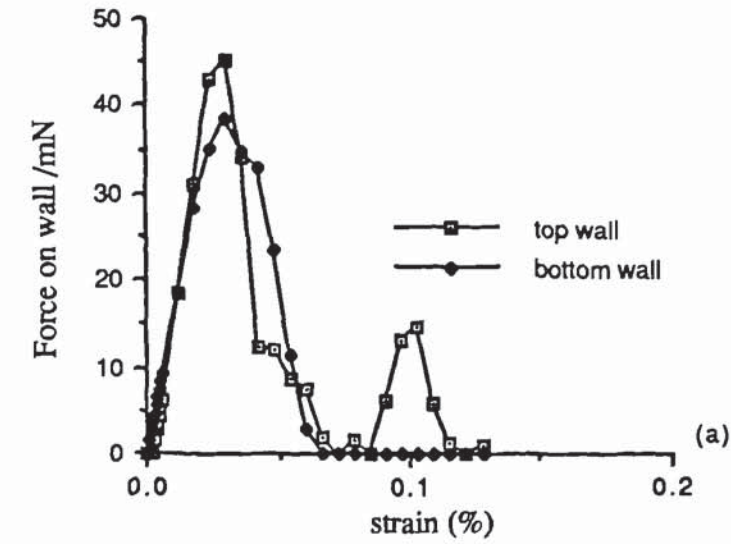
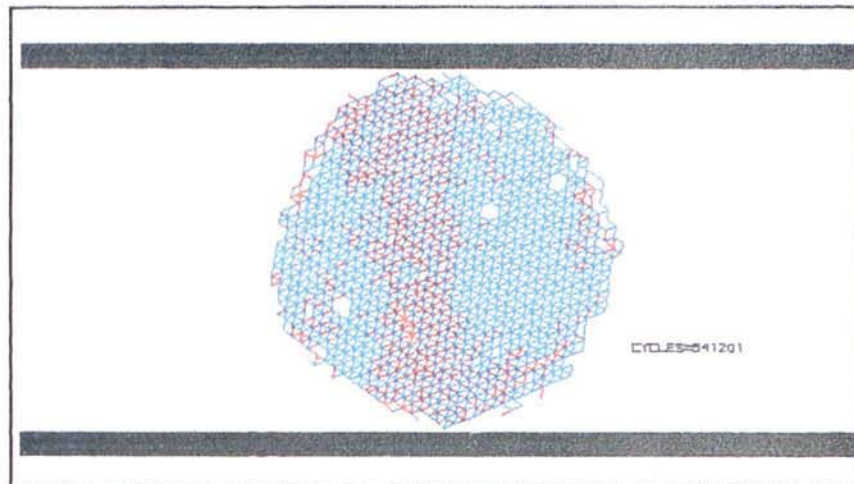C2 Figures for $\gamma = 3.0$ J/m^{-2}, Velocity of Walls $= \pm 0.02$ m/s
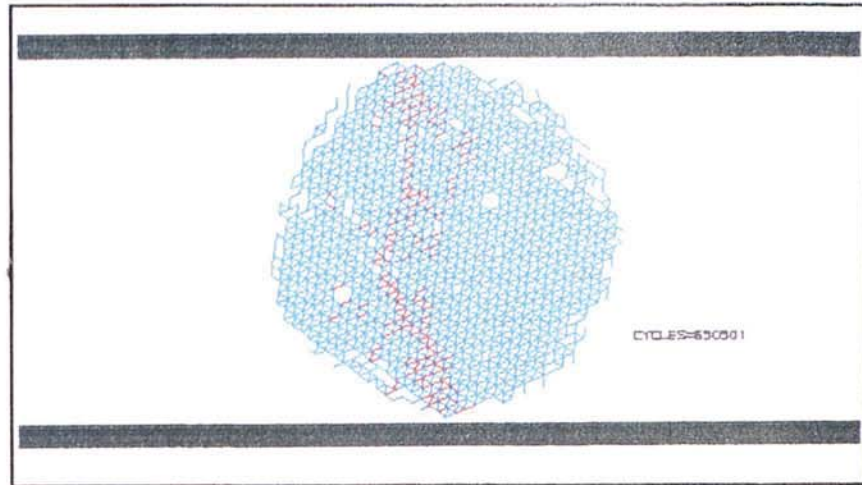
C3a Lattice plot when wall force is maximum , γ = 3.0 J/m^{-2}, Velocity of walls = ±0.03m/s
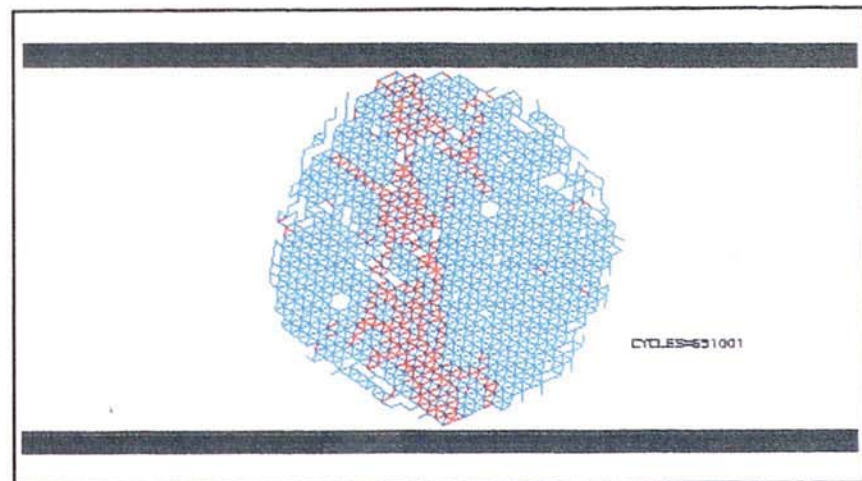
C3b Lattice plot when wall force is zero, γ = 3.0 J/m^{-2}, Velocity of walls = ±0.03m/s
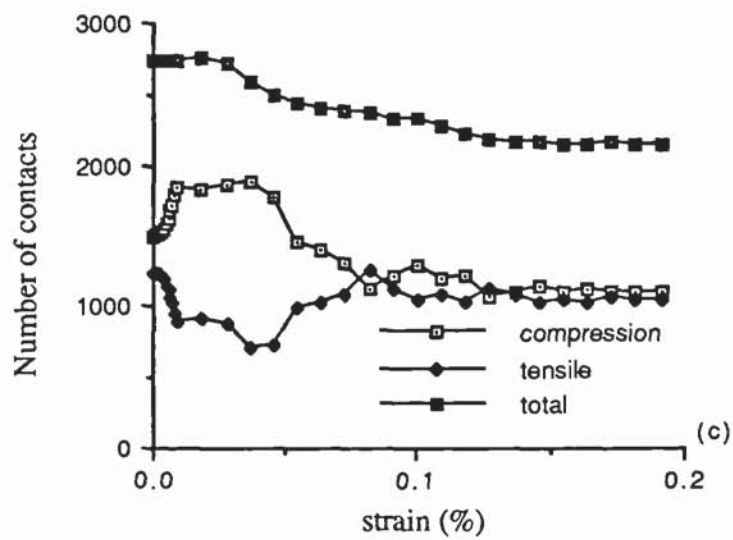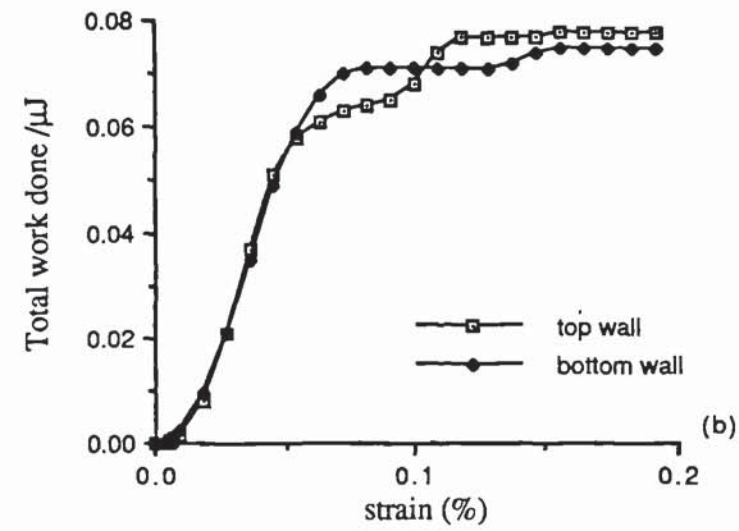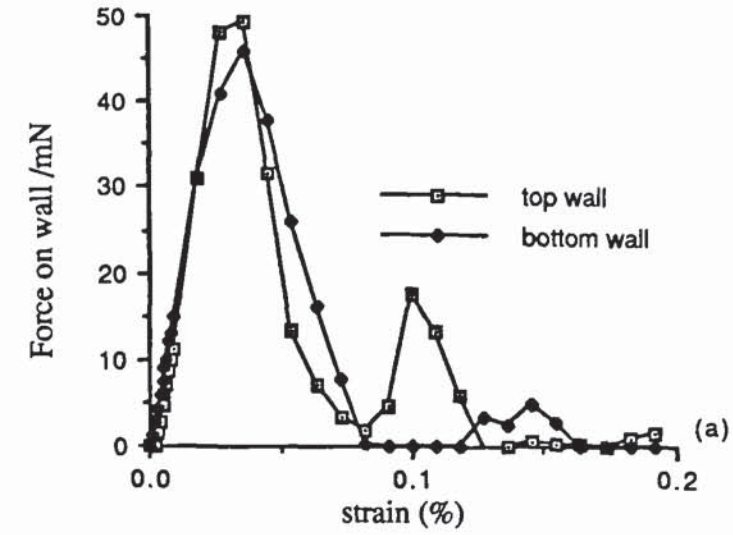
C4 Figures for $\gamma = 3.0$ J/m^{-2}, Velocity of walls $=\pm 0.03$ m/s
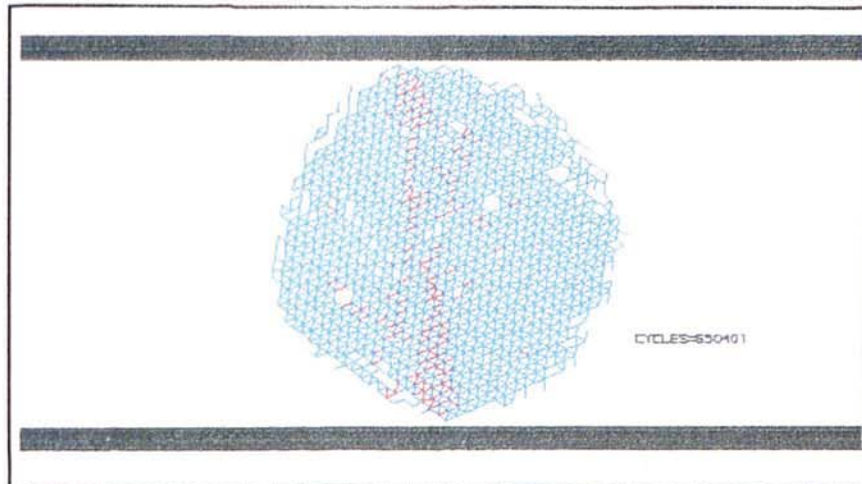
C5a Lattice plot when wall force is maximum, $\gamma = 3.0$ J/m^{-2}, Velocity of walls = ±0.04m/s
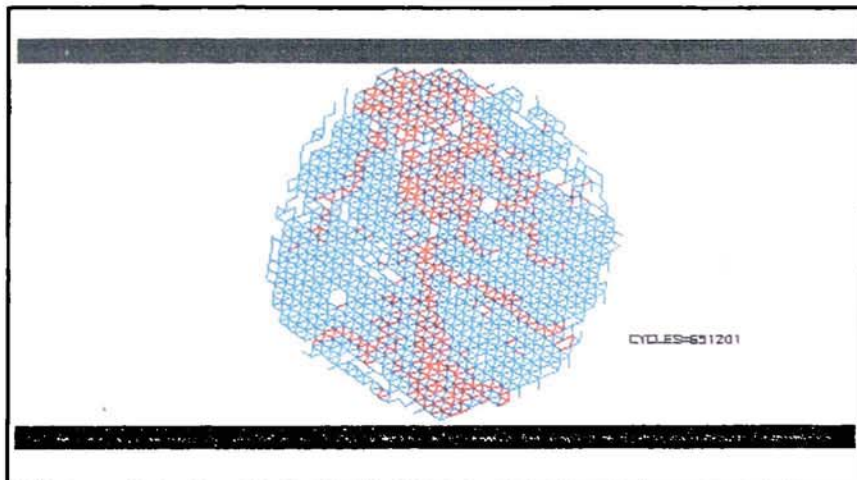
C5b Lattice plot when wall force is zero, $\gamma = 3.0$ J/m^{-2}, Velocity of walls = ±0.04m/s
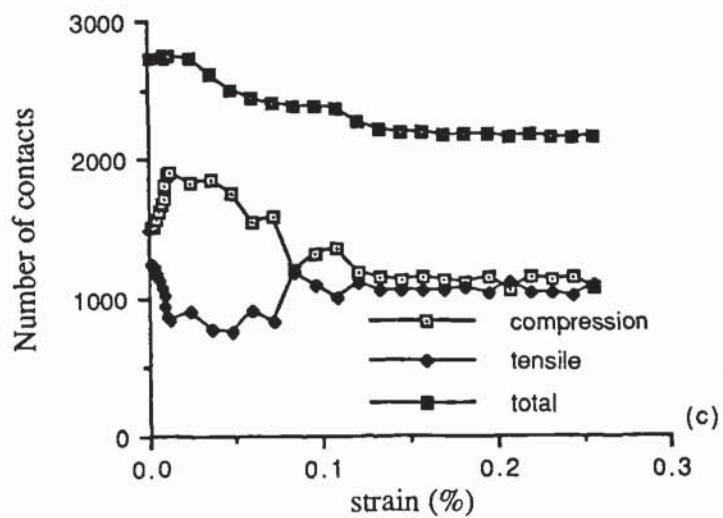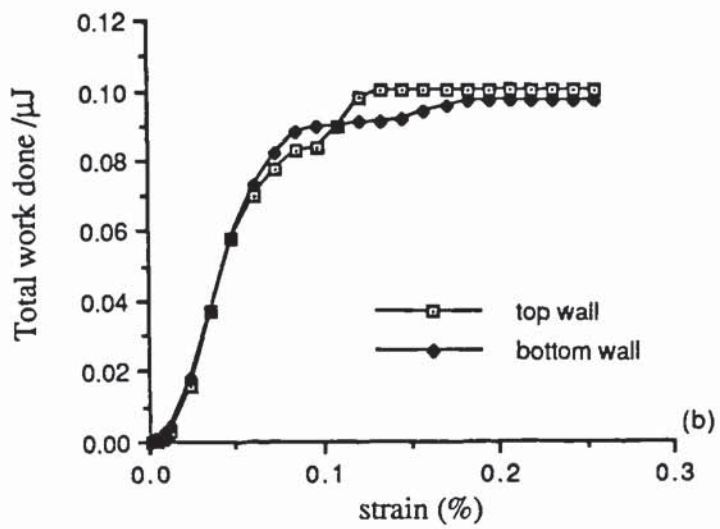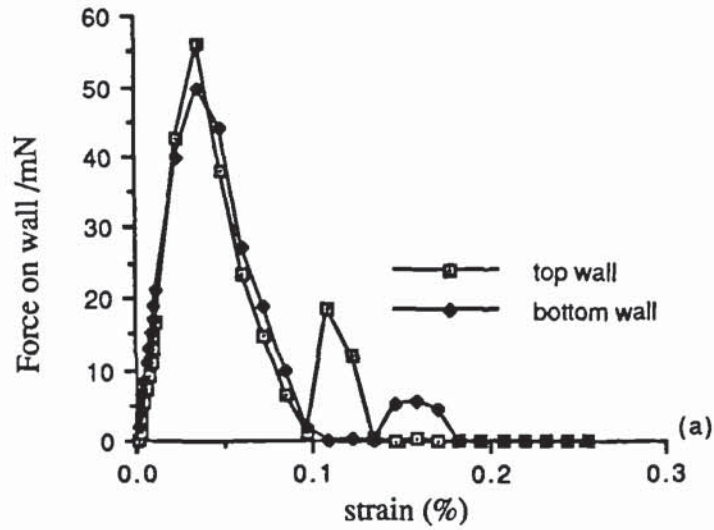
C6 Figures for $\gamma = 3.0$ J/m^{-2}, Velocity of walls $= \pm 0.04$ m/s

295
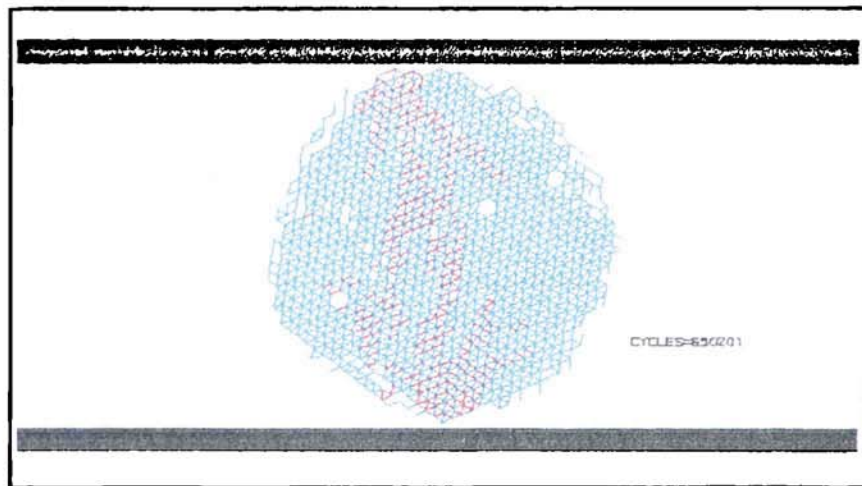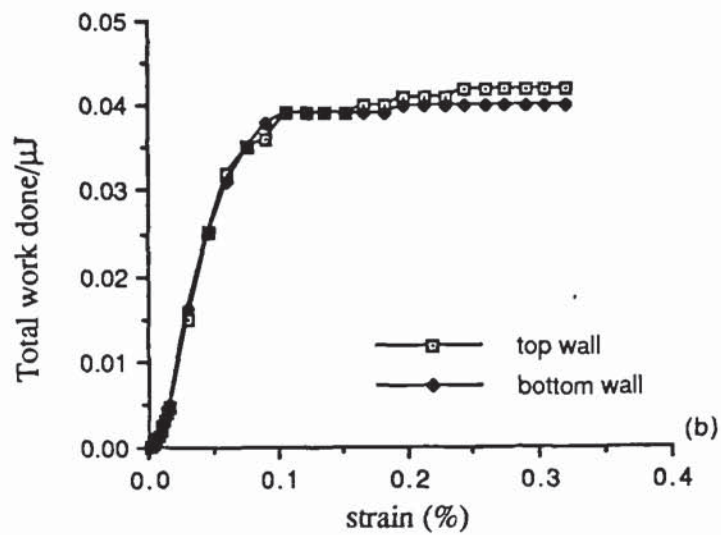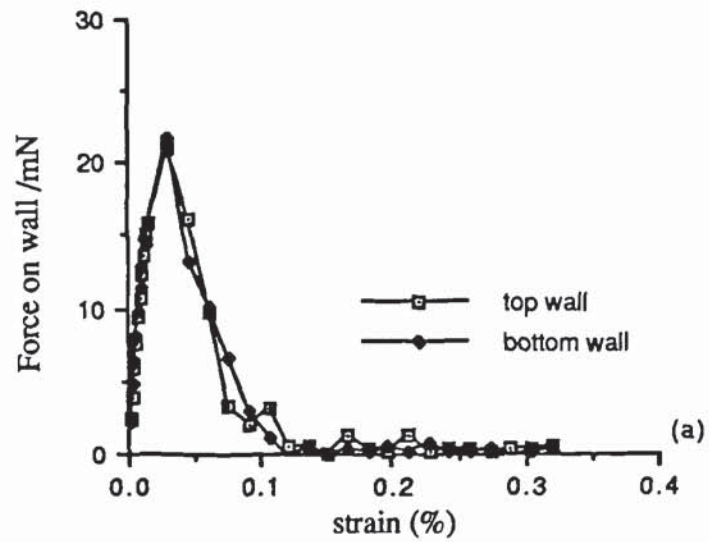
C7a Lattice plot when wall force is maximum, $\gamma = 3.0$ J/m^{-2}, Velocity of walls = ± 0.25m/s
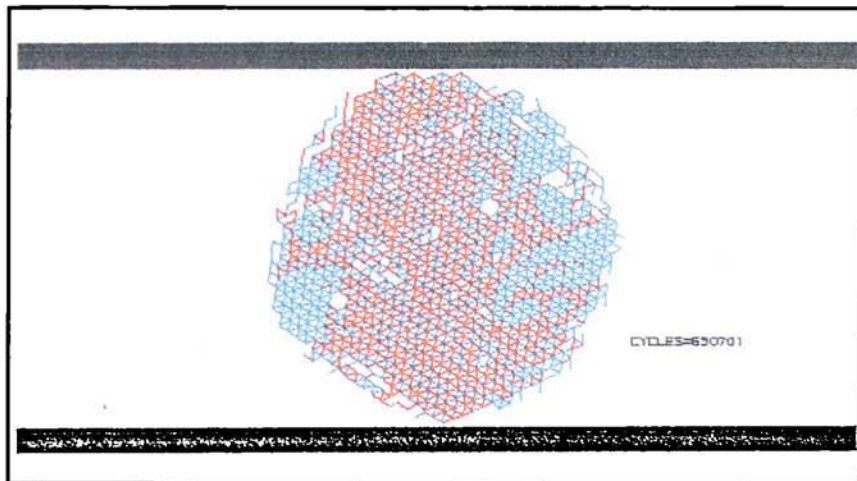
C7b Lattice plot when wall force is zero, $\gamma = 3.0$ J/m^{-2}, Velocity of walls = ± 0.25m/s

(a)

(b)
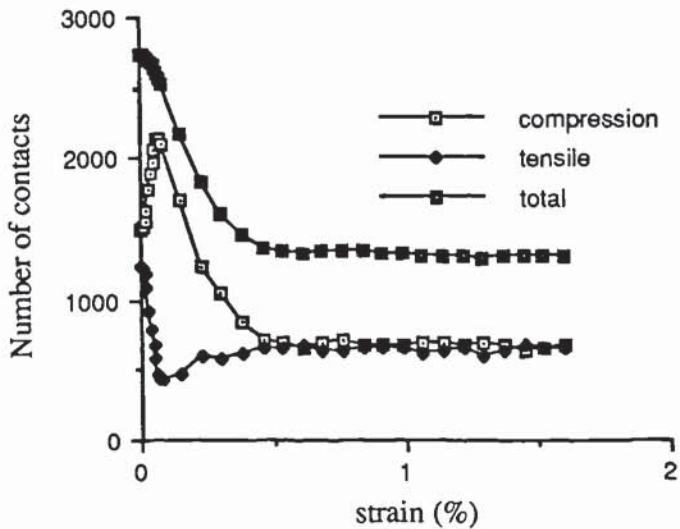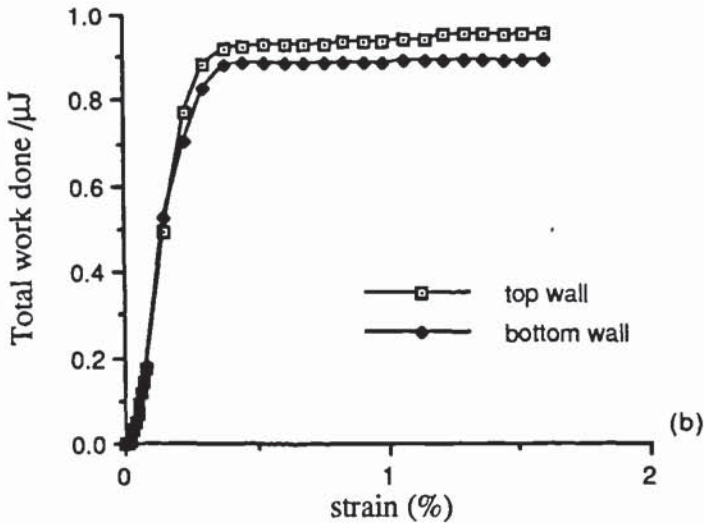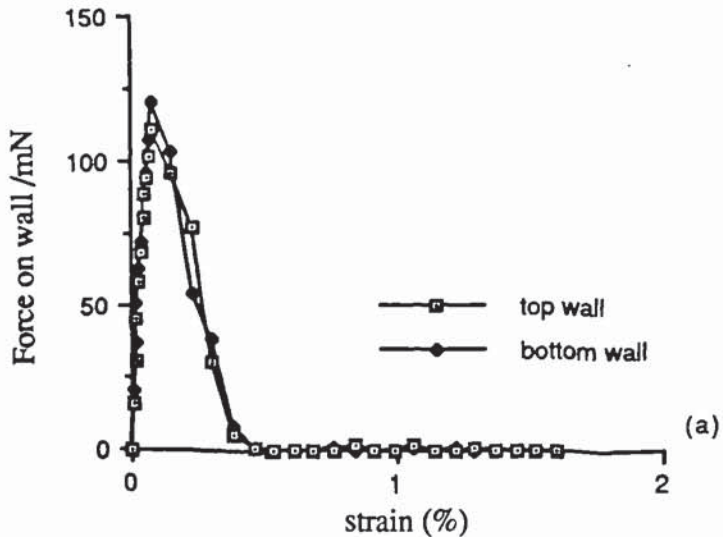
C8 Figures for $\gamma = 3.0$ J/m^{-2}, Velocity of walls $= \pm 0.25$ m/s
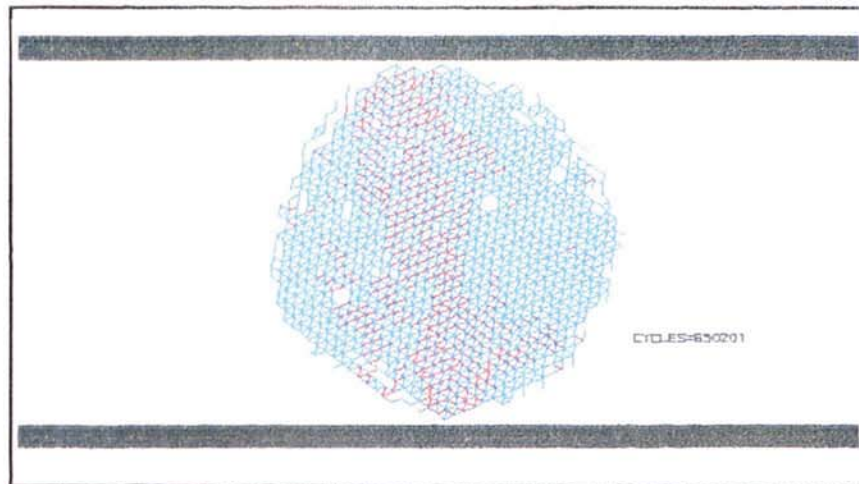
C9a Lattice plot when wall force is maximum, γ = 3.0 J/m^{-2}, Velocity of walls = ±0.4m/s
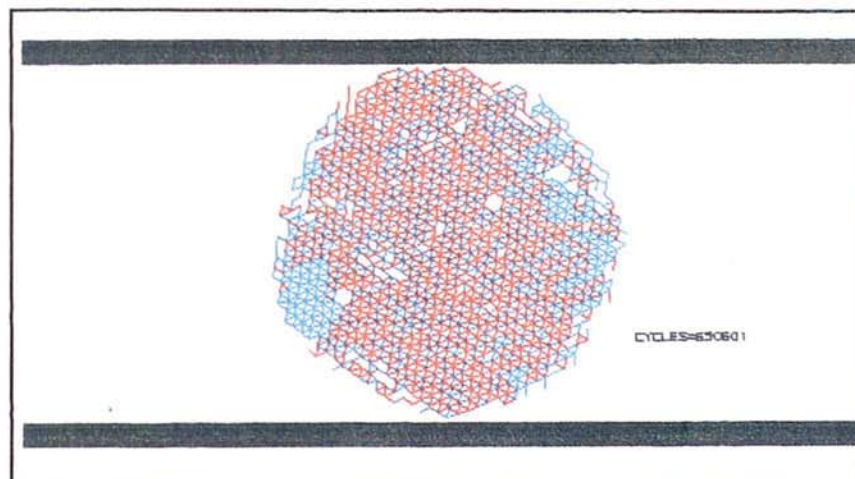
C9b Lattice plot when wall force is zero, γ = 3.0 J/m^{-2}, Velocity of walls = ±0.4m/s

298
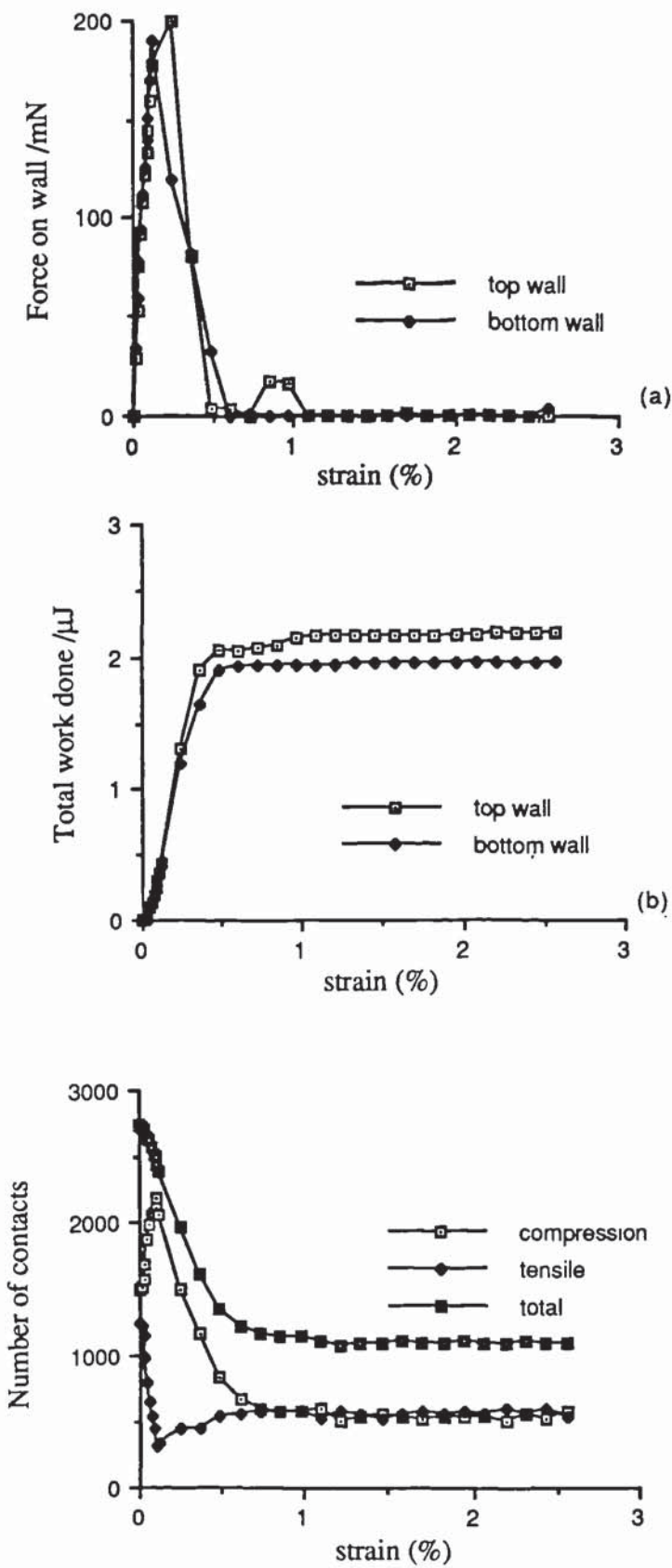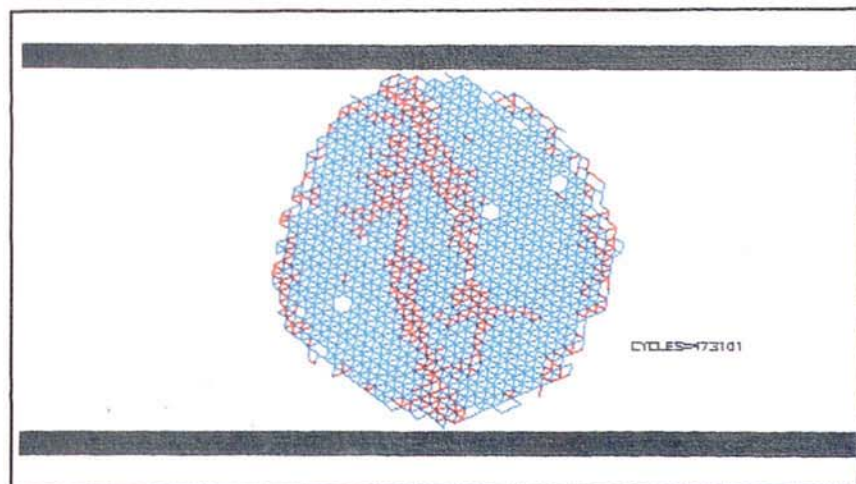
C10 Figures for $\gamma = 3.0$ J/m^{-2}, Velocity of walls $= \pm 0.4$m/s
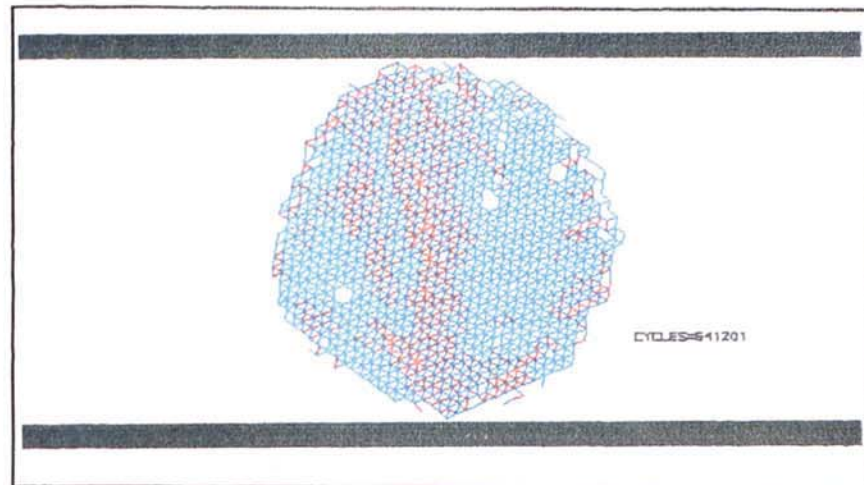
C11a Lattice plot when wall force is maximum, $\gamma' = 2.0$ J/m^{-2}, Velocity of walls = ± 0.05m/s
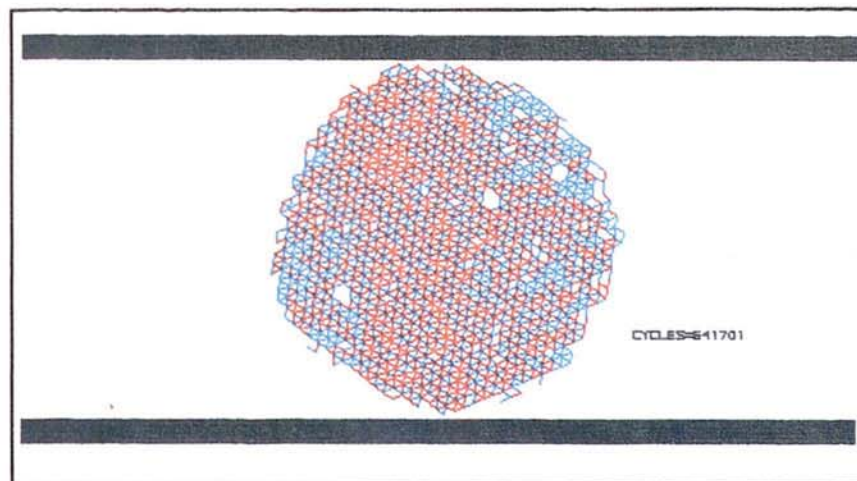
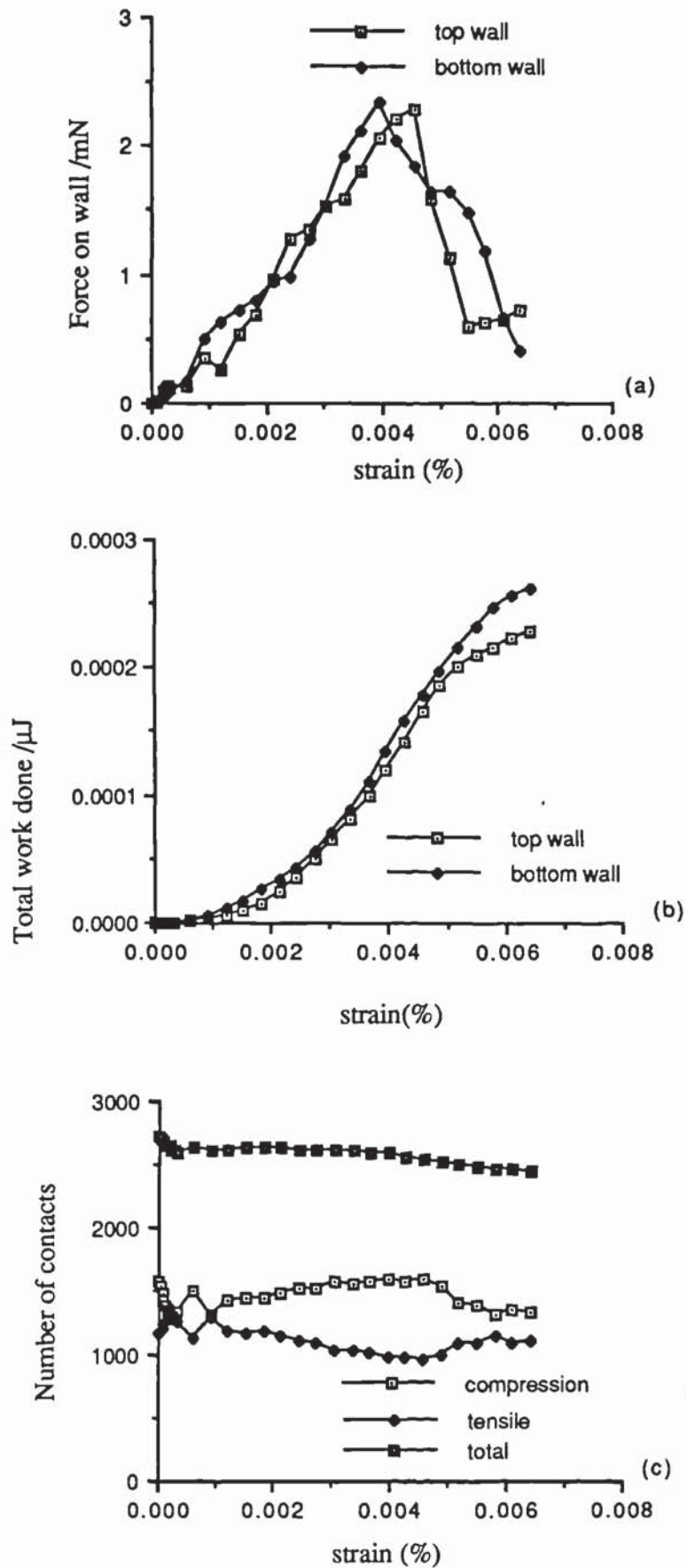C11b Lattice plot when wall force is zero, $\gamma = 2.0$ J/m^{-2}, Velocity of walls = ± 0.05m/s
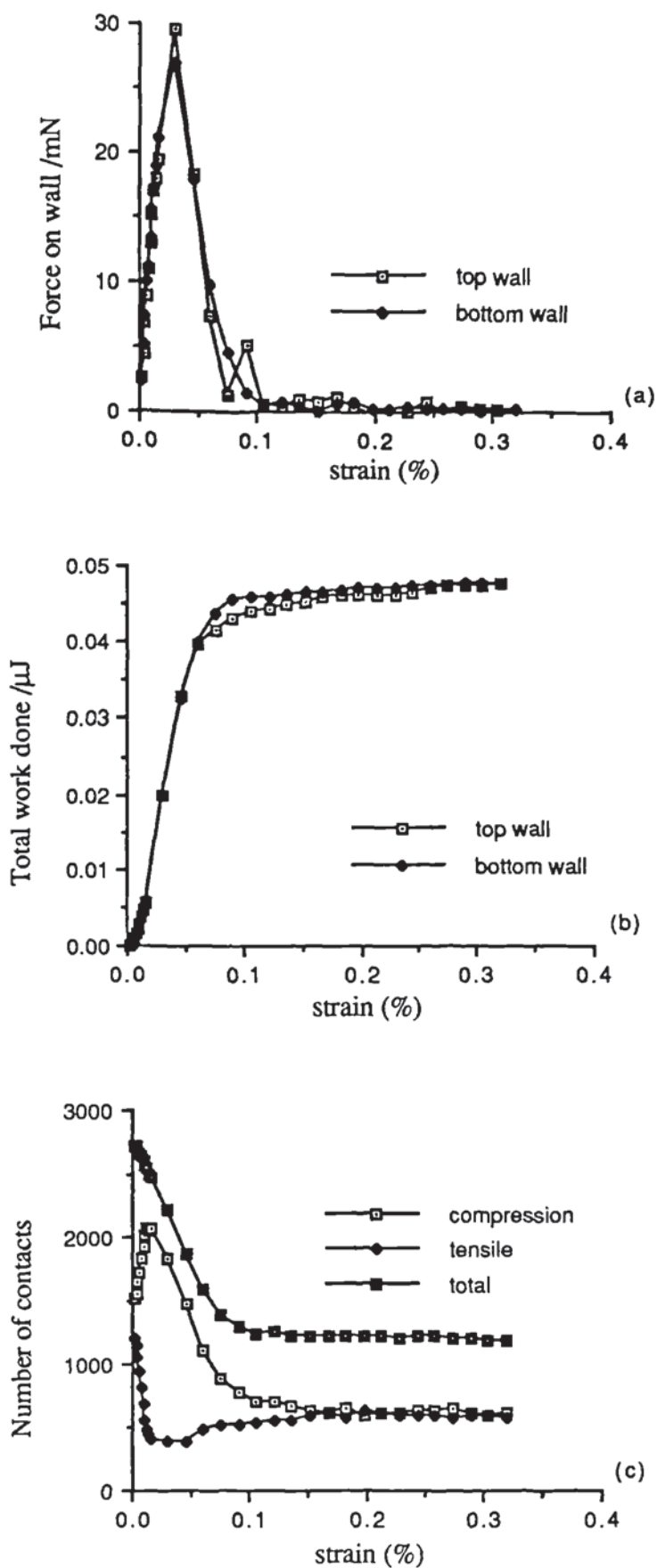
C12 Figures for $\gamma = 2.0$ J/m^{-2}, Velocity of walls = ± 0.05 m/s
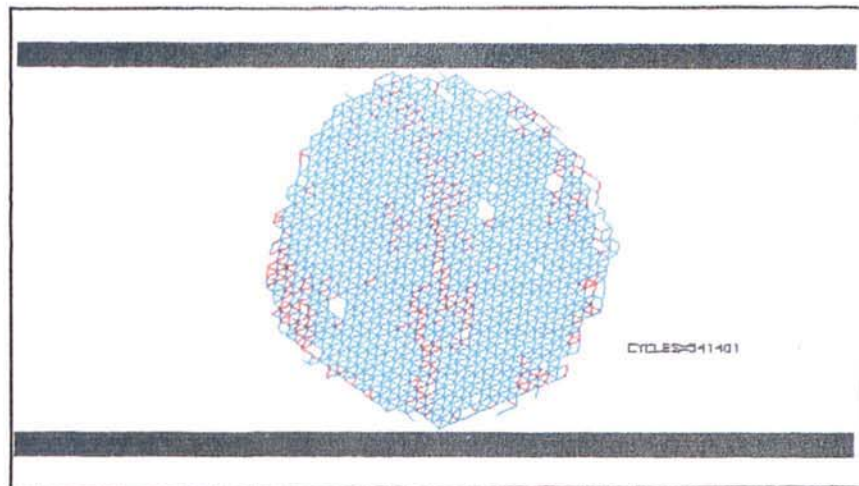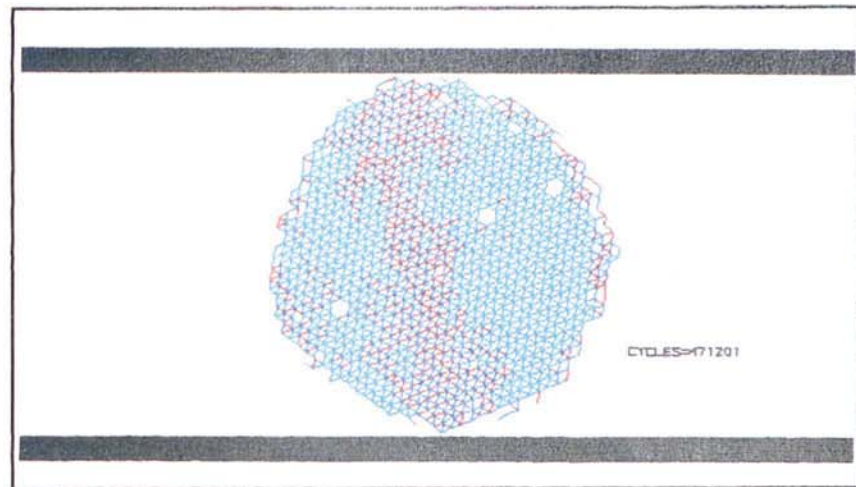
C13a Lattice plot when wall force is maximum, $\gamma = 1.0$ J/m^{-2}, Velocity of walls = ±0.005m/s
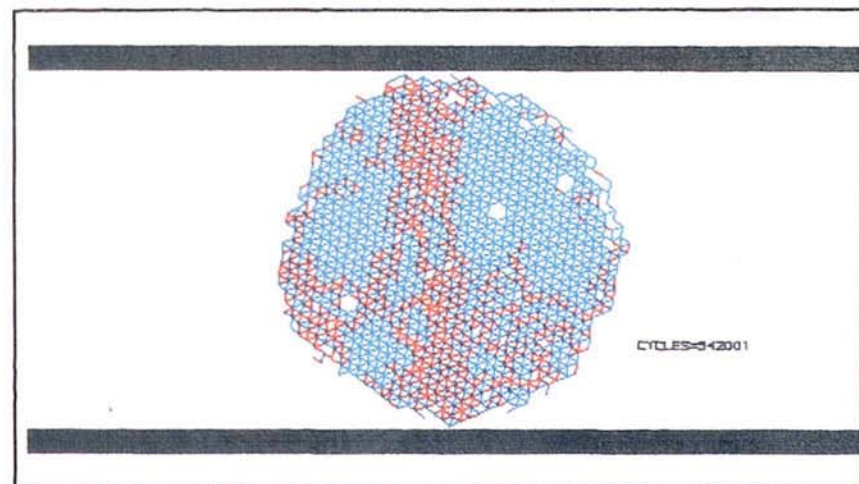
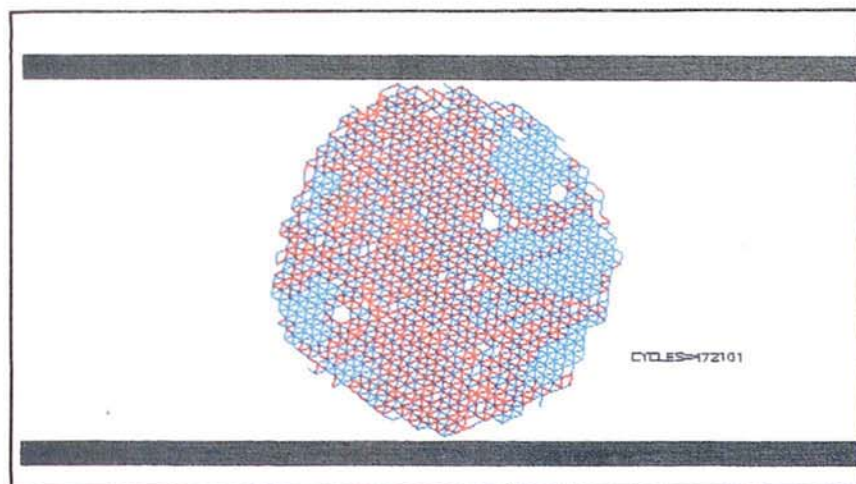C13b Lattice plot when wall force is zero, $\gamma = 1.0$ J/m^{-2}, Velocity of walls = ±0.005m/s
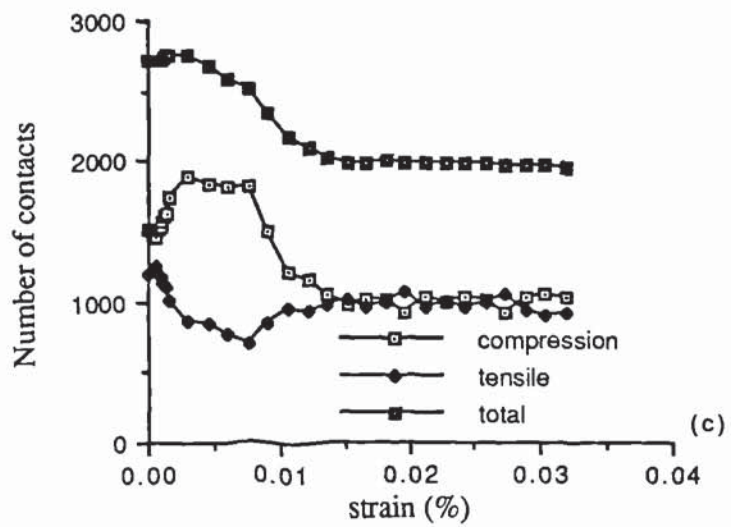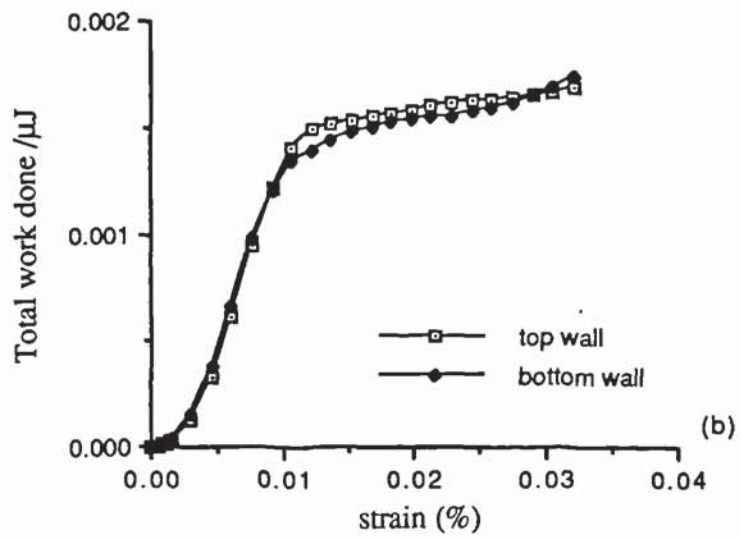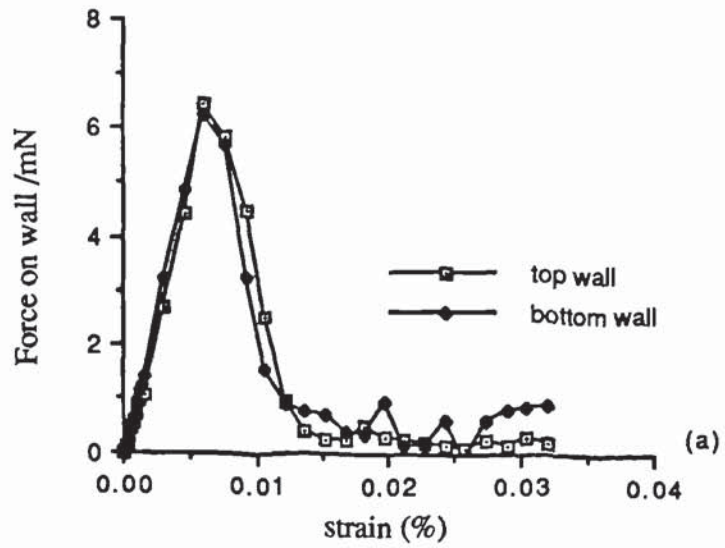
C14 Figures for $\gamma = 1.0$ J/m^{-2}, Velocity of walls $= \pm 0.005$ m/s
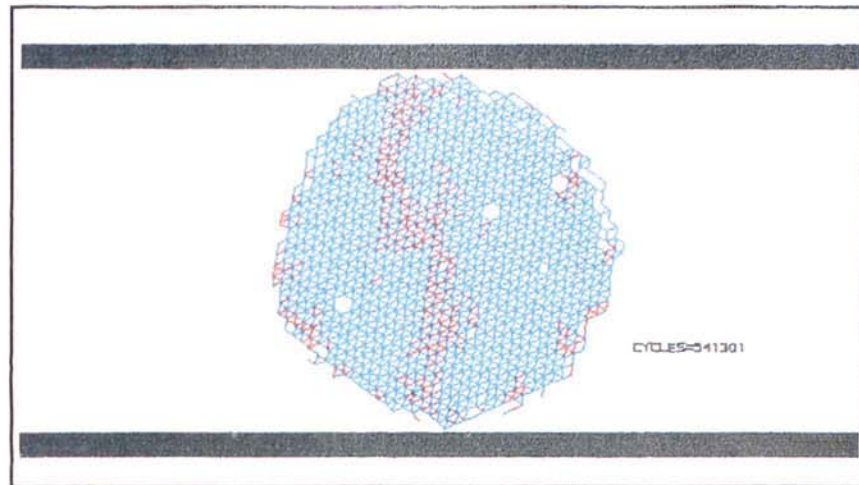
C15a Lattice plot when wall force is maximum, γ = 1.0 J/m^{-2}, Velocity of walls = $\pm$0.01m/s
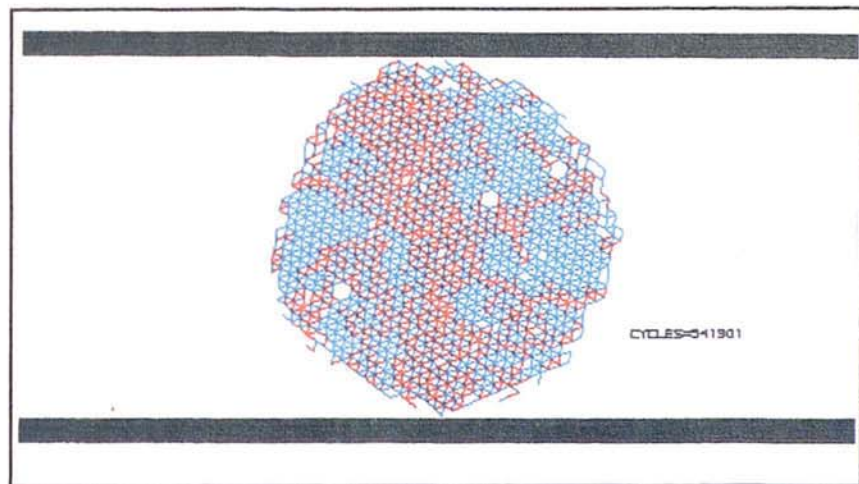
C15b Lattice plot when wall force is zero, γ = 1.0 J/m^{-2}, Velocity of walls = $\pm$0.01m/s
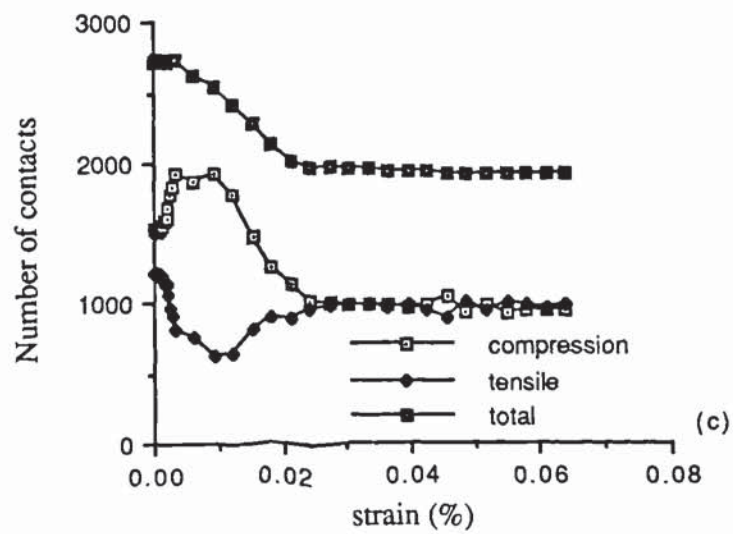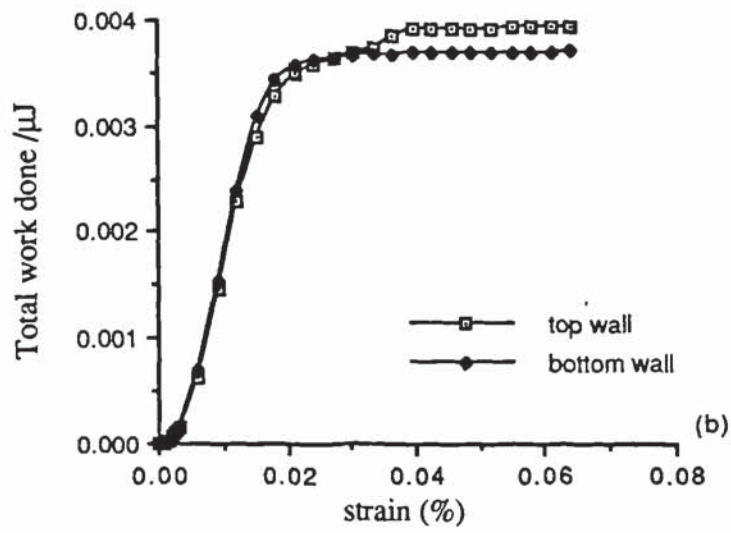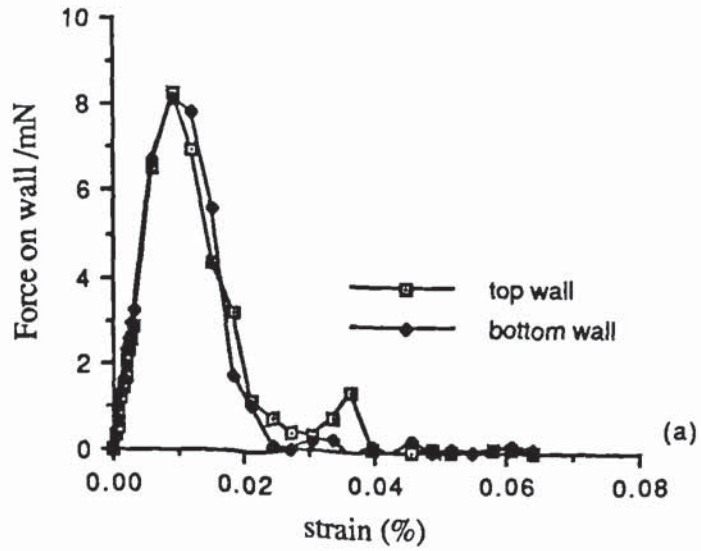
C16 Figures for $\gamma = 1.0$ J/m^{-2}, Velocity of walls = ±0.01 m/s
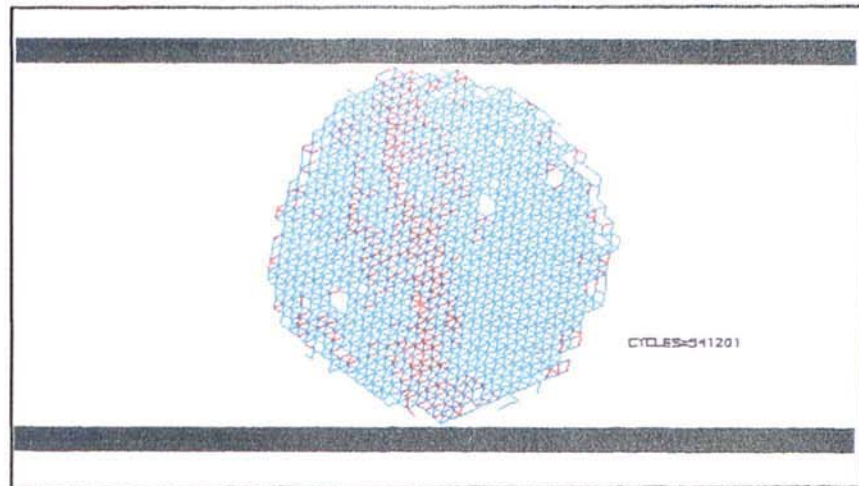
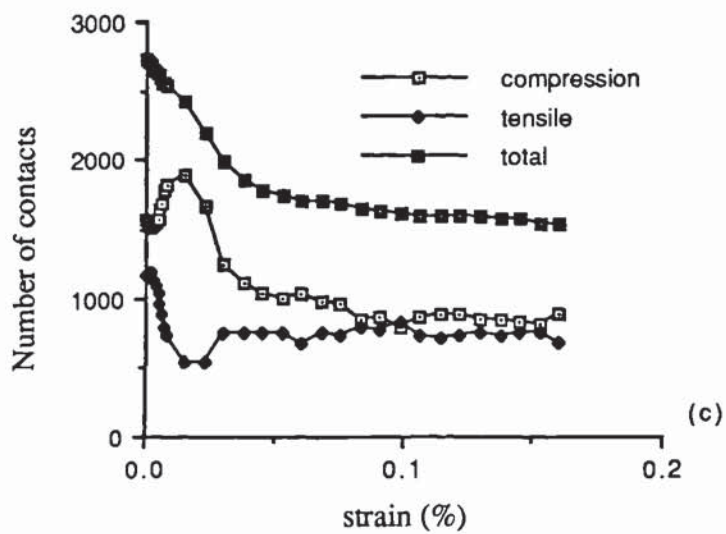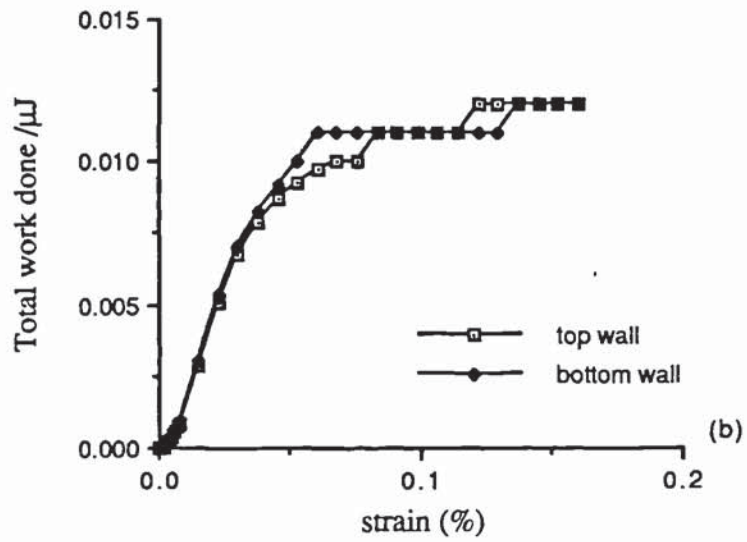C17a Lattice plot when wall force is maximum, $\gamma = 1.0$ J/m^{-2}, Velocity of walls = ± 0.025m/s
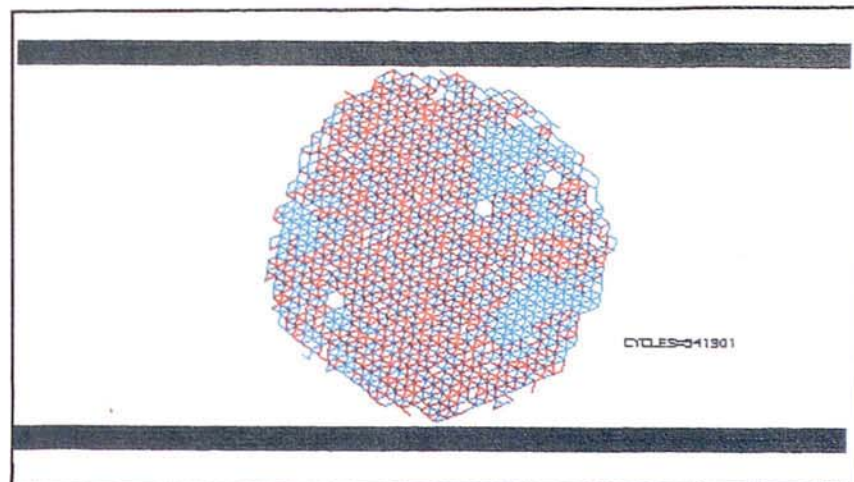
C17b Lattice plot when wall force is zero, $\gamma = 1.0$ J/m^{-2}, Velocity óf walls = ± 0.025m/s
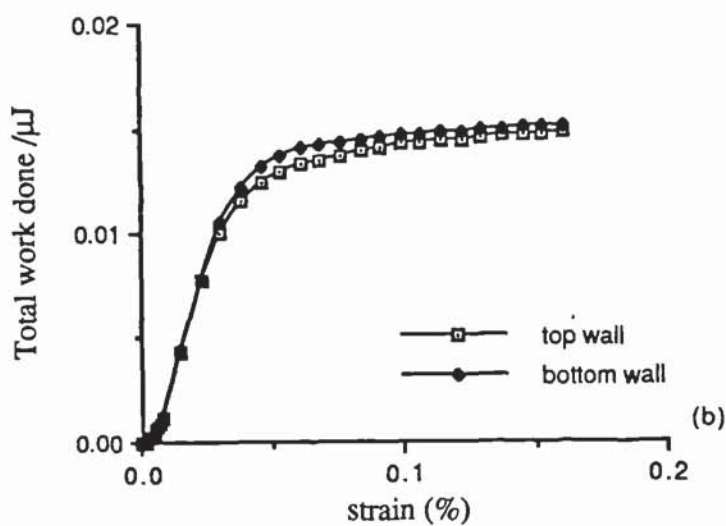
C18 Figures for $\gamma = 1.0$ J/m^{-2}, Velocity of walls = ± 0.025 m/s

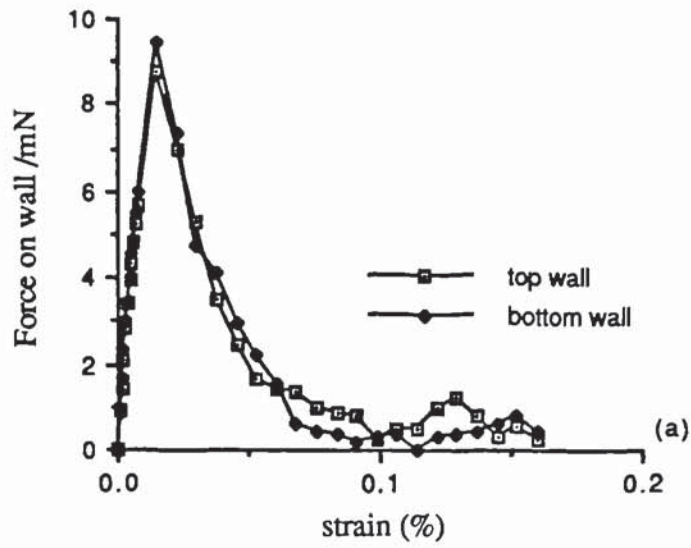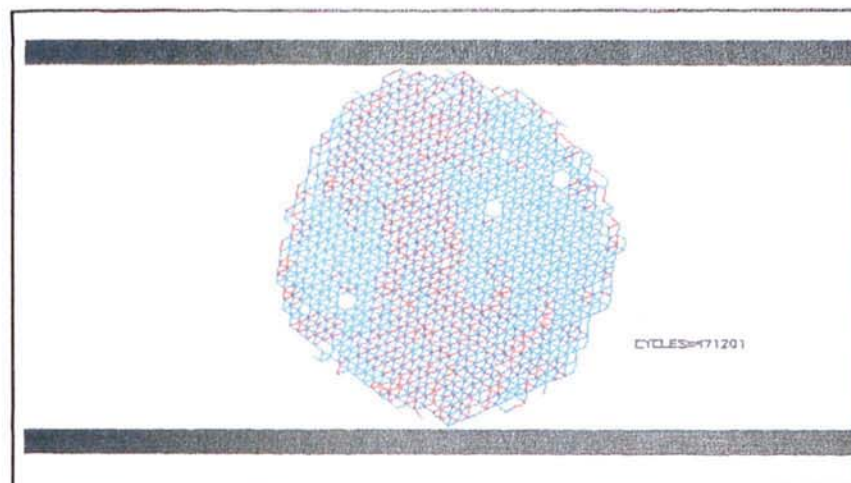C19a Lattice plot when wall force is maximum, $\gamma = 1.0$ J/m^{-2}, Velocity of walls = ±0.05m/s
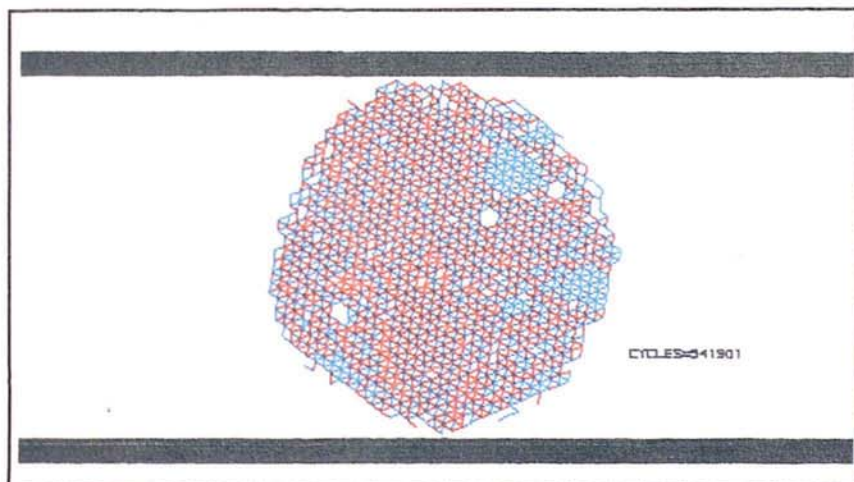
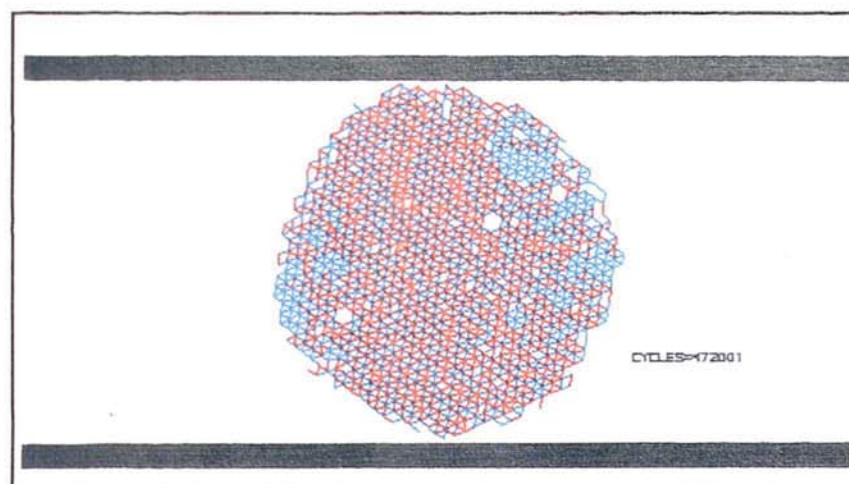C19b Lattice plot when wall force is zero, $\gamma' = 1.0$ J/m^{-2}, Velocity of walls = ±0.05m/s
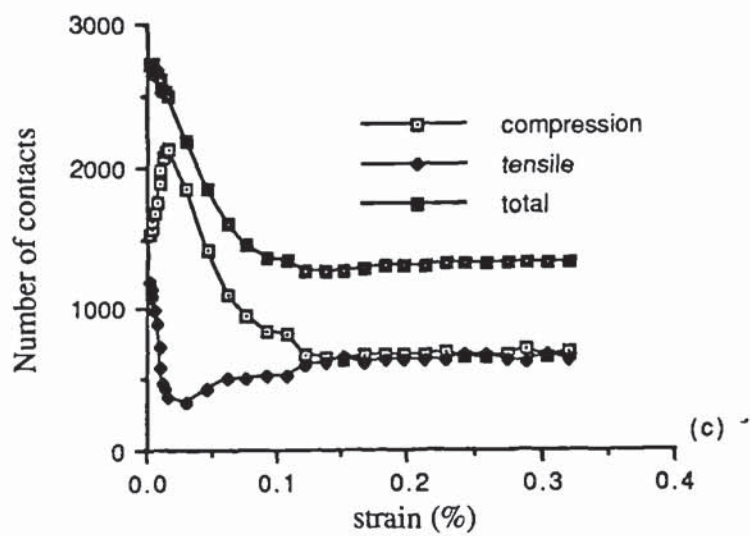
C20 Figures for $\gamma = 1.0$ J/m^{-2}, Velocity of walls $= \pm 0.05$ m/s
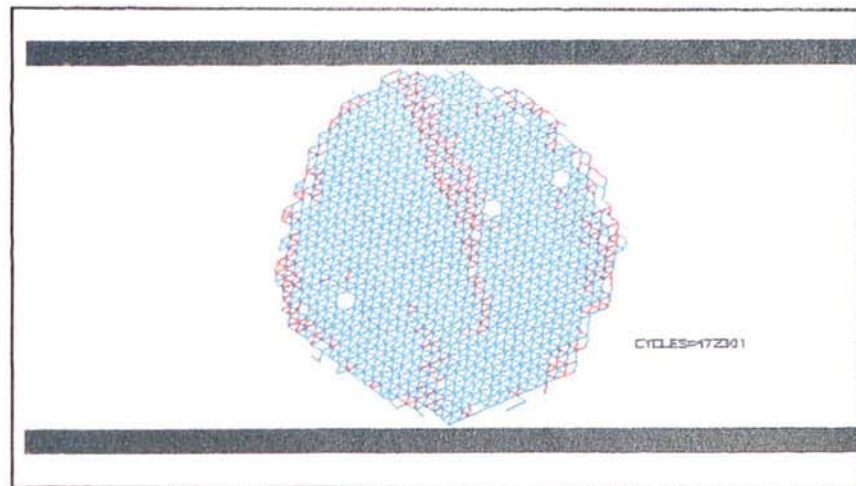
C21a Lattice plot when wall force is maximum, $\gamma = 0.3$ J/m^{-2}, Velocity of walls = ±0.001m/s

C21b Lattice plot when wall force is zero, $\gamma = 0.3$ J/m^{-2}, Velocity of walls = ±0.001m/s

C22 Figures for $\gamma = 0.3$ J/m^{-2}, Velocity of walls = ± 0.001m/s
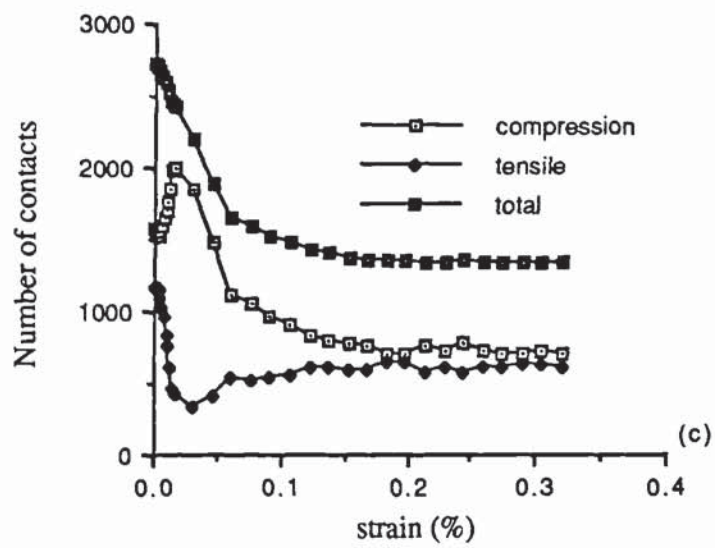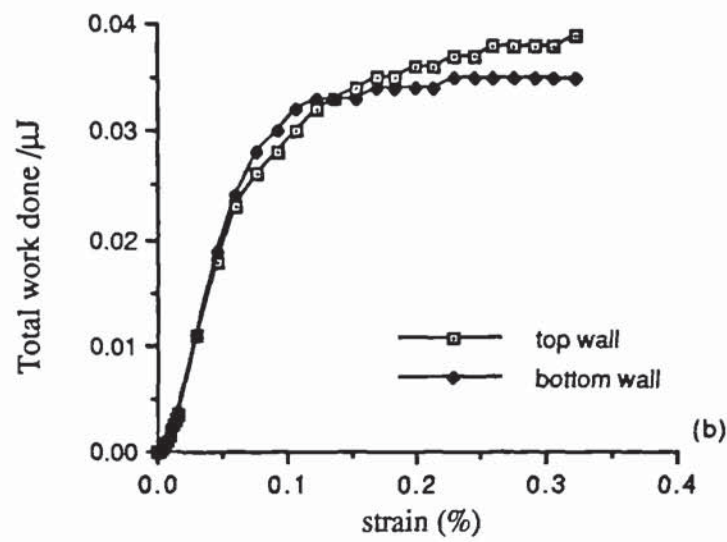
C23a Lattice plot when wall force is maximum, $\gamma = 0.3$ J/m^{-2}, Velocity of walls = ±0.025m/s

C23b Lattice plot when wall force is zero, $\gamma = 0.3$ J/m^{-2}, Velocity of walls = ±0.025m/s

C24 Figures of $\gamma = 0.3$ J/m^{-2}, Velocity of walls = ± 0.025m/s
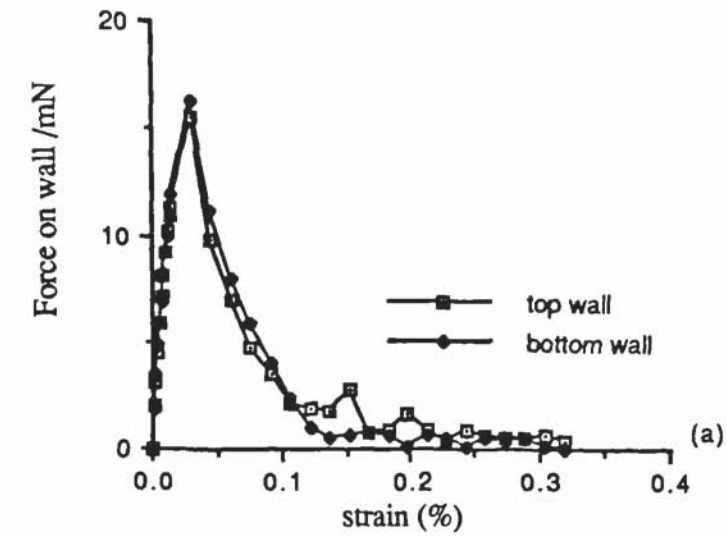
C25a Lattice plot when wall force is maximum, $\gamma = 0.3$ J/m^{-2}, Velocity of walls = ± 0.05m/s

C25b Lattice plot when wall force is zero, $\gamma = 0.3$ J/m^{-2}, Velocity of walls = ± 0.05m/s

314

C26 Figures for $\gamma = 0.3$ J/m^{-2}, Velocity of walls = ± 0.05 m/s